Winter 2007

Sonic Boom Focusing Prediction and Delta Wing Shape Optimization for Boom Mitigation Studies

Nitin Khasdeo
Old Dominion University

SONIC BOOM FOCUSING PREDICTION AND DELTA WING SHAPE OPTIMIZATION FOR BOOM MITIGATION STUDIES

by

Nitin Khasdeo
M. Tech. January 2002, Indian Institute of Technology, Kharagpur, India

A Dissertation Submitted to the Faculty of
Old Dominion University in Partial Fulfillment of the
Requirement for the Degree of

DOCTOR OF PHILOSOPHY

AEROSPACE ENGINEERING

OLD DOMINION UNIVERSITY
December 2007

Approved by:

Dr. Osama A. Kandil (Director)

Dr. Oktay Baysal (Member)

Dr. Chuh Mei (Member)

Dr. Duc Nguyen (Member)

ABSTRACT

SONIC BOOM FOCUSING PREDICTION AND DELTA WING SHAPE OPTIMIZATION FOR BOOM MITIGATION STUDIES

Nitin Khasdeo
Old Dominion University, 2007
Director: Dr. Osama Kandil

Supersonic travel over land would be a reality if new aircraft are designed such that they produce quieter ground sonic booms, no louder than 0.3 psf according to the FAA requirement. An attempt is made to address the challenging goal of predicting the sonic boom focusing effects and mitigate the sonic boom ground overpressure for delta wing geometry.

Sonic boom focusing is fundamentally a nonlinear phenomenon and can be predicted by numerically solving the nonlinear Tricomi equation. The conservative time domain scheme is developed to carry out the sonic boom focusing or super boom studies. The computational scheme is a type differencing scheme and is solved using a time-domain scheme, which is called a conservative type difference solution. The finite volume method is used on a structured grid topology. A number of input signals Concorde wave, symmetric and ax symmetric ramp, flat top and typical N wave type are simulated for sonic boom focusing prediction. A parametric study is launched in order to investigate the effects of several key parameters that affect the magnitude of shock wave amplification and location of surface of amplification or "caustics surface." A parametric studies includes the effects of longitudinal and lateral boundaries, footprint and initial shock strength of incoming wave and type of input signal on sonic boom focusing.

Another very important aspect to be looked at is the mitigation strategies of sonic boom ground signature. It has been decided that aerodynamic reshaping and geometrical optimization are the main goals for mitigating the ground signal up to the acceptance level of FAA. Biconvex delta wing geometry with a chord length of 60 ft and maximum

thickness ratio of 5% of the chord is used as a base line model to carry out the fundamental research focus. The wing is flying at an altitude 40,000 ft with a Mach number of 2.0. Boom mitigation work is focused on investigating the effects of wing thickness ratio, wing camber ratio, wing nose angle and dihedral angle on mitigating the sonic-boom ground signature.

Optimal shape design for low sonic boom ground signature and least degradation of aerodynamic performance are the main goals of the present work. Response surface methodology is used for carrying out wing shape optimization. Far-field computations are carried out to predict the sonic boom signature on the ground using the full-potential code and the Thomas ray code.

ACKNOWLEDGMENTS

The first place in these acknowledgements belongs to my advisor Dr O. A. Kandil for all the help and support he has given me throughout the years. He has guided me flawlessly and has always been available to answer all my questions and correct my mistakes with immense clarity and speed. I also want to thank him for giving me an opportunity to come to Old Dominion University for my PhD program.

I wish to thank Dr. Oktay Baysal, Dr. Chuh Mei and Dr. Duc Nguyen for participating in my dissertation committee and willingness to help. I also would like to thank you graduate program director Dr. Brett Newman for the support and guidance during my PhD program.

During my years at Old Dominion University I benefited from the friendship of my colleagues. I am grateful to my Indian, Korean and Turkish friends in the Aerospace Engineering Department, a lot many names to mention for making life in and outside the office more fun.

My father instilled in me the value of higher education. He passed away before I started at Old Dominion and he would have very much liked to see me finish this work. I am eternally grateful to my mother Mrs Anju Khasdeo for having the vision to send me abroad at that stage.

I would like to thank my elder brothers and my younger brother Lalit Khasdeo who encouraged me at every step of my life and stood behind everything when I am away from home. I would like to thank my wife Manu for always believing in me and offering me her unconditional love. Finally, I would like to thank my family for always believing in me and encouraged me at every step of my life. This thesis would not have been possible without their loving support and help. Thank you

To my father Mr. Manik Rao Khasdeo

TABLE OF CONTENTS

LIST OF TABLES

LIST OF FIGURES

Figure Page

LIST OF ABBREVIATIONS AND SYMBOLS

ϕ	Acoustical potential or Velocity potential
t	Pseudo time variable
τ	Dimensionless phase variable
x	Dimensionless axial variable along the tangent to the caustic surface
z	Dimensionless normal distance to the caustic from
δ	Characteristic thickness of diffraction boundary layer at the caustic
μ	Measurement of nonlinear effects relative to the diffraction effects
ρ_0	Ambient stagnation density
v_0	Ambient stagnation velocity
c_0	Ambient speed of sound at stagnation conditions
M	Acoustical Mach number
ω	Omega is a characteristic frequency
F	Function is the dimensionless time waveform of the incoming signal
z*	Normal distance to the caustic from O
R_{sec}	Radius of curvature of the intersection of the caustic surface with the Oxz plane
R_{cau}	Relative radius = $1/(1/R_{sec} - 1/R_{ray})$
R_{ray}	Radius of curvature of the projection in the plane
c_0	Ambient speed of sound at stagnation conditions
T_{ac}	Characteristic duration of incoming signal near point O
β	Nonlinearity parameter = $(1+\gamma)/2$
M_{ac}	acoustical Mach number = $P_{ac}/\rho_0 c_0^2$
p_{max}	signal maximum overpressure
∞	Free stream
ξ	Derivative relative to these coordinates
η	Derivative relative to these coordinates
ζ	Derivative relative to these coordinates
c	wing or airfoil chord

H	Altitude
h	distance below aircraft or wing
P	static pressure
P_∞	free stream static pressure
q_∞	Dynamic pressure
S	wing area
U	longitudinal velocity component
V	lateral velocity component
W	vertical velocity component
C_d	drag coefficient = $drag/ q_\infty S$
C_l	lift coefficient = $lift/ q_\infty S$
C_P	Pressure coefficient =Overpressure Ratio = $(p - p_\infty)/q_\infty$
ΔP	Change in Pressure $P-P_\infty$
α	Angle of attack

ABBREVIATIONS

FAA	Federal Aviation Authority
RMS	Root mean square
CFD	Computational fluid dynamics
CFL3D	Computational Fluids Laboratory 3 Dimensional
EFP	Euler-Full Potential
GASF	Grid adaptation and shock fitting
SQP	Sequential Quadratic Programming

CHAPTER 1
INTRODUCTION

Supersonic travel over land would be a reality only if new aircrafts are designed such that they produce quieter ground sonic booms. An aircraft traveling faster than the speed of sound creates a boom on the ground. When aircraft travels at very high speeds the waves in front of the aircraft are bunched up at a common surface and create a much stronger shock wave. A strong shock wave will have a very high, abrupt pressure rise. When these strong shock waves propagates through the atmosphere and reaches ground, a thunder like sound is heard that is commonly known as a sonic boom. Sonic boom theory was first referred to in the literature by Whitham [1, 2] in the late 1950's. After Whitham, many researchers including Busemann [3], Walkden [4], Jones [5], and others [6 - 10], explained sonic boom phenomenon and worked on mitigating the boom effects on ground level. Sonic boom ground overpressure for Concorde aircraft flying at a cruising speed of Mach 2.0 generates more than 2.0 psf, which is serious enough to hurt the human hearing or even crack glass windows or, in some cases, can lead to a structure failure. According to the Federal Aviation Authority (FAA) [11] aircraft is not allowed to fly overland if it exceeds the overpressure of 0.3 psf, and 2.0 psf is quite beyond the permissible limit.

The initial rise in pressure, or leading shock, is due to the coalescence of various shock waves emanating from the forward components of the aircraft, while the aft pressure rise usually stems from recompression shocks emanating from the aft regions of the aircraft. Research is aimed at reducing the magnitude of both the forward and aft strong shock waves at the near field. The most intense sonic boom is the focused sonic boom due to aircraft transonic acceleration from Mach 1 to supersonic cruise speed. Sonic boom focusing develops during aircraft accelerations, climbing, turning and maneuvering. Sonic boom focusing essentially involves an unsteady shock wave interaction that leads to amplification in shock wave strength just above the ground at surfaces called "Caustics" as defined by Guirads [12] in 1965. The amplification could be two to four times the carpet boom shock strength. The focused boom response is also known as a

---

The journal model used for this dissertation is the AIAA Journal.

"super boom". Accurate prediction capability of focused sonic boom at caustic surface can significantly influence the research guidelines for supersonic aircraft development. In the current research work a prediction solver for sonic boom focusing phenomenon using conservative computational fluid dynamics (CFD) solution approach is developed. A parametric study is carried out in order to identify the important parameters that significantly affect the magnitude of shock wave amplification and location of caustic surface.

Table 1.1 lists some of the noise level associated with the day to day life events. Anything above 120 db is not acceptable for human hearings. As mentioned earlier sound levels with sonic boom could be higher then 2.0 psf (160 db).

Sound Pressure (N/m^2)	Sound Level (dB)	Typical Source
0.00002	0	Threshold of human hearing
0.002	40	Quite office
20	120	Human pain threshold
200	140	Jet aircraft taking off at 25 m
2000	160	Peak level at ear of 0.303 caliber rifle

Table 1.1 sonic Boom noises of daily life events

The goal in supersonic configuration design is biased towards boom minimization. The ideal approach would be to distribute lift and volume in such a way that the longitudinal and span wise distribution of pressure propagated to the ground has the lowest possible pressure increments due to shocks, thus, minimizing the boom, associated with physical discomfort and structural damage.

Numerous approaches to shape optimization alone are considered to lead to sonic boom pressure levels as low as 0.3 psf, the objective that DARPA [11] has set for the Quiet Supersonic Platform (QSP) [13] program. In the current work biconvex delta wing shape is considered as base line geometry and investigated for important geometry parameter and their effects on sonic boom ground signature. An optimization study is also carried out for obtaining the low boom geometry profile that least degrades on aerodynamic performance. In the current research work a multi-objective shape optimization strategy is employed to meet the goal set by DARPA [11] and the FAA [11].

1.1 Motivation

It is understood that the development of high speed supersonic jets is increasingly demanded in the commercial and military sectors [14]. Sonic boom and sonic boom focusing are the potential reason to completely stop the development of civil supersonic transport aircrafts according to the FAA [11]. A lot of work has already been published over the last four decades producing deep insight into the sonic boom problems related with supersonic commercial jets. The boom focusing has a greater impact as compared to normal sonic boom as the amplification involved in sonic boom focusing could be higher than two to four times that of the normal boom strength. The computational tools that can predict sonic boom focusing effect with much higher accuracy are in great demand for supersonic transport aircraft research. Extensive research is desired for prediction and mitigation approaches as well as for sonic boom problems.

1.1.1 Supersonic Air Transportation

As indicated in figure 1.1 there was no supersonic civil transport aircraft in operation after Concorde stopped its operation in 2003. Over the years there has been increasing demand for supersonic civil transportation over land.

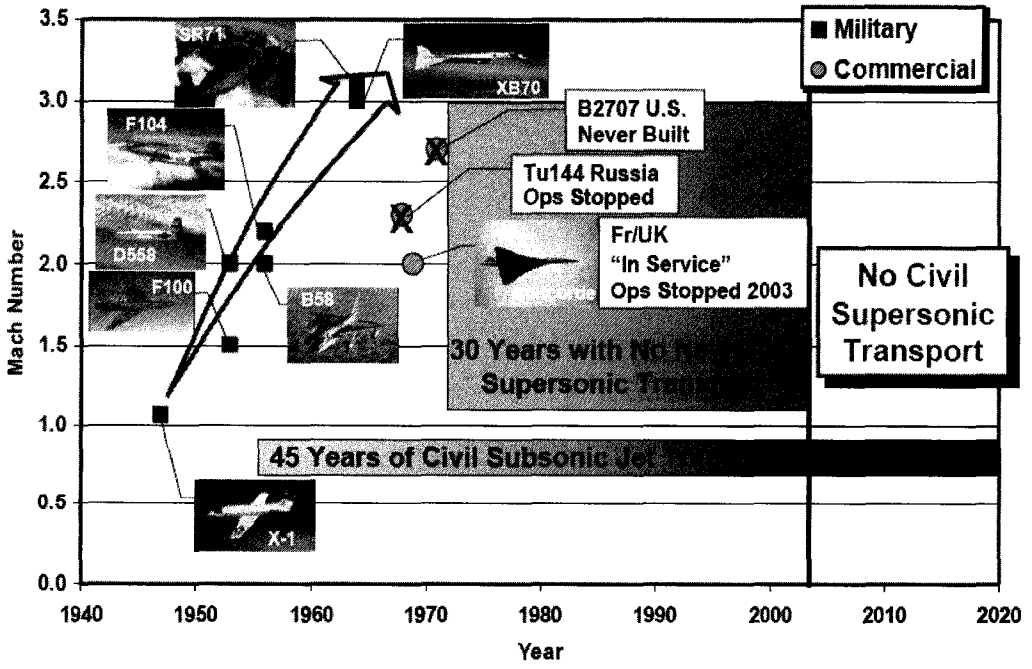

Figure 1.1 Supersonic Jet Transport Scenarios [14]

Supersonic travel can significantly save time and cost with non stop flights from the USA to countries in Asia, Europe and Japan. The British-French Concorde made its maiden flight in 1969, and from 1976 it routinely flew supersonic trans-Atlantic flights over seas. Figure 1.1 shows the major developments in supersonic business jet development over the last 60 years.

Supersonic business jet operations over land have been drawing great attention after the end of the Concorde service was announced. It is believed, however, that civilian supersonic aircraft may take a viable return in the business jet market. It's been possible to cut down the huge cruise times for transatlantic flights with supersonic flights, but at the same time one need to look into the operating costs for supersonic travel. They should not be substantially higher than those for subsonic travel.

Aerion and SAI (Supersonic Aerospace International) unveiled two distinctive business jet designs [15] at the National Business Aviation Association meeting. Gulf Stream is also developing concepts for its own supersonic business jet [14]. Northrop Grumman [16] and Lockheed Martin Corporation [17] are also among the top competitors for business jet research. However, all the key players are moving cautiously; substantial time and money will be required.

1.1.2 Sonic Boom Mitigation

The sonic boom manipulation and controlling strategies started in late 50's with Busemann [3]. George [18] and Seebass [19] contributed significantly in many approaches based on the Whitham F function [1, 2] approach to addressing the boom mitigation problem. Darden [20] added the atmospheric effects and nose bluntness observations for mitigating the boom on the ground. The most important issue is to choose a criterion to minimize the ground signature. There could be many design parameters and objectives for boom mitigation study and one need to go through the sensitivity analysis in order to choose the design parameters. Researchers have used one or more design variables and associated them with a sonic boom ground signature.

In Fig 1.2 the red line sketch shows the generation of an undesired N shape shock wave signature on the ground. There are multiple shocks generated with different shock strengths in the near field depending upon the aerodynamic shape of the aircraft. When these shocks propagate through the atmosphere they merge and create a much stronger shock on the ground. Similar merging happens at the rear portion of the aircraft with recompression shock waves. This interaction leads to a typical N wave shape of sonic boom signature on the ground.

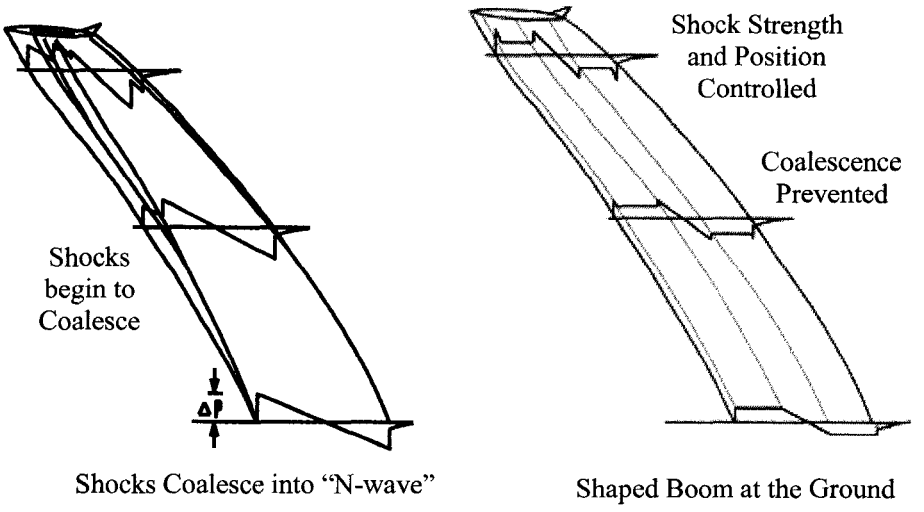

Figure 1.2 Flat top profiles with shape optimization [21]

The idea here is to come up with an aerodynamic shape with which one can prevent the merging of leading and trailing shock so that one can obtain a flat top profile with reduced boom strength on the ground. The blue line sketch in Fig 1.2 shows how one can obtain the reduced peak flat top sonic boom signature ground. This approach was proposed by George and Seebass [21]. George and Seebass's approach is successfully implemented by Northrop Grumman in the SSBD program [16] with F5E aircraft. Figure 1.3 shows the major changes made by Northrop Grumman under SSBD mission [16].

All the changes were made to address the leading shock impact on the ground. The nose angle and total thickness for the lower front portion of the aircraft has decreased to a lower value. After reshaping the front lower portion of the F5E aircraft it was demonstrated that the peak has been reduced by 25% with flat top sonic boom signature on the ground as shown in Fig 1.4.

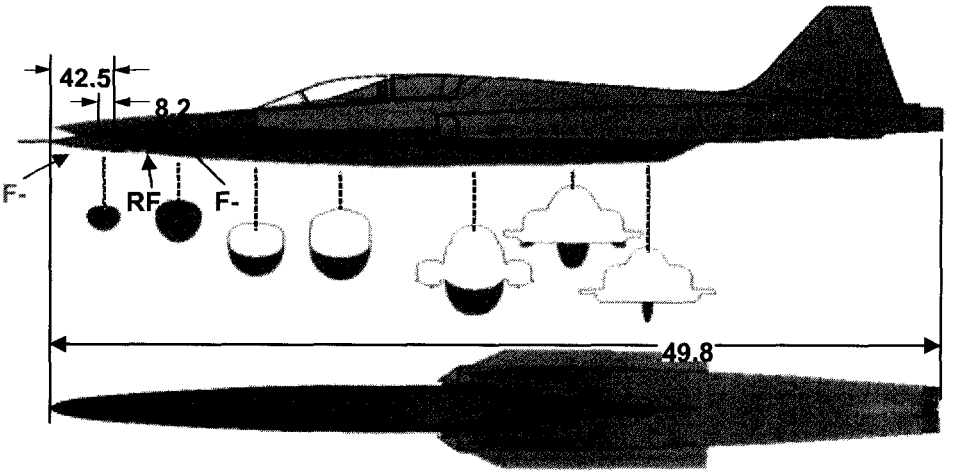

Figure 1.3 Reshaping of F5E Aircraft [16]

SSBD was an excellent validation of design methodology; it provides a confidence level for understanding the acoustic signature propagation. SSBD also acts as an experimental proof for shaped sonic boom ground signature possibility.

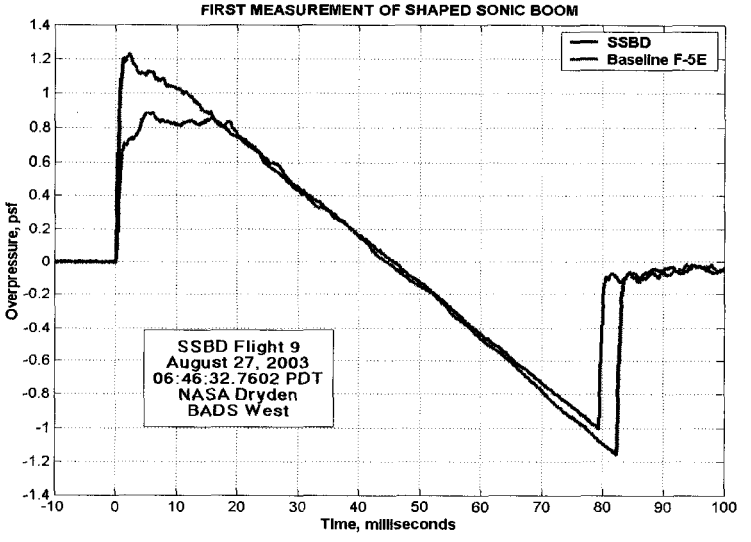

Figure 1.4 Boom Reduction after reshaping of F5 [16]

Some of the other geometry parameters such as dihedral and anhedral also have been considered for shape optimization for boom mitigation study. Earlier studies by Hunton [22], Carlson [23] motivated designers to include dihedral as a parameter contributing towards lowering boom levels. Carlson [23] noted that when Mach cuts were used to calculate the equivalent axisymmetric body area distribution the dihedral provided an

effective lengthening of the wing over the zero dihedral geometry. Bobbitt, Kandil and Yang [24] also have shown 10 and 14 % boom reduction with 15 deg and 20 deg dihedral angle respectively, with a biconvex delta wing. Figure 1.6 shows the variation in leading shock strength with altitude. Figure 1.5 shows the comparison for a straight delta wing over dihedral delta wing with dihedral angle of 15 deg and 20 deg. Many such ideas have motivated the continuation of research in this direction for mitigating the boom effects.

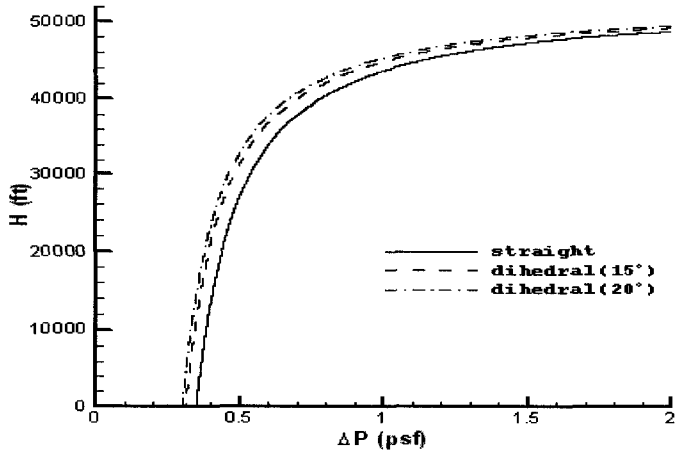

Figure 1.5 Dihedral effects on sonic boom propagation [24]

One also needs to consider the effects on lift and drag of the aircraft while optimizing geometry parameters for lowering the boom on the ground. Dihedral study on sonic boom [24] reported some loss in lift coefficient and gain in drag coefficient. A multi objective optimization approach is needed for least degradation of aerodynamics performance while achieving the desired levels of reduction in sonic boom ground signature.

1.1.3 Sonic Boom Focusing

Sonic boom focusing happens during aircraft acceleration, climbing, turning or maneuvering at supersonic speed. Depending on the flight and atmospheric conditions, the shock wave formed by supersonic flight can reach the observer on the ground in four major forms—primary boom, secondary boom, focused boom, and shadow-zone boom. In the current research work primary boom in general, is referred to as sonic boom and the rest of the three booms only appear with accelerating flights and are referred to as sonic boom focusing or super boom. Figure 1.6 shows one of the cases for unsteady

shock interaction that leads to amplification of the shock waves and result in focused boom at caustic surfaces. The amplification could be more than three times depending upon the shape, flying altitude and speed of the aircraft.

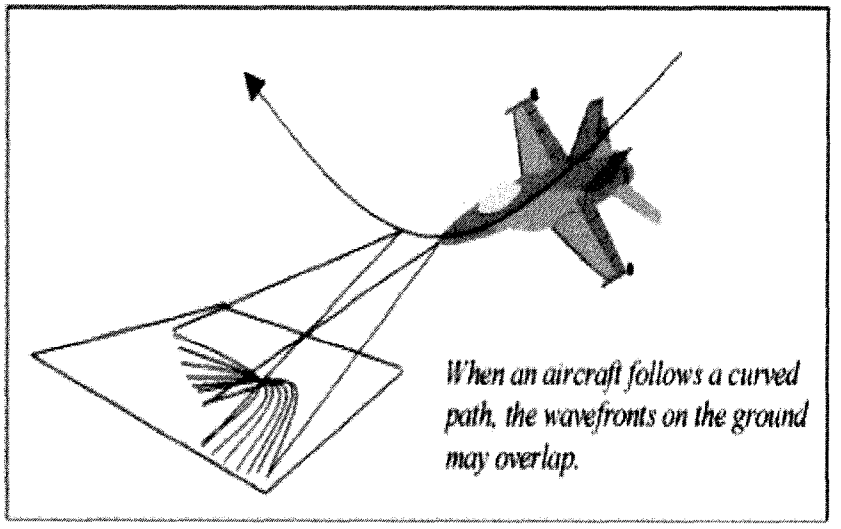

Figure 1.6 Sonic booms focusing with Accelerating Aircraft [25]

Typically shock waves propagate from the upper atmosphere towards the ground in the illumination zone. The shock waves get focused at a surface called caustics just above the ground. Waves are bounced back in the upper atmosphere above the caustics line and exponentially decay below the caustics surface and eventually die out in the shadow zone. Focused boom is the boom with the maximum peak pressure possible during the focusing phenomenon.

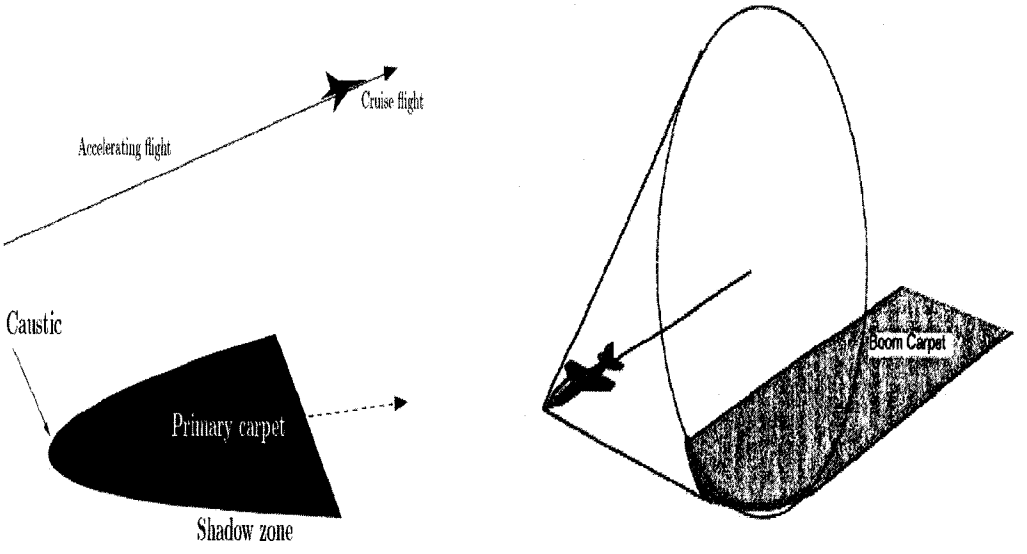

Figure 1.7 Focusing Phenomenon at Caustic Surface [25]

Secondary boom focusing effect [26] has not been discussed in the current research work. Secondary boom has a significantly low impact on the environment, and normally it is well below the level that would cause any kind of annoyance. Figure 1.7 shows the caustics surface and shadow zone for sonic boom focusing phenomenon. Magnitude of amplification and location of caustic surface primarily depends upon the altitude of the flying aircraft, speed of flying, aerodynamic shape, non-linearity and turbulence effects of the atmosphere. Sonic boom focusing is a regular phenomenon with supersonic flight and must be addressed for a viable supersonic civil transport aircraft's development.

1.2 Sonic Boom - Environmental Concern

As of 1973, civil supersonic flights are forbidden over land. It is commonly accepted that loud and unexpected noises tend to disorient and startle people, and studies conducted by NASA [27] indicates that reaction to sonic boom is far more severe than reaction to other types of noise at analogous amplitude levels. However, the long-term health effects of daily exposure to sonic booms are yet to be investigated, and a quantitative measure of acceptability has not been established.

NASA Langley Research Center has conducted three groups of studies on sonic booms that include, laboratory, in home and in the field. The in home study [27] conducted by NASA presented participants with simulated sonic booms played within their normal home environment. The results of this study indicates increase in the number of boom occurrences increases the annoyance in a manner consistent with equal energy theory [27] and proves that having asymmetrical waveforms were less annoying than symmetrical waveforms of an equivalent perceived level.

H K Chenge [28] et al. demonstrated that sonic boom could severely affect sea water life. Experiments conducted by Chenge [28] have confirmed that a boom propagated undersea affects sea life. Furthermore, there is fear that sonic booms will pose a threat to aquatic life, fowl, farm and wild animals [28]. Therefore, the environmental impact of sonic boom needs to be carefully evaluated and precise noise regulations for sonic boom need to be devised for the sea as well. Such regulations could substantially limit the

profitability of a new SST or stop its implementation altogether. Table 1.2 lists sonic boom generated by some of the civil and military supersonic aircrafts [25]. Sonic boom overpressure generated by the Concorde aircraft at Mach number 2 is beyond the acceptable limit of the FAA [11], so it was only allowed to fly supersonic over sea.

Vehicle	Mach number	Altitude (ft)	Sonic boom overpressure (psf)
SR-71	3	80,000	0.9
Concorde SST	2	52,000	1.94
F-104	1.93	48,000	0.8
Space shuttle	1.5	60,000 (landing)	1.25

Table 1.2 sonic Boom noises of civil and military aircraft [25]

Figure 1.8 shows the experimental measurements of the ground boom propagated from an SR-71 flying at a free stream Mach number of 1.5 and a flight altitude of 48,000 ft. Figure 1.8 also compares the sonic boom overpressure for XB-70, SR-71, Concorde, F-104 and space vehicles. The strength of the sonic boom is usually measured in pounds per square foot of the overpressure of the initial shock wave.

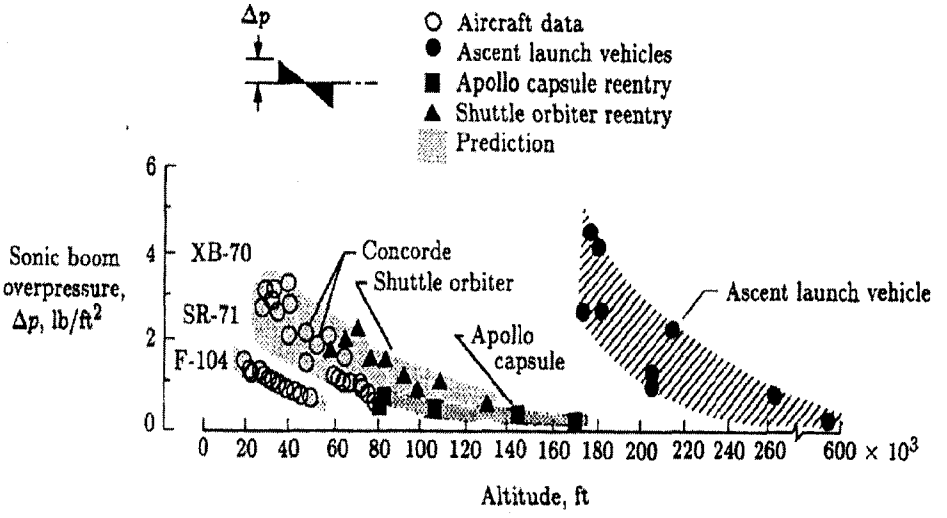

Figure 1.8 Sonic boom overpressures - civil and military supersonic jet [29]

1.3 Problem of Interest

Research interests for the current work is to develop computational methods to predict sonic boom focusing effects, carry out the parametric studies and also carry out a shape

optimization study for mitigating the sonic boom ground signature. A computational scheme is formulated in a conservative form to predict the focusing behavior. The sonic boom prediction, mitigation and shape optimization studies are the direction toward a low boom configuration. Biconvex shape delta wing geometry is considered a baseline case to carry out the shape optimization study. The shape design parameters considered for the current study are maximum thickness ratio, maximum camber ratio, lower front portion nose angle and dihedral angle of the wing.

1.3.1 Super Boom Prediction and Parametric Studies

Sonic boom focusing essentially is an unsteady non linear shock wave interaction governed by non linear Tricomi equation [12]. A computational scheme is proposed to solve the non linear Tricomi equation in conservative form without splitting the partial differential equation (PDE) in non conservative forms.

A parametric study is desired in order to identify the important parameters that significantly affect the shock wave amplification at caustic and location of caustics. Parametric studies can help to understand and predict the crucial flow behavior of boom focusing phenomenon. Location of caustic and amplitude of boom focusing is vital information for supersonic transport aircraft development. Different types of input wave signal, flight Mach number, altitude, location of computational domain and footprint and strength of incoming wave are the major parameters to be looked at for the paramedic study.

1.3.2 Wing Shape Optimization for Boom Mitigation

Aerodynamic shape optimization is identified as a key factor for sonic boom mitigation on the ground. One of the goals of the current study is to investigate the effects of wing shape parameters on mitigation of sonic-boom ground signature. In the current mitigation study the baseline shape is a biconvex delta wing with 60 ft of chord length and maximum thickness ratio of 5% of the chord. Individual effects of maximum wing thickness ratio, maximum wing camber ratio, lower front surface nose angle and dihedral

angle of the wing need to be investigated on sonic boom mitigation. One must also investigate the combined effects on boom of the design variables considered earlier. Finally, optimization of the wing shape parameter is proposed to come up with optimized variables for low boom profile delta wing geometry keeping in mind the lowest possible lift loss and minimum drag gain. One tries to obtain a set of design variables that would optimize the prescribed objective function subject to a set of constraints that define the boundaries of the solution space. The choice of the design variables is made to suit the need for sonic boom minimization and discovered during the individual effects studies. Constraints are imposed to satisfy the physics of the problem or to generate a realistic solution. For the current work two objectives are defined. One involves minimize the near field shock strength or the sonic boom level, and the second objective is to maximizing the lift to drag coefficient ratio, thus maximizing the aerodynamic performance.

There are limits, however, in what can be achieved in making the low boom overpressure distribution without degrading the aerodynamic performance. There are also structural and weight constraints and supersonic and transonic stability and control concerns to contend with.

1.4 Computational Approaches

A two dimensional method is developed for predicting the sonic boom focusing by solving the nonlinear Tricomi equation. The computational scheme is implemented on a rectangular domain with a structured grid system. Prediction results are generated for an incoming N wave, incoming Concorde wave and other types of incoming waves. Parametric studies are conducted by varying the location and the size of the lateral and longitudinal boundaries. Parametric studies are also conducted for the footprint and shock strength for both N wave and Concorde wave cases.

Near-field domain around the delta wing is computed using an Euler-equations solver CFL3D code [30] from NASA LaRC. CFL3D is a structured grid solver capable of running on multi processing environments. Once the preliminary shock is captured a

shock fitting and grid adaptation GASF [31] is run to obtain a fine shock fitted grid. CFL3D is rerun on the fitted and adapted grid to obtain the shock with much greater accuracy in the near filed solution. The near field solution for an angle of attaché cases is computed with an unstructured grid solver FUN3D [32]. Structured and unstructured grid generation work is done using Gridgen software from Point wise Inc [33].

Design Expert software [34] is used for the optimal shape design of a delta wing shape. Multi objective optimization is considered for minimizing the ground level boom signature. First, the most important objective is to reduce the boom effect on the ground, and the second objective is to maximize the aerodynamic performance, i.e. increase the lift to drag ratio. The optimization code Design-Expert software (DES) [34] uses the various optimization approaches including factorial design to investigate the individual and coupled effects for desirability of design variable for the objectives set for the study. Optimal design parameters are determined after a sequence of CFD runs are conducted and a series of CFD model results are obtained. Response models are obtained by fitting the CFD input data of the individual responses.

Once a near field pressure signature is calculated, a propagation model is needed to propagate this signature to the ground. Conventional propagation models assume standard atmospheric properties to obtain the pressure and temperature values at different altitudes that are then used to obtain the sonic boom pressure signature on the ground. In the far-field domain the full-potential equation [35] is numerically solved. The reason behind choosing the full-potential equation versus using the Euler equations or the multi-pole linear equation for the far-field computations is computational efficiency (versus the substantial computational time needed for the Euler equations marching several miles [6-8 miles]) and carrying the nonlinear effects of the propagating waves (versus the multi-pole linear equation).

Thomas code [36] has also been employed for the quick estimation of sonic boom ground overpressure. Thomas code [36] is based on the linear approach and comes with reasonable accuracy in computing the propagation phenomenon. The Thomas program

was developed to directly use the near field pressure signature from the wind tunnel tests. The code directly inputs the pressure jump and prorogates it to the ground.

The CFD computation and propagation of the shock waves of the optimized wing are then carried out from a 40,000 ft altitude to the ground to investigate the effect of the optimized wing shape on the sonic-boom ground signature. Full potential code [35] is able to predict the non linear behavior of flow very accurately over a linearized axisymmetric approach. Computational cost and time becomes the only concern while carrying out the boom propagation study using a full potential nonlinear solver [35]. An alternative approach could be to use the non linear full potential solver up to an altitude where merging of the shocks is already over and then to switch the solver to linearized axisymmetric flow.

1.5 Research Objectives and Assumptions

In this section the design and research objectives have been made clear in terms of their limitation and applicability. For the sonic boom focusing problem, computation results are limited to two dimensional conditions only. No three dimensional effects have been considered for the prediction of super boom phenomena. A sonic boom focusing effect is only considered for a typical N shape wave and not the actual aircraft shock pattern, although some of the results are obtained for a Concorde wave and conceptual aircraft waveforms. For a particular aircraft one needs to study the shock pattern emitted by that aircraft.

Nonlinearity of the atmosphere has been ignored and atmosphere is considered to be linear while solving the nonlinear Tricomi equation. Figure 1.9 shows the variation in atmospheric temperature. Atmosphere is composed of many layers such as troposphere, stratosphere, thermosphere, mesosphere [29] etc. Troposphere extends from the earth's surface to an altitude of about 11 km. It is a region of rising and falling packets of air. The stratosphere follows next, to an altitude of about 47 km. with the air flow mostly horizontal. Aircraft do not cruise beyond the stratosphere, so atmospheric layers beyond the stratosphere are not considered. However, the standard atmospheric temperature

predictions are correct only in an average sense and could in general vary with time, season, humidity, latitude, etc.

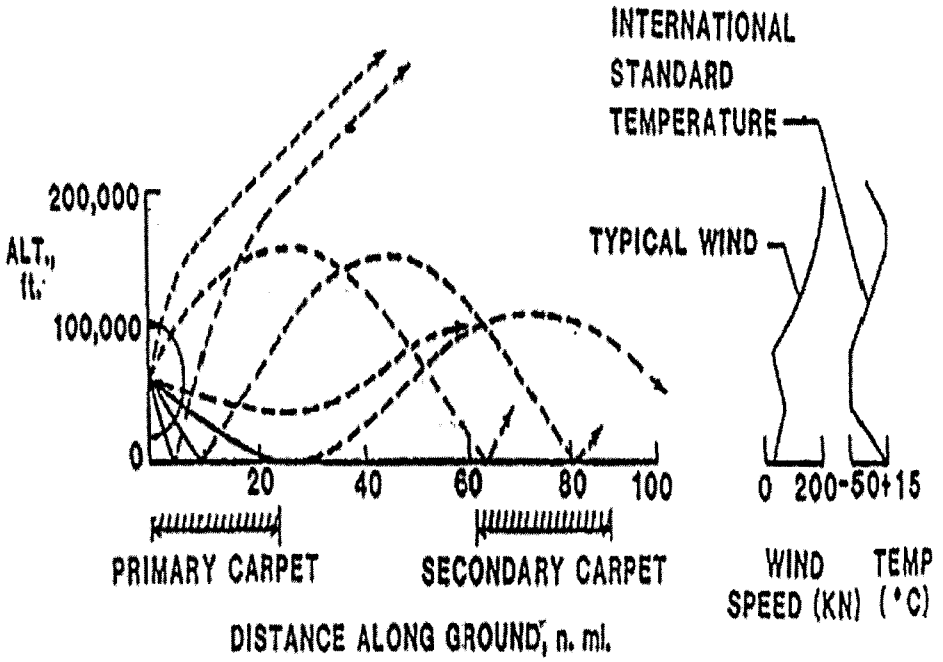

Figure 1.9 Non linearity of the atmosphere [29]

Only primary carpet focusing has been considered for computation. Secondary carpet computations are not given attention as they are a rebound of shock waves from the atmosphere and this leads to focusing on secondary carpet too. Figure 1.9 shows the secondary carpet for very weak rebounded shock waves. The effects in secondary boom focusing are not predominant and are ignored in the current work.

The fundamental strategy in minimizing the sonic boom was addressed for a biconvex profile delta wing configuration. The study can be extended to actual aircraft geometry. Sonic boom propagation is carried out using the full potential solver [35] which is found to be capable of predicting accurate ground sonic boom signature. Euler or full Navier-Stokes solver could be an alternative to the potential code for much greater accuracy. Computational time and the cost can be an issue if such code is being used. Accuracy of optimization results can be improved with a higher number of CFD runs. The computational cost with a higher number of CFD runs becomes very high. Further, much more sophisticated optimization approaches like gradient based optimization or a genetic algorithm can be employed for optimization purposes.

1.6 Dissertation Layout

Chapter 2 gives a literature survey and a historical review of sonic boom and sonic boom focusing research. The major development in theory and formulation of the problems has been outlined. Chapter 3 elaborates on formulation and computational techniques employed and developed for prediction of sonic boom focusing and sonic boom mitigation. A sonic boom focusing mathematical formulation and computational scheme are discussed in detail. Important parameters are identified for super boom parametric studies as well.

Chapter 3 explains the formulation and CFD software for obtaining the near field Euler solution. The sonic boom mitigation approach is typically involved in prediction and optimization of various aerodynamic shapes for the boom effects. Chapter 3 also talks about the optimization approach two level factorial designs for optimizing the delta wing geometry parameters.

In chapter 4 the results obtained from the sonic boom focusing code have been discussed for an N pattern shock wave, Concorde wave and some other input waves. Chapter 4 also discusses the parametric studies observation. The result obtained by a conservative approach has also been validated with the available solution.

Further, in Chapter 5 sonic boom mitigation results are produced and discussed for a base line configuration of biconvex delta wing geometry. Chapter 5 also summarizes the boom studies carried out for thickness, camber, nose angle and dihedral angle effects. An optimization study is carried out, and results are discussed for low boom configuration.

Finally, chapter 6 summarizes the results obtained in the current work and provides recommendations for future work.

CHAPTER 2
BACKGROUND AND LITERATURE SURVEY

The first theoretical results of sonic boom came from ballistic projectiles analysis by Whitham [1] in 1952. Whitham [1] explained in detail the generation of the flow pattern from a ballistic projectile, explaining that it is generated continuously as the aircraft flies supersonically. The flow pattern from a projectile is precisely the shock-wave pattern due to a supersonic flight. Since then many theories have been developed and extensive literature has been published to understand and validate the sonic boom hypothesis. This chapter summarizes major developments in sonic boom and sonic boom focusing theories. Some of the work done in the area of shape optimization for boom mitigation research has also documented.

2.1 Historical Review of Super Boom Research

The presence of sonic boom focusing was not given high importance until some of the observations made due to focused boom. Boom focusing is more annoying than primary boom and may cause easily observable building vibration and rattling. The evaluation of its community acceptance is still at a very early stage and more of the importance has been given to primary boom with steady flight conditions.

The boom focusing phenomenon can be defined and classified using the theory of catastrophes [37]. The important result of catastrophe theory is discussed by Berry [38] in 1976 for the far field wave field where it is considered that caustics serve as a structurally stable focuses. The focusing in almost any flight condition leads to a smooth envelope of boom rays, known as a fold caustic in the terminology of catastrophe theory [37, 38]. Higher-order focusing, such as that indicated by a cusped envelope of boom rays, is known as a cusp caustic in terms of catastrophe theory [37].

Geometrical theory [12] is introduced to calculate the linear wave's amplification near a fold caustic. The theory of geometric acoustics fails near a caustic and must be replaced

by an acoustic theory without the simplifying assumptions of the geometric theory. Geometric acoustic predicts infinite amplitude at the caustics surface where essentially it fails. Diffraction [12] can help in addressing the failure. The analytical solution obtained by the Airy function [39] also leads to infinite amplitude if incoming waves present shock [12]. The geometric acoustics approaches obviously is physically meaningless, and laboratory experiments performed by Sturtevant and Kulkarny, in 1976 [40], despite an important amplification of amplitude and a change in the temporal waveform associated with diffraction, clearly show a limitation of the amplitude.

A simplifying boundary-layer approximation is made by Buchal & Keller [41, 42] in many cases near the caustics. With this approximation the linear governing equation reduces to the Tricomi equation, for which the basic solutions are well known. Guiraud [12] was the first to propose nonlinearities as the additional limiting mechanism for the case of fold caustics. He derived the so-called nonlinear Tricomi equation satisfied by the pressure field around the caustic. Appropriate introduction diffraction to the first order in an appropriately defined diffraction boundary layer (DBL) in the neighborhood of the caustic leads to a linear Tricomi equation. Seebass (1970) [43] has found a way to linearize the nonlinear Tricomi equation through a Legendre transformation. If no shock is present near the caustic, his transformation effectively linearize the problem.

An approximate numerical solution was designed by Gill and Seebass in 1973 [44] based on the hodograph transform. Estimations by Plotkin and Cantril [45] and later by Downing et al. [46] showed the Gill and Seebass solution [44] matched reasonably well with flight tests. Using the asymptotic method of matched expansions Cramer and Seebass (1978) [47] showed that around the cusped caustic, the pressure is governed by the Khokhlov–Zabolotskaya (KZ) equation [48] (1969).

In accordance with Guiraud's (1965) [12] assumptions on the fold caustic and with the theory of catastrophes, similar equations were subsequently derived by Rosales and Tabak [49] and Auger and Coulouvrat [50, 51] for prediction of the amplitude near a cusp caustic.

The effects of maneuvers as well as of winds in a horizontally stratified atmosphere were considered in the first computer model by Hayes et al [52, 53] known as the ARAP model. In 1969, Hayes [52, 53] et al. showed that Whitham's theory [1, 2] could be generalized for non-uniform atmosphere using geometric acoustics. Nonlinearity of the atmospheric properties, like variation of pressure, density, temperature and thus the speed of sound are included in the calculation. Hayes [53] also included aircraft acceleration effects and maneuvering in the calculation. This was a significant development because atmospheric gradients and aircraft maneuver have a large impact on sonic boom focusing.

Geometric acoustics, isentropic wave theory and ray theory are well suited to explain the nonlinear wave propagation through the stratified atmosphere, although the theories will fail around the region of the caustic. The concept of waves and rays is shown in Fig 2.1. A wave front is a geometric entity, and a ray is the trajectory of a signal point, hence a rather kinematics entity. Waves emitted at different time tend to converges at a place known as the caustic surface or surface of amplification.

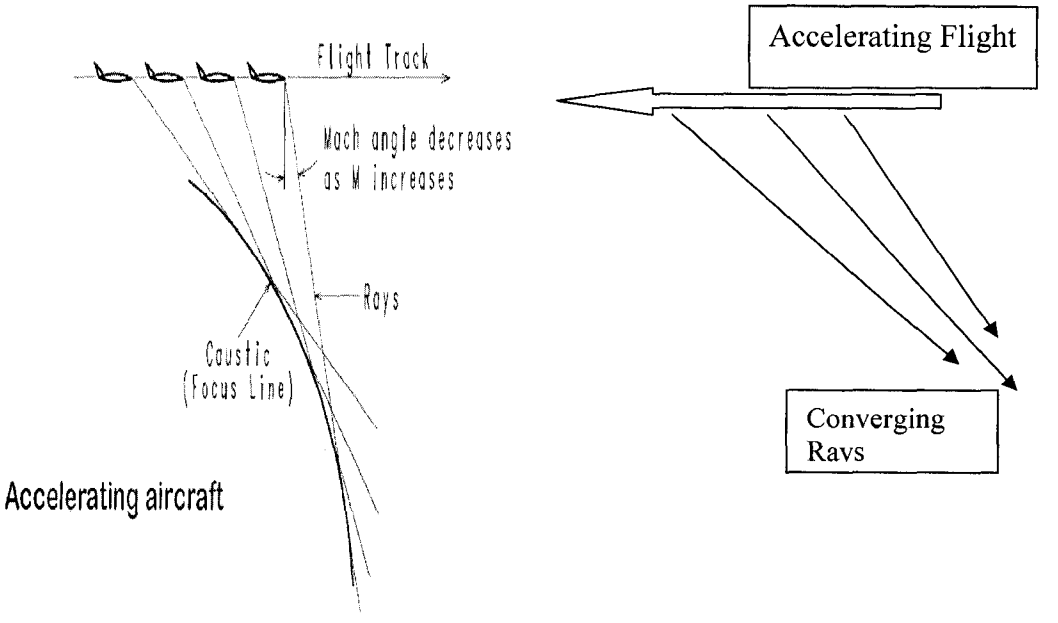

Figure 2.1 Shock Wave Focusing

Rays, ray tubes and the ray tube area are basic concepts from geometric acoustics. In geometric acoustics, signals are propagated along rays. Each ray is the trajectory of a wave front and ray tracing determines the shape of the ray tube. A small group of rays in a neighborhood makes a ray tube. Ray tube area in a given direction is the area intercepted by the ray tube and the plane normal to that direction. A point at which the ray-tube area of geometric acoustics becomes zero is a focal point. Barring certain exceptional cases, focal points form a caustic surface that is an envelope of the rays.

In a uniform medium, rays are straight. In a non-uniform medium, particularly where the speed of sound varies, the rays will be refracted as they pass through the medium (just as light rays are refracted as they pass from air into water). A general approach for ray tracing and ray tube area calculation for arbitrary atmospheric conditions (including wind) and flight maneuvers is presented by Hayes's [53]. Plotkin [45] introduced the wind effect explicitly in Hayes approach. In addition, the equations were further simplified for steady and level cruise conditions.

In late 1972, Thomas [36] proposed a new algorithm, the waveform parameter method, where ray tracing was accomplished by numerically integrating a set of ray paths through the atmosphere rather than evaluating a set of closed-from quadratures in Hayes's method [53]. The waveform parameter approach approximates the waveform using an arbitrary number of linear segments and defines three waveform parameters for each segment as a function of time. Then, coupled ordinary differential equations for these waveform parameters are derived from conservation laws along the rays and solved with given initial and boundary conditions. The corresponding solutions for the waveform parameters [36] determine the physical variables at any point along the ray paths. One of the great advantages of the waveform parameter method over the F-function method [1] is that it is fairly easy to implement on a computer since the problem can be reduced to the solution of coupled ordinary differential equations. Therefore, it can be applied to any shape signature and provides a continuous evolution of the shape as the signature is propagated. It does not use age variables to account for nonlinear distortion and does not require an area-balancing criterion to locate the shock waves.

Guirads's [12] formulation of non linear Tricomi equation is re-derived in various scenarios by Coulouvrat and Marchiano [54-57]. Auger and Coulouvrat [50] have presented an algorithm using the Fast-Fourier Transform (FFT) to solve the nonlinear, non-conservative Tricomi equation, which was expressed in terms of the dimensionless acoustic pressure. Coulouvrat [54-57] developed the Tricomi equation considering a boundary layer around the cusp where the main physical mechanisms are diffraction and local nonlinear effects.

Kandil and Zheng [58] presented the nonlinear Tricomi solver using a non conservative approach. The focusing prediction is obtained by splitting the nonlinear Tricomi equation into two parts; the first part corresponds to a linear unsteady Tricomi equation and the second part is the nonlinear, unsteady Burgers equation. The solution of the unsteady linear Tricomi equation is followed by the solution of the nonlinear, unsteady Burgers equation to obtain the solution of the total nonlinear Tricomi equation. Kandil and Zheng [58] developed three computational schemes. The first is a frequency-domain (FD) fast–Fourier transform (FFT) scheme, the second is a time-domain (TD) finite-difference scheme, and the third is a TD finite-difference scheme with overlapping grid (OLG).

2.2.1 Review of the Super Boom Computational Tools

A summary of the major software's developed over a few decades to predict the sonic boom focusing phenomenon is presented here. The following is a recap of the most significant computational models and their features.

1 Hayes or ARAP: The first computer model [53] regarded as having all details correct. It calculates boom for an arbitrarily maneuvering aircraft in an arbitrary horizontally stratified atmosphere.

2 Thomas Code: A computer model developed by NASA [36] shortly after Hayes and with similar capabilities. It is notable for the use of the waveform parameter method of signature aging.

3 TRAPS: TRAPS [59] is developed for the purpose of tracing over the-top booms. It follows Hayes's formulation, but it uses ray distance rather than altitude as its independent variable so that it can handle vertically turning rays. It accounts for the passage of a boom through caustics via a Hilbert transform. TRAPS [59] accept atmospheric data in standard meteorological format. It can smooth input trajectories via cubic spline fits. It is successful in predicting where focusing reaches the ground, but it gives too large amplitudes.

4 ZEPHYRUS: A reformulation of the basic Hayes method [53], aimed at incorporating as many physical effects as possible. Treats over-the-top booms similarly to TRAPS. Accounts for molecular relaxation shock structure using the Pestorius algorithm. ZEPHYRUS [59] was mainly written to resolve this discrepancy of TRAPS. It incorporates the air absorption effects and predicts lower values for the overpressures as compared to TRAPS overshoots. However, ZEPHYRUS is much more computer intensive than TRAPS.

5 PC-Boom3: PCBOOM [59] is industry standard software developed by Wyle laboratories. Evolved from the Thomas code, this program addresses focal zones by application of the Gill–Seebass [44] focus solution and Guiraud's scaling law [12]. Accepts initial signatures either as F-functions or Thomas-style dp, or can generate simplified Carlson F-functions from a built-in aircraft list. Computes boom footprints on the ground for a complete flight. Part of a system that includes a menu-driven user interface and graphical outputs of footprints and signatures. Drawing contours still requires some custom programming, but the bulk of the work is accomplished via readily available libraries. The contours appear on the user's computer screen virtually instantaneously. Variation MDBOOM [60] incorporates area-rule F-function calculation and the Page–Plotkin method [60] for matching to CFD near-field solutions.

6 Carlson: A manual procedure for computing N-wave booms in steady flight. Computes carpet width and boom signatures across the carpet. Includes shape factor charts for most aircraft, and also has a procedure for computing the shape factor. Well worth examining, even if you are going to use one of the computer programs. A

factor that must also be noted is that much of today's state of the art computer software has been made feasible by the rapid growth of computer power. Boom calculations that were major undertakings a decade or two ago can now be performed in seconds or minutes.

7 SOBER Program: More recently, as part of the SOBER program [61] code was developed that, includes nonlinearity, absorption and relaxation effects by various chemical species and uses real meteorological data. It supersedes both TRAPS and ZEPHYREUS [51] as it predicts, in reasonable computing time, results that agree well with focusing observations. In the focusing of weak shock waves, for an N-wave incident on a fold caustic the linear Tricomi equation gives rise to a reflected wave which is a U-wave with infinite peaks. Such singularities are an unphysical result. The established modeling approach for eliminating these singularities is to combine diffraction effects with nonlinear effects. This procedure leads to a so-called nonlinear Tricomi equation.

2.2 Historical Review of Sonic Boom Research

The first recognized boom theory was presented by Whitham in 1952 [1]. According to Whitham, linear theory approximations are applicable in the flow as long as approximate characteristics are replaced by the exact characteristics. He developed a concept of F function which relates the flow field to the lengthwise area distribution of an axisymmetric body. Walkden [4] extended the theory to lifting body configuration. Carlson [7] and Hunton [8] validated the preliminary theory by experimental studies.

For a smooth body $$F(y) = \frac{1}{2\pi} \int_0^y \frac{S''(t)}{\sqrt{y-t}} dt \qquad \text{.....2.1}$$

S (t) is the cross sectional area of the body. If the body is discontinuous a similar expression can be developed. The F function approach is limited to axis-symmetric body and is applicable only at a large distance from the body.

$$\frac{\Delta p(x,r,\theta)}{\gamma p M^2} = \frac{1}{2} C_p \cong \frac{1}{\sqrt{2\beta r}} F(t,\theta) \quad \text{.....2.2}$$

If the near-field pressure distribution is available, either by wind-tunnel experiment or by CFD simulation, the F-function can be obtained easily by using the relation in equation 2.2. If one used equation 2.2 there is no need to have the aircraft geometrical detail to computer F function. However, the computation should be implemented beyond enough distance such that Whitham's far-field assumptions [1] are satisfied.

However wind tunnel data is expensive to obtain and the F-function method can be complicated for complex geometries. A nonlinear Euler analysis with the aid of rapid development in CFD was used to obtain near-field data by Siclari et al. [62] in the early 1990's. The work in this thesis follows this approach with more sophisticated meshing techniques and numerical solutions.

2.2.1 Sonic Boom Mitigation and Optimization Methods

Sonic boom mitigation mainly involved in reducing the magnitude of the front and rear shock waves rather than paying too much attention to the complete shock system. In fact, it has often been the approach used to alter the boom signature such that ramps, flattops and multi-shock shapes are created in the ground. The accurate and efficient computation and propagation of such shaped booms is a much more challenging task than for N-waves. To date, there have only been a few studies related to the ability of CFD-based sonic signature methods to predict the phenomenon accurately and none of them has particularly focused on the propagation of shaped booms.

DARPA instantiated research needs are focused on reduction of the magnitude of just the initial peak of boom signature. The Quiet Supersonic Platform (QSP) program [13] (0.3 psf), hides the importance of the rest of the signature, which often arises from the more geometrically complex aft portion of the aircraft where empennage and engine nacelles and diverters create more complicated flow patterns. Moreover, such designs often have two shock waves very closely following each other in the front portion of the signature a behavior that is not robust and is therefore undesirable. Sonic boom minimization began

with Busemann [3] in 1955 who pointed out how to eliminate the sonic boom due to aircraft volume. The Whitham F-function [1] approach based on the cross-sectional area distribution and the lift distribution of the generating vehicle is used extensively for sonic boom mitigation. Modified linearized theory and geometric acoustics are used to determine ground pressure signatures from the F-Function.

Later in 1969 -1972, Seebass [10, 19, 21, 43, 44, 63, and 64], George [9, 21, 18, 63, and 64] and Darden [20, 65-69] contributed to sonic boom mitigation which includes an abundance of blunt nose. The Seebass-George F function [63, 64] has a simple analytical form that can be inverted to produce the equivalent area distribution, which was used to shape the aircraft. Figure 2.2 represents the Seebass-George's F-function for lesser degrees of nose bluntness.

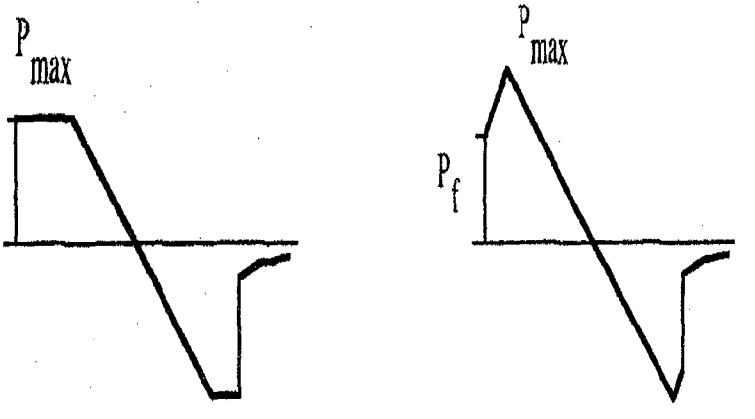

Figure 2.2 Boom pressure signatures proposed by Seebass and George [64]

The Seebass-George [63, 64] low-boom design method is an inverse approach because the aircraft shape is derived from a given sonic boom pressure signature. Figure 2.3 describes the Seebass-George [63, 64] sonic boom minimization method with the nose bluntness modifications made by Darden. The method solves for the required equivalent area which, produces the sonic boom signatures shown in Figure 2.2. Both signatures were thought to be less disturbing to people. The first signature minimizes the overpressure, while the other minimizes the shock intensities. The F-function illustrated in Figure 2.3 produces the pressure signatures given in Figure 2.2

However, there are limitations to the Seebass-George [63, 64] low boom design as it is only applicable to flat-top and ramp shaped booms, drag is not considered for optimization, there is reduced design space due to equivalent area constraints, lift distribution needs to be specified and error in equivalent area matching has unpredictable effect on boom signature. Despite Darden's modification to address some of the issues including nose bluntness [65], this approach is not efficient and applicable for the need of the day.

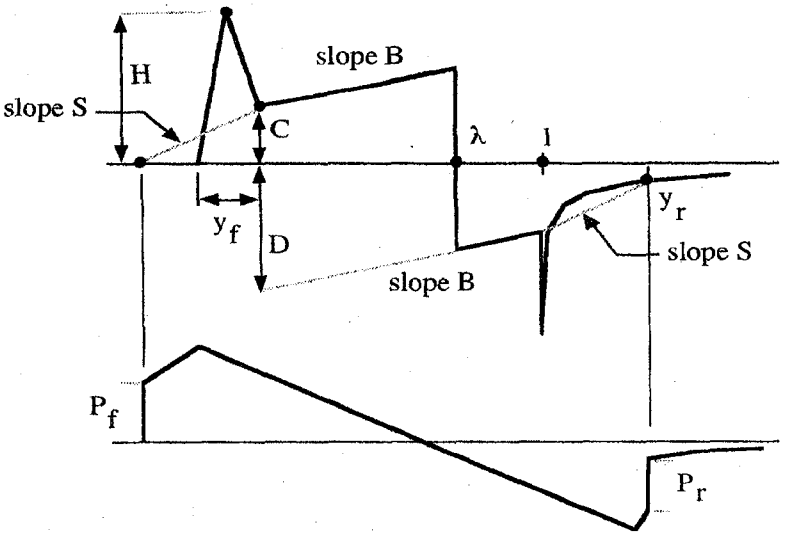

Figure 2.3 Darden's Modification to Seebass-George F function approach [65]

It is likely that a more aerodynamically efficient design could be achieved with a different mid-field signature of similar loudness. Smooth volume and lift variation is required by the Seebass-George method. This significantly constrains the design degrees of freedom for drag minimization. Although the Seebass-George method [63, 64] offers a simple approach to designing an aircraft with shaped sonic boom, the resulting design usually does not reproduce the specified shaped booms because of wing-body aerodynamic interaction. One has to iterate between volume and lift in order to match the equivalent area. An alternative approach would be applying recent CFD based aerodynamic shape optimization techniques to solve the wing body aerodynamic interaction to match the equivalent area.

Even for a conventional supersonic aircraft with a highly swept wing, it is difficult to match the area profile exactly because of complex aerodynamic interactions of the wing, tail and body and nacelles. Any subsequent error in the area will, in general, have an unpredictable effect on the sonic boom. Depending on the configuration, the area deviation at certain locations may have greater impact on the boom than at other locations. The minimization of sonic boom with simple constraints is a problem that is usually handled by a simplified inverse design approach. The other design considerations are important to this problem and are not easily incorporated into an inverse problem; alternatively it employs nonlinear optimization and direct analysis.

The current proposed method takes a more direct approach, using recent techniques in numerical aerodynamic shape optimization to shape the aircraft in relation to the predicted boom, rather than the area distribution. The low-boom design approach employed here utilizes numerical optimization techniques to minimize the sonic boom. Mathematically, optimization involves maximizing or minimizing a scalar objective whose value is a function of the design variables subject to any constraints present.

The fundamental difference between the current method and the Seebass-George method is not in the use of optimization but in the use of the sonic boom signature instead of the equivalent area in the optimization. The objective function in the optimization is a value computed directly from the sonic boom signature, whereas if numerical optimization is applied to the Seebass-George [63, 64] method, the objective would be to minimize the difference in the equivalent areas. In the direct optimization approach the objective is to minimize the maximum overpressure of the sonic boom subject to the given lift and drag constraints. Optimization begins with an initial set of design variables with the bounding limit as an iterative process. It continues the design variables and is continuously modified until they meet the design objective.

Nonlinear optimization in many cases led to unspectacular reductions in signature. Indeed, in many of these methods, it is difficult to see significant improvement in the optimized designs. One of the reasons for frequent failure of search methods in boom

minimization is the highly nonlinear character of the relation between geometric design variables and a signature-based objective. Experience with the interactive design code provides a clear indication of difficulties with conventional optimization. The sudden appearance of multiple shocks, the coalescence of shocks, and the change in sensitivity of shock peaks depending on the strength of other peaks, leads to one of the most difficult aerodynamic optimization problems. The design space is generally filled with many local optima and, depending on the details of the aero analysis and propagation code, may exhibit discontinuities in objective or constraint gradients.

As described in the previous section several problem formulations were investigated, but several different search methods were also employed. The conclusion of this study was that for the complete design problem (including geometric design variables, multidisciplinary constraints, and boom/performance objectives), the presence of multiple local minima, created by the physics of the problem itself or introduced by noise in the computations, prevented successful application of conventional gradient-based search methods. Optimization codes, SQP [70] methods such as SNOPT, achieved little progress on this problem, due to nonlinearity (as under these methods one needs to find the derivative of the function).

Alternative optimization methods that do not require gradient information (e.g. nonlinear simplex) showed somewhat better performance, but consistently converged on local minima. This led to exploration of less efficient but more robust schemes such as genetic algorithms [71] (GA) and other stochastic approaches. The GA [71] was most effective, although very inefficient, consistently finding a better solution than could be achieved by the other optimizers, but at the cost of many thousands of function evaluations even for 8-10 variable problems. This suggests that one approach to these problems is to combine robust but inefficient search methods with powerful parallel computational facilities.

The Stanford University group [72] decided to apply its expertise in multidisciplinary design optimization (MDO), advanced nonlinear analysis and design methods, and adjoint based design methodologies to the supersonic business jet design problem. Jameson used coupled adjoint formulation for shape optimization of SST. The cost of

solving the adjoint equation is comparable to that of solving the flow equation. Hence, the cost of obtaining the gradient is comparable to the cost of two function evaluations, regardless of the dimension of the design space.

Design-Expert software (DES) [34] is used to obtain the optimized shape parameters for low sonic boom configuration. A response surface method (RSM) [73] is a very powerful optimization tool in the statistical design of experiments (DOE) [34]. Before employing RSM [73] process one should take full advantage of a far simpler tool for DOE a two□level factorials design, which can be very effective for screening the vital factors (including interactions) from the many trivial ones that have no significant impact. Assuming the potential for further research, follow up the screening studies by doing an in□depth investigation of via RSM, then generate a "response surface" map and move the process to the optimum location. This article provides a brief discussion of RSM with applications to plastics and rubber.

Optimal design parameters are determined after a sequence of CFD runs are conducted and a series of CFD model results are obtained. Response models are obtained by fitting the CFD input data of the individual responses. The fitted responses are obtained as local approximations. This design contains no replicates because they would generate identical responses from the deterministic computer simulation. Therefore, the ANOVA [34] does not include any pure error, nor does it provide a test on lack of fit.

2.2.2 Sonic Boom Propagation Methods

The Thomas program [36] was developed to directly use the near field pressure signature from the wind tunnel tests. The waveform parameter method developed by Thomas [36] is different from the code developed by Hayes and Kulsrud [52] rather than using the F-function as a starting point, the Thomas code [36] uses a jump in the pressure at some radius to propagate the acoustic waves.

Sometimes one could argue that the methods are equivalent. However, there are two fundamental differences between the two methods. This forms the practical difference between these two methods. The other difference is theoretical. The near field pressure

may not correspond to the pressure obtained from the F-function. Hence, care has to be taken to measure the near field pressure sufficiently far away from the aircraft so that geometrical acoustic principles can be applied. For far field propagation Thomas ray tracing [36] code is used for quick estimation of ground boom overpressure signature. The propagation method used by Bobbitt, Kandil et al [31] based on potential flow is found to be an accurate one for nonlinear propagation for complete understanding of the flow feature.

For a propagation code it is difficult to identify where the inner Euler or midfield solutions are matched. It is only the magnitude of the pressures that is matched and most often radial and lateral gradients intrinsic to a fully 3D methodology are not. Based on the above deficiencies one can see there is a need for a higher order fully 3D propagation methodology to do the kind of boom optimization research required. Potential flow method [31] is based on the three dimensional full-potential equations, is matched point for point to the inner Euler solution, and utilizes both adaptive-grid and shock-fitting solution algorithms.

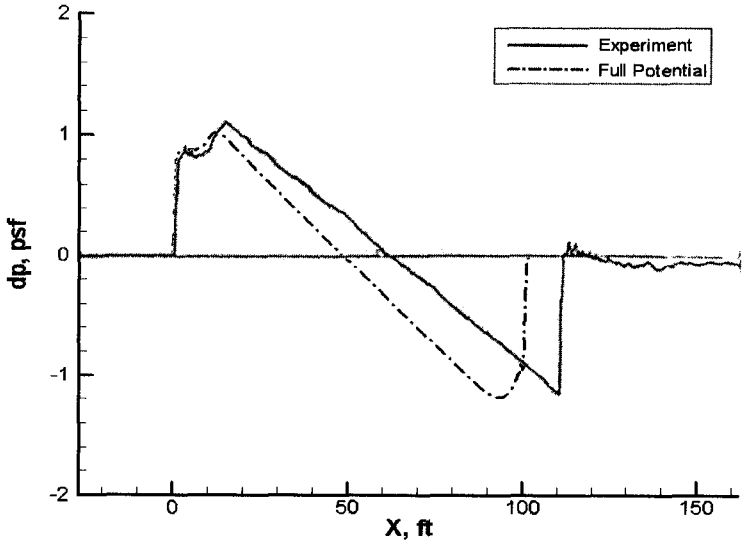

Figure 2.4 F5E experimental data versus Full Potential Method [74]

The potential code shows excellent comparison with F5E experimental data [74] of boom propagation as shown in Fig 2.4. The code has also been used on various simple delta wing configurations to predict the sonic boom ground signature [24]. The full potential equation is used to propagate to the ground; the near field signature is calculated using

the Euler equations. Potential flow code takes input from Euler solver and propagates the signal to the ground. Since the Euler equations solution does not exactly satisfy the potential equations, a methodology is formulated to determine the potential and its derivatives at the interface between the Euler and potential "domains." The conservative form of the full- potential equation is solved using a space marching, upwind scheme. This scheme is "augmented" by a sub-block technique that facilitates the treatment of the varying speed of sound.

2.3 Sonic Boom Design Configuration

Much of the work done in the 1980's and early 1990's is related to the sonic boom reduction of supersonic transport airplanes. A two cycle design process is a common approach to meet the target equivalent area distribution based on low sonic boom constraints. In the first cycle, plane form is optimized and in the second cycle camber and twist of wings are modified to meet the target equivalent area distribution.

Many organizations are actively involved at present in designing a feasible and economically viable Quite Supersonic Platform (QSP) [13]. NASA has been actively involved in high speed civil transport (HSCT) research. Gulf Stream Aerospace and Boeing [14] have also made significant progress in supersonic transport research. Some of the industry designs and their salient features are discussed next.

2.3.1 Elementary design Concorde Configuration

The Concorde was designed in the 1960's and early 1970's through the combined efforts of British Aerospace and ONERA. The first commercial supersonic aircraft to operate successfully was the Concorde. Figure 2.5 below presents a schematic of the Concorde.

The Concorde has a needle shaped design; the pilots would not be able to see the runway during take-off and landing. To help improve the view, the nose is drooped down for take-off and landing. The aircraft is pitched at a very high angle of attack. The wing plan form is given a smooth continuously varying sweep. Nacelles are placed under the wing and there is no horizontal tail or canard surface. Stability is achieved by 41 fly-by-wire

controls and stability augmentation systems. While transitioning from subsonic to supersonic regime, the design allowed for fuel to be moved to change the center of gravity. However, supersonic flight over land was not possible because of an unacceptably loud sonic boom.

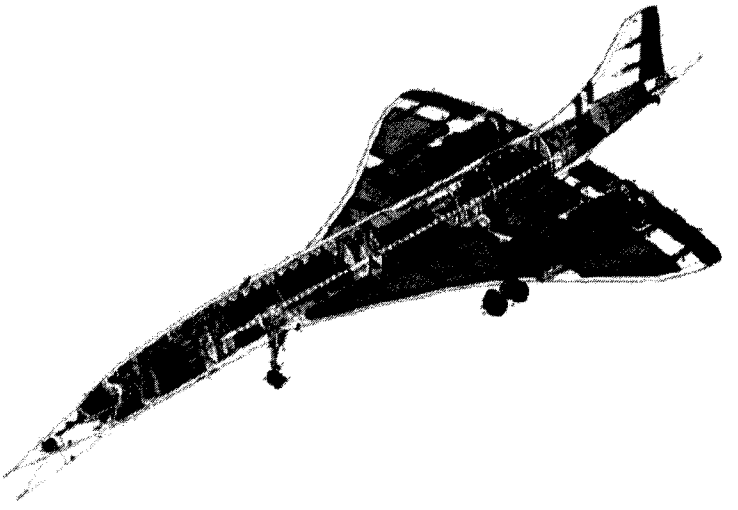

Fig 2.5 Concorde Supersonic Jet

2.3.2 SSBD Program Northrop Grumman

The Shaped Sonic Boom Demonstration (SSBD) program [16] is a $7 million cooperative agreement between Northrop Grumman, DARPA and NASA's Langley Research Center and Dryden Flight Research Center. Other government and industry entities are participating in the program as well.

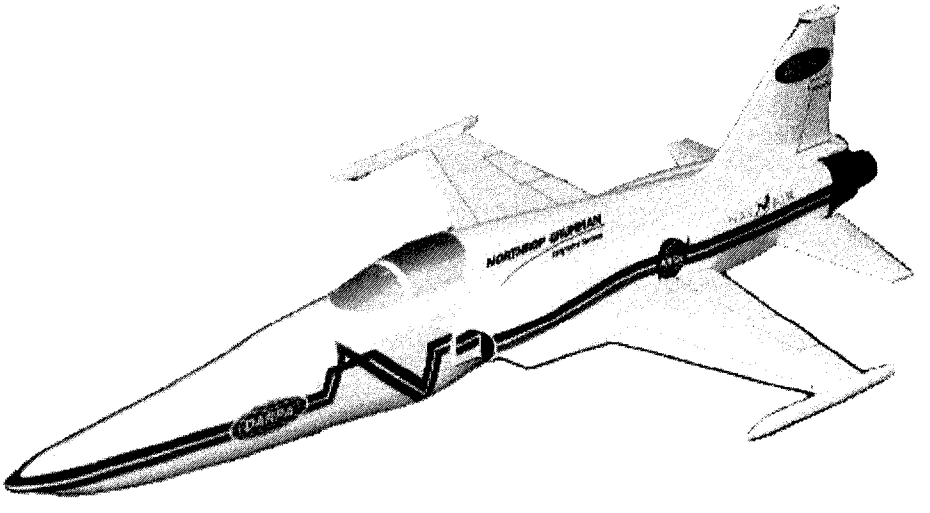

Fig 2.6 Modified shape of F5E Aircraft [13]

The F-5E's modifications, which were designed and installed by Northrop Grumman, include a specially shaped "nose glove" and the addition of an aluminum substructure and a composite skin to the underside of the fuselage. Figure 2.6 shows the modified shape of the F5E aircraft. DARPA's QSP program [13] is an effort to identify and mature technologies that could allow military and business aircraft to operate with reduced sonic boom. Northrop Grumman Integrated Systems has been working under contract with the QSP program since 2000 at its Advanced Systems Development Center in El Segundo. As part of that work, the company has designed a long-range supersonic military aircraft and validated key integration technologies associated with that design.

Northrop Grumman is attempting to quiet the sonic boom with a modified F-5E whose specially-shaped-nose may keep shock waves from forming into the abrupt wave that reaches ground level in the form of a sonic boom. The modified aircraft is expected to produce an especially flat top shape sonic boom with significantly less intensity than the conventional sonic boom produced by an unmodified F-5E.

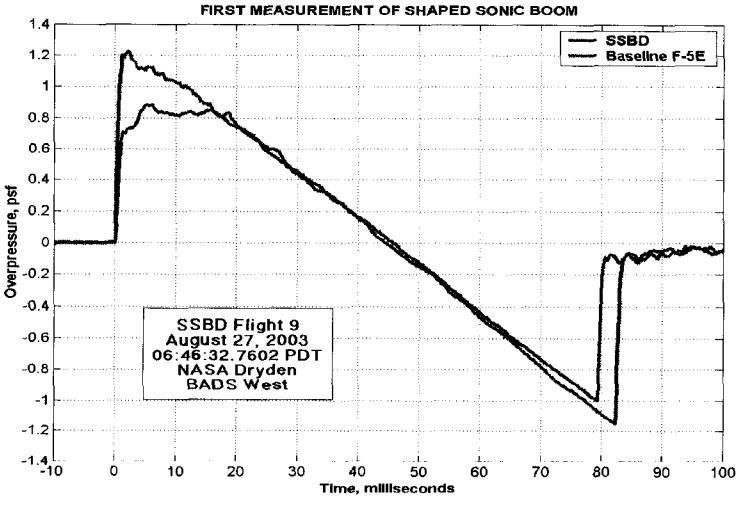

Fig 2.7 Reduction in Overpressure for modified F5E [16]

Figure 2.7 shows the comparison of ground boom signatures of the base line and modified shape of F5 aircraft. The experimental data are obtained by propagating the signature through standard atmosphere for a cruise Mach number of 1.4 and cruise altitude of 32000 ft. The flight tests were conducted on August 27, 2003 at Edwards Air Force base in California.

2.3.3 QUITE Design Lockheed Martin

Lockheed-Martin has been conducting studies to design a quiet supersonic transport (QSST) [17] with funding from Supersonic Aerospace International (SAI). Their design is based on the idea of a tail-braced wing for sonic-boom suppression. Lockheed's design is depicted in Figure 2.8.

Fig 2.8 Lockheed Quite Design [17]

Lockheed's design has the nacelles under the wing. In order to remove the adverse effect of the nacelle interference, the wing is reflexed to counteract the negative effect of the nacelles. This is different from the traditional wing reflexing in addition to the camber slope change. The thickness slope is also changed to make the flow on the top surface of the wing unchanged while at the same time canceling the shock reflection from the lower surface of the wing. The tail-braced joined wing design provides sufficient structural stiffness to the aircraft and also increases the effective length of the aircraft.

Anhedral rear wing causes stability concerns and is compensated by having a tail to carry less than 25% of the total lift. Lockheed claims to have achieved a 55 dba sound level which is less than the loudness level while talking normally.

2.3.4 Aerion Business Jet Program

The Aerion SBJ [15] is designed to operate effectively under the existing sonic boom regulation with the potential to adapt as the regulations are changed. For flights over the United States where aircraft must stay below Mach 1.0, Aerion cruises efficiently at Mach 0.98. In other populated parts of the world the regulation requires that sonic boom does not reach the ground. There, Aerion can cruise as fast as Mach 1.1 without creating a sonic boom on the ground. Over the oceans and other uninhabited areas, Aerion can cruise up to Mach 1.6. Figure 2.9 shows the Aerion supersonic business jet.

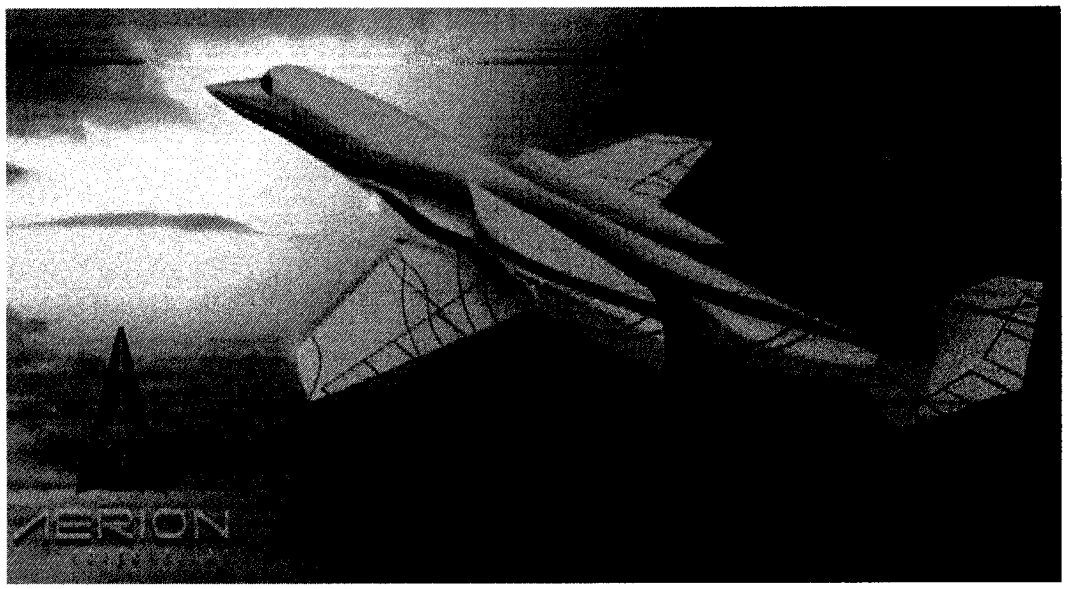

Fig 2.9 Aerion Supersonic Business Jet [15]

The baseline Aerion aircraft has a relatively low sonic boom, with an initial overpressure of about 0.8 psf. This is less than the boom of many supersonic fighters and much less than the Concorde. Relatively minor changes to the Aerion design can reduce the overpressure to 0.5 psf. Over the next several years, regulation for low sonic boom will be developed, and low boom technology will be improved. Aerion will then develop low boom aircraft to operate under the new regulations. The aircraft will be fuel efficient at cruise speeds just below the speed of sound, allowing it to perform short and long-haul overland missions with the same economies as today's large business jets. The range is roughly the same at both subsonic and supersonic speeds and will exceed 4,000 nautical miles. The aircraft has a low boom signature and boomless cruise up to Mach 1.1.

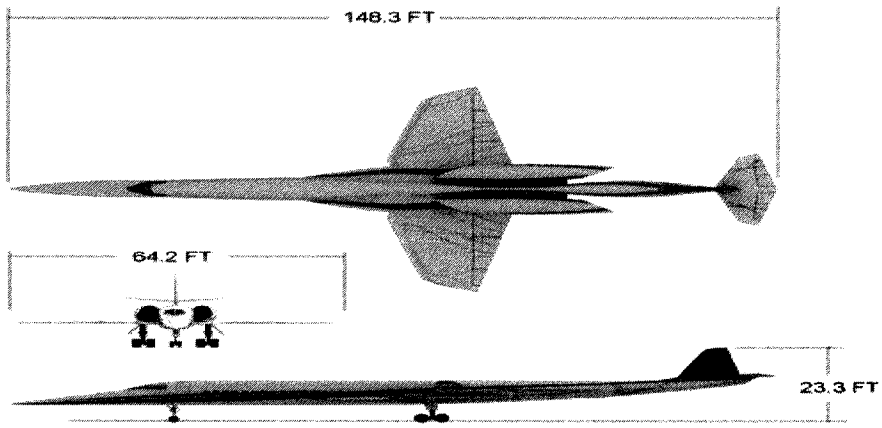

Fig 2.10 Aerion Supersonic Business Jet [15]

Figure 2.10 shows the front, top and side view of the aircraft. The performance data is listed in table 2.1. Its maximum cruise speed will be Mach 1.6. Aerion can carry 8 to 12 passengers on board, equipped with twin Pratt & Whitney JT8D-219 engines. Cabin size will be between today's super-midsize and large business jets. Cabin height is six feet. The cabin can accommodate eight to 12 passengers in a variety of configurations.

Maximum cruise speed:	1.6 Mach
Long range cruise (supersonic):	1.5 Mach
No boom cruise (supersonic):	~1.1 to 1.2 Mach
High speed cruise (subsonic):	.99 Mach
Long range cruise (subsonic):	.95 Mach
Maximum takeoff weight:	90,000 pounds
Basic operating weight:	45,100 pounds
Maximum fuel:	45,400 pounds
Engines:	Two PW JT8D-219
Thrust:	Flat rated to 19,600
Wing area:	1,200 sq. ft.
Approach speed:	120 kts*
Balanced field length:	< 6,000 feet
Landing distance, wet runway:	3,460 feet
Range (NBAA IFR):	> 4,000 nm
Ceiling:	51,000 feet

* typical end of mission weight

Table 2.1 Aerion Supersonic Business Jet Performance Data [15]

2.4 Supersonic Business Jet Technological Challenges

The two most important barriers for supersonic flight over land are sonic boom and sonic boom focusing. Sonic boom focusing is involved with unsteady supersonic flight and the focused boom effect could be four times higher than normal sonic boom impact. Computational tools for boom focusing prediction are very important in order to carry out design and development of civil supersonic transport aircraft over land.

The important step towards supersonic aircraft development is to optimize the shape of the aircraft so that the near field flow shock system and thus the boom on the ground is controlled. Designers are compelled to work on aerodynamic shape optimization so that they have been able to address the boom constrained imposed by the FAA [11]. In addition to lowering the boom it is equally important not to degrade the aerodynamic performance. CFD as a design tool can be used to build a baseline configuration to adjust the shape of the near field shock system as a design objective. One can also investigate the potential design feature instead of investigating the whole aircraft. This can substantially expedite the design process and more sensible design studies can be made at the full scale level.

CHAPTER 3
PROBLEM FORMULATION AND SOLUTION METHODS

This chapter elaborates on the methodology of the computational algorithm and scheme implemented to solve the nonlinear Tricomi equation. Grid generation and convergence criteria are also discussed. A structured grid system is used to compute the flow with a rectangular domain. Parametric study metrics are also discussed in order to identify the important parameter for boom focusing. A sequential program is developed and ported on Linux and Windows operating systems.

Chapter 3 also outlines the detail formulation and solution method to carry out CFD simulations and shape optimization study for delta wing boom mitigation. Near field CFD results were obtained using the structured grid solver CFL3D [30] and the unstructured grid solver FUN3D [32]. Grid adaptation techniques are also discussed for structured and unstructured grid solvers. Towards the end of the chapter 3 a response surface method [73] is discussed for optimizing the design variables. A multi objective optimization approach is adopted for minimizing the sonic boom ground signature with least degradation of aerodynamics performance.

3.1 Sonic Boom Focusing

The sonic boom focusing involves unsteady shock wave interaction and is governed by the nonlinear Tricomi equation. A nonlinear Tricomi equation is a mixed type of equation and needs to be descretized with a type differencing scheme [75].

A conservative form of the nonlinear Tricomi equation is solved using a time-domain scheme. This scheme can also be called a conservative time domain (CTD). The non linear Tricomi equation earlier was solved in non conservative form [54-58] by splitting into linear and nonlinear parts. The current method is developed in conservative forms without splitting into linear and non linear forms. The computational scheme is a node based type differencing scheme implemented for two dimensional flows. The

computation is performed on a rectangular domain with structured grip topology. Normally higher grid density is considered to be able to predict the flow feature with desired accuracy.

3.1.1 Non Linear Tricomi Equation

In this section a nonlinear Tricomi equation is developed using an acoustical perturbation approach [57]. Acoustical perturbation effects are assumed to be very small and normally disregarded in fluid dynamics considerations. If the acoustical perturbations effects are included, the expression for density and velocity can be modified with $\rho(x,t)=\rho_0(x)+\rho_a(x,t)$ and $v(x,t)=v_0(x)+v_a(x,t)$ respectively [57]. Similar expressions can be developed for pressure and entropy.

The modified steady state basic flow equations of mass, momentum and energy equations can be written as follows.

Mass Equation [68]

$$\left(\frac{\partial}{\partial t}+V_0.\nabla\right)\rho_a+\rho_0\nabla.V_a=-V_a.\nabla\rho_0-\rho_a\nabla.\rho_0-\nabla.(\rho_aV_a) \qquad \text{.....3.1}$$

Momentum Equation [57]

$$\rho_0\left(\frac{\partial}{\partial t}+V_0.\nabla\right)V_a+\nabla.p_a=\frac{\rho_a}{\rho_0}\nabla.p_a-\rho_0(V_a.\nabla)V_0-\rho_a\frac{\partial V_a}{\partial t}-\rho_0(V_a.\nabla)V_a-\rho_a(V_0.\nabla)V_a-\rho_a(V_a.\nabla)V_0$$

.....3.2

Acoustical amplitude is known for the pressure amplitude Pa. The left-hand side of each equation involves only linear terms that would remain even in the nonlinear terms in the right-hand side (last term for the mass and energy equations, second line for the momentum equations, three last terms for the state equation). All cubic and higher-order nonlinear terms have been omitted, as the present study is limited to weakly nonlinear waves (small acoustical Mach number). It is noticeable that the last terms in the momentum equation involve both nonlinearities and heterogeneity.

Now we seek the solution of the above equations under the following form using the generalized eikonal function and the high frequency approximation

$$\tau = t - \psi(x) \qquad \text{.....3.3}$$

$$\rho_a(x,t) = \hat{\rho}_a(x,\tau) \qquad \text{.....3.4}$$

$$v_a(x,t) = \hat{v}_a(x,\tau) \qquad \text{.....3.5}$$

$$p_a(x,t) = \hat{p}_a(x,\tau) \qquad \text{.....3.6}$$

The new function ψ(x) is called a generalized eikonal function [57]. The quantity τ is called the retarded time. The objective is to make some additional approximations to reduce that number of unknown to pressure and generalized eikonal function. Introduction of the (generalized) eikonal function is useful in the high frequency case. Indeed, let us assume that the pressure field is a frequency wave

$$p_a = p_a(x)\exp(-i\omega\tau) \qquad \text{.....3.7}$$

Substitution will lead to an equation where smaller magnitude terms can be dropped and the modified equation with leading terms becomes [57]

Mass equation

$$\frac{1}{c_0^2}(1 - V_0.\nabla\psi)\frac{\partial p_a}{\partial\tau} - \rho_0\nabla\psi.\frac{\partial V_a}{\partial\tau} = O(\varepsilon) \qquad \text{.....3.8}$$

Momentum equation

$$\rho_0(1 - V_0.\nabla\psi)\frac{\partial V_a}{\partial\tau} - \nabla\psi.\frac{\partial p_a}{\partial\tau} = O(\varepsilon) \qquad \text{.....3.9}$$

Eikonal equation

$$\frac{1}{c_0^2}(1 - V_0.\nabla\psi)^2 - (\nabla\psi)^2 = 0 \qquad \text{.....3.10}$$

Eikonal equation is not a well posed equation. It may be singular or there can be multiple solutions or no solution at a point. The first case corresponds to caustics, and the second case corresponds to shadow zones. To remove the singularity, normally diffraction is introduced. Diffraction is a physical effect which can be dominant in some situations.

Alternatively, one needs to come up with the approach which modifies the eikonal function and provides a single nonlinear and time domain formulation. A paraxial approximation describing diffraction in a homogeneous, non moving medium can lead to a KZ (Khokhlov and Zabolotskaya 1969) equation [48].

Substituting $$\psi = \frac{x}{c_0} \qquad \text{.....3.11}$$

One can obtain the KZ equation [57]

$$\frac{2}{c_0}\frac{\partial^2 p_a}{\partial \tau \partial x} - \frac{\beta}{\rho_0 c_0^4}\frac{\partial^2 p_a}{\partial \tau^2} = \frac{\partial^2 p_a}{\partial y^2} + \frac{\partial^2 p_a}{\partial z^2} \qquad \text{.....3.12}$$

This can be made dimensionless using the following parameter

$$\bar{\tau} = \omega\tau \qquad \text{.....3.13}$$

$$\bar{x} = \beta k M x \qquad \text{.....3.14}$$

$$\bar{y} = y/a \qquad \text{.....3.15}$$

$$\bar{z} = z/a \qquad \text{.....3.16}$$

$$\bar{p}_a = p_a / P_0 \qquad \text{.....3.17}$$

Where omega is a characteristic (angular) frequency, $k = \omega / c_0$ is the associated wave number and "a" is the characteristic transverse dimension. P_0 is the characteristic amplitude for pressure and M is the associated acoustical Mach number.

For a weakly heterogeneous nonmoving fluid we assume $c_0(x) = < c_0 > + \Delta c_0(x)$, where the actual sound speed differs from the mean sound speed $< c_0 >$ only by a small but fluctuating quantity $\Delta c_0(x)$ for this case ψ can be replaced with $\psi = \frac{x}{< c_0 >}$, which will modify the KZ equation to a nonlinear Tricomi equation (developed by Coulouvrat [54-56] 1997, 2002) and can be expressed by the equation.

$$\frac{\partial^2 \bar{p}}{\partial \bar{z}^2} - \bar{z}\frac{\partial^2 \bar{p}}{\partial \bar{\tau}^2} + \frac{\mu}{2}\frac{\partial \bar{p}^2}{\partial \bar{\tau}^2} = 0 \qquad \text{..... 3.18}$$

Where μ measures the nonlinear effects relative to the diffraction effects. The steady nonlinear Tricomi equation is modified as an unsteady equation by adding a pseudo unsteady term $\partial^2 \phi / \partial \tau \partial t$, which will tend to zero when the pseudo time marching scheme reaches the steady solution of $\phi(t \to \infty, \tau, z)$. The modified equation is given by [54-56]

$$\frac{\partial^2 \phi}{\partial \tau \partial t} = \frac{\partial^2 \phi}{\partial z^2} - z \frac{\partial^2 \phi}{\partial \tau^2} + \frac{\mu}{2} \frac{\partial}{\partial \tau} \left[\left(\frac{\partial \phi}{\partial \tau} \right)^2 \right] \quad \text{..... 3.19}$$

Where

φ = Acoustical potential

t = Pseudo time variable

τ = Dimensionless phase variable = $[t - x\ (1\text{-}z / R_{sec}) / c_0] / T_{ac}$

x = Dimensionless axial variable along the tangent to the caustic surface

z = $[2/ (c_0^2 T_{ac}^2 R_{cau})]^{1/3}$ z* = z* / δ = Dimensionless normal distance to the caustic

δ = $1/ [2/ (c_0^2 T_{ac}^2 R_{cau})]^{1/3}$

Where δ = Characteristic thickness of diffraction boundary layer at caustic

z* = Normal distance to the origin of caustic

R_{sec} = Radius of curvature of intersection of the caustic surface with caustic plane

R_{cau} = Relative radius = $1/ (1/ R_{sec} - 1/ R_{ray})$

R_{ray} = Radius of curvature of the projection in the plane

c_0 = Ambient speed of sound at stagnation conditions

T_{ac} = Characteristic duration of incoming signal near origin of caustic

μ = $2 \beta M_{ac} [R_{cau} / (2 c_0 T_{ac})]^{2/3}$ = Non linear effects relative to diffraction effects

β = $(1+\gamma) / 2$ = Nonlinearity parameter

M_{ac} = $P_{ac} / \rho_0\ c_0^2$ = Acoustical Mach number

P_{ac} = Signal maximum overpressure

ρ_0 = Ambient stagnation density

In terms of p, which is related to ϕ by $p = \frac{\partial \phi}{\partial \tau}$ the equation is given by

$$\frac{\partial p}{\partial t} = \frac{\partial^2 p}{\partial z^2} - z \frac{\partial^2 p}{\partial \tau^2} + \frac{\mu}{2} \frac{\partial}{\partial \tau} \left[(p)^2 \right] \quad \text{.....3.20}$$

The conservative form can be written as

$$\frac{\partial p}{\partial t}+\frac{\partial^2 p}{\partial z^2}+\frac{\partial^2}{\partial \tau^2}(-z\ p+\frac{\mu}{2}\ p^2)=0 \qquad \text{.....3.21}$$

The sign of the pseudo unsteady term is insignificant since it is reduced to zero with the pseudo time marching scheme. The differencing equation of $\frac{\mu}{2}\frac{\partial^2}{\partial \tau^2}(p^2)$ is linearized in the numerical algorithm. With the process of linearization, equation 3.21 can be written in terms of ϕ in the same form as that of equation 3.21. The conservative form of the nonlinear Tricomi equation in terms of ϕ is expressed by equation 3.22. [54]

$$\frac{\partial \phi}{\partial t}+\frac{\partial^2 \phi}{\partial z^2}+\frac{\partial^2}{\partial \tau^2}(-z\ \phi+\frac{\mu}{2}\ \phi^2)=0 \qquad \text{.....3.22}$$

A finite-volume scheme has been developed to solve equation 3.22 in terms of ϕ instead of p.

3.1.2 Grid Generation for Tricomi Solver

The Cartesian grid topology is used on a rectangular computational domain. Grid refinement is incorporated for improving the accuracy of the results. The number of grid points used in the z direction is 1000 and in the τ direction is 8000. Grid independence studies have shown that the solution does not change with further improvement in grid size in τ and z direction.

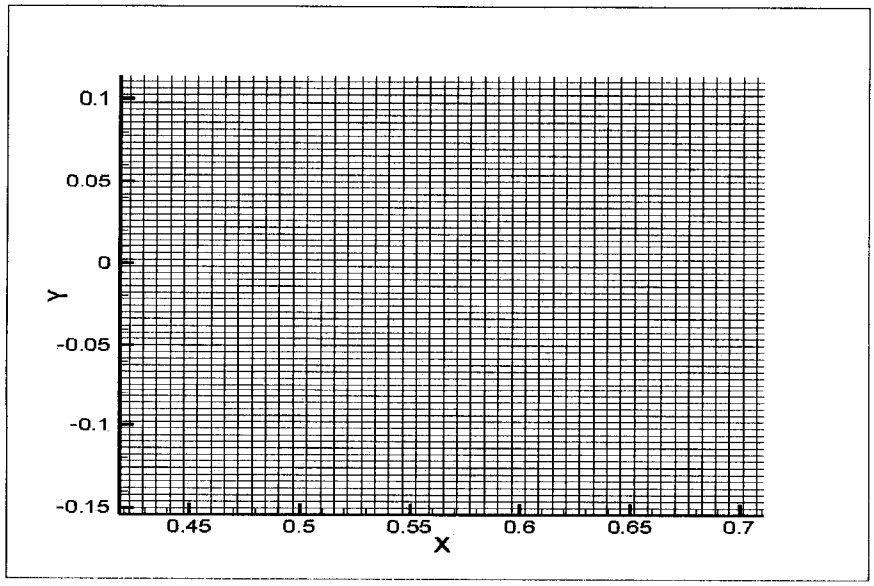

Figure 3.1 Computational Grids for CTD Scheme

Figure 3.1 shows the zoom in the structured grid topology used for computation of conservative time domain solver. Shock capturing is the major concern and grid below 8 mil grid point leads in dissipation of the computational result. Satisfactory result obtained only with 8 mil grid points after iterating to at least 20000 time steps.

3.1.3 Boundary condition

A 2D flow field is considered for computation of a nonlinear Tricomi equation. The boundary conditions imposed on four computational boundaries are discussed below.

1. The boundary condition imposed on the left and right boundary is due to the fact that for a transient signal, field vanishes for very large times i.e. in τ direction which we call a time-like direction. The expression for no disturbance boundary condition before and/or after the acoustic waved has passed is given in equation 3.23.

$$\varphi(z, \tau \to \pm\infty) = 0 \qquad \text{..... 3.23}$$

2. A no disturbance boundary condition is imposed on bottom boundary as well. The flow field vanishes exponentially as we go away from the caustic line and into the shadow zone. Away from the caustic surface in the shadow zone the acoustic pressure decreases exponentially

$$\varphi(z \to -\infty, \tau) \to 0 \qquad \text{..... 3.24}$$

3. On the top boundary incoming wave boundary condition is imposed. The reflection boundary condition is implemented inside the formulation in order to match the geometrical acoustics approximation far away from the caustic in the illumination zone.

$$\varphi(z \to +\infty, \tau) = z^{-1/4}[F(\tau + \frac{2}{3}z^{-3/2}) + G(\tau - \frac{2}{3}z^{-3/2})] \qquad \text{..... 3.25}$$

In equation 3.25 F is the incoming waveform and therefore is known, whereas G is the outgoing waveform with diffraction effects and not known. One can avoid the

unknown function G in computation by imposing radiation boundary condition on the top expressed in equation 3.26. It also has been noticed with such a radiation condition, that it can lead to numerical instability with sharp singularity nature of the radiation boundary condition and hence the boundary is imposed in terms of velocity potential instead of pressure field. The boundary condition imposed on the top boundary in terms of velocity potential is expressed in equation 3.27.

$$z^{1/4}\frac{\partial p}{\partial \tau}+z^{-1/4}\frac{\partial p}{\partial z}\rightarrow 2\frac{\partial F}{\partial \tau}(\tau+\frac{2}{3}z^{3/2}) \qquad \text{..... 3.26}$$

$$z^{1/4}\frac{\partial \phi}{\partial \tau}+z^{-1/4}\frac{\partial \phi}{\partial z}\rightarrow 2F(\tau+\frac{2}{3}z^{3/2}) \qquad \text{..... 3.27}$$

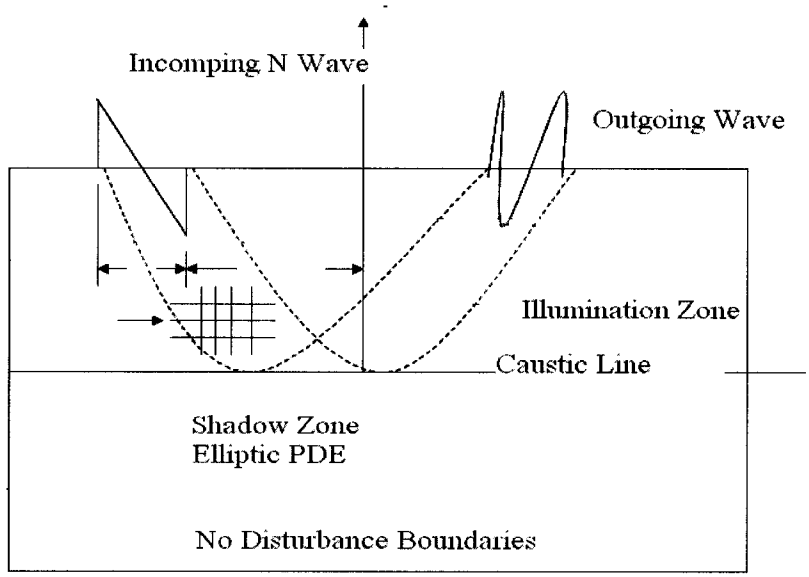

Figure 3.2 Computational Domain

3.1.4 Solution Procedure

The Nonlinear Tricomi Equation can be expressed in indicial notation by equation 3.28.

$$\varphi_{zz}+(-z+\mu\frac{\varphi^2}{2})_{\tau\tau}=0 \qquad \text{..... 3.28}$$

$$(\hat{j}\frac{\partial}{\partial z}+\hat{i}\frac{\partial}{\partial \tau})\bullet[\hat{j}\frac{\partial \varphi}{\partial z}+\hat{i}\frac{\partial}{\partial \tau}(-z\varphi+\mu\frac{\varphi^2}{2})]=0 \qquad \text{..... 3.29}$$

$$\text{Let } \frac{\partial \varphi}{\partial z}=\theta \text{ and } \frac{\partial}{\partial \tau}(-z\varphi+\mu\frac{\varphi^2}{2})=w \qquad \text{..... 3.30}$$

The equation will become

$$(\hat{j}\frac{\partial}{\partial z}+\hat{i}\frac{\partial}{\partial \tau})\bullet(\hat{j}\theta+\hat{i}w)=0 \quad \ldots\ldots 3.31$$

$$\frac{\partial \theta}{\partial z}+\frac{\partial w}{\partial \tau}=0 \quad \ldots\ldots 3.32$$

$$\overline{F}=\hat{j}\theta+\hat{i}w \quad \ldots\ldots 3.33$$

$$\nabla\bullet\overline{F}=\frac{\partial \theta}{\partial z}+\frac{\partial w}{\partial \tau} \quad \ldots\ldots 3.34$$

Solved using type differencing scheme

If:

Hyperbolic $z-\mu\varphi>0$ 3.35

Parabolic $z-\mu\varphi=0$ 3.36

Elliptic $z-\mu\varphi<0$ 3.37

$\frac{\partial \theta}{\partial z}$ Term is descretized by central differenced

Term is descretized by differenced-depending

$$w=\frac{\partial}{\partial}(-z\varphi+\mu\frac{\varphi^2}{2}) \quad \ldots\ldots 3.38$$

The solution can be obtained by

$$\iint\nabla\bullet\overline{F}=0 \quad \ldots\ldots 3.39$$

Converting to surface Integral

$$\oint\hat{F}\bullet\hat{n}ds=0 \quad \ldots\ldots 3.40$$

$$-\int_1 wdz+\int_2\theta d\tau+\int_3 wdz-\int_4\theta d\tau=0 \quad \ldots\ldots 3.41$$

$$-w_{m=\frac{1}{2},n}\Delta z+\theta_{m,n+\frac{1}{2}}\Delta\tau+w_{m+\frac{1}{2},n}\Delta z-\theta_{m,n-\frac{1}{2}}\Delta\tau=0 \quad \ldots\ldots 3.42$$

$$(w_{m+\frac{1}{2},n}-w_{m-\frac{1}{2},n})\Delta z+(\theta_{m,n+\frac{1}{2}}-\theta_{m,n-\frac{1}{2}})\Delta\tau=0 \quad \ldots\ldots 3.43$$

Equation 3.34 is solved using a type differencing scheme. The computational algorithm for the flux calculation is governed by the mixed type nature of the nonlinear Tricomi

equation. The Tricomi equation is hyperbolic in nature for $z-\mu\varphi>0$, parabolic for $z-\mu\varphi=0$ and elliptic in nature for $z-\mu\varphi<0$. As implemented by Murman and Cole [75] for transonic problems of switching the descretization from upwind to central differencing is employed in the algorithm. The $z-\mu\varphi=0$ is a separating barrier where flow changes from the illumination zone to shadow zones and the type of governing equation changes from hyperbolic to elliptic, thus the descretization scheme. The term θ is descretized by a central difference scheme and the term w is descretized by the upwind or central difference depending upon the nature of the governing equation.

If $z-\mu\varphi>0$ then the point is hyperbolic, and backward differencing is used

$$w_{m+\frac{1}{2},n}=\frac{\partial}{\partial\tau}(-z\varphi)_{m+\frac{1}{2},n}+\frac{\partial}{\partial\tau}(\mu\frac{\varphi^2}{2})_{m+\frac{1}{2},n} \qquad \text{..... 3.44}$$

$$w_{m+\frac{1}{2},n}=-\frac{(z\varphi)_{m,n}-(z\varphi)_{m-1,n}}{\Delta\tau}+\frac{\mu}{2}\frac{(\frac{\varphi^2}{2})_{m,n}-(\frac{\varphi^2}{2})_{m-1,n}}{\Delta z} \qquad \text{..... 3.45}$$

According Newton linearization [16]

$$(\frac{\varphi^2}{2})_{m,n}{}^{k+1}=(\frac{\varphi^2}{2})^k_{m,n}+(\varphi)^k_{m,n}(\varphi^{k+1}_{m,n}-\varphi^k_{m,n}) \qquad \text{..... 3.46}$$

$$(\frac{\varphi^2}{2})_{m,n}{}^{k+1}=(\varphi)^k_{m,n}(\varphi)^{k+1}_{m,n}-(\frac{\varphi^2}{2})^k_{m,n} \qquad \text{..... 3.47}$$

$$w_{m+\frac{1}{2},n}=-\frac{(z\varphi)_{m,n}-(z\varphi)_{m-1,n}}{\Delta\tau}+\frac{\mu}{2}\frac{(\varphi)^k_{m,n}(\varphi)^{k+1}_{m,n}-(\frac{\varphi^2}{2})^k_{m,n}-(\varphi)^k_{m-1,n}(\varphi)^{k+1}_{m-1,n}-(\frac{\varphi^2}{2})^k_{m-1,n}}{\Delta\tau} \qquad \text{..... 3.48}$$

Similar expression is developed for

$$w_{m-\frac{1}{2},n}=\frac{\partial}{\partial\tau}(-z\varphi)_{m-\frac{1}{2},n}+\frac{\partial}{\partial\tau}(\mu\frac{\varphi^2}{2})_{m-\frac{1}{2},n} \qquad \text{..... 3.49}$$

$$w_{m-\frac{1}{2},n} = -\frac{(z\varphi)_{m-1,n} - (z\varphi)_{m-2,n}}{\Delta\tau} + \frac{\mu}{2}\frac{(\varphi)^k_{m-1,n}(\varphi)^{k+1}_{m-1,n} - (\frac{\varphi^2}{2})^k_{m-1,n} - (\varphi)^k_{m-2,n}(\varphi)^{k+1}_{m-2,n} - (\frac{\varphi^2}{2})^k_{m-2,n}}{\Delta\tau} \quad \text{..... 3.50}$$

For θ

$$\theta_{m,n+\frac{1}{2}} = (\frac{\partial\varphi}{\partial z})_{m,n+\frac{1}{2}} = \frac{\varphi_{m,n+1} - \varphi_{m,n}}{\Delta z} \quad \text{..... 3.51}$$

$$\theta_{m,n-\frac{1}{2}} = (\frac{\partial\varphi}{\partial z})_{m,n-\frac{1}{2}} = \frac{\varphi_{m,n} - \varphi_{m,n-1}}{\Delta z} \quad \text{..... 3.52}$$

Substitute the above terms in equation 3.43

For the τ sweep

$$-\frac{(z\varphi^{k+1})_{m,n} - 2(z\varphi^{k+1})_{m-1,n} + (z\varphi^{k+1})_{m-2,n}}{(\Delta\tau)^2} + \mu\frac{(\varphi)^k_{m,n}(\varphi)^{k+1}_{m,n} - (\frac{\varphi^2}{2})^k_{m,n} - 2(\varphi)^k_{m-1,n}(\varphi)^{k+1}_{m-1,n} + 2(\frac{\varphi^2}{2})^k_{m-1,n}}{(\Delta\tau)^2} \quad \text{..... 3.53}$$

$$\frac{+(\varphi)^k_{m-2,n}(\varphi)^{k+1}_{m-2,n} - (\frac{\varphi^2}{2})^k_{m-2,n}}{(\Delta z)^2} + \frac{\varphi^k{}_{m,n+1} - 2\varphi^k{}_{m,n} + \varphi^k{}_{m,n-1}}{(\Delta z)^2} = 0$$

For the z sweep

$$-\frac{(z\varphi^k)_{m,n} - 2(z\varphi^k)_{m-1,n} + (z\varphi^k)_{m-2,n}}{(\Delta\tau)^2} + \mu\frac{(\frac{\varphi^2}{2})^k_{m,n} - 2(\frac{\varphi^2}{2})^k_{m-1,n} + (\frac{\varphi^2}{2})^k_{m-2,n}}{(\Delta\tau)^2} \quad \text{.....}$$

$$+\frac{\varphi^{k+1}{}_{m,n+1} - 2\varphi^{k+1}{}_{m,n} + \varphi^{k+1}{}_{m,n-1}}{(\Delta z)^2} = 0 \quad \text{3.54}$$

For $z - \mu p < 0$ the flow is elliptic and central differencing is used

$$w_{m+\frac{1}{2},n} = -\frac{(z\varphi)_{m+1,n} - (z\varphi)_{m,n}}{\Delta\tau} + \frac{\mu}{2}\frac{(\frac{\varphi^2}{2})_{m+1,n} - (\frac{\varphi^2}{2})_{m,n}}{\Delta z} \qquad \text{..... 3.55}$$

$$w_{m+\frac{1}{2},n} = -\frac{(z\varphi)_{m+1,n} - (z\varphi)_{m,n}}{\Delta\tau} + \frac{\mu}{2}\frac{(\varphi)^k_{m+1,n}(\varphi)^{k+1}_{m+1,n} - (\frac{\varphi^2}{2})^k_{m+1,n} - (\varphi)^k_{m,n}(\varphi)^{k+1}_{m,n} - (\frac{\varphi^2}{2})^k_{m,n}}{\Delta\tau}$$

..... 3.56

$$w_{m-\frac{1}{2},n} = \frac{\partial}{\partial\tau}(-z\varphi)_{m-\frac{1}{2},n} + \frac{\partial}{\partial\tau}(\mu\frac{\varphi^2}{2})_{m-\frac{1}{2},n} \qquad \text{..... 3.57}$$

$$w_{m-\frac{1}{2},n} = -\frac{(z\varphi)_{m,n} - (z\varphi)_{m-1,n}}{\Delta\tau} + \frac{\mu}{2}\frac{(\varphi)^k_{m,n}(\varphi)^{k+1}_{m,n} - (\frac{\varphi^2}{2})^k_{m,n} - (\varphi)^k_{m-1,n}(\varphi)^{k+1}_{m-1,n} - (\frac{\varphi^2}{2})^k_{m-1,n}}{\Delta\tau}$$

..... 3.58

Descretized term for the τ sweep

$$\begin{aligned} &-\frac{(z\varphi^{k+1})_{m+1,n} - 2(z\varphi^{k+1})_{m,n} + (z\varphi^{k+1})_{m-1,n}}{(\Delta\tau)^2} \\ &+\mu\frac{(\varphi)^k_{m+1,n}(\varphi)^{k+1}_{m+1,n} - (\frac{\varphi^2}{2})^k_{m+1,n} - 2(\varphi)^k_{m,n}(\varphi)^{k+1}_{m,n} + 2(\frac{\varphi^2}{2})^k_{m,n}}{(\Delta\tau)^2} \\ &\frac{+(\varphi)^k_{m-1,n}(\varphi)^{k+1}_{m-1,n} - (\frac{\varphi^2}{2})^k_{m-1,n}}{(\Delta z)^2} + \frac{\varphi^k{}_{m,n+1} - 2\varphi^k{}_{m,n} + \varphi^k{}_{m,n-1}}{(\Delta z)^2} = 0 \end{aligned} \qquad \text{..... 3.59}$$

Descretized term for the z sweep

$$\begin{aligned} &-\frac{(z\varphi^k)_{m+1,n} - 2(z\varphi^k)_{m,n} + (z\varphi^k)_{m-1,n}}{(\Delta\tau)^2} + \mu\frac{(\frac{\varphi^2}{2})^k_{m+1,n} - 2(\frac{\varphi^2}{2})^k_{m,n} + (\frac{\varphi^2}{2})^k_{m-1,n}}{(\Delta\tau)^2} \\ &+\frac{\varphi^{k+1}{}_{m,n+1} - 2\varphi^{k+1}{}_{m,n} + \varphi^{k+1}{}_{m,n-1}}{(\Delta z)^2} = 0 \end{aligned}$$

..... 3.60

The numerical cost to pay for this is that the method requires a sufficiently large domain in time. This appears perfectly manageable from a computational point of view by choosing for an incoming N wave of duration 1 a time domain equal to [-2.67 to 3.67].

3.1.5 Overview Focusing Parametric Studies

Once sonic boom focusing results using conservations time domain [76, 77] are predicted for N wave and Concorde wave cases, an attempt is made to investigate the sensitivity parameters affecting boom amplification. In the current work a few parameters have been identified as a potential cause of boom amplification. A parametric study [76] is carried out for the parameters listed below.

1. Effects of lateral Boundary
2. Effects of bottom and top boundaries
3. Effect of Boom strength
4. Effects of footprint of input wave
5. Effects of input wave type
6. Effects of number of grid point

3.2 Sonic Boom Near Field Prediction

Near field computation is carried out using CFL3D structure grid solver and FUN3D unstructured grid solver. Shock capturing is the major concern for the study and grid adaptation and shock fitting has been carried out. Grid adaptation and shock fitting GASF [31, 35] method is employed on structured grid computation. Optigrid software [78] is used for grid adaptation in case of unstructured mesh. CFL3D accepts the PLOT3D format grid and CFL3D format grid. FUN3D has multiple choices for grid. FAST unformatted grid is used for FUN3D computation.

3.2.1 CFL3D - Structured Grid Solver

The computational algorithm employed in CFL3D for the three-dimensional Navier-Stokes code CFL3D is described in CFL3D online manual by Robert T. Biedron and Christopher L. Rumsey [30]. The governing equations, which are the thin-layer approximations to the three-dimensional time-dependent compressible Navier-Stokes equations, can be written in terms of generalized coordinates as

$$\frac{\partial Q}{\partial t}+\frac{\partial (F)}{\partial \xi}+\frac{\partial (G)}{\partial \eta}\frac{\partial (H)}{\partial \zeta}=0 \qquad \text{..... 3.61}$$

A general, three-dimensional transformation between the Cartesian variables and the generalized coordinate is the implied jacobian of the transformation J

$$Q=\frac{1}{J}\begin{bmatrix}\rho\\ \rho u\\ \rho v\\ \rho w\\ e\end{bmatrix} \qquad \text{..... 3.62}$$

$$J=\frac{\partial(\xi,\eta,\zeta,t)}{\partial(x,y,z,t)} \qquad \text{..... 3.63}$$

$$F=\frac{1}{J}\begin{bmatrix}\rho U\\ \rho Uu+\xi_x p\\ \rho Uv+\xi_y p\\ \rho Uw+\xi_z p\\ (e+p)U-\xi_t p\end{bmatrix} \qquad \text{..... 3.64}$$

Q is the vector of conserved variables, density, momentum, and total energy per unit volume. F, G and H are inviscid fluxes. The numerical algorithm uses a semi-discrete finite-volume formulation, resulting in a consistent approximation of the conservation laws in integral form

$$\frac{\partial}{\partial t}\iiint_V Q dv+\iint_S \vec{f}.\vec{n} ds=0 \qquad \text{..... 3.65}$$

$$\left(\frac{\partial Q}{\partial t}\right)_{i,j,k} + (F)_{i+1/2,j,k} - (F)_{i-1/2,j,k} + (G)_{i,j+1/2,k} - (G)_{i,j-1/2,k} + (H)_{i,j,k+1/2} - (H)_{i,j,k-1/2} = 0 \quad \text{..... 3.66}$$

The discrete values are regarded as average values taken over a unit computational cell similarly; discrete values are regarded as face-average values. The index denotes a cell-center location and corresponds to a cell-interface location. The interface flux is determined from a state-variable interpolation and a locally one-dimensional flux model. Van leer's flux-vector splitting (FVS) [79] and flux difference splitting of ROE [80] is used and each term is split into forward and backward-moving pieces. The convective and pressure terms are differenced using either the upwind flux-difference splitting technique of ROE [80] or flux-vector-splitting technique of Van Leer the MUSCL (Monotone Upstream-centered Scheme for Conservation Laws) [79] approach of Van Leer is used to determine state-variable interpolations at the cell interfaces. For solutions with discontinuities (such as shock waves), schemes of an order higher than one generally require a flux limiter to avoid numerical oscillations in the solution. CFL3D has several limiter options which include smooth limiter min-mod limiter.

3.2.2 Structured Grid Adaptation

Accuracy of the computational fluid dynamics solution is vital for the propagation of an aircraft's sonic boom pressure wave through real atmosphere. Once shocks are captured, a grid adaptation scheme, based on the density gradient, is implemented to obtain a crisper shock without any dissipation effect. Structure grid adaptation is employed looking at the density gradient in the near field solution. Once the location of the jump is identified the grid clustering is done around the jump location.

This is followed by a shock-fitting scheme that is based on a searching algorithm and the Rankine-Hugoniot conservation equations of mass, momentum and energy equations. The repetitive solution cycles of the grid-adaptation and shock-fitting (GASF) [31, 35]

schemes minimize the root mean square of relative errors percentage in the mass, momentum and energy equations across the shock.

3.2.3 FUN3D - Unstructured Grid Solver

FUN3D [32] was born in the late 1980s as a research code. The code's original purpose was to study existing algorithms and to develop new algorithms for unstructured-grid fluid dynamic simulations spanning incompressible flow to transonic flow. The project has since grown into a suite of codes that cover not only analysis but also adjoint-based error estimation, mesh adaptation, and design optimization of fluid dynamic problems extending into the hypersonic regime. Meanwhile, algorithms developed in FUN3D are at the core of other CFD codes such as USM3D [81].

The fully unstructured three-dimensional (FUN3D) suite of codes is employed in this study. The compressible flow solver employs an unstructured finite-volume tetrahedral method for conserved variable, **Q**, i.e.

$$\vec{Q} = \lfloor \rho, \rho u_1, \rho u_2, \rho u_3, \rho e \rfloor^t \qquad \text{..... 3.67}$$

Where ρ is density, u, v, and w are velocity components, and E is total energy per unit volume. The node-based variables, **Q**, are computed by driving the flow equation residual **R** to steady-state with an implicit point-iterative method or an implicit line relaxation scheme. FUN3D is able to solve incompressible and compressible formulations of the Euler and Reynolds-averaged Navier-Stokes (RANS) flow equations, either tightly or loosely coupled to the Spalart-Allmaras (S-A) one-equation turbulence model. When the S-A model is included, the turbulence model quantity is included in **Q**. The present study employs only the Euler equations due to the area of interest being the near-field at more than 5 body lengths. The solution of **Q** allows the calculation of integral quantities $\boldsymbol{f}$ (e.g., lift and drag).

FUN3D has the ability to employ various upwind methodologies that include Roe flux-difference splitting [73], Van Leer flux-vector splitting [79], AUFS, HLLC. The

turbulence models that can be used are Spalart Allmaras and k-omega/SST. The solver is also equipped with sensitivity analysis and design optimization features.

$$\frac{\partial \vec{Q}}{\partial t}+\frac{\partial \vec{F}_i}{x_i}=0 \;\; ; \mathrm{i}=1,2,3 \qquad \ldots\ldots\ldots\ldots\ldots\ldots 3.68$$

$$\vec{Q}=\left\lfloor \rho, \rho u_1, \rho u_2, \rho u_3, \rho e \right\rfloor^t \qquad \ldots\ldots\ldots\ldots\ldots\ldots 3.69$$

$$p=(\gamma-1)\rho\left(e-\frac{u_1^2+u_2^2+u_3^2}{2}\right) \qquad \ldots\ldots\ldots\ldots\ldots\ldots 3.70$$

$$\vec{F}_i=\left\lfloor \rho u_i, \rho u_1 u_i+\delta_{i1}p, \rho u_2 u_i+\delta_{i2}p, \rho u_3 u_i+\delta_{i3}p, \rho u_i\left(e+\frac{p}{\rho}\right)\right\rfloor^t \qquad \ldots\ldots\ldots\ldots\ldots\ldots 3.71$$

After the flow solution is known, the discrete adjoint equations are solved to complete the dual problem. The first step is to linearize the flow equation residual and output function with respect to the flow solution Q. After this linearization, an adjoint variable is solved for each of the flow equations.

FUN3D provides multiple adaptation strategies to improve an adapted computational mesh to enhance the accuracy of solution with lower density mesh. Some of the adaptation methods implemented in FUN3D solvers are

1. Mesh Movement Gradient-Based Adaptation
2. Full Gradient-Based Adaptation
3. Mesh Movement via Spring Analogy,
4. Mesh Movement via Frequency Analogy

The spring adaptation capability, integrated into the FUN3D solver, is a simple tool that can provide clustering of points to a shock for a relatively well designed initial mesh. A gradient-based adaptation capability that allows for node insertion and deletion, node movement, and edge swapping has been developed for FUN3D. Gradient-based adaptation method has some convenient parameters which the user can choose to adapt

the solution in the unstructured mesh. Some of the parameters used in the current study are adapt_output_error; adapt _maxratio, and adapt_maxedge etc.

3.2.4 Unstructured Grid Adaptation with Optigrid

In addition to FUN3D is grid adaptation capability, Optigrid software [78] is used for unstructured mesh adaptation. Optigrid has more freedom and control than FUN3D for adapting the mesh. Optigrid also allows checking and visualizing the adapted mesh as one goes along the iteration for mesh adaptation. In order to adapt a grid to minimize the error throughout the computational domain, Optigrid first estimates the difference or error, between the exact solution and the numerical solution of a given flow problem on a grid of size. Of course, for most problems, except those with an exact solution, the error can only be guessed.

The global error has various sources:

1. Error resulting from the descretization of a continuum over a finite grid;
2. Grid-related errors, such as inappropriate grid distribution and misaligned grids;
3. Geometric approximations of solid boundaries;
4. Addition of stability and convergence enhancers, such as artificial viscosity, damping, smoothing and up winding.
5. Incomplete convergence of the flow solver should it slow down or stall;
6. Computer round-off error.

A grid adapted by OptiGrid will minimize error sources 1 to 3, as new grid points will be placed or displaced, automatically, where needed to accurately capture the flow characteristics. For error sources 4 and 5, experience indicates that the flow solver usually requires less and less artificial viscosity as the grid gets optimized and, in addition, that convergence of the flow solver is improved. Round-off error is intrinsic to numerical calculations and is unaffected by OptiGrid. OptiGrid [78] is based on minimizing the difference between the PDE and its descretized form. Using a 1-D Taylor expansion of both the exact (PDE) and numerical solutions (descretized), the truncation error can be estimated within an element.

Several adaptation strategies are implemented in OptiGrid. These are categorized as follows:

- ✓ Moving Nodes: Equi-distribute the error throughout the domain by moving the position of the grid points.
- ✓ Refinement: Reduce the error throughout the domain by adding new grid points where the error is higher than a target error threshold.
- ✓ Coarsening: Equi-distribute the error throughout the domain by removing grid points where the error is lower than the target error threshold.
- ✓ Edge Swapping: Reconnect edges to optimize their orientation and to better align the grid to uni-directional flow features.

The best strategy is a combination of all four operations to minimize and make the error uniform everywhere, while maintaining an acceptable number of grid points (memory requirement). Node movement is the only continuous operation and it may be viewed as the driving force of mesh adaptation. Refinement, coarsening, and edge swapping are binary (yes/no) operations that complement the action of node movement and should be viewed as a way to accelerate convergence to an optimum grid. If the initial grid is well suited to the flow, the mesh adaptation may require no more than 3-4 main iterations.

Optigrid [78] adapts the grid in the following sequence:

1. Node movement is performed on boundaries to smooth out the grid on surfaces. This may be repeated several times, based on the user input.
2. Edge refinement and swapping on boundaries are performed according to a user-specified curvature criterion so as to better represent regions of high curvature.
3. Node movement is performed in the entire computational domain
4. Edge refinement and coarsening are performed simultaneously in the entire domain, including boundaries.
5. Edge swapping is performed in the entire computational domain, including boundaries, in order to optimize the shape of elements. This is repeated several times based on the user input.

6. Node movement is performed in the entire computational domain, including boundaries, in order to smooth the adapted mesh (repeated several times based on the user input).

3.3 Overview Far Field Propagation

A number of methods and computer codes are available for predicting the evolution of supersonic aircraft's pressure signature as it propagates to the ground through a "real" stratified atmosphere. The most utilized sonic boom propagation codes are based on linear acoustic ray tracing and the Blokhintsev invariant. If, in addition, equivalent axisymmetric-body, F-function methodology [1] is utilized, the code developed by Hayes [52] is employed. Where a pressure distribution is available, then the Thomas code [36] is the preferred approach. This method is also based on the acoustic ray tracing methodology but employs several waveform parameters to describe the evolution of the pressure wave. Thomas code is normally used in combination with a near-field Euler CFD calculation to propagate sonic boom signatures to the ground.

In the current study a non linear full potential code [31, 35] is used for far field computations. Since the Euler equations solution does not exactly satisfy the potential equation, a methodology is formulated to determine the potential and its derivatives at the interface plane between the Euler and potential domains.

3.3.1 Compressible Full Potential Solver

The detail of computation scheme implemented for non linear full potential solver for sonic boom propagation [35] is discussed in this section. The full potential equation is used to propagate, to the ground; the near field signature is calculated using the Euler equations. Since the Euler equations solution does not exactly satisfy the potential equations, a methodology is formulated to determine the potential and its derivatives at the interface plane between the Euler and potential domains.

Starting with this interface solution the conservative form of the full-potential equation is solved using a space-marching, upwind scheme [35]. This scheme is "augmented" by a

sub-block technique which facilitates the treatment of the varying speed of sound with altitude. Grid adaptation and shock fitting have been also applied to the main blocks and sub-blocks of the propagation code. The repetitive solution cycles of the grid-adaptation and shock-fitting (GASF) [31] schemes minimize the root mean square of relative errors in the mass, momentum and energy across the shock. Grid adaptation and shock fitting GASF [31] have been applied to the main blocks and sub-blocks of the propagation code.

The conservative form of the full- potential equation is solved using a space marching, upwind scheme. This scheme is "augmented" by a sub-block technique, which facilitates the treatment of the varying speed of sound. The three-dimensional full-potential equation written in conservation-law form is given by

$$(\rho\phi_x)_x + (\rho\phi_y)_y + (\rho\phi_z)_z = 0 \qquad \text{..... 3.72}$$

$$\rho = \left[1 + \tfrac{\gamma-1}{2} M_\infty^2 (1 - \phi_x^2 - \phi_y^2 - \phi_z^2\right]^{\frac{1}{\gamma-1}} \qquad \text{..... 3.73}$$

In computational domain, it can be written as

$$\left(\rho\frac{U}{J}\right)_\xi + \left(\rho\frac{V}{J}\right)_\eta + \left(\rho\frac{W}{J}\right)_\zeta = 0 \qquad \text{..... 3.74}$$

Where

$$\begin{Bmatrix} U \\ V \\ W \end{Bmatrix} = \begin{bmatrix} a_{11} & a_{12} & a_{13} \\ a_{21} & a_{22} & a_{23} \\ a_{31} & a_{32} & a_{33} \end{bmatrix} \begin{Bmatrix} \phi_\xi \\ \phi_\eta \\ \phi_\zeta \end{Bmatrix} \qquad \text{..... 3.75}$$

And a_{ij} are the metric coefficients.

$$J = \frac{\partial(\xi,\eta,\zeta)}{\partial(x,y,z)} = \begin{bmatrix} \xi_x & \xi_y & \xi_z \\ \eta_x & \eta_y & \eta_z \\ \zeta_x & \zeta_y & \zeta_z \end{bmatrix} \qquad \text{..... 3.76}$$

The $\left(\frac{\rho U}{J}\right)_{\xi}$ term is differenced using an upwind scheme and $\left(\frac{\rho V}{J}\right)_{\eta}$ and $\left(\frac{\rho W}{J}\right)_{\zeta}$ are differenced using a central differencing scheme. In the central differencing scheme an artificial density dissipation term is added for use if needed.

At the interface the velocity components (u, v, w) of the Euler solution are transformed into velocity potentials that are used for the initial conditions of the full-potential solver. The steps of the computational process are discussed in the report by Kandil and Zang [35].

Two types of interfaces are used; one is the interface in the marching direction (Type I) and the other is the interface in the peripheral direction (Type II). For Interface Type I, the flow is supersonic and the direction of flow is perpendicular to the interface. For interface Type II, the flow perpendicular to interface is subsonic flow and needs to be iterated between the sub blocks until the error is reduced to the desired tolerance level and convergence is achieved.

The atmospheric conditions vary continuously with the altitude. To simulate the real flow, a sub-block technique has been developed to account for this variation. In each sub-block, atmospheric conditions are assumed as uniform flow and the free-stream conditions are determined from the altitude conditions at the midpoint altitude of this sub-block.

3.3.2 Thomas Ray Tracing Approach

The waveform parameter method [36] developed by Thomas is different from the code developed by Hayes [52]. Rather than using the F-function as a starting point, Thomas code uses pressure at some radius below the aircraft to propagate the acoustic waves. One could argue that both these methods developed by Hayes [52] and Thomas [36] are equivalent; however, there are fundamental differences between the two methods.

The Thomas program [36] was developed to directly use the near field pressure signature from the wind tunnel tests. Hence, care has to be taken to measure the near field pressure sufficiently far away from the aircraft so that geometrical acoustics principles can be applied. Geometrical acoustics, like geometrical optics, is a field where sound waves are treated as rays. Refraction and propagation of acoustic waves through layers of changing refractive indices can be computed using the well known Snell's law for waves.

Sonic boom pressure signatures are traced to the ground altitude using ray acoustics. Therefore, it is possible that under certain flight and atmospheric conditions, the ray tube area might vanish. This causes the linearized acoustic solutions to break down. In order to overcome these singular solutions, equations for focus of weak shock waves were obtained by Guiraud and scaling laws [12] were developed.

3.4 Overview Optimization

The Response Surface Method (RSM) [73] design helps to quantify the relationships between one or more measured responses and the vital input factors. If five or more design variables are considered a two-level factorial screening should be done. The objective is to find a desirable location in the design space. This could be a maximum, a minimum or an area where the response is stable over a range of the design variables. Goals might include meeting a set of specifications for several responses simultaneously.

Design-Expert [34] is used for carrying out the optimization study. It offers several optimization strategies depending on the number of design factors or design variables and responses. Design-Expert software's numerical optimization will maximize, minimize or target a single response, a single response and subject to upper and/or lower boundaries on other responses and combinations of two or more responses.

One can determine how many design points are needed for a good response surface design. The response surface method produces a mathematical model that you can use to predict a response. You should provide the following design features to build a good model:

1. Enough unique design points to estimate all the terms in the postulated model: linear, 2FI, quadratic or cubic. The number of model terms increases in proportion to the number of factors studied.
2. Extra unique design points, above what's needed for estimating the model and pure error to test how the model fits the data. These points must be at locations in the design space that are different from the model points. They are used in a "Lack of Fit" test for the model. One should specify at least four of these extra points to give an adequate statistical test.
3. Replicates some design points to estimate the experimental, or pure, error. This is the error to be expected in the response if the experiment is repeated starting from scratch. Typically, the center point of the design is repeated, often four or more times. This gives an adequate estimate of the variation of the response and provides the number of degrees of freedom needed for an adequate statistical test of the model. You may choose to duplicate other points in the design if you desire better estimates of the response at those areas in the experimental space.

As a guide, here is a table of the number of coefficients in linear, quadratic, and cubic equations for the given number of factors. In summary, to ensure success in RSM modeling, you should allow for sufficient model points, plus at least 4 replicate points, plus at least 4 other points to determine the fit of the model.

# FACTORS	LINEAR	QUADRATIC	CUBIC
2	3	6	10
3	4	10	20
4	5	15	35
5	6	21	56
6	7	28	84
7	8	36	120

Table 3.1 Number of factor for various methods

Myers and Montgomery [73] describe a multiple response method called desirability. The method makes use of an objective function, called the desirability function. It reflects the desirable ranges for each response. The desirable ranges are from zero to one (least to

most desirable respectively). The simultaneous objective function is a geometric mean of all transformed responses. If any of the responses or factors falls outside their desirability range, the overall function becomes zero. For simultaneous optimization each response must have a low and high value assigned to each goal. The optimal design parameters determined after a sequence of CFD runs has been conducted and a series of CFD models result are already obtained.

From a mathematical point of view, the objective is to find the optimized design variable in this case (nose angle, thickness, camber and dihedral angle) X1, X_2... X_k that maximize or minimize the r system response variables Y_1, Y_2... Y_r (Lift to drag ratio L/D and Peak shock strength RHO).

Response models are fit from CFD input data. The fitted responses are local approximations. In the multiple response case, finding the process operating conditions that simultaneously maximize (or minimize, as desired) all the responses is quite difficult, and often impossible. Almost inevitably, one must make some trade-offs in order to find process operating conditions that are satisfactory for most (and hopefully all) the responses. When the responses exhibit adequate linear fit (i.e., the response models are all linear), the objective is to find a direction or path that simultaneously considers the individual paths of maximum improvement and balances them in some way.

3.4.1 Single Response Approach

If X1, X_2, ...,X_k are design variables for the response of interest, Y. A first-order model will serve as a good local approximation in a small region close to the initial operating conditions

$$Y = b_0 + b_1 X_1 + b_2 X_2 + \ldots\ldots\ldots + b_k X_k \qquad \ldots\ldots\ldots\ldots\ldots\ldots 3.77$$

There are two main decisions to make for optimization

1. Determine the search direction;
2. Determine the length of the step to move from the current operating conditions.

Suppose a first-order model has been fit and provides a useful approximation. As long as lack of fit (due to pure quadratic curvature and interactions) is very small compared to the main effects, the steepest ascent can be attempted. To determine the direction of maximum improvement we use

1. The estimated direction of steepest ascent, given by the gradient of Y, if the objective is to *maximize* Y.
2. The estimated direction of steepest descent, given by the negative of the gradient of Y, if the objective is to *minimize* Y.

The direction of the gradient, $\boldsymbol{g}$, is given by the values of the parameter estimates, that is, $\boldsymbol{g}' = (b_1, b_2, ..., b_k)$. Since the parameter estimates $b_1, b_2, ..., b_k$ depend on the scaling convention for the factors, the steepest ascent (descent) direction is also scale dependent. That is, two experimenters using different scaling conventions will follow different paths for process improvement. This does not diminish the general validity of the method since the region of the search, as given by the signs of the parameter estimates, does not change with scale. An equal variance scaling convention, however, is recommended. The coded factors x_i, in terms of the factors in the original units of measurement, X_i, are obtained from the relation

$$x_i = \frac{X_i - (X_{low} + X_{high})/2}{(X_{high} - X_{low})/2} \quad i = 1, 2, ...k \qquad \text{..... 3.78}$$

This coding convention is recommended since it provides parameter estimates that are scale independent, generally leading to a more reliable search direction. The coordinates of the factor settings in the direction of steepest ascent, positioned a distance ρ from the origin, are given by:

Maximize $\quad b_0 + b_1X_1 + b_2X_2 + ... + b_kX_k \qquad$ 3.79

Subject to: $\quad \sum_{i=1}^{k} x_i^2 \le \rho^2 \qquad$ 3.80

This problem can be solved with the aid of an optimization solver (e.g., like the solver option of a spreadsheet). However, in this case this is not really needed, as the solution is a simple equation that yields the coordinates.

3.4.2 Multiple Response Approach

For multiple responses a weighted priority strategy for the path of steepest ascent for each response is used.

1. Compute the gradients $\boldsymbol{g_i}$ ($i = 1, 2 \ldots k$) of all responses. If one of the responses is clearly of primary interest compared to the others, use only the gradient of this response Otherwise, continue with step 2.
2. Determine relative priorities π_i for each of the **k** responses. Then, the weighted gradient for the search direction is given by

$$g = \frac{\pi_1 g_1 + \pi_2 g_2 + \ldots\ldots \pi_k g_k}{\sum_{i=1}^{k} \pi_i} \qquad \ldots\ldots\ldots\ldots\ldots\ldots\ldots 3.81$$

And the weighted direction is $$d = \frac{g}{\| g \|} \qquad \ldots\ldots\ldots\ldots 3.82$$

3.4.3 Summary : Optimization Approaches

In the current study single and multiple response surface essentially uses a steepest descent approach for finding out the optimized variables. A search direction is obtained by weighted gradient in the case of a multiple response study. Priorities for each of the response surfaces can be explicitly defined and a weighted search direction is obtained.

Delta wing shape is optimized with a multiple response surface optimization approach. Two response surfaces are desired for maximizing the aerodynamic performance and minimizing the sonic boom ground signature. Each of the responses is given an equal priority.

CHAPTER 4
RESULT - PREDICTION SONIC BOOM FOCUSING USING CONSERVATIVE COMPUTATIONAL SOLUTION

Chapter 4 presents the results obtained for sonic boom focusing prediction using a conservative time domain (CTD) approach. A two dimensional computer program is developed on a structured grid system to solve the non-linear Tricomi equation. A solution is obtained for the N-wave case, Concorde input wave and other incoming shock waves. A validation study is also presented to validate the developed computer program for linear and nonlinear cases. Some of the results are also compared with earlier methods developed [54-58] based on non-conservative schemes.

4.1 Introduction – Sonic Boom Focusing or "Super Boom"

Sonic boom focusing or "Super Boom" is predicted by solving the conservative form of the nonlinear Tricomi equation. Computational results are obtained and discussed for numerous incoming shock waves. Later in chapter 4 elaborate parametric studies [76] are presented for N-wave and Concorde-wave. Parametric study [76] is carried out in order to identify the validity of computational domain size, effect of input type/shape of the incoming wave, effect of footprint width (FPW) and shock strength. Parametric studies can help in better understanding for focusing phenomenon and setting guidelines for new design strategies for supersonic business jets. The nonlinear atmospheric viscosity μ is assumed to be constant and is taken as 0.08. The most test cases are run for 20,000 time steps to achieve the residual level of $10E^{-12}$ with grid size of 8.1 million.

4.1.1 Incoming N-Wave

A rectangular domain with z ranging from -2.0 to 2.0 and τ ranging from -3.17 to 4.17 dimensionless units is chosen for the computational domain. The number of grids in the z direction is 1000 and in the τ direction is 8,192. The F function of equation 3.27 in chapter 3 on the upper boundary z = 2.0 is used as an incoming N-wave, which extends from τ = -1.386 to τ = – 2.386 (duration of 1) with p_{max} = 1.0 and p_{min} = -1.0. Figure 4.1

(left part) shows the incoming N wave. Input N wave made non dimensional for pressures and duration. Non dimensional pressure p = 1.0 is equivalent to 2.25 psf and τ = 1 is equivalent to 150 [ms]. The non dimensional time step for the pseudo time integration is taken as 0.001.

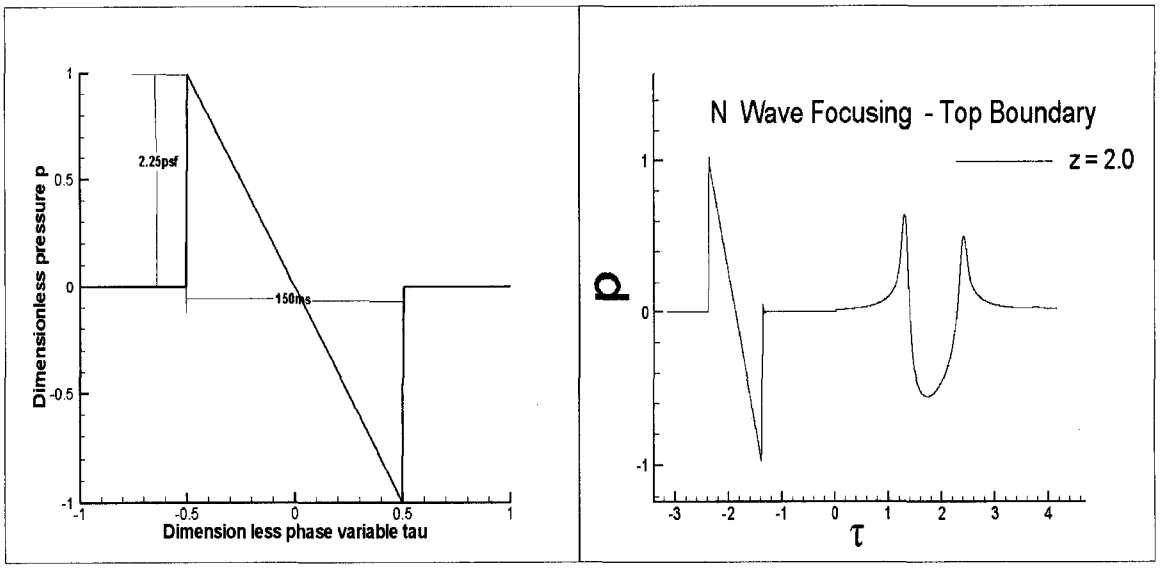

Fig 4.1 N Wave Type Signal

The right part of Fig. 4.1 shows the incoming and outgoing waves at z = 2.0. In each iteration step, the top boundary condition is explicitly imposed. The captured caustic surface appears just above the ground and is shown by a solid black line in Figure 4.2.

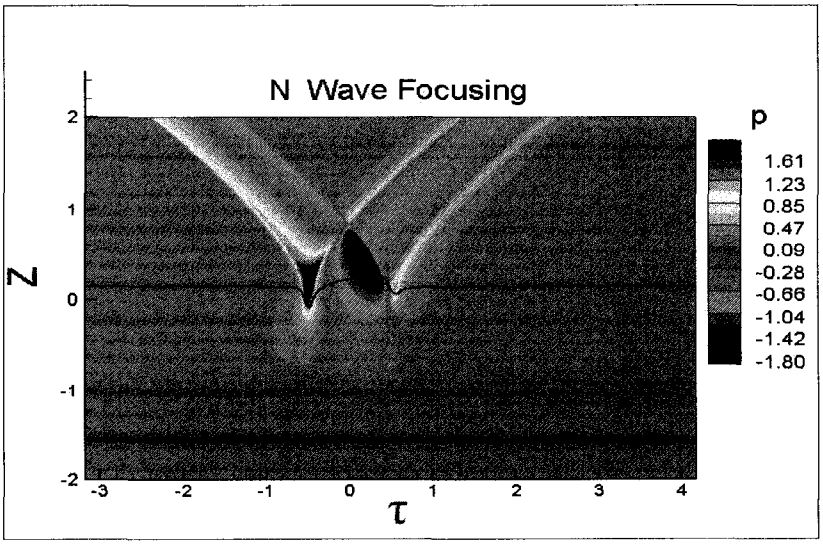

Fig 4.2 Pressure Contours for N wave

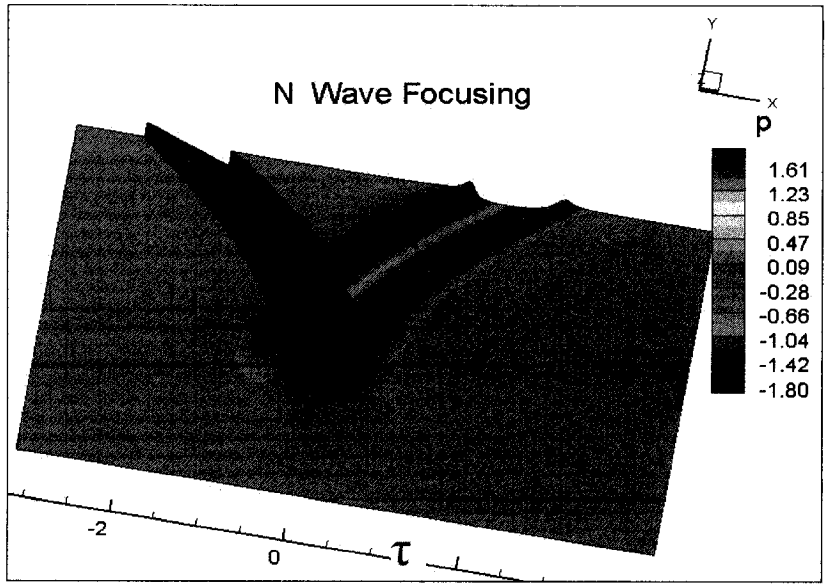

Fig 4.3 Pressure Contours for N wave

Figure 4.3 shows the pressure contour for the incoming N-wave. Figure 4.4 shows the pressure variations at various z locations of the incoming wave as it progresses in the domain toward the caustic surface. The pressure wave in the shadow zone at z = -1.0 is also shown in Fig 4.4.

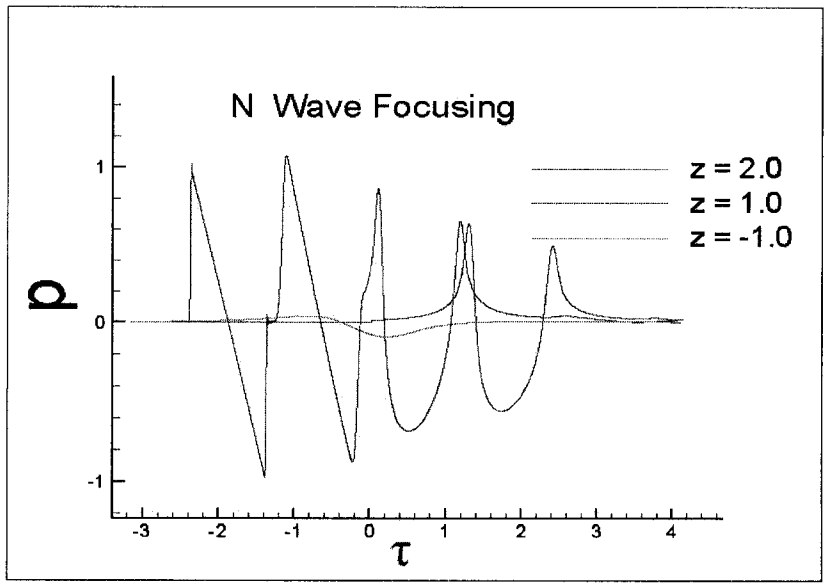

Fig 4.4 Pressure plot at various z locations

Figure 4.5 shows peak pressure location z = 0.1378 with a non dimensional peak pressure value of 2.898. After the focused boom at the caustic surface, shock waves are bounced back in the upper atmosphere above the caustics surface in the illumination zone and exponentially decay and eventually die out below the caustic surface in shadow zone as

shown in Fig 4.4.The second highest peak was found at z =1.1077 and the lower peak was found at z = -1.432. The wave is completely suppressed in the shadow zone (z -1.5).

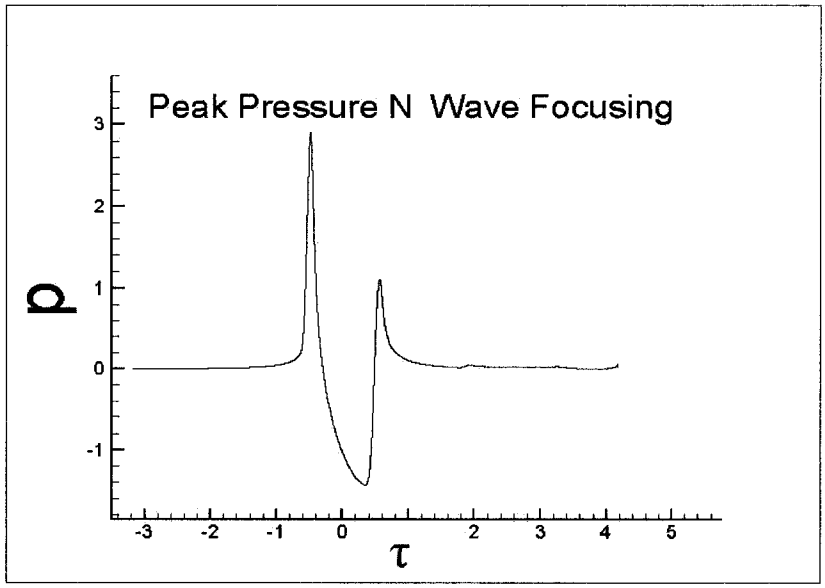

Fig 4.5 Peak Pressure for N wave for $\mu = 0.08$

Pressure contours in Fig 4.3 show the incoming wave as it progresses toward the caustic surface and the outgoing wave as it originates from the caustic surface. These results conclusively show that the super boom response is predicted. The case has been run for 20,000 time steps until the total error of the pseudo time term is reduced to 10^{-12}.

4.1.2 Validation Study for the N Wave Focusing

N wave focusing phenomenon can be solved with an analytical approach only for a linear case with $\mu = 0$ by Fourier transformation of Airy function [39], whereas no analytical solution is available for nonlinear cases. Efficiency of the algorithm is validated against the analytical solution for the linear case of $\mu = 0$. The computational result presents all the features of the evolution of the pressure waveforms while approaching the caustic.

Figure 4.6 shows the comparison of the solution obtained with the conservative scheme to the analytical solution of Airy function at the caustic surface. It has also been validated that merging happens just above the ground at the caustic line. Results obtained from the developed scheme show an excellent match with the peak pressure and location of caustic with analytical solution for the linear case.

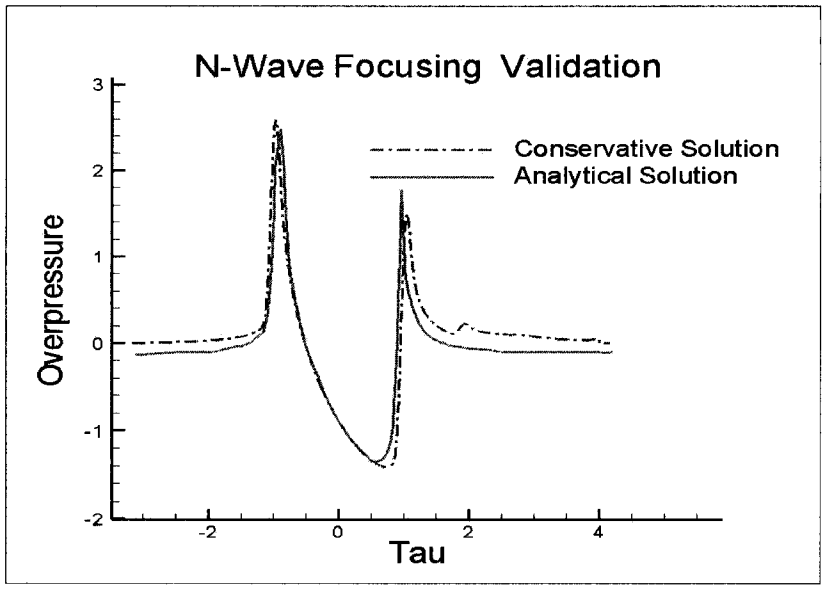

Fig 4.6 Validation of N wave focusing with analytical solution at caustic $\mu = 0$

Guirad's scaling law [12] is the only quantitative validation for nonlinear cases. Grid independence is achieved in all computed cases with convergence of 10E $^{-12.}$ A convergence test is also considered as a part of validation study.

4.1.3 Incoming Concorde Wave

Figure 4.7 shows the Concorde aircraft input wave signal. The input is made non dimensional for super boom effect computation. The F- functions of equation 3.27 on the upper boundary z = 2.0 are used as an incoming Concorde wave, which extends from τ = -1.386 to τ = – 2.386 (duration of 1) with p_{max} = .733 and 1.0, and p_{min} = -1.1378.

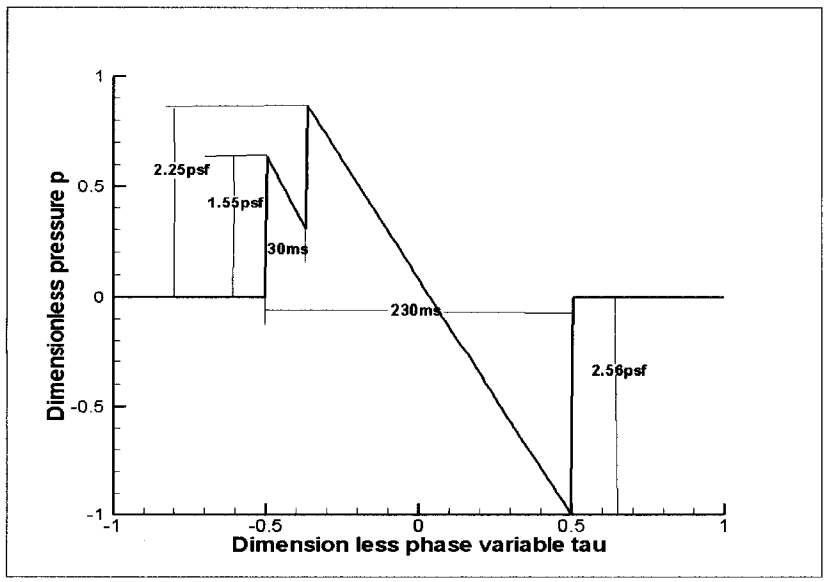

Fig 4.7 Concorde-aircraft wave

With these dimensionless pressure and duration, p = 1 is equivalent to 2.25 psf and τ = 1 is equivalent to 230 [ms]. Computational domain size is ranges from -2.0 to 2.0 in z direction and -2.67 to 3.67 in the τ direction. Figure 4.8 shows the pressure contour and caustic surface with solid black which appears just above the ground.

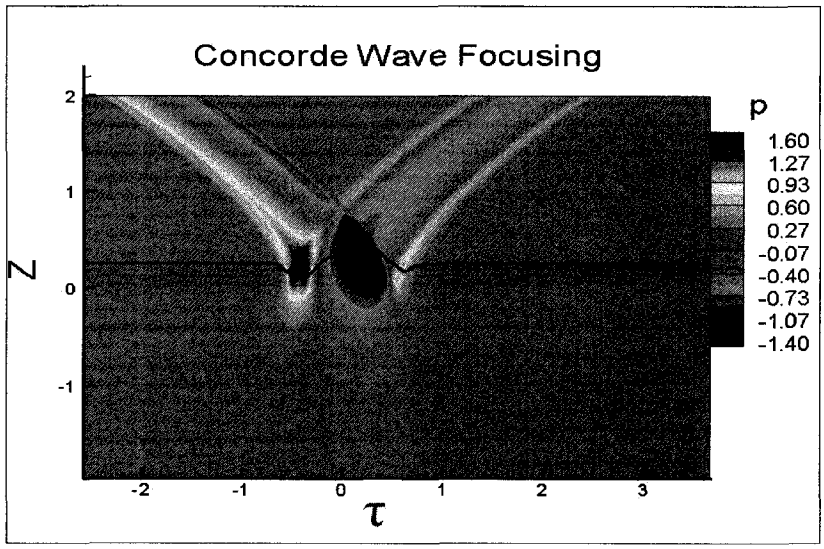

Fig 4.8 Pressure Contours for Concorde-aircraft wave

Figure 4.9 shows the pressure contours of the incoming wave as it progresses toward the caustic surface. The pressure contour of Fig 4.9 also shows the outgoing wave as it originates from the caustic surface. Figure 4.10 shows the pressure variations along the z locations (z = 2.0, 1.0 -1.0) of the incoming Concorde wave as it progresses toward the caustic surface.

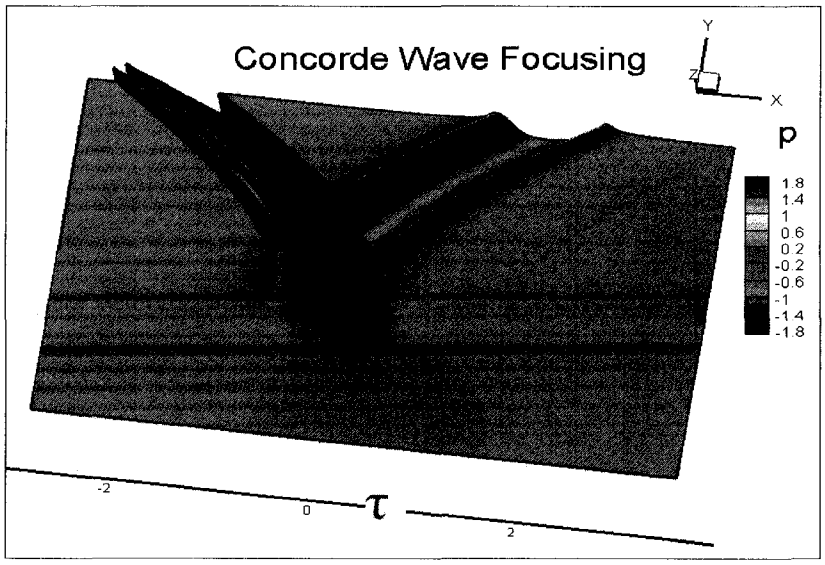

Fig 4.9 Concorde Focusing Pressure Contour

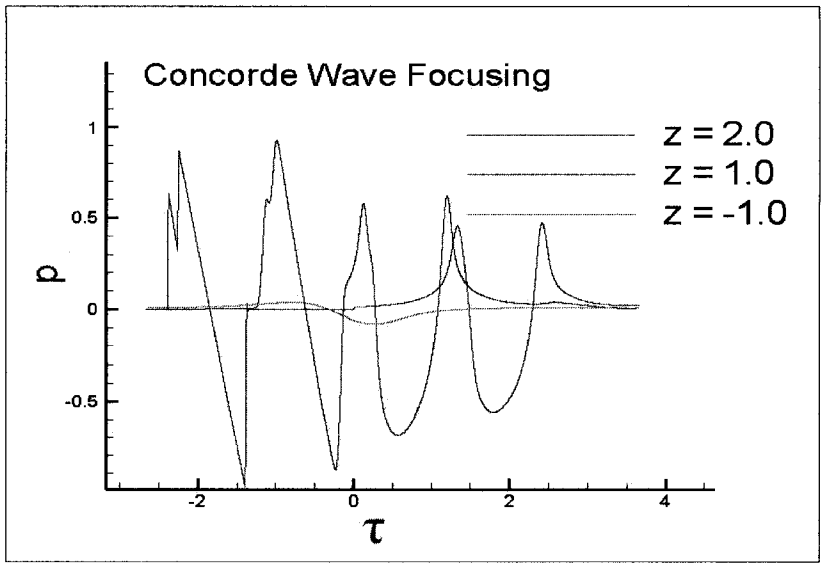

Fig 4.10 Pressure plot at various z locations

Shock waves are bounced back in the upper atmosphere above the caustic surface in the illumination zone and exponentially decay and eventually die out below the caustic surface in shadow zone as shown in Fig 4.10. A similar observation has been made earlier with the N wave case study and confirm that super boom response is predicted.

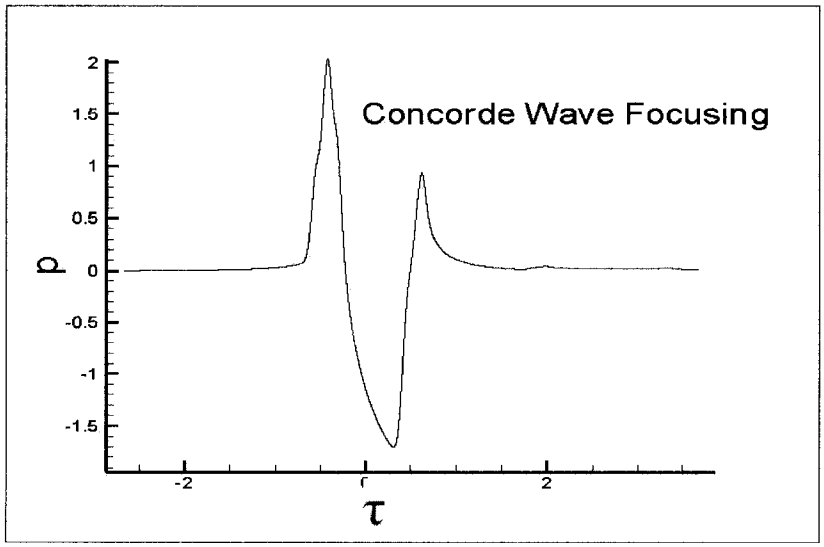

Fig 4.11 Peak Pressure for Concorde wave

Location of the caustic surface is found to be at z = 0.269 with peak amplification pressure P_{max} = 1.985 as shown in Fig 4.11. Amplification is found to be lesser as compared to the N-wave incoming signal. The distance between the two peaks of the Concorde wave also has a significant effect on peak pressure at the caustic surface. The computation is done until the convergence level reaches 10^{-12} and μ is assumed to 0.08.

4.1.4 Validation Study for the Concorde Wave Focusing

Concorde wave focusing has been validated against the result published by Auger and Coulouvrat [50]. The result shows a good match with the earlier published result by Auger et al. [50]. Peaks overpressure observed at caustics plane by the conservative approach are a little higher compared to published results [50]. The Coulouvrat approach is based on a non conservative solution of nonlinear Tricomi equation. It is also observed that location of surface of amplification matches are in excellent agreement. The nonlinear viscosity μ is assumed to be 0.075 for the computation.

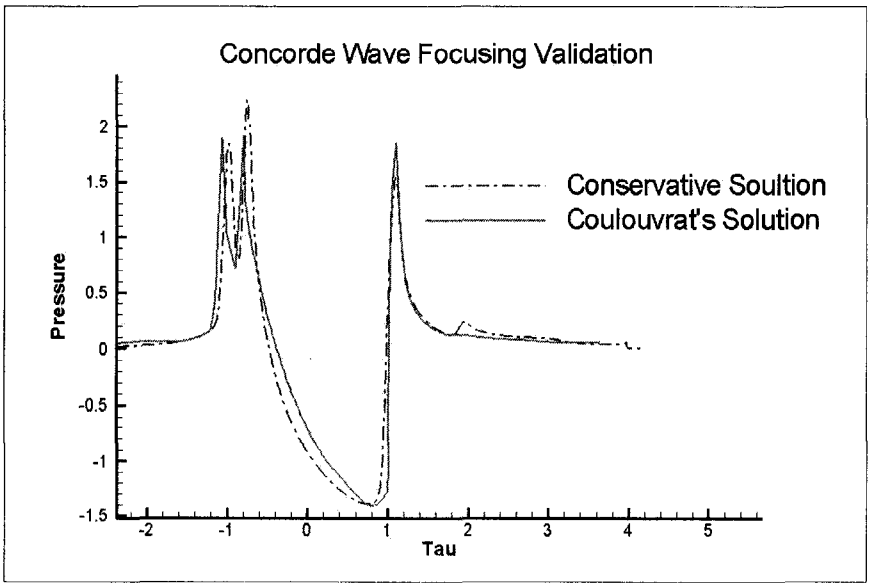

Fig 4.12 Concorde wave validation

Validation of the conservative Tricomi solver is concluded considering the solver shows a good match with available results [50]. Predicted results also satisfy Guirads's scaling laws [12]. Solution after the convergence proved to be independent of the initial guess. At the last grid, independence study is also counted toward the validation of conservative Tricomi solver for sonic boom focusing prediction.

4.2 Sonic Boom Focusing – Parametric Studies

It is important to identify and study the parameters which affect the magnitude of amplification and location of caustic surface. Understating such parameters would greatly influence the design and development of supersonic business jets. It has already been mentioned before; focusing is a regular phenomenon with accelerating flight and could be

influenced by parameters such as flying altitude, atmospheric non linearity, aircraft shape, flying mach number, etc. In the next section four parameters are computationally studied and discussed for their contribution towards peak pressure development and location of focusing for super boom effects.

4.2.1 Other Types of Input Signal

Other input types of waves have been studied to investigate their focusing responses. The focusing amplification and location of caustic surface have been studied for sine wave, symmetric ramp, asymmetric ramps, symmetric and asymmetric flat types, and stepped type input waves.

4.2.1.1 Incoming Symmetric Ramp Wave

The grid size and domain size is unchanged for the study. The F function on the upper boundary z = 2.0 is used as a symmetric ramp wave. Figure 4.13 shows the incoming symmetric ramp wave and incoming and outgoing waves at z = 2.0.

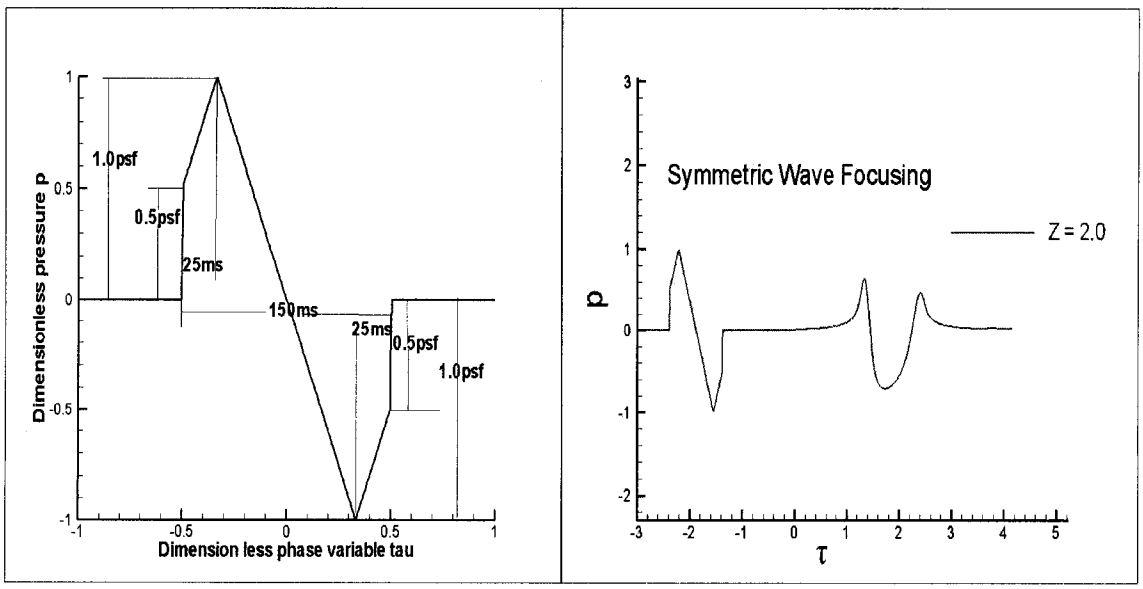

Fig 4.13 Symmetric Ramp Incoming and outgoing waves

The input wave extends from $\tau = -1.386$ to $\tau = -2.386$ (duration of 1) with $p_{max} = 1.0$ and $p_{min} = -1$. With these dimensionless pressures and duration p = 1.0 is equivalent to 1.00 psf and $\tau = 1.0$ is equivalent to 150 [ms]. Figure 4.14 shows the pressure contours for symmetric ramp wave focusing.

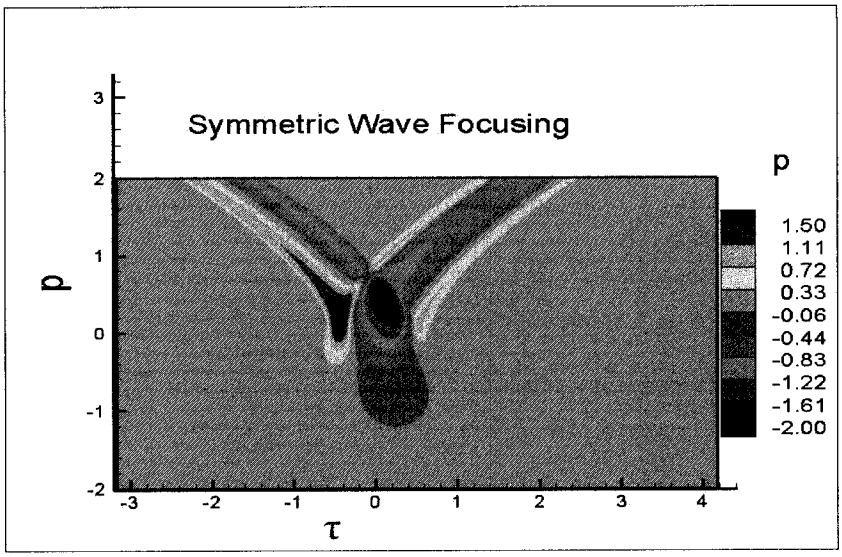

Fig 4.14 Pressure contour Symmetric Ramp Wave

Fig 4.15 shows the pressure variations at various z locations of the incoming wave as it progresses toward the caustic surface. The pressure wave in the shadow zone dies out after z = -1.0. Figure 4.16 shows the peak pressure of 2.78 at caustic surface z = 0.13.

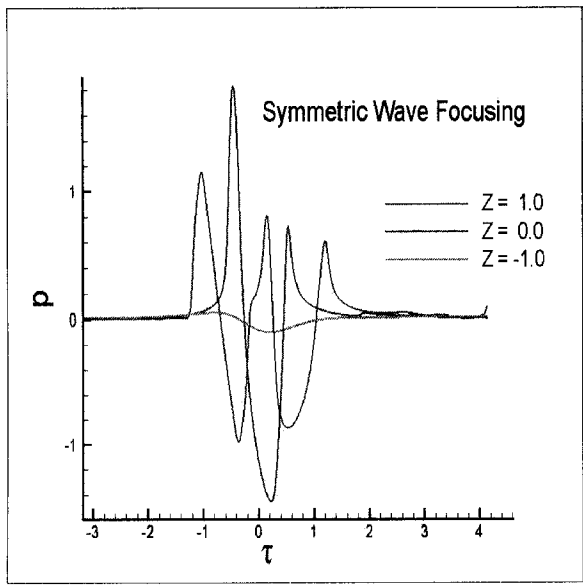

Fig 4.15 Pressure profile for Symmetric Wave

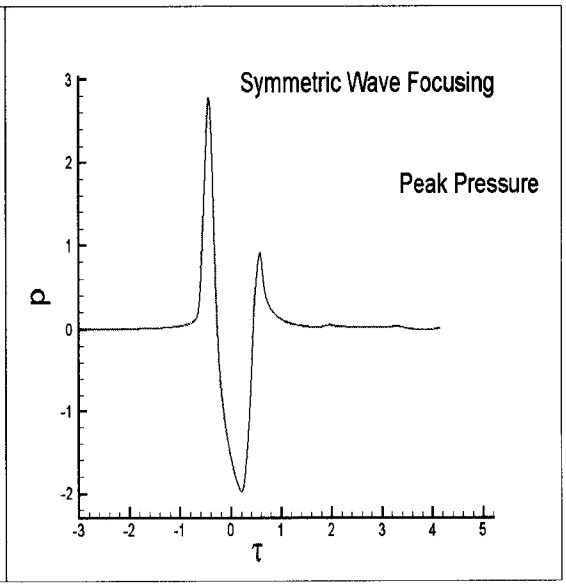

Fig 4.16 Peak Pressure at Caustic

4.2.1.2 Incoming Sine Wave

Figure 4.17 shows the pressure contour for sine wave focusing. The F function on the upper boundary z = 2.0 is used as a sine wave. The input wave extends from τ = -1.386 to τ = – 2.386 (duration of 1) with p_{max} = 1.0 and p_{min} = -1.0. Dimensionless pressures p = 1.0 is equivalent to 1.00 psf and duration τ = 1.0 is equivalent to 150 [ms].

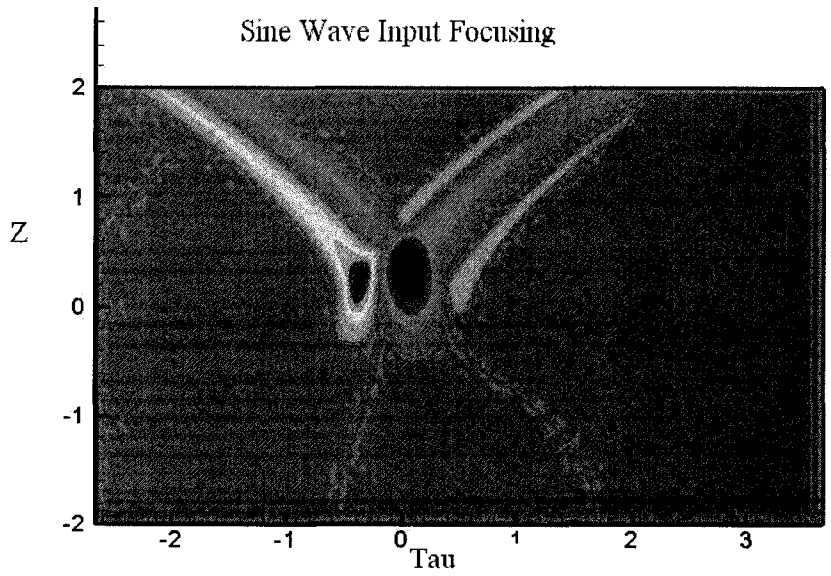

Fig 4.17 Pressure Contour for sine wave input

Figure 4.18 shows the incoming and outgoing waves at z = 2.0. Figure 4.19 shows the peak pressure of 2.8627 at caustic surface z = 0.237.

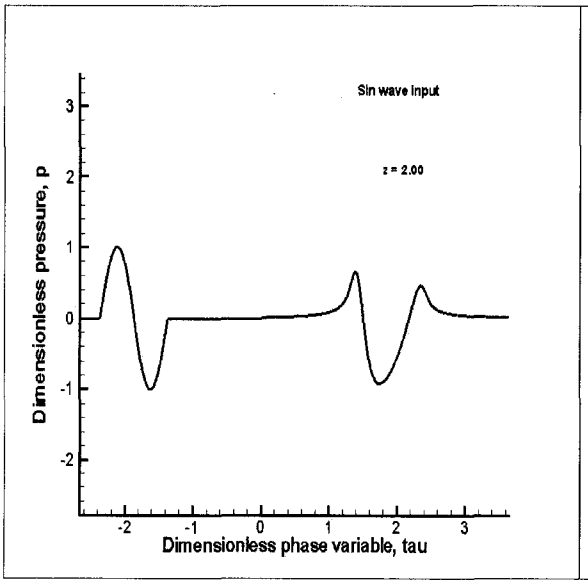

Fig 4.18 Top Boundary for sine wave

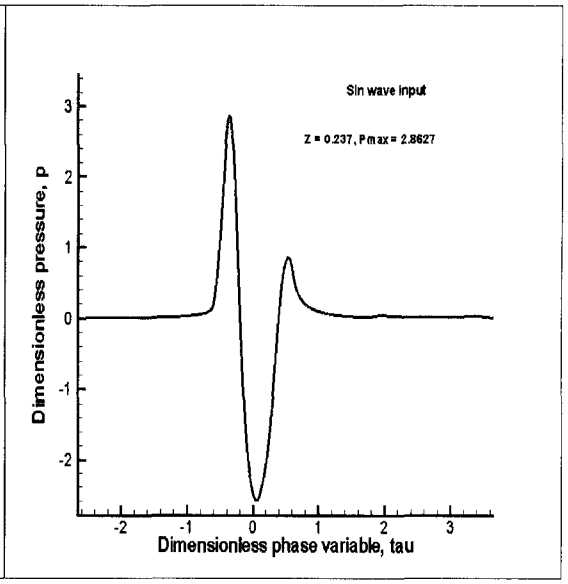

Fig 4.19 Peak Pressure sine wave

4.2.1.3 Incoming Symmetric Flat-Top Wave

The F function on the upper boundary z = 2.0 is used as a symmetric flat top wave as shown in Fig 4.20. The right part of Fig 4.20 shows the incoming and outgoing waves at z = 2.0. The input wave extends from $\tau = -1.386$ to $\tau = -2.386$ (duration of 1) with $p_{max} = 0.5$ and $p_{min} = -0.5$. The dimensionless phase variable $\tau = 1$ is equivalent to 150 ms.

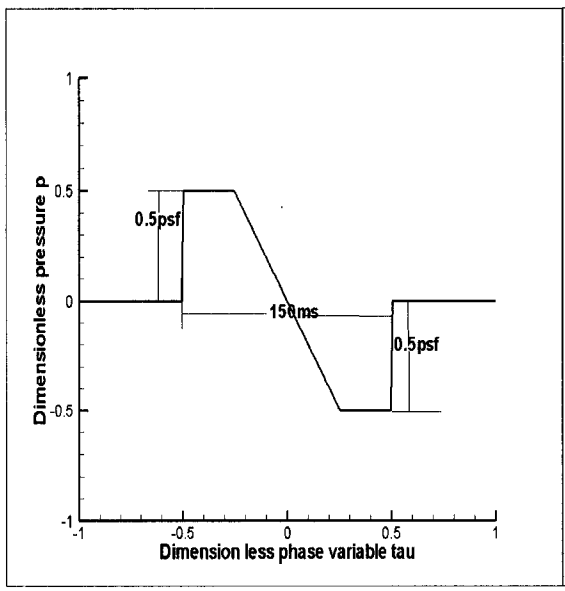

Fig 4.20 Symmetric flat top wave

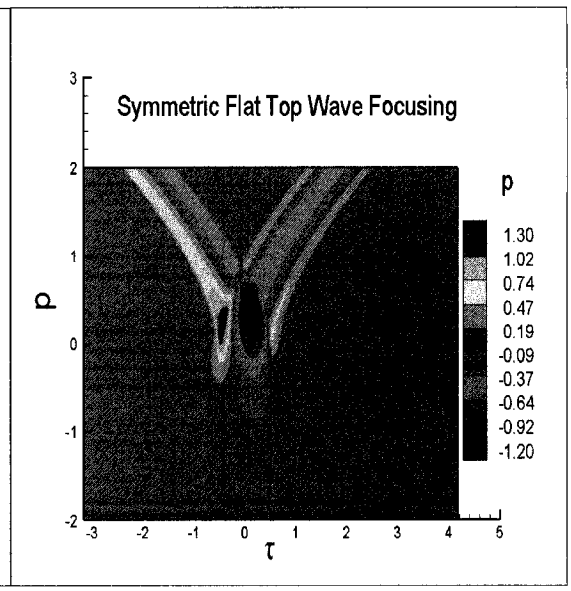

Fig 4.21 Pressure contour for focusing

Figure 4.21 shows the pressure contour for symmetric flat top wave focusing. Figure 4.22 shows the pressure variations at various z locations (1.0, 0 and -1.0) of the incoming wave as it progresses in the domain toward the ground. Figure 4.23 shows the peak pressure of 1.803 at caustic surface z = 0.18. Peak pressure is found to be lowering as compared to the N wave case with flat top profile and lower shock strength of incoming waves.

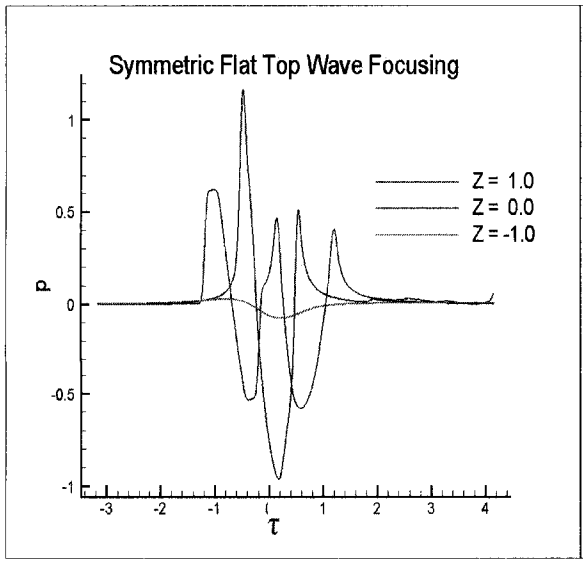

Fig 4.22 Pressure profile for Symmetric Wave

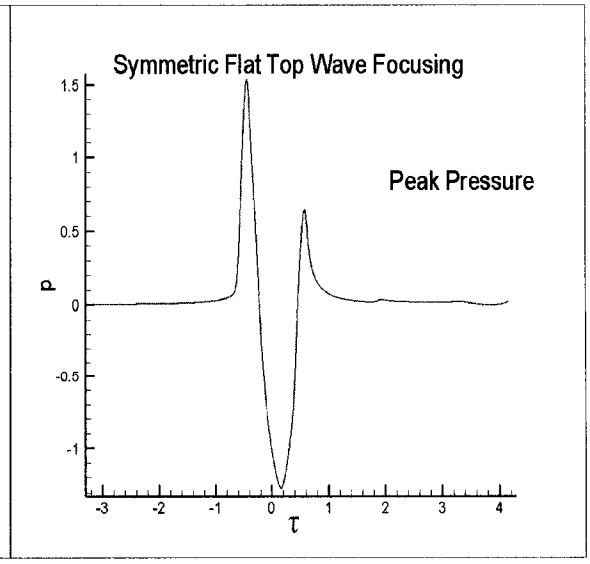

Fig 4.23 Peak Pressure at Caustic

4.2.1.4 Incoming Asymmetric Flat-Top Wave

The F function of the upper boundary z = 2.0 is used as an asymmetric flat-top wave as shown in Fig 4.24. The right part of Fig 4.24 shows the incoming and outgoing waves at z = 2.0. The input wave extends from $\tau = -1.386$ to $\tau = -2.386$ with $p_{max} = 0.5$ and $p_{min} = -1.0$. The dimensionless phase variable $\tau = 1$ is equivalent to 150 [ms].

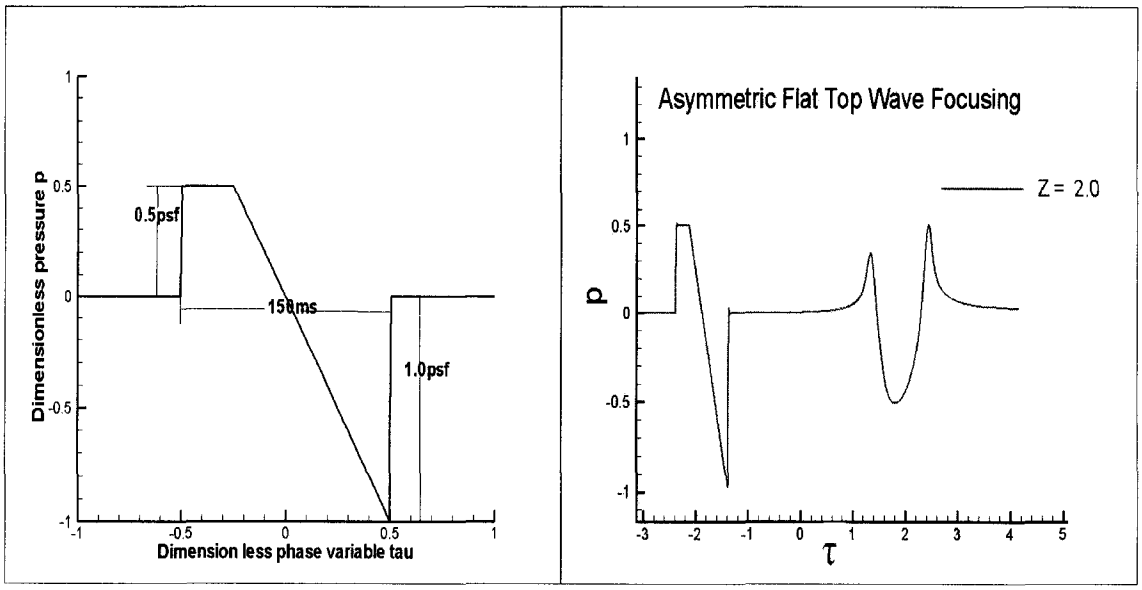

Fig 4.24 Pressure profile asymmetric flat top and Pressure profile top boundary

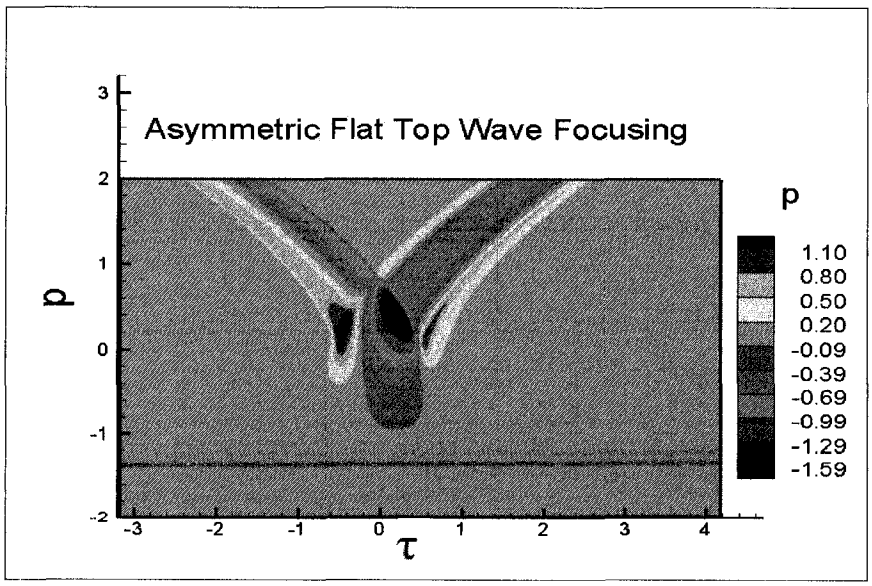

Fig 4.25 Pressure contour asymmetric flat top

Figure 4.25 shows the pressure contour for asymmetric flat top wave focusing. Figure 4.26 shows the pressure variations at various z (1.0, 0 and -1.0) locations of the incoming

wave as it progresses in the domain toward the ground. The pressure wave in the shadow zone dies out after z = -1.0. Figure 4.27 shows the peak pressure of 2.05 at caustic surface z = 0.23. The number of iteration and grid points used for computing the flow variable remains unchanged unless specified.

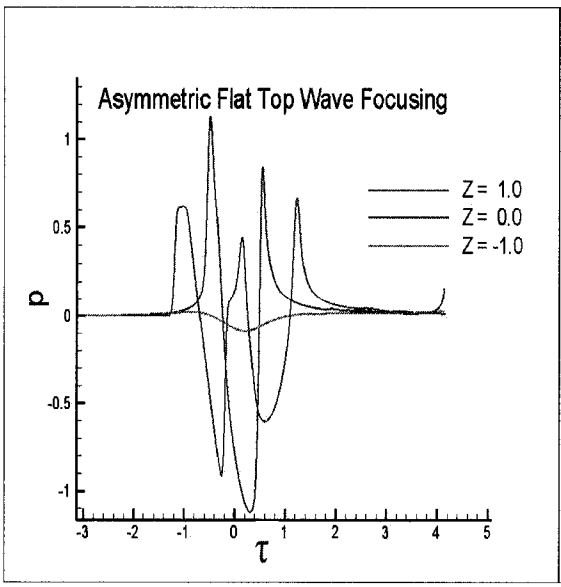

Fig. 4.26 Pressure profile for asymmetric flat top

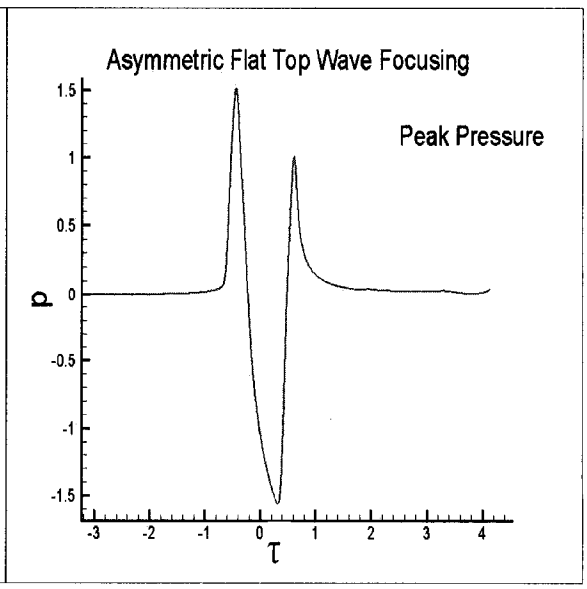

Fig. 4.27 Peak pressure at caustic

4.2.1.5 Incoming Asymmetric Ramp Type A

The F function of the upper boundary z = 2.0 is used as an asymmetric ramp type Figure 4.28 shows the incoming and outgoing waves for asymmetric ramp type A.

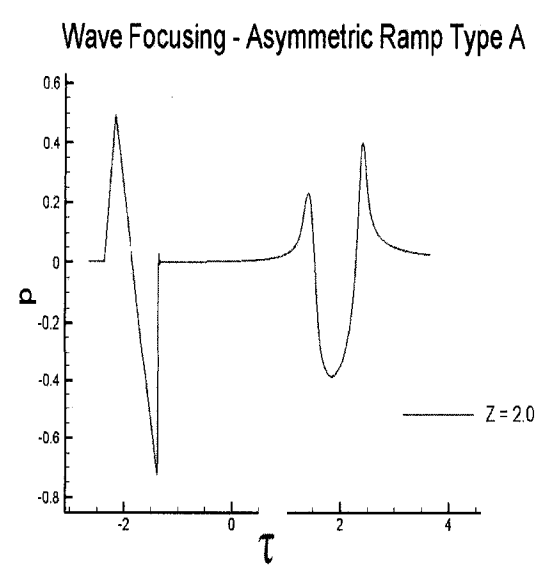

Fig .4.28 Incoming and outgoing waves

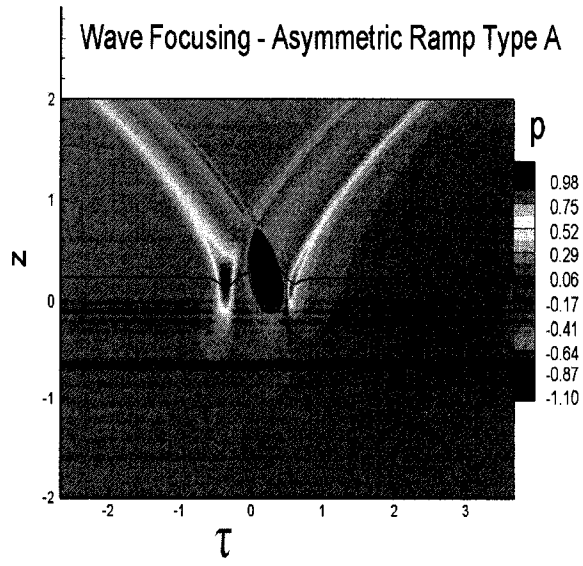

Fig. 4.29 Pressure contour asymmetric ramp type A

The input wave extends from τ = -1.386 to τ = – 2.386 (duration of 1.0) with p_{max} = 0.5 and p_{min} = -0.75. The dimensionless phase variable τ = 1.0 is equivalent to 150 [ms]. Fig. 4.29 shows the pressure contour for an asymmetric flat top wave focusing. In Fig. 4.29 solid black line represents the location of the caustic surface where the amplification of the waves is taking place. Fig.4.30 shows the isometric view for focusing phenomenon.

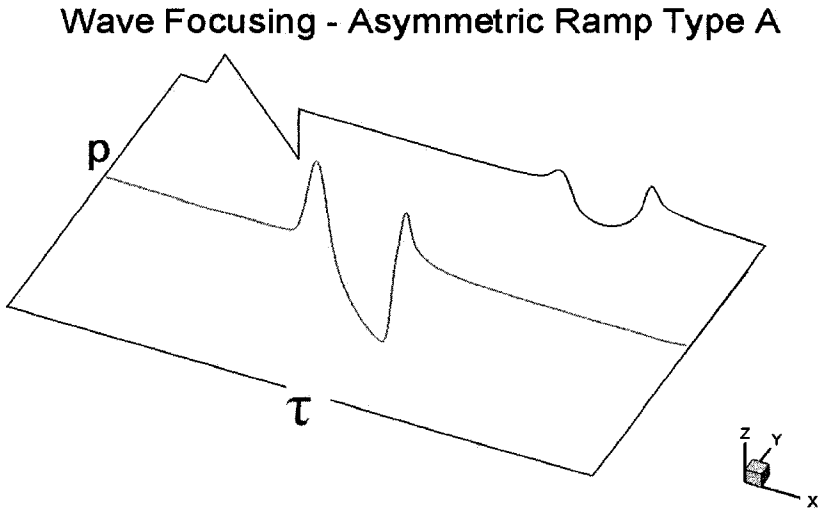

Fig. 4.30 shows the input wave and amplified wave after focusing took place.

Fig. 4.31 shows the pressure variations at various z (1.0, 0 and -1.0) locations of the incoming wave as it progresses in the domain toward the ground. Figure 4.32 shows the peak pressure of 1.25 at caustic surface z = 0.17.

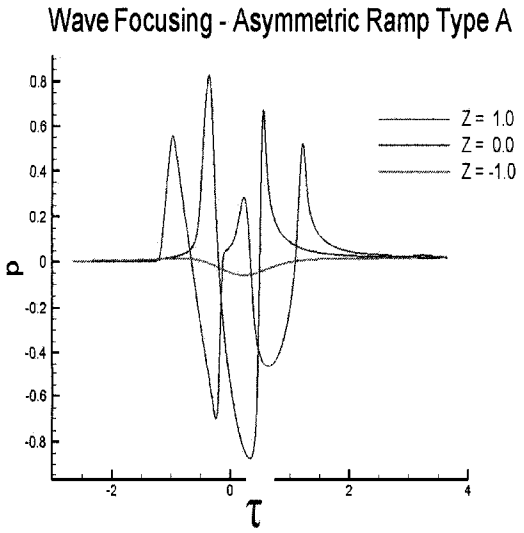

Fig. 4.31 Pressure variations asymmetric ramp A

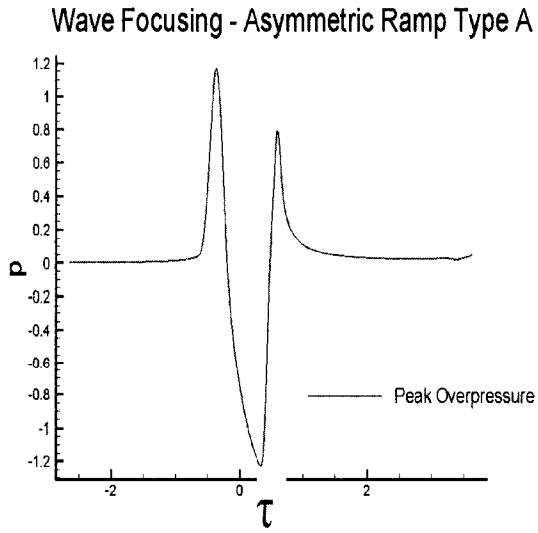

Fig. 4.32 Peak pressure at caustic

4.2.1.6 Incoming Ramp Type B

The F function on the upper boundary z = 2.0 is used as an asymmetric ramp type B wave as shown in Fig. 4.33. The input wave extends from $\tau = -1.386$ to $\tau = -2.386$ (duration of 1) with $p_{max} = 1.0$ and $p_{min} = -1.0$.

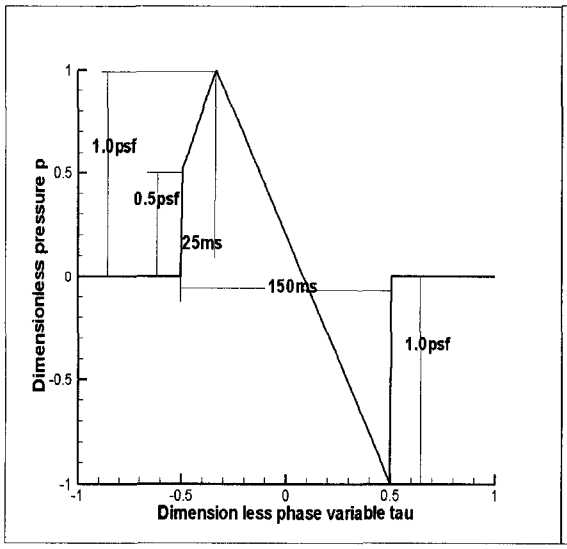

Fig. 4.33 Pressure profile ramp B

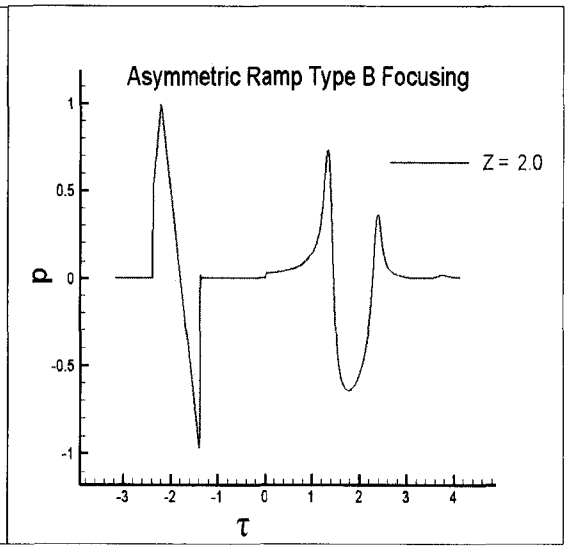

Fig. 4.34 Incoming and outgoing waves on top

The dimensionless phase variable $\tau = 1$ is equivalent to 150 [ms]. Fig. 4.34 shows the incoming and outgoing waves at the top boundary.

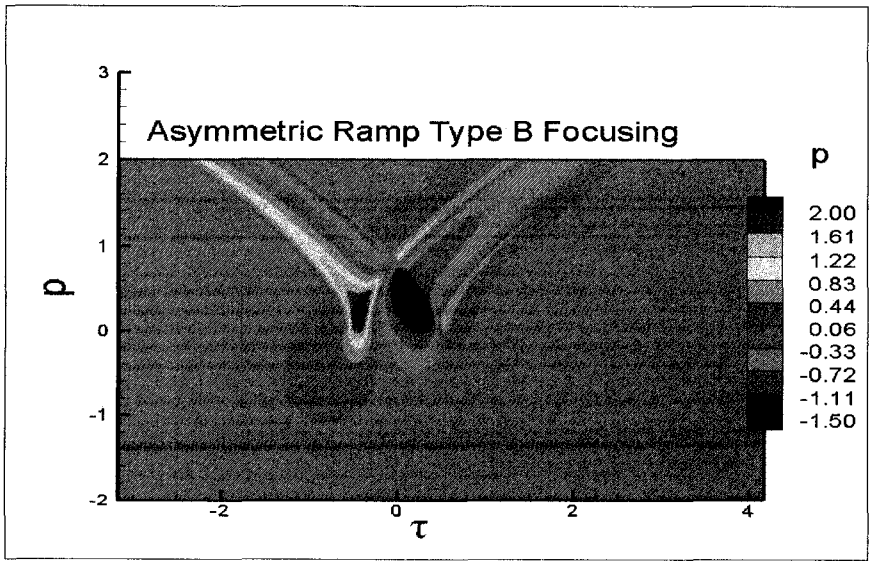

Fig. 4.35 Pressure contour ramp type B

Fig. 4.35 shows the pressure contour for asymmetric flat top wave focusing. Fig. 4.36 shows the pressure variations at various z (1.0, 0 and -1.0) locations of the incoming

wave as it progresses in the domain toward the ground. The pressure wave in the shadow zone dies out after z = -1.0. Figure 4.37 shows the peak pressure of 1.0824 at caustic surface z = 0.166. The number of iteration and grid points used for computing the flow variable remains unchanged unless specified.

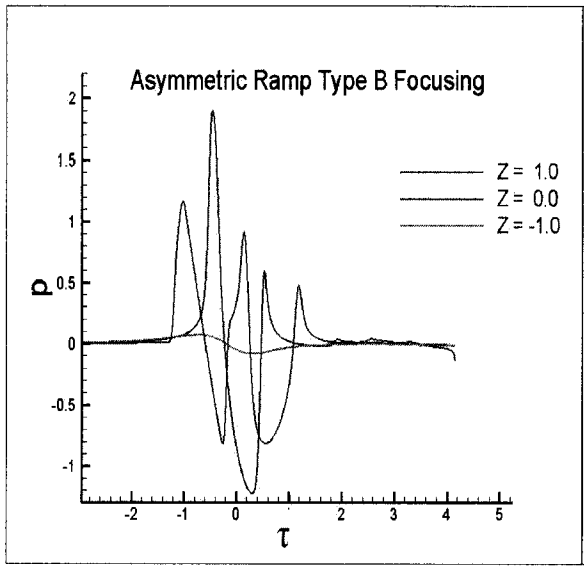

Fig 4.36 Pressure profile asymmetric ramp B

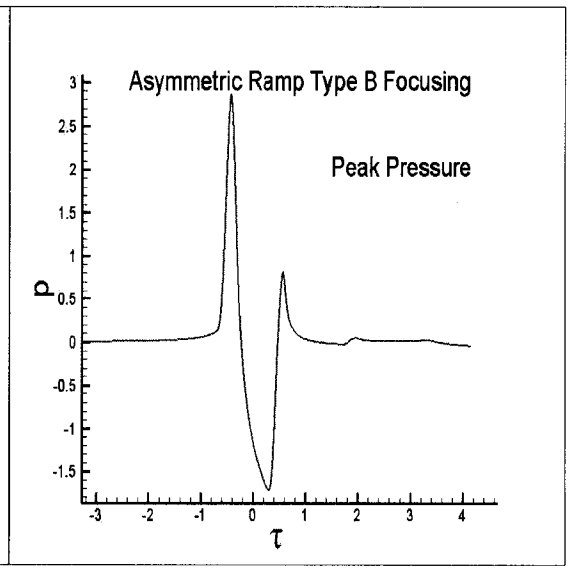

Fig 4.37 Peak pressure at caustic

4.2.1.7 Incoming Symmetric Ramp Wave B

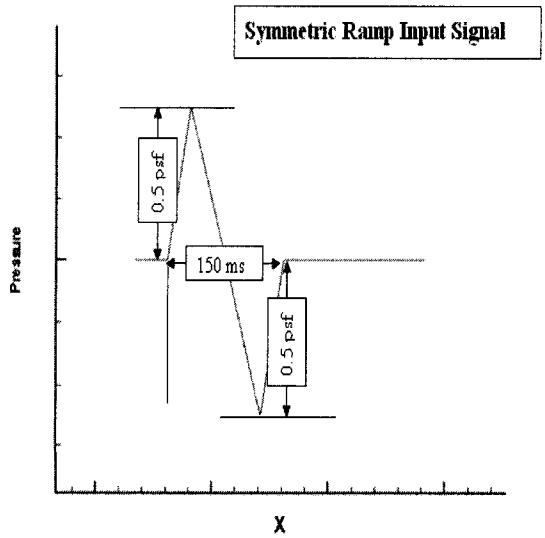

Fig. 4.38 Incoming symmetric ramp B

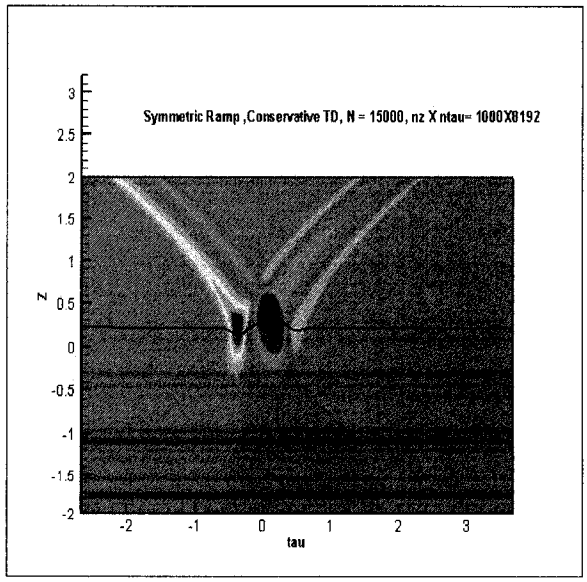

Fig. 4.39 Pressure Contour Sym Ramp B

Fig. 4.38 shows the pressure signature for incoming symmetric ramp B. Fig. 4.39 shows the pressure contour for asymmetric flat top wave focusing. The pressure wave in the

shadow zone dies out after z = -1.0 as shown in Fig 4.40. Fig. 4.41 shows the peak pressure of 1.1721 at caustic surface z = 0.205. Focusing phenomenon is successfully predicted in the case of the symmetric ramp wave B case as well.

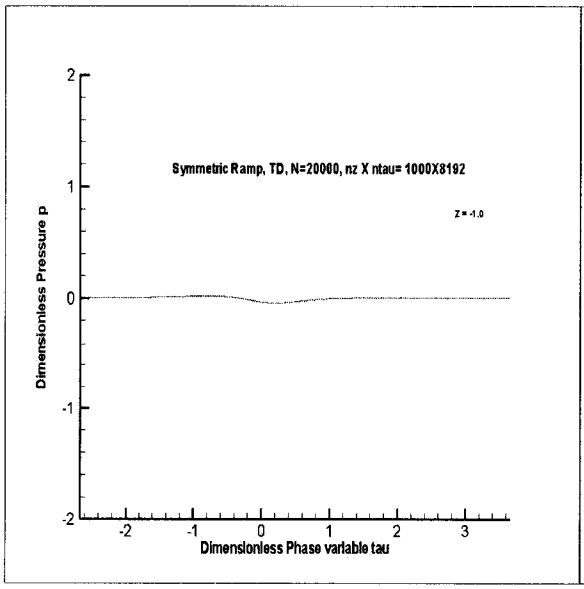

Fig. 4.40 Shadow zone profile symmetric ramp B

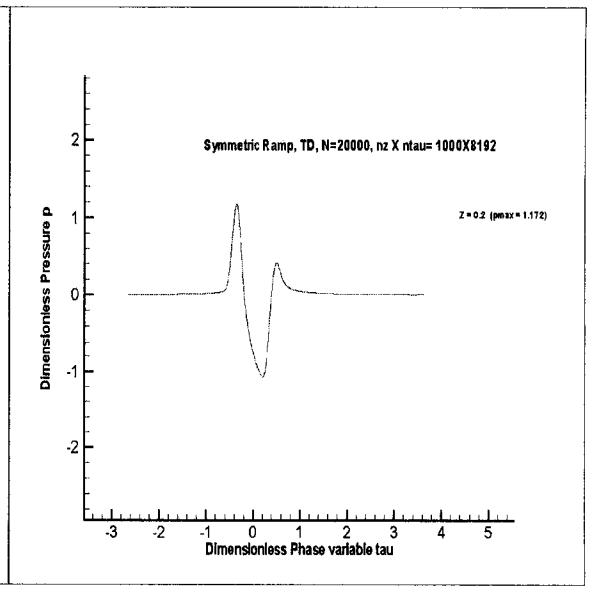

Fig. 4.41 Peak pressure at caustic Sym ramp B

4.2.1.8 Incoming Asymmetric Ramp Type B

Figure 4.42 shows the pressure signature for the incoming symmetric ramp B. Figure 4.43 shows the pressure contour for asymmetric flat top wave focusing. The pressure wave in the shadow zone dies out after z = -1.0 as shown in Fig. 4.44.

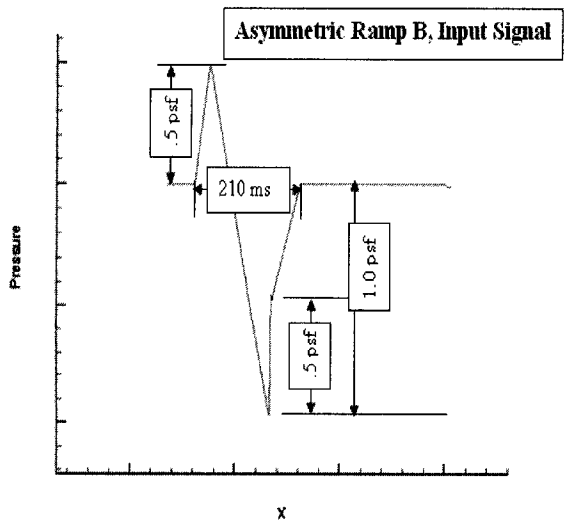

Fig. 4.42 Asymmetric ramp B incoming wave

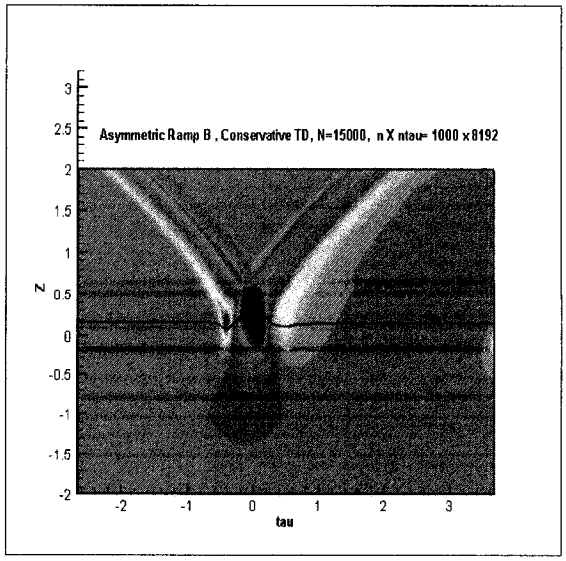

Fig .4.43 Pressure contour Asym ramp B

Figure 4.45 shows the peak pressure of 1.0825 at caustic surface z = 0.166. Focusing phenomenon is successfully predicted for asymmetric ramp incoming wave B.

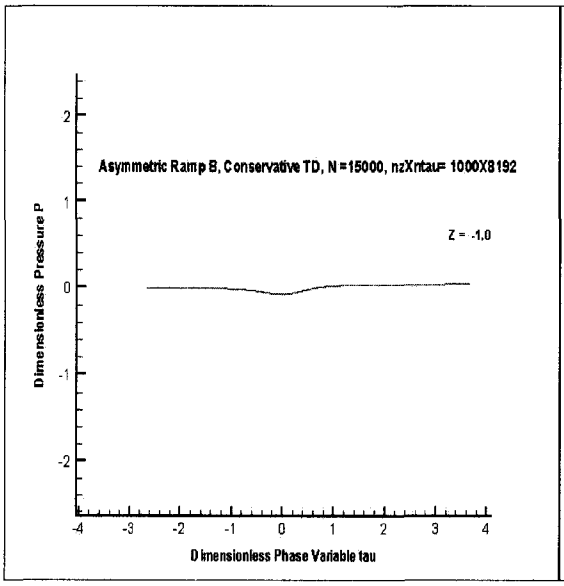

Fig 4.44 Pressure profile asymmetric ramp B

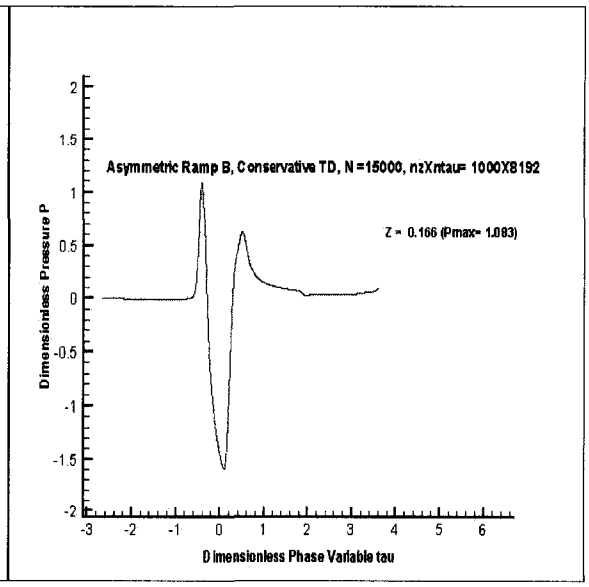

Fig 4.45 Peak pressure at caustic asy ramp B

4.2.1.9 Validation with Non Conservative Solution

The result obtained by the conservative method for symmetric wave B, asymmetric ramp A and asymmetric ramp B is validated against the earlier methods based on a non conservative approach. Figure 4.46 shows incoming and outgoing waves at the top boundary of the computational domain for the three cases considered for validation study.

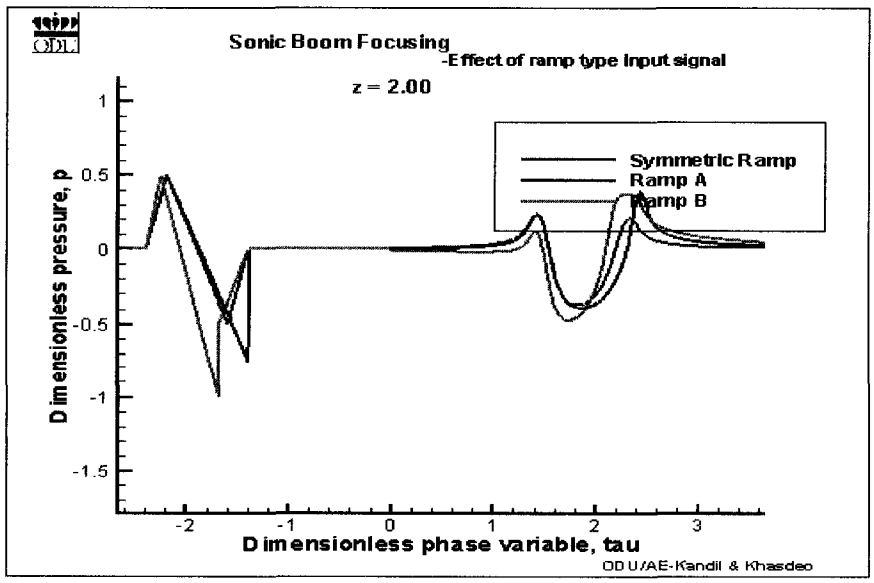

Fig 4.46 Pressure profile Comparison

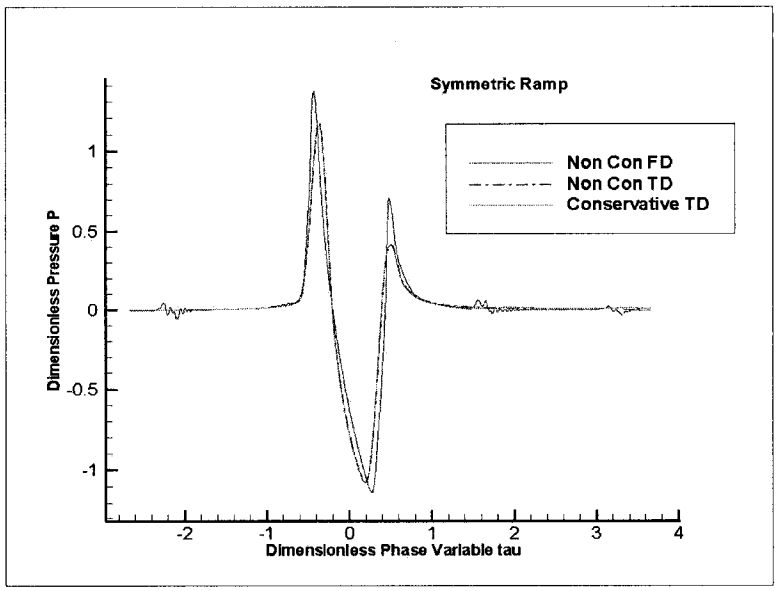

Fig 4.47 Symmetric Ramp B Validation

The non conservative solution is obtained by two approaches one is using a frequency domain and the other is a using time domain solution. Figure 4.47 shows the peak pressure at caustic surface for the considered incoming waves. Non conservative solution obtained using frequency domain approach shows overshoot in the peak pressure as compared to the time domain approach of non conservative and conservative solutions. Table 4.1 shows the comparison for all the computational approaches.

	Solution Methods		P_{max}	Z of P_{max}	Peak II	P_{min}	Grid
Symmetric Ramp B	Non conservative	FD	1.374	0.227	0.709	-1.13	1000X1024
		TD	1.1719	0.203	0.415	-1.075	1000X8192
	Conservative TD		1.1721	0.205	0.414	-1.08	1000X8192

Table 4.1 Validation of Symmetric Ramps B focusing

A similar observation has made for asymmetric ramp A and asymmetric ramp B cases as well. Figure 4.48 shows the peak pressure compassion for asymmetric ramp A case and Fig 4.49 shows the comparison for asymmetric ramp B case. The non conservative solution obtained using frequency domain overshoot the peak pressure in both the asymmetric case A and B. The conservative solution shows the second higher value in all the methods. However, the differences in results are within the considerable limits. The observation is found to be consistent with second highest peak pressure as well. The

frequency domain overshoot at the second highest peak pressure as well.

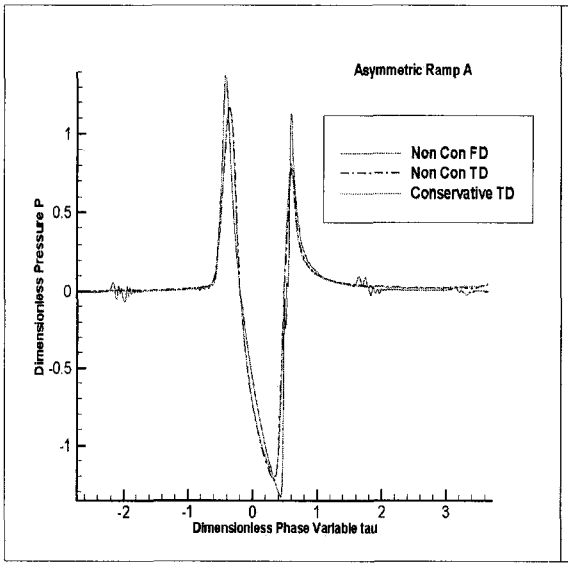

Fig 4.48 Asymmetric Ramp A Validation

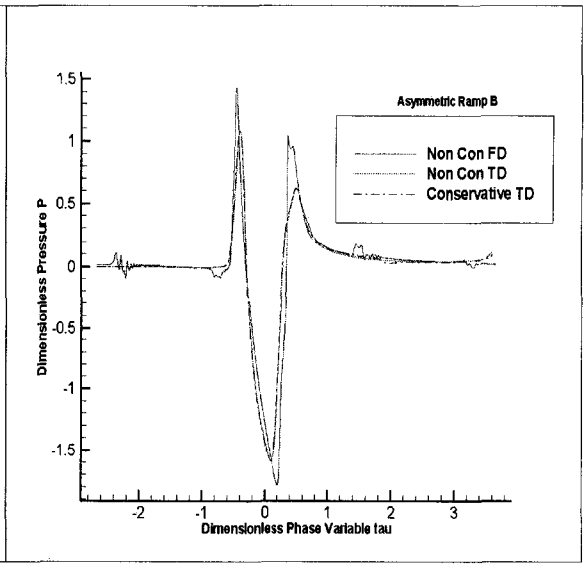

Fig 4.49 Asymmetric Ramp B Validation

	Solution Methods		P_{max}	Z of P_{max}	Peak II	P_{min}	Grid
Asymmetric Ramp A	Non Conservative	FD	1.378	0.238	1.127	-1.33	1000X1024
		TD	1.1714	0.202	0.791	-1.22	1000X8192
	Conservative TD		1.1725	0.202	0.811	-1.20	1000X8192

Table 4.2 Validation of Asymmetric Ramps A focusing

A comparison for the computational approaches is listed in Table 4.2 for asymmetric ramp A and in Table 4.3 for asymmetric ramp B. Location of caustic surface has not changed much in the symmetric and asymmetric ramp A case but for asymmetric ramp B the frequency domain shows the caustic surface well above the ground as compared to the time domain method of non conservative and conservative solutions.

	Solution Methods		P_{max}	Z of P_{max}	Peak II	P_{min}	Grid
Asymmetric Ramp B	Non conservative	FD	1.42	0.20	1.027	-1.784	1000X1024
		TD	1.0814	0.167	0.613	-1.587	1000X8192
	Conservative TD		1.0825	0.166	0.618	-1.593	1000X8192

Table 4.3 Validation of Asymmetric Ramps B focusing

4.2.1.10 Summary for Type of Input Waves

A number of different types of incoming waves are considered for parametric study. The peak focusing amplification and location of caustic surface have been studied for sine wave, symmetric ramp, asymmetric ramps, symmetric and asymmetric flat types and stepped type input waves.

As observed with all the incoming input wave cases, shock waves progress toward the ground and get amplified at caustics surface. The caustics surface is found to be just above the ground. Shock waves are bounced back in the illumination zone and die out in the shadow zone. The wave is completely suppressed in the shadow zone after z = -1.5. Pressure contours show the incoming wave as it progresses toward the caustic surface and the outgoing wave as it originates from the caustic surface. These results conclusively show that the super boom response is predicted.

The N wave shows the maximum amplification with peak pressure values of 2.898 at z = 0.1378. The focusing solution obtained for Concorde wave creates a focused boom at the caustic surface z = 0.269 with peak amplification pressure P_{max} = 1.985. Normally, amplification is found to be less with stepped shock system as in the case of the Concorde wave.

The symmetric wave shows higher amplification over the asymmetric case for ramp type and flat top incoming waves. Asymmetric ramp type A shows the peak pressure of 1.25 at the caustic surface z = 0.17. Symmetric ramp wave shows the peak pressure of 2.78 at the caustic surface z = 0.13. Asymmetric flat top shows the peak pressure of 1.0824 at the caustic surface z = 0.166 for asymmetric flat top wave focusing, whereas symmetric flat top wave focusing shows the peak pressure of 1.803 at the caustic surface z = 0.18. The sin wave also shows higher focused boom with peak pressure of 2.8627 at caustic surface z = 0.237. Peak shock amplification and location of surface of amplification, i.e. the caustic surface, primarily depends upon the initial shock strength and type of incoming wave. N-wave type signal has shown the maximum amplification at the caustic surface. All the cases were run for 20,000 time steps until the total error is reduced to 10^{-12}

4.2.2 Effects of Shock Strength and Footprint on Super Boom

The next parameter considered for parametric study is the effect of footprint length and shock strength. Five combinations with shock strength are predicted to study the effects of footprint length. The number of grid point is 1000 in the z direction and 8000 in the τ direction. Computation is carried out for 20000 iterations to achieve a desired level of accuracy.

4.2.2.1 **Foot Print = 1.5, Shock Strength = 1.0**

The F function on the upper boundary z = 2.0 is used as an N wave with footprint length of 1.5. The shock strength is kept unchanged at 1. The pressure level is at p_{max} = 1.0 and p_{min} = -1.0. Figure 4.50 shows the pressure contour of the focusing phenomenon.

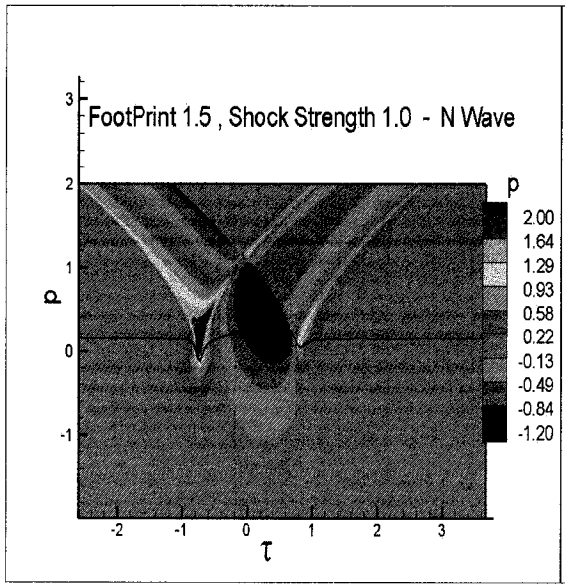

Fig 4.50 Pressure contour FPW 1.5

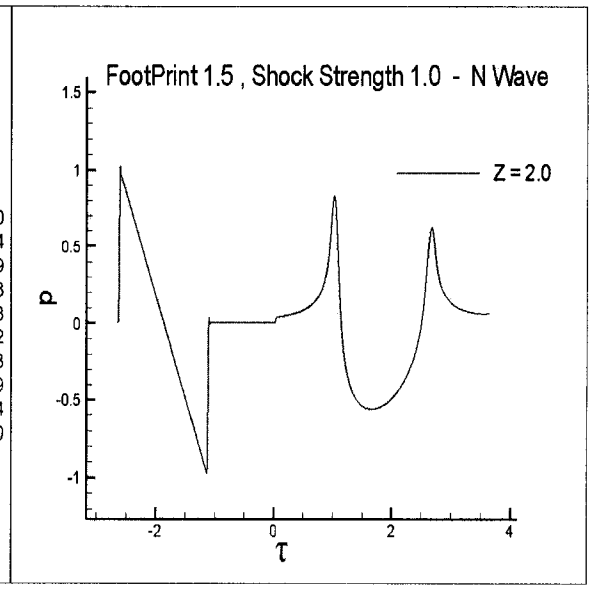

Fig 4.51 Pressure profile on top boundary FPW 1.5

Figure 4.51 shows the pressure profile on the top boundary of the computational domain. Figure 4.52 shows the pressure profile at various z (1.0, 0 and -1.0) locations of the incoming wave as it progresses in the domain toward the ground. The pressure wave in the shadow zone dies out after z = -1.0. Figure 4.53 shows the peak pressure of 3.2022 at caustic surface z = 0.1454. The number of iteration and grid points used for computing the flow variable remains unchanged unless specified.

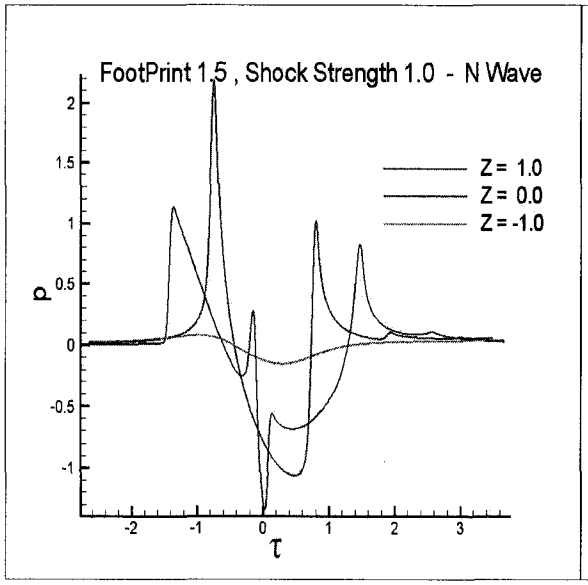

Fig 4.52 Pressure profile for FPW =1.5

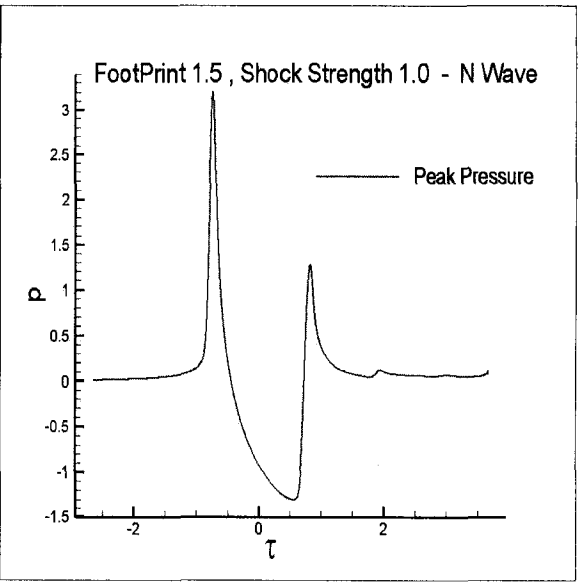

Fig 4.53 Pressure profile on top boundary

4.2.2.2 **Foot Print = 1.5, Shock Strength = 1.5**

The F function on the upper boundary z = 2.0 is used as an N wave with footprint length of 1.5. The shock strength is kept changed at 1.5 Figure 4.54 shows the pressure contour of the focusing phenomenon. Figure 4.55 shows the pressure profile on the top boundary of the computational domain. The caustic surface or surface of boom amplification is shown by a solid black line in Fig 4.54.

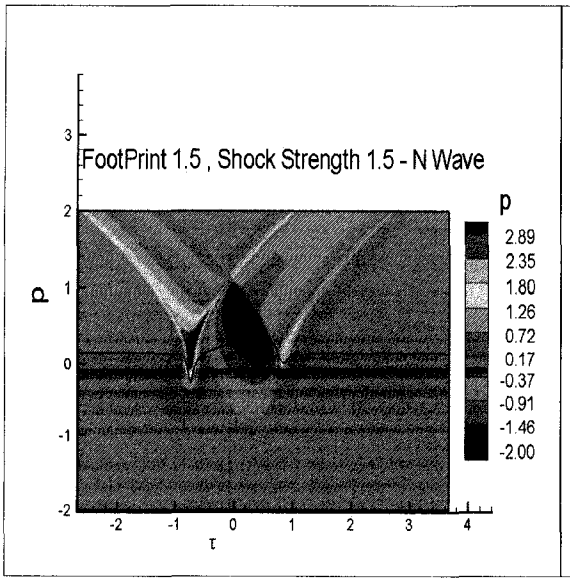

Fig 4.54 Pressure contour FPW 1.5

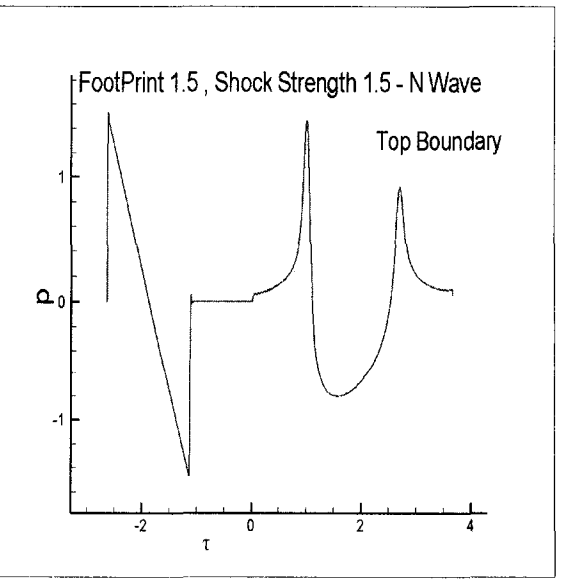

Fig 4.55 Pressure profile on top boundary FPW 1.5

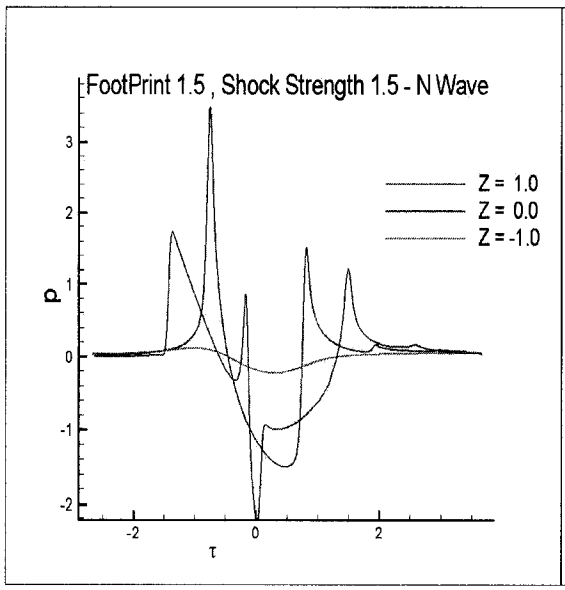

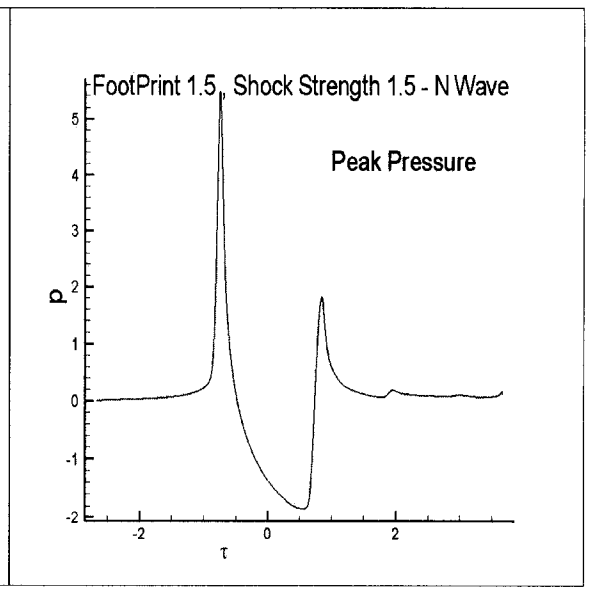

Fig 4.56 Pressure profile FPW 1.5

Fig 4.57 Peak Pressure profile at caustic FPW 1.5

Figure 4.56 shows the pressure variations at various z (1.0, 0 and -1.0) locations of the incoming wave as it progresses in the domain toward the ground. The pressure wave in the shadow zone dies out after z = -1.0. Figure 4.57 shows the peak pressure of 5.4706 at caustic surface z = 0.1525. Peak pressure increases significantly as with increase in foot width and initial shock strength as observed in this study. The number of iteration and grid points used for computing the flow variable remains unchanged unless specified.

4.2.2.3 Foot Print = 2.0, Shock Strength = 1.0

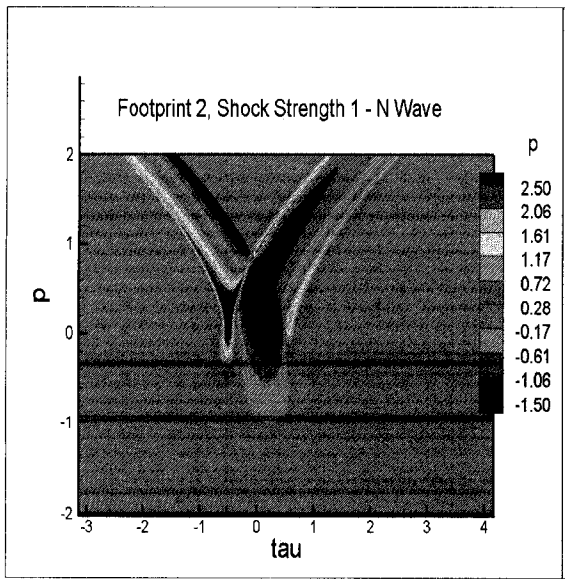

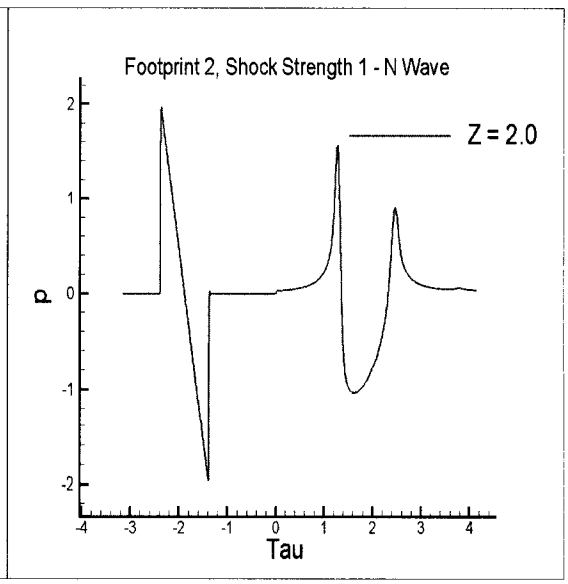

Fig 4.58 Pressure contour FPW 2.0

Fig 4.59 Pressure profile on top boundary FPW 2.0

The F function on the upper boundary z = 2.0 is used as an N wave with footprint length of 2.0. The shock strength is unchanged at 1.0. The pressure levels are at p_{max} = 1.0 and p_{min} = -1.0. Figure 4.58 shows the pressure contour of the focusing phenomenon. Figure 4.59 shows the pressure profile on the top boundary of the computational domain. Figure 4.60 shows the pressure variations at various z (1.0, 0 and -1.0) locations of the incoming wave as it progresses in the domain toward the ground.

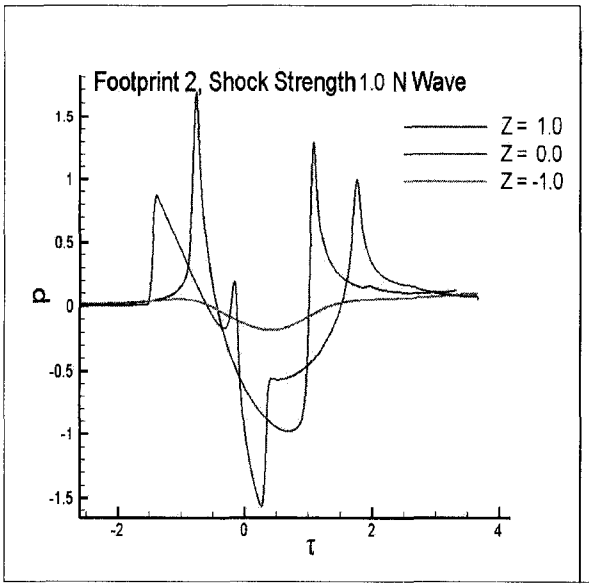

Fig 4.60 Pressure contour FPW 2.0

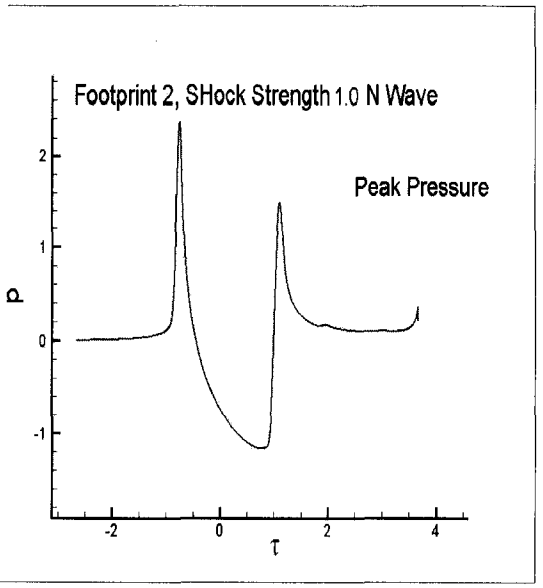

Fig 4.61 Peak Pressure FPW 2.0

Figure 4.61 shows the peak pressure of 2.3575 at caustic surface z = 0.1455. The number of iteration and grid points used for computing the flow variable remains unchanged unless specified.

4.2.2.4 **Foot Print = 2.0, Shock Strength = 2.0**

The F function of the upper boundary z = 2.0 is used as an N wave with footprint length of 2.0. The shock strength is changed at 2.0. The pressure levels are at p_{max} = 1.0 and p_{min} = -1.0. Figure 4.62 shows the pressure contour of the focusing phenomenon. Figure 4.63 shows the pressure profile on the top boundary of the computational domain. Figure 4.64

shows the pressure variations at various z (1.0, 0 and -1.0) locations of the incoming wave as it progresses in the domain toward the ground.

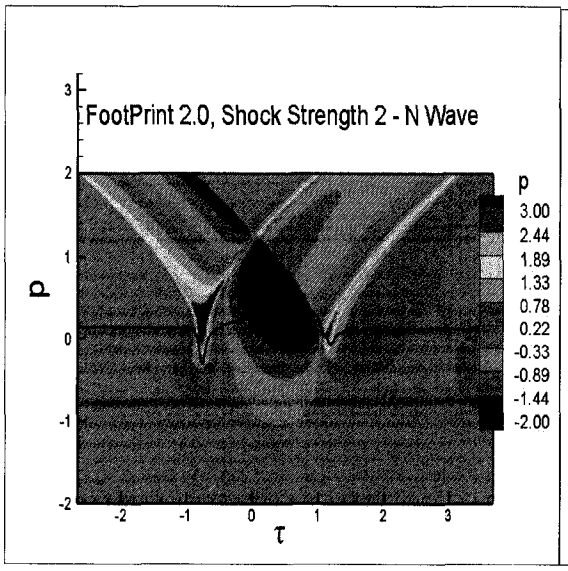

Fig 4.62 Pressure contour FPW 2.0

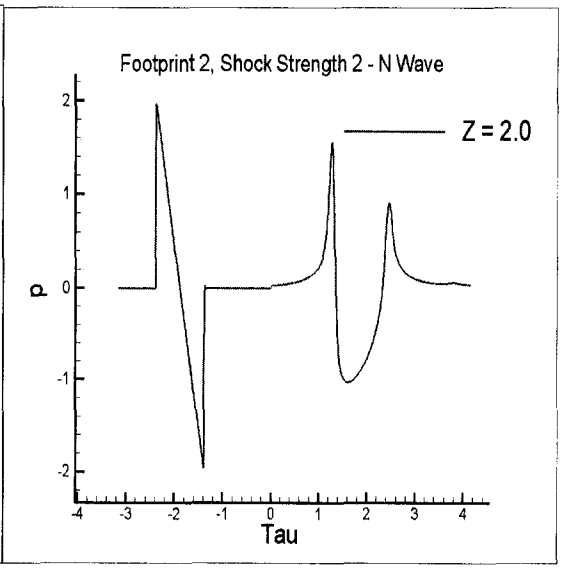

Fig 4.63 Pressure profile on top boundary FPW 2.0

Figure 4.65 shows the peak pressure of 2.3575 at caustic surface z = 0.1455. As indicated in the current study, increasing foot print width alone does not give a significant rise in the magnitude of focused boom at caustic. Foot print width effects are predominant with an increase in initial shock strength. The higher foot print width with low initial shock strength will give lower focused peak pressure at caustics. The number of iteration and grid points used for computing the flow variable remains unchanged.

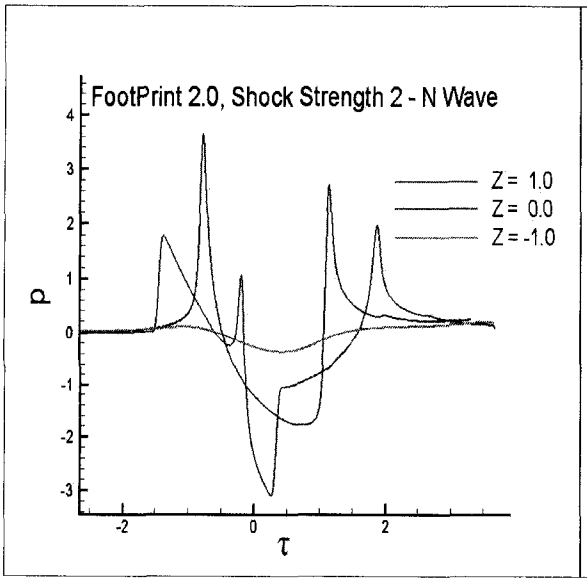

Fig 4.64 Pressure profile FPW 2.0

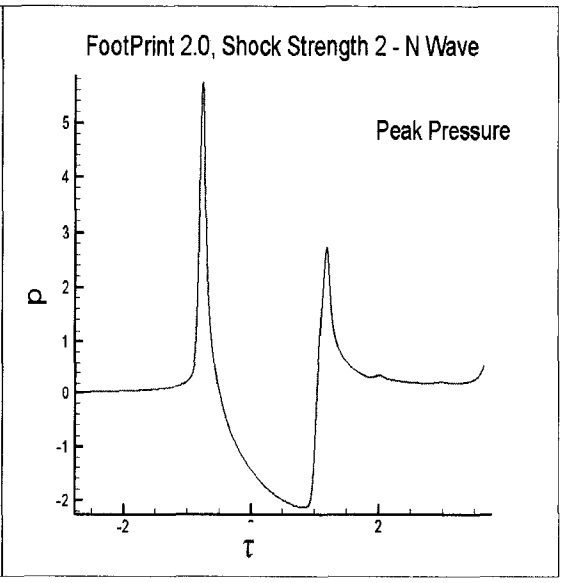

Fig 4.65 Peak Pressure at caustic FPW 2.0

4.2.2.5 Summary of Shock strength and Footprint Study

N Wave		P_{max}	Z of P_{max}	2nd Pressure Peak	P_{min}	Grid N z x Nτ
FPW	Initial Shock Strength					
1.0	**1.0**	**2.8986**	**0.1378**	**1.104**	**-1.433**	**1000X8192**
1.5	**1.0**	3.2022	0.1454	1.284	-1.300	1000X8192
2.0	**1.0**	2.3575	0.1455	1.482	-1.163	1000X8192
1.5	**1.5**	5.4706	0.1525	1.818	-1.852	1000X8192
2.0	**2.0**	5.7482	0.1516	2.718	-2.126	1000X8192

Table 4.4 Footprint and Shock Strength Comparison

Table 4.4 shows a summary of this investigation of footprint width and initial shock strength on sonic boom focusing. It is observed that the effects of the incoming shock foot-print width and its level of strength has a significant effect on magnitude of shock wave amplification and location of caustic surface where focusing is taking place. The reference case has a dimensionless width and strength of 1.0 and 1.0 for the incoming N wave.

If the footprint is increased to 1.5 without changing the initial shock strength shows increase in focused boom. It is observed that the footprint width (FPW) wave with 1.5 provides a longer time for interaction between the incoming wave and outgoing wave, producing a higher super boom of 3.2. It is higher by 10.47% in comparison with the reference case. However, when the FPW is increased to 2.0 keeping the strength as 1.0, the super boom drops to 2.3575, which is a decrease of 18.67% in comparison with the reference case. On the other hand, if the FPW is kept at 1.5 and the strength of the incoming shock is increased to 1.5, then super boom increases to 5.47, which is about an 88.73% increase in peak pressure level. Further increasing foot print width to 2.0 and initial shock strength to 2.0 shows about 98.30% increase with p_{max} = 5.7482 in peak pressure at the caustic surface. The location of caustics surface found to be shifting upward with increase in footprint width and shock strength.

4.2.3 Effects of Top and Bottom Boundary on Super Boom

The next parameter considered for parametric study is the effect of top and bottom boundary locations. It is considered to be a vital look into how amplification and location of caustic surface is affected by the altitude of flying i.e. the upper top boundary of the computational domain. For better understanding the focusing phenomenon lower boundary or bottom boundary effects are also taken into account. The number of grid points is 1000 in the z direction and 8000 in the τ direction. Computation is carried out for 20000 iterations to achieve a desired level of accuracy in the result.

4.2.3.1 **Base Case Longitudinal Boundaries**

No changes have been made for the incoming input wave. The upper and lower boundaries are only varied to investigate the effect on focusing phenomenon. For the base case the top boundary is at the z = 2.0 and bottom boundary is at z = -2.0. Figure 4.66 shows the pressure contour for z base case. The solid black line in Fig 4.66 represents the location of surface of amplification. Figure 4.67 shows the peak pressure of 2.896 at caustic location of z = 0.138 for the base case without any change in boundaries.

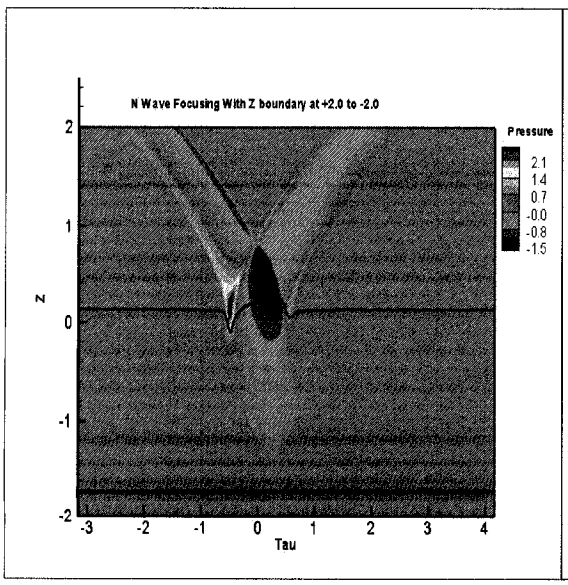

Fig 4.66 Pressure contour Z Base

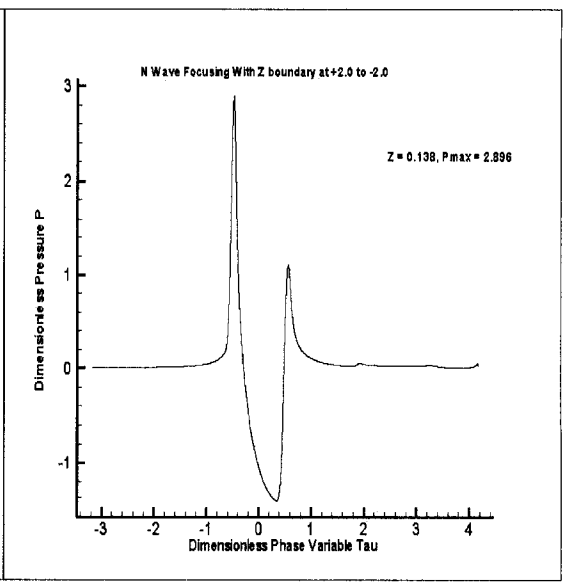

Fig 4.67 Peak Pressure at caustic Z base

4.2.3.2 Top Enlarged Boundary

No changes have been made for the oncoming input wave. For an enlarged top boundary z is kept to 2.5 and the bottom boundary is at z = -2.0. Figure 4.68 shows the pressure contour of the focusing phenomenon with an enlarged upper boundary. Figure 4.69 shows the peak pressure of 2.9171 at caustic location of z= 0.152 for the enlarged upper boundary and no change in lower boundaries. The solid black line in Fig 4.68 represents the location of surface of amplification.

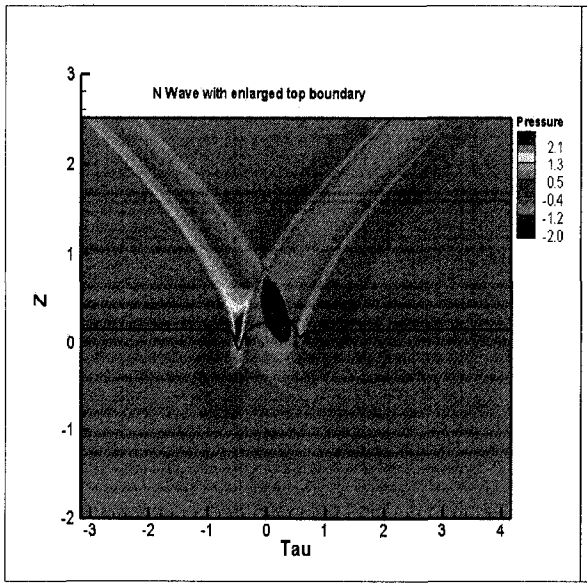

Fig 4.68 Pressure contour top enlarged

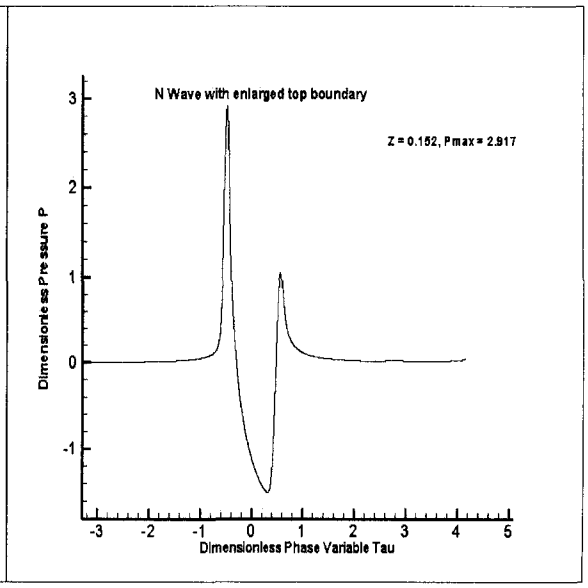

Fig 4.69 Peak Pressure at caustic top enlarged

4.2.3.3 Bottom Enlarged Boundary

No changes have been made for the oncoming input wave. For an enlarged bottom boundary z is kept to -3.0 and the top boundary is at the z = 2.0. Figure 4.70 shows the pressure contour of the focusing phenomenon with an enlarged lower boundary.

Figure 4.71 shows the peak pressure of 2.865 at caustic location of z= 0.1408 for the enlarged lower boundary and no change in upper boundaries. The solid black line in Fig 4.70 represents the location of surface of amplification. It is observed that with an enlarged bottom boundary the peak shock pressure is reduced to 2.865 as compared to the base case (peak pressure of 2.896) and enlarged top boundary (peak pressure of 2.9171).

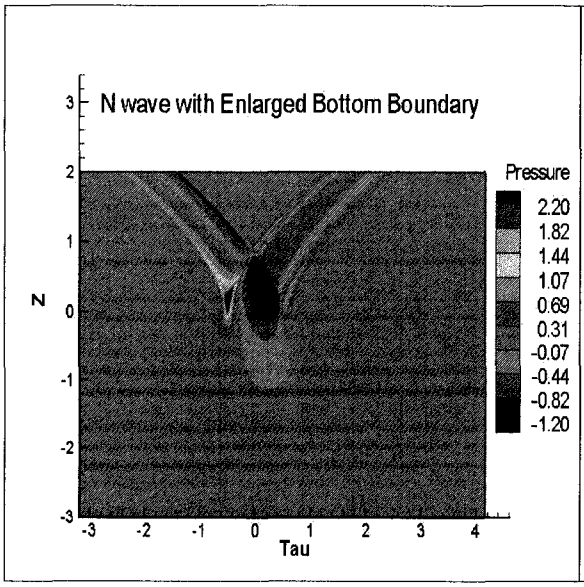

Fig 4.70 Pressure contour bottom enlarged

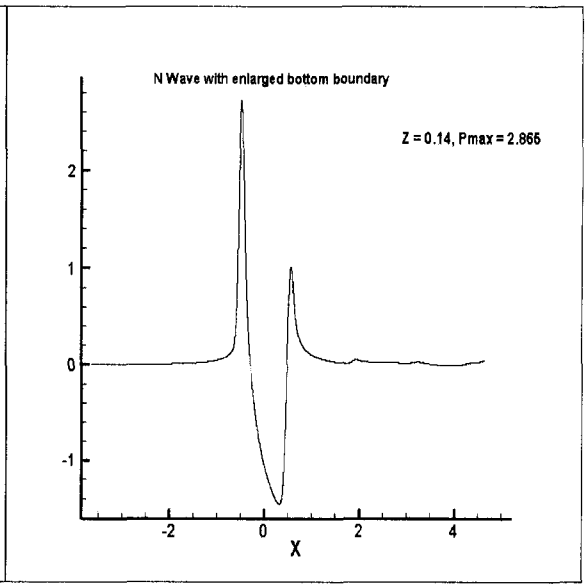

Fig 4.71 Peak Pressure at caustic bottom enlarged

4.2.3.4 Top and Bottom Enlarged Boundary

No changes have been made for the oncoming input wave. For this case the bottom boundary z is kept to -3.0 and the top boundary is at z = 2.5. Figure 4.72 shows the pressure contour of the focusing phenomenon with enlarged lower and upper boundaries. Figure 4.73 shows the peak pressure of 2.81 at caustic location of z = 0.157 for the enlarged lower boundary and upper boundaries. The solid black line in Fig 4.72 represents the location of surface of amplification.

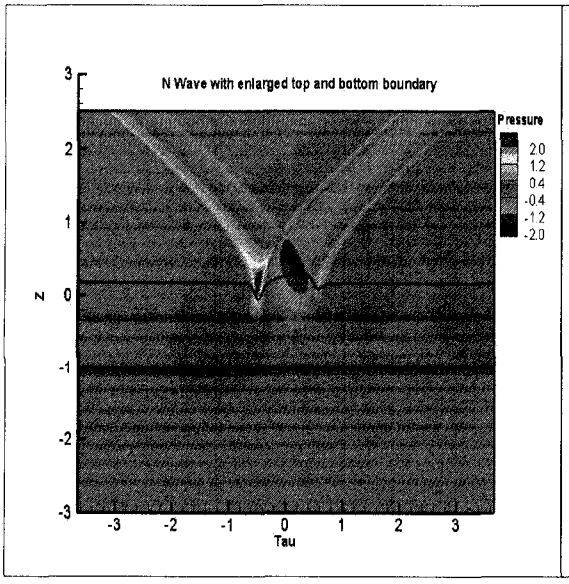

Fig 4.72 Pressure contour both enlarged

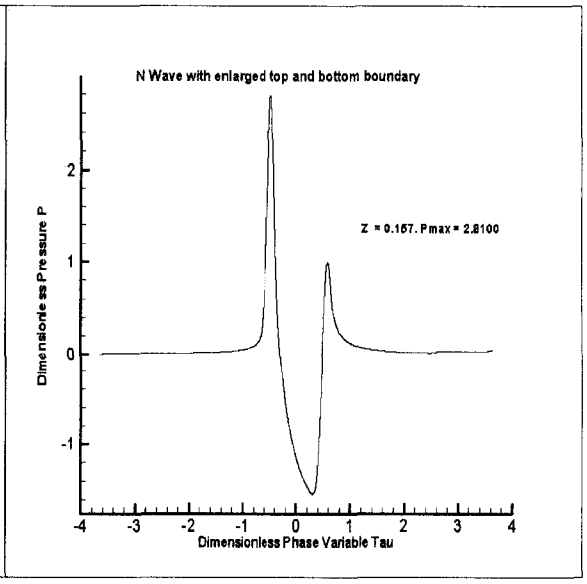

Fig 4.73 Peak Pressure at caustic both enlarged

4.2.3.5 Summary for Z Boundary Effects for N Wave

N Wave	Z Boundary Range	P_{max}	Z of P_{max}	2nd Pressure Peak	P_{min}	Grid N z x Nτ
Case with τ [-3.17, 4.17]	**[2.0, -2.0]**	**2.8967**	**0.1380**	**1.1050**	**-1.433**	**1000X8192**
Z lower enlarged	[2.0, **-3.0**]	2.8651	0.1408	1.0838	-1.4371	1250X8192
Z upper enlarged	[**2.5**, -2.0]	2.9171	0.152	1.0510	-1.5057	1000X8192
Z lower and upper enlarged	[**2.5, -3.0**]	2.8100	0.157	0.9980	-1.5357	1250X8192

Table 4.5 Effect of upper and lower boundaries on N wave focusing

The lateral boundaries are fixed and thus τ range from [-3.17, 4.17]. For the enlarged lower boundary Z = -3.0 keeping the upper boundary location fixed at Z = 2. Comparing these results with those of the base case of the z domain of [-2.0, 2.0], there are small effects. The p_{max} increases by 0.2% and the second pressure peak decreases by 0.2%. Next, the upper boundary is enlarged to Z = 2.5 keeping the lower boundary fixed at Z = -2.0. The effects are still small. The p_{max} increases by 2.78%, but the second pressure peak increases by 10%. Finally, the lower and upper boundaries are set at Z [-3.0, 2.5]. The p_{max} increases by 3.01% and the second pressure peak increases by 2.7%.

4.2.3.6 Summary for Z Boundary Effects for Concorde Wave

Concorde-aircraft Wave	Z Boundary Range	P_{max}	Z of P_{max}	2nd Pressure Peak	P_{min}	Grid N z x Nτ
Case with τ [-3.17, 4.17]	**[2.0, -2.0]**	**1.9854**	**0.269**	**0.8931**	**-1.6956**	**1000X8192**
Z lower enlarged	[2.0, **-3.0**]	1.9850	0.270	0.8914	-1.6966	1250X8192
Z upper enlarged	[**2.5**, -2.0]	2.0422	0.266	0.8665	-1.7335	1000X8192
Z lower and upper enlarged	[**2.5, -3.0**]	2.0472	0.267	0.8684	-1.7285	1250X8192

Table 4.6 Effect of upper and lower boundaries on Concorde wave focusing

Similar parametric investigation is carried out for a Concorde aircraft wave. The effects of locations of the lower and upper boundaries are much smaller than those of the N wave. Tables 4.5 and Table 4.6 show the summary of the computational results for the N wave and the Concorde-aircraft wave.

4.2.4 Effects of Left and Right Boundary on Super Boom

The next parameter considered for parametric study is the effect of left and right boundary locations. It is considered to be a vital look into how amplification and location of the caustic surface is affected by the lateral boundaries of the computational domain. This would also help in understanding whether there is any secondary boom focusing happening in the neighborhood. The upper and lower boundaries are kept constant at 2.0 and -2.0 respectively. The number of grid points is 1000 in the z direction and 8000 in the τ direction. Computation is carried out for 20000 iterations to achieve a desired level of accuracy.

4.2.4.1 **Base Case for Left and Right Boundary Effects**

No changes have been made for the oncoming input wave. The left and right boundaries are only varied to investigate the effect on focusing phenomenon. For the base case the left boundary is at the τ = -2.67 and the right boundary is at the τ = 3.67. Figure 4.74 shows the pressure contour for the τ base case. Figure 4.75 shows the peak pressure of 2.896 at caustic location of the z = 0.138 for the base case without any change in boundaries.

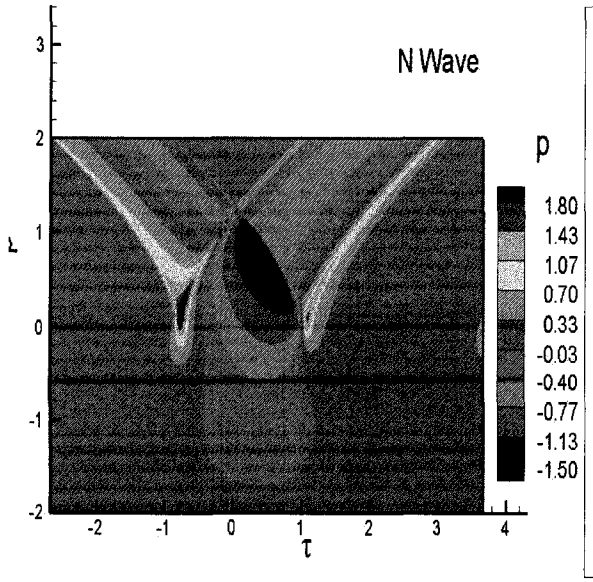

Fig 4.74 Pressure contour tau base

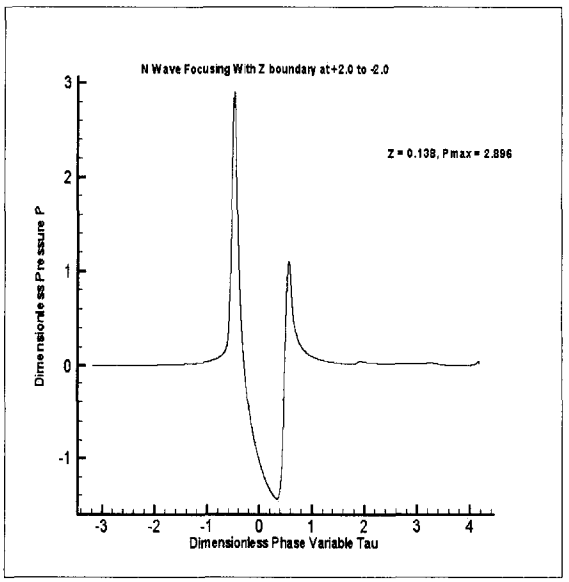

Fig 4.75 Peak Pressure at caustic tau base

4.2.4.2 Enlarged Left Boundary

No changes have been made for the oncoming input wave. For this case the left boundary is enlarged to the $\tau = -3.67$ and the right boundary is at $\tau = 3.67$. Figure 4.76 shows the pressure contour for the τ left enlarged boundary base case. Figure 4.77 shows the peak pressure of 2.900 at caustic location of $z = 0.138$ for the base case without any change in boundaries.

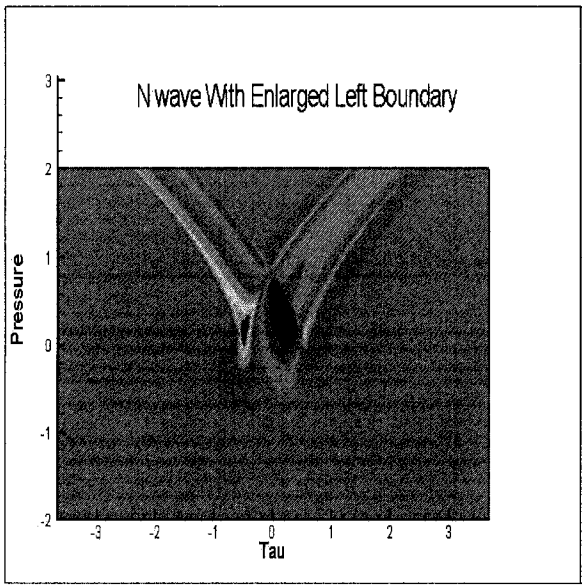

Fig 4.76 Pressure contour left enlarged

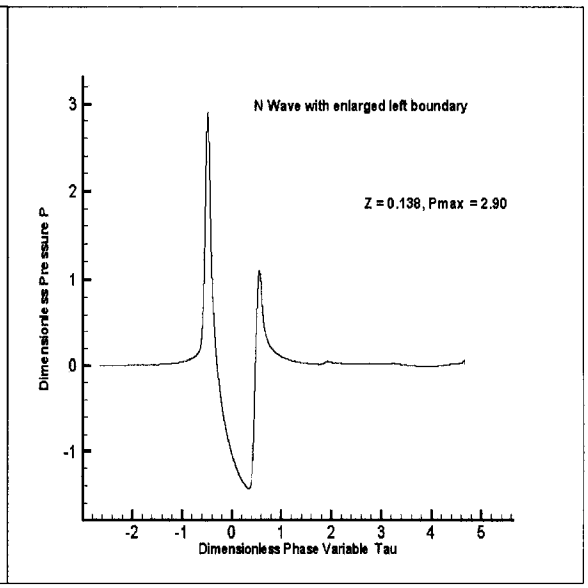

Fig 4.77 Peak Pressure at caustic left enlarged

4.2.4.3 Enlarged Right Boundary

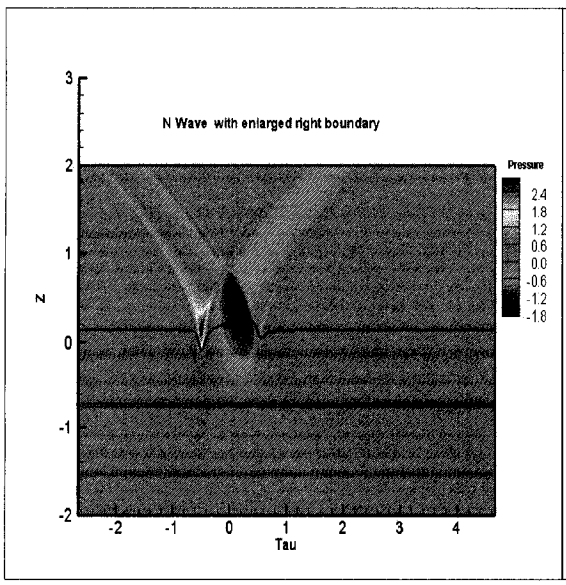

Fig 4.78 Pressure contour right enlarged

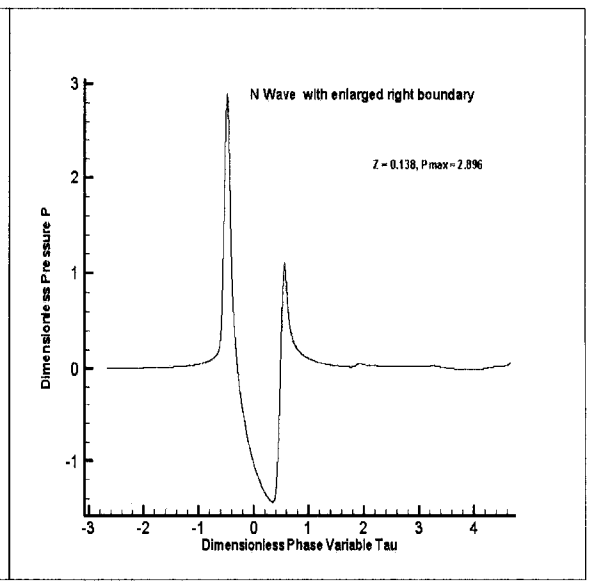

Fig 4.79 Peak Pressure at caustic right enlarged

No changes have been made for the oncoming input wave. For this case the left boundary is enlarged to τ = -2.67 and the right boundary is at τ = 4.67. Figure 4.78 shows the pressure contour for the τ right enlarged boundary case. Figure 4.79 shows the peak pressure of 2.896 at caustic location of z = 0.138 for the base case without any change in boundaries. The solid black line in Fig 4.78 represents the location of surface of amplification.

4.2.4.4 Left and Right Enlarged Boundary

No changes have been made for the oncoming input wave. For this case the left boundary is enlarged to τ = -3.67 and the right boundary is enlarged to τ = 4.67. Figure 4.80 shows the pressure contour for the τ left and right enlarged boundary case. Figure 4.81 shows the peak pressure of 2.893 at caustic location of z = 0.138 for the base case without any change in boundaries. The solid black line in Fig 4.80 represents the location of surface of amplification.

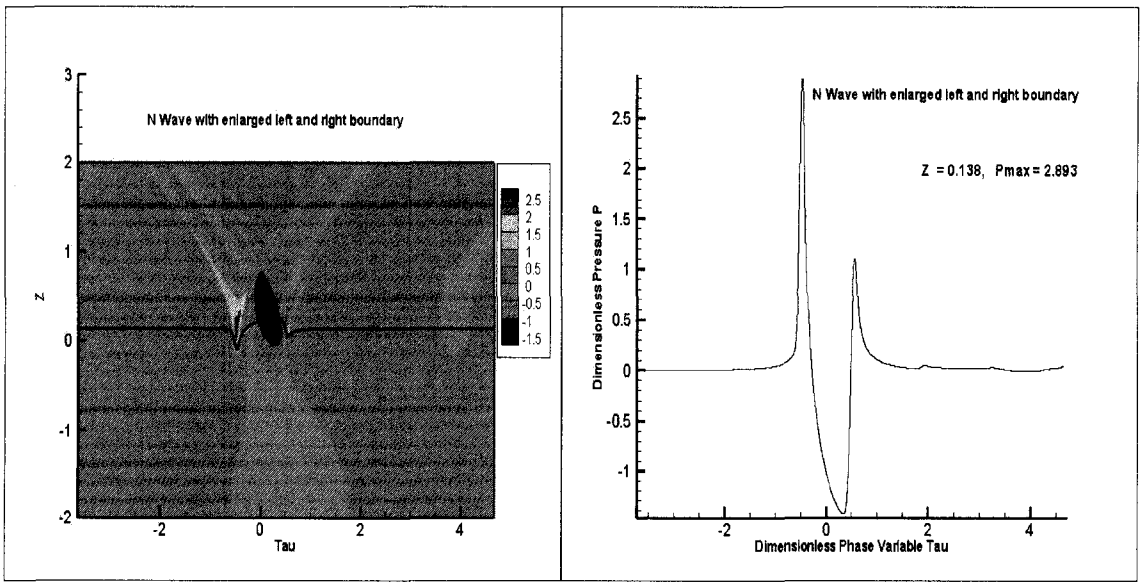

Fig 4.80 Pressure contour both enlarged Fig 4.81 Peak Pressure at caustic both enlarged

4.2.4.5 Summary for Lateral Boundary Effects on Super Boom

The left and right boundaries of the computational domain are enlarged. First, the right boundary is enlarged to τ = 4. 67 keeping the left boundary fixed at 2.67. Comparing these results with those of the reference domain, there are no appreciable effects to worry

about. Next, the left boundary is enlarged to $\tau = -3.67$ keeping the right boundary fixed at 3.67. Again, the results after 20,000 time steps do not show appreciable effects in comparison with those of the reference domain

Concorde Aircraft Wave	τ Boundary Range	P_{max}	Z of P_{max}	2nd Pressure Peak	P_{min}	Grid N z x Nτ
Reference Domain	**[-2.67, +3.67]**	**2.0398**	**0.2667**	**0.9324**	**-1.700**	**1000X8192**
τ left Enlarged	[**-3.67**, +3.67]	2.0409	0.2664	0.9383	-1.703	1000X9486
τ right Enlarged	[-2.67, **+4.67**]	2.0444	0.2663	0.9383	-1.700	1000X9486
τ both Enlarged	[**-3.67, +4.67**]	2.0427	0.2662	0.9354	-1.702	1000X10780

Table 4.7 Effect of lateral boundaries on Concorde wave focusing

Finally, the right and left boundaries are enlarged to $\tau = -3.67$ and $\tau = 4.67$. For this case as well the results do not show any appreciable effects in comparison with those of the reference computational domain. The magnitude of peak pressure and surface of amplification, i.e. the caustics surface are found to be insensitive to lateral boundaries. Similar parametric investigation was carried out for an incoming N wave and the results confirmed the conclusion that the locations of the left and right boundaries do not have appreciable effects on the sonic boom focusing results. Peak pressure for the N wave was found to be constant about 2.89 and the caustic surface is found to be at 0.138 in all cases. The second maximum peak and lowest minimum peak is also unchanged with lateral boundaries. Tables 4.7 and Table 4.8 show a summary of these computational results for a Concorde-aircraft wave and an N wave after 20,000 time steps.

N Wave	τ Boundary Range	P_{max}	Z of P_{max}	2nd P_{max}	P_{min}	Grid N z x Nτ
Reference Domain	**[-2.67, +3.67]**	**2.89623**	**0.13802**	**1.1042**	**-1.432**	**1000X8192**
τ left Enlarged	[**-3.67**, +3.67]	2.90034	0.13815	1.1018	-1.435	1000X9486
τ right Enlarged	[-2.67, **+4.67**]	2.89623	0.13824	1.1037	-1.433	1000X9486
τ both Enlarged	[**-3.67, +4.67**]	2.89384	0.13800	1.1019	-1.434	1000X10780

Table 4.8 Effect of lateral boundaries on N wave focusing

4.2.5 Effects of Grid points on Super Boom

Grid Size	Pmax	Zmax	Peak II	Pmin
1000X8000	1.985	0.269	0.894	-1.695
1000X9000	2.028	0.267	0.902	-1.703
1000X10000	2.059	0.266	0.920	-1.707
1000X11000	2.085	0.266	0.930	-1.709
1000X12000	2.094	0.266	0.940	-1.709

Table 4.9 Effect of grid points on Concorde wave focusing

The investigation is carried out for a Concorde-aircraft wave. Keeping the number of grid points in the Z direction fixed at 1,000, the effects of the grid refinement in the τ direction is investigated. Four computational runs, which increase the number of grid points in the τ direction from 8,000 to 12,000 with a grid step increase of 1,000, are used. Table 4.9 shows the summary of the results. The pressure results are asymptotically converging with the p_{max} reaching 2.094, which is 5.49% higher than the value of the reference case.

4.3 Summary For Parametric Study

To summarize, the following observations are made in parametric study:

1. The initial shock strength has a direct effect on amplitude of sonic boom focusing at caustics. The higher the shock strength higher would be the peak amplification pressure. Caustics surface location is found to be shifting upward with high initial shock strength.
2. The type of input wave also has a crucial importance in focusing phenomenon. Normally amplification is found to be less with stepped shock system as in the case of the Concorde wave.
3. The symmetric wave shows higher amplification over asymmetric case for ramp type and flat top incoming waves.
4. It is observed that the wave with footprint width (FPW) 1.5 provides a longer time for interaction between the incoming wave and outgoing wave, producing a

higher super boom. However if the FPW is increased considerably without any increase in shock strength the super boom effect drops.

5. Lower and upper boundaries are found to influence the magnitude of amplification and location of caustics surface. Peak pressure has increased with enlargement of the upper boundary and decreased with enlargement of lower boundaries.
6. Parametric investigation shows that the locations of the left and right boundaries do not have appreciable effects on the focused sonic boom at the caustic surface. Peak pressure for the N wave was found to be constant at about 2.89 and the caustic surface is found to be at 0.138 in all cases of lateral boundary effects.
7. The peak pressure magnitude is asymptotically converging with grid independence studies.

CHAPTER 5
RESULT- SONIC BOOM MITIGATION AND DELTA WING SHAPE OPTIMIZATION

Computational results obtained for sonic boom mitigation study of biconvex delta wing geometry is presented in this chapter. Mitigation research involves reducing both the shock originating from the front and rear portion of the flying object. Delta wing geometry is chosen as base line geometry for the research study and later the approach can be implemented on a wing body configuration. In some aircraft as in the case of the F5 the leading shock that reaches to ground is due to aircraft wing and not the body, this is also one of the reasons the wing was chosen for study and not the complete aircraft.

The base line delta wing geometry has a biconvex profile with chord length of 60 ft and maximum thickness ratio of 5.0% of the chord. The wing is flying at an altitude of 40,000 ft with the speed of Mach number 2.0. Maximum thickness ratio, maximum camber ratio, dihedral angle and nose angle of the front lower portion of the wing are considered important design parameters to be studied. Individual effects of the design variables on the near-field overpressure and the aerodynamic performance are presented and discussed [82, 83]. This is followed by combined effects and optimization of the wing parameters for low boom ground signature with least loss in lift to drag ratio.

CFL3D [30] Euler solver is used for the computational results produced for individual studies of thickness, camber, nose angle and dihedral angle. Later CFL3D [30] is also used for combined studies and optimization work of delta wing design parameters at zero degree angle of attack study. Structured grid adaptation is done using grid adaptation and the shock fitting algorithm GASF [35]. In the end of chapter 5 some of the results are produced using FUN3D [32] software on unstructured mesh for a 2.24 degree angle of attack. FUN3D is primarily used to extend the mitigation study for complex geometries due to the ease of mesh generation with unstructured meshes. Unstructured meshes are produced using Gridgen software [33] and ICEM CFD meshing [84] software. Optigrid

software [78] is used for improved mesh adaptation. All the results for optimization are produced using Design Expert software [34].

5.1 Biconvex Delta Wing CFD Solution

CFL3D [30] Euler solver is used to compute the flow over biconvex delta wing base line geometry configuration. A multi block structured grid is generated using a code written in FORTRAN. Gridgen software [33] is also used to generate the structured grid around the wing. Grid adaptation and shock fitting GASF [35] is used to fit the leading shock and trailing shock. The structured grid dimension is 137X113X155 in X, Y and Z direction.

5.1.1 CFL3D Near field Solution

Figure 5.1 shows the YZ plane of the three dimensional structured grid system. The structured grid consists of the three block and the second block houses the delta wing. Figure 5.2 shows the complete three dimension grid around the delta wing. It's very important to have a very fine adapted and shock fitted grid to avoid the shock dissipation and achieve the desired level of accuracy in computational result.

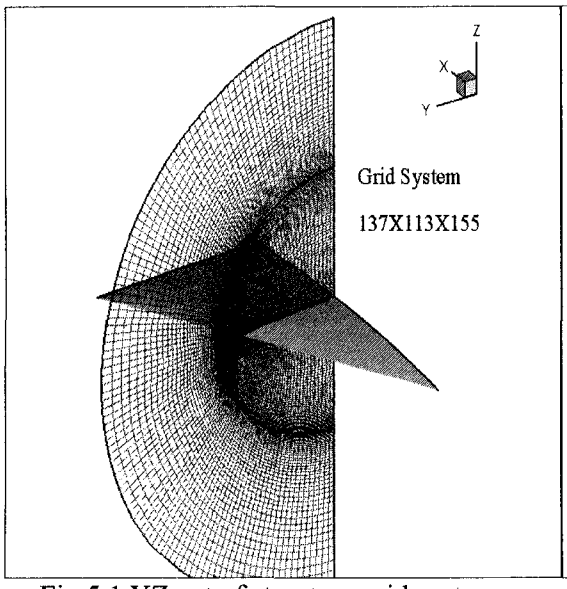

Fig 5.1 YZ cut of structure grid system

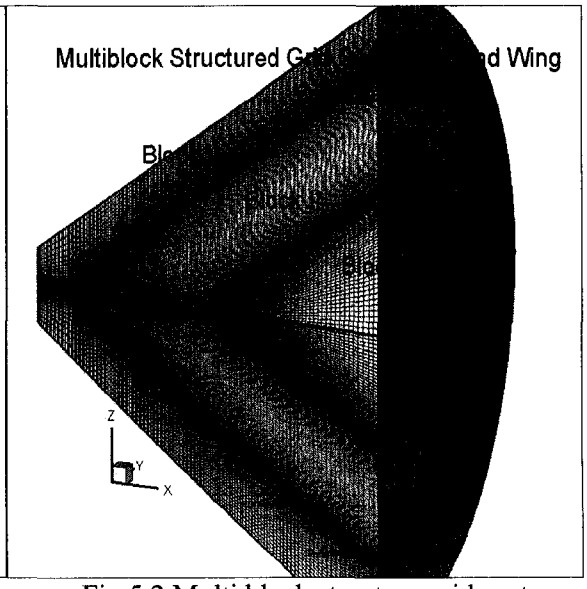

Fig 5.2 Multi block structure grid system

Figure 5.3 shows the density contours from the solution obtained from CFL3D Navier Stokes solver. As observed from the near field density contour, flow has a very strong leading and trailing shocks, which could potentially reach to the ground and create an

undesired sonic boom annoyance. Similar shock pattern exist on the top surface of the biconvex delta wing.

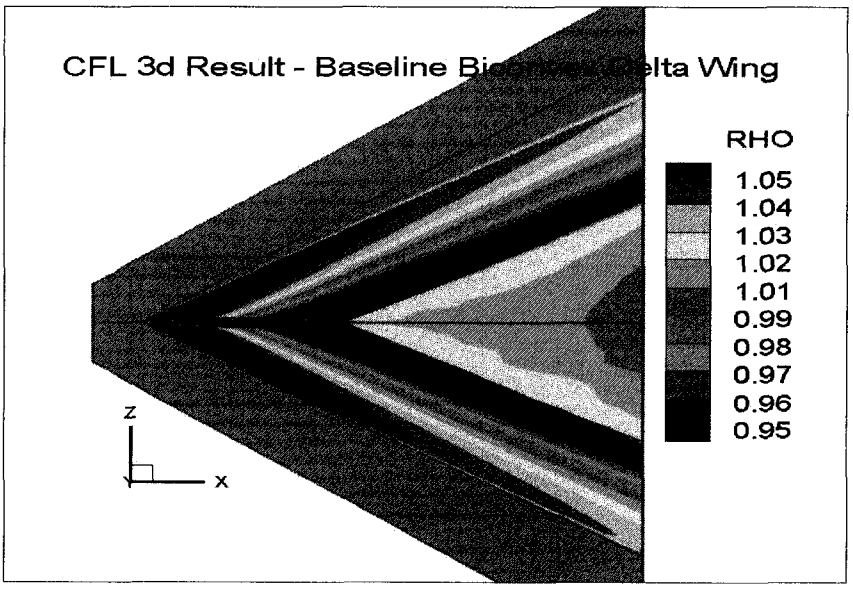

Fig 5.3 CFL3d near Field Density Contour

5.1.2 Grid Adaptation for Structured Grid System

Once the preliminary captured shock solution is obtained, the basic structured mesh is adapted to the solution in order to capture the leading and trailing shock with much greater accuracy. Figure 5.4 shows the YZ cut of the adapted grid system for leading and trailing shock.

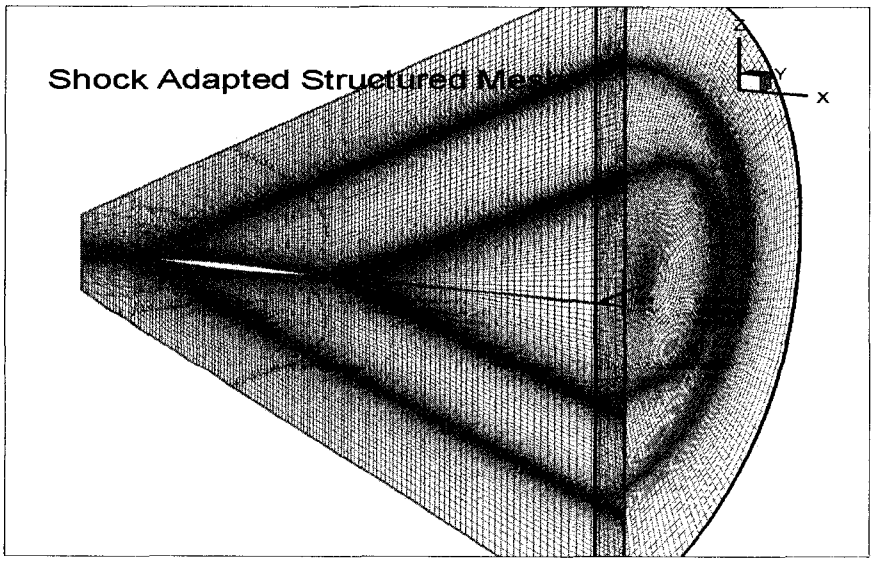

Fig 5.4 YZ cut of adapted structure grid system

Grid adaptation and shock fitting GASF [35] code looks at the gradient of density as a criterion for fitting and adapting the leading and trailing shocks of the delta wing. Two adaptation iterations are normally enough to obtain the properly shock fitted structured mesh. Figure 5.5 shows the full three dimensional adapted and shock fitted grid system.

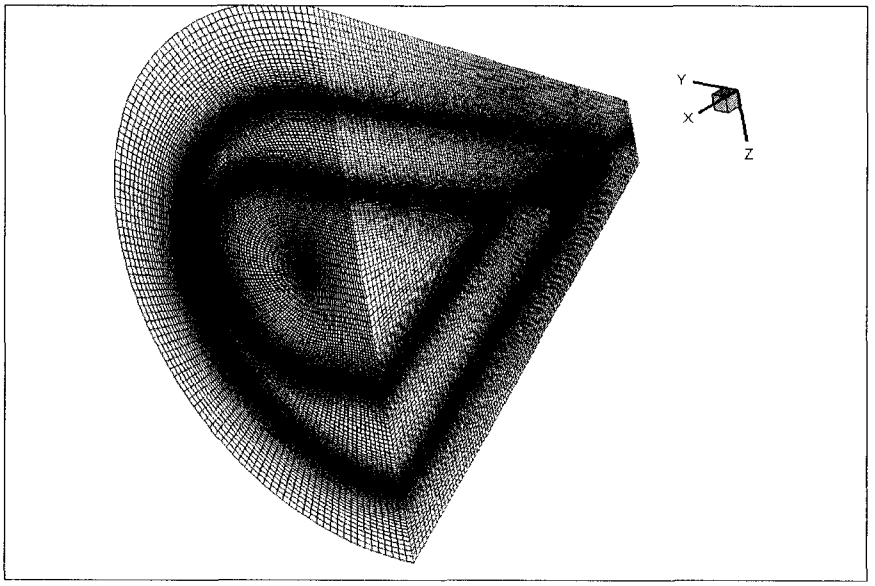

Fig 5.5 Adapted 3d structure grid system

5.2 Effect of Maximum Thickness Ratio of Delta wing CFL3D

The first geometry parameter considered for mitigation study is the maximum thickness ratio. Just to validate the concept maximum thickness varied to upper and lower permissible design limits and obtained the near field CFD solution. The lower limit for maximum thickness is kept as 2.0 % of chord length and the upper limit is kept at 6.0% of chord length.

5.2.1 Maximum Thickness Ratio Study for Mitigation

In this section, 5.2.1, the effects of maximum thickness ratio on near field density are presented. The density contour shows the strength of shocks, which represents the sonic boom level. Figure 5.6 shows the geometrical profile of a biconvex wing with total thickness ratio of 2, 4, 5 and 6% or lower surface thickness of 1.0, 2.0, 2.5 and 3.0 %. The density contour of Fig 5.7 indicates that there are much stronger shocks with maximum thickness ratio of 6.0 % of the chord.

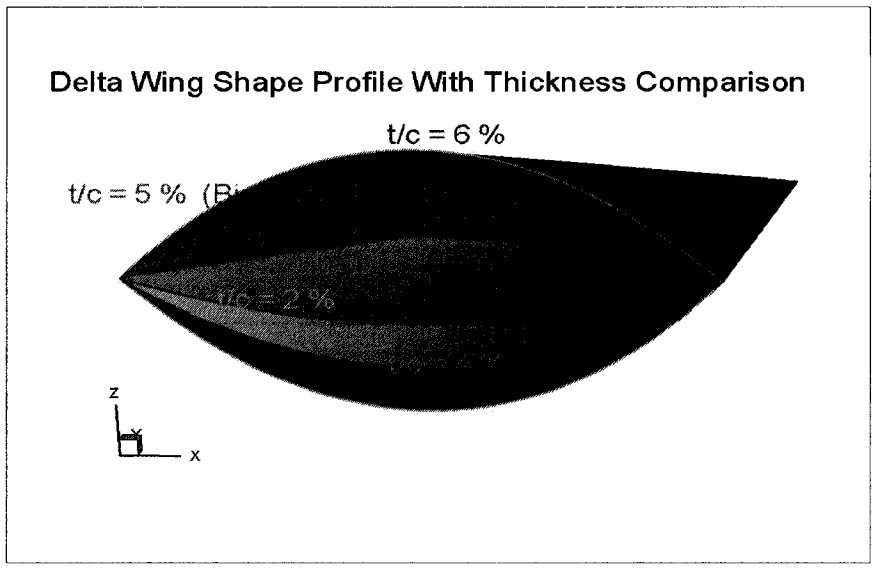

Fig 5.6 Wing profile for various maximum thickness ratios

Higher thickness tries to object and deflect the flow strongly and result in high strength shocks. Thus the study made it clear to go about lower thickness profile for low boom configuration. Reducing the thickness alone is not feasible as one tries and needs to carry as much volume possible. Keeping in mind that one must carry the higher volume, only lower surface thickness is reduced and the upper surface thickness is kept unchanged.

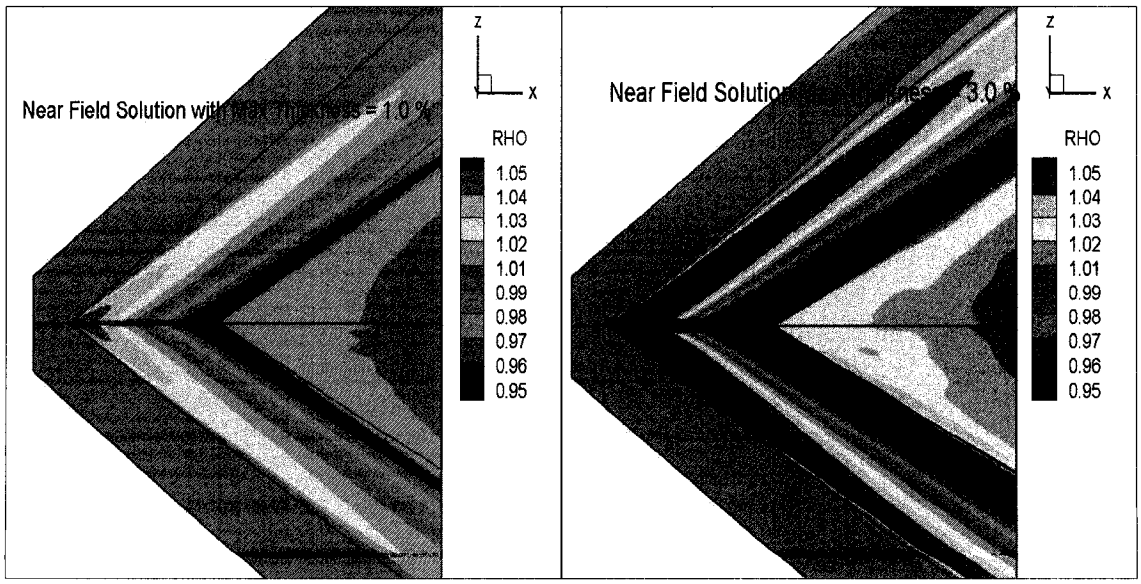

Fig 5.7 Density contour of 1% thickness of lower surface

This has been accomplished by keeping the upper half of the wing with one half of the original maximum thickness ratio of 2.5% and the lower half of the wing with one half of the new maximum thickness ratio of 3%, 2% and 1%.

The focus of the study is to control the effects of the booms coming out from the lower surface.

a. Lower Surface thickness 1.0% of the chord

Figure 5.8 shows a comparison of the overpressure of the original case of 2.5 % maximum thickness and 1.0 % lower surface thickness. There is a significant reduction in overpressure from 0.07 to 0.03 for leading shock strength of the wing with reduction in lower surface thickness. The reduction in overpressure with trailing shock is even higher to the value of -0.1 to -0.05.

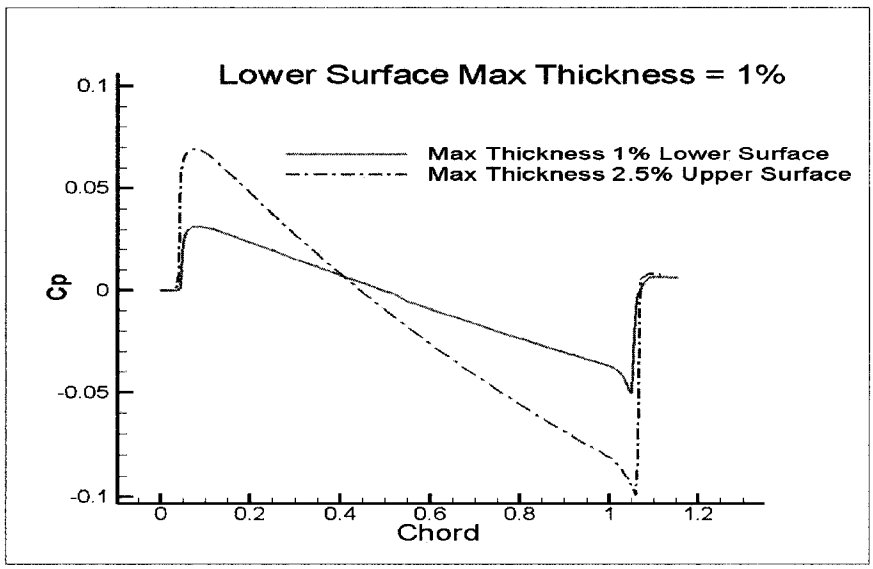

Fig 5.8 Overpressure ratio of 1% thickness of lower surface

b. Lower Surface thickness 2.0% of the chord

Figure 5.9 shows a comparison of the overpressure of the original case of 2.5 % maximum thickness and 2.0 % thickness for lower surface of the wing. The drop in both shock strength is not very high as the thickness reduction in the lower surface is comparably low. However the overpressure ratio is reduced from 0.07 to 0.055 in the leading shock of the wing. The reduction in overpressure with trailing shock produces similar trends and reduction is found to be from -0.1 to -0.085. Observation once again indicates that higher thickness it creates a higher turning angle for the free stream flow and results in high strength shock.

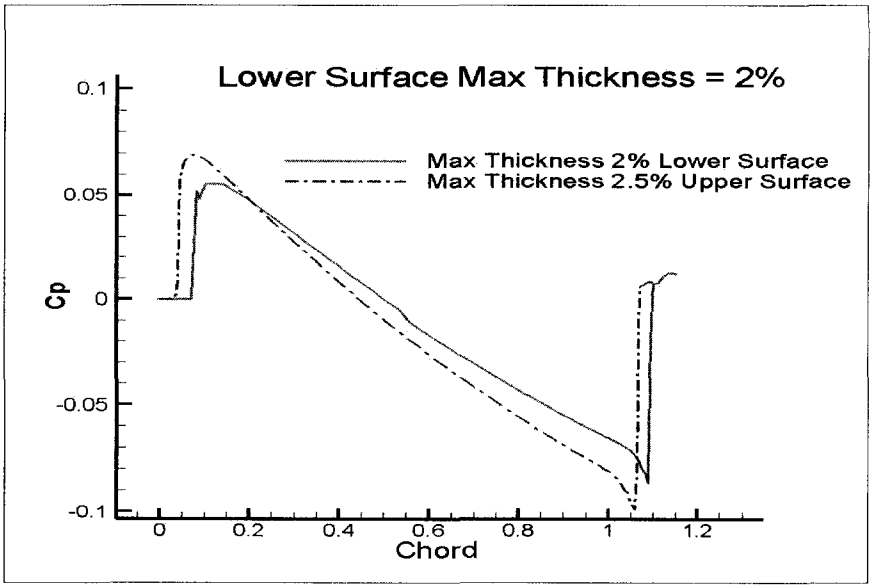

Fig 5.9 Overpressure ratio of 2% thickness of lower surface

c. Lower Surface thickness 3% of the chord

Figure 5.10 shows a comparison of the overpressure of the original case of 2.5 % maximum thickness and 3% of the maximum thickness for the lower surface. There is an increase in the overpressure as compared to the original thickness of 2.5%. This signifies that reduction in thickness directly reduces the boom impact and increasing thickness has the adverse effect on boom mitigation. The overpressure ratio is increased from 0.07 to 0.087 in the leading shock of the delta wing and negative overpressure with trailing shock is increased to be -0.12 from -0.1.

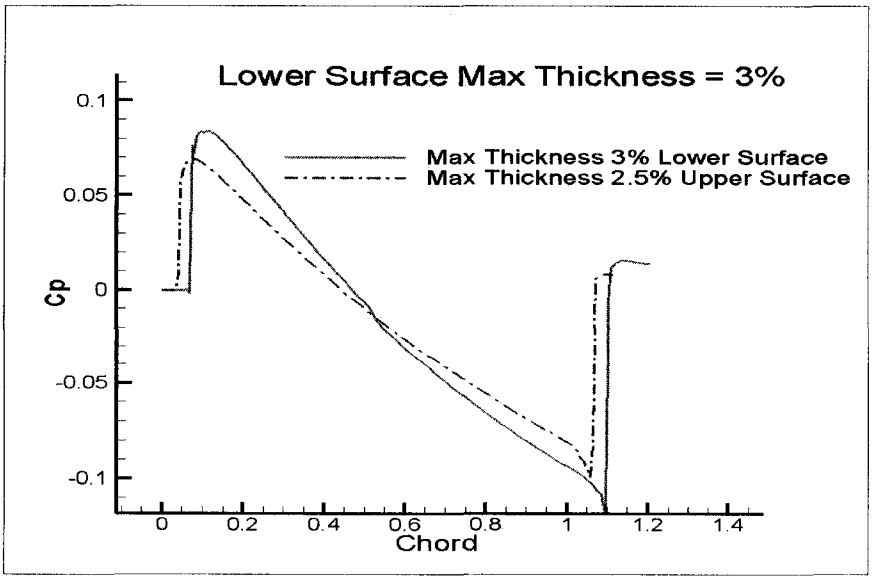

Fig 5.10 Overpressure ratio of 3% thickness of lower surface

d. Summary of thickness study CFL3D

It is clear from the thickness study that reducing maximum thickness helps in mitigating the sonic boom effect on the ground and also has been found in the literature [82, 83]. Figure 5.11 shows a comparison of the overpressure of the original case of 2.5 % maximum thickness with 3, 2 and 1% of the maximum thickness. There is almost a linear decrease in overpressure ratio with decrease in maximum thickness of the delta wing. As the thickness decreases it tends to deflect the flow with a higher deflection angle and leads to stronger shocks. The smaller the thickness ratio the smaller the shock angle and the weaker the shock. This is evident in Fig 5.11 of maximum thickness ratio comparison with unchanged upper surface of the biconvex delta wing.

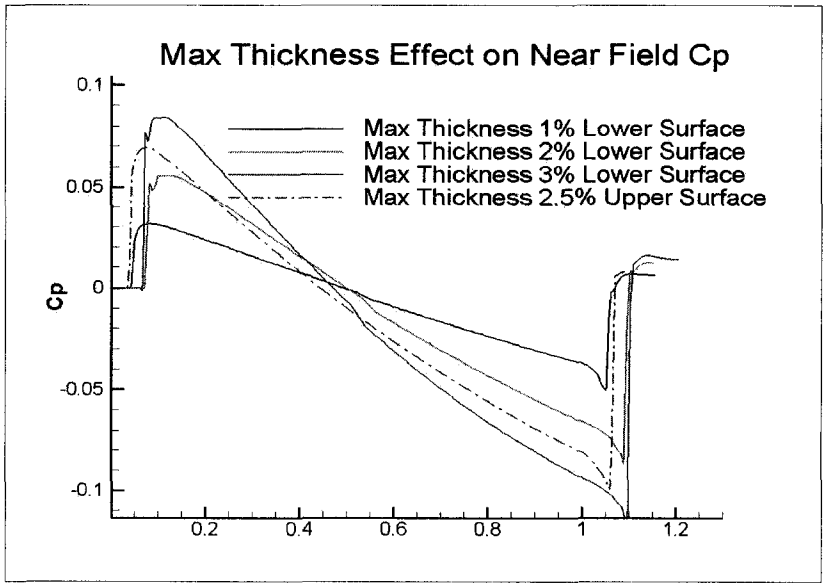

Fig 5.11 Overpressure ratio comparison with thickness

5.2.2 Effect on Aerodynamic Performance **CFL3D**

The effect of decreasing the maximum thickness ratio is favorable on the lift and drag coefficient, as observed in Fig 5.12. Lift is found to be increase and drag is found to decrease with a decrease in maximum thickness. It should be noted that the computed lift coefficient is obtained for a zero degree angle of attack flow condition hence increase in the lift coefficient is not as much as the decrease in drag coefficient. Lift is almost zero for the 2.0 % thickness ratio as this configuration almost close to the symmetrical lower and upper surface and result in zero lift coefficients.

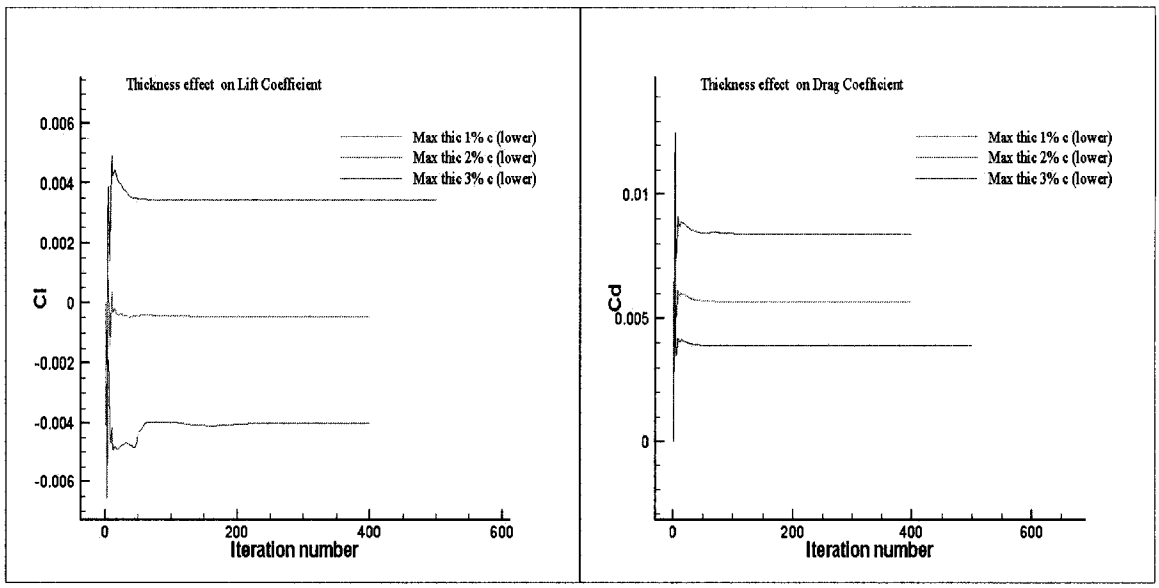

Fig 5.12 Effect of maximum thickness ratio on the lift and drag coefficients

5.3 Maximum Camber Effect of Delta Wing **CFL3D**

Next, the effect of the maximum camber ratio is investigated. The original wing section is symmetric with zero camber ratios. In this investigation, a maximum camber ratio at the mid-chord location has been added to the biconvex section with a 5.0% maximum thickness ratio. The maximum camber ratio has been assigned the values of 0.5 %, 1%, 1.5 % and 2 %, respectively. These four cases have been solved using the CFL3D Euler solver with the same structured grid size of 137X113X155.

5.3.1 Maximum Camber Effects on Near Field Overpressure CFL3D

In the following section the effect of maximum camber ratio on near field density and overpressure ratio is presented. For the camber study camber is added at the mid chord location for the upper and lower surface as shown in Fig 5.13 and Fig 5.14. The maximum camber ratio found to be affecting the near field overpressure ratio and thus the sonic boom ground signature [83, 85]. The increasing camber shows the favorable change in near field overpressure ratio and thus can help in reducing the sonic boom on the ground. Figure 5.13 and Fig 5.14 shows the delta wing profile with camber ratio of 1.5 and 2.0 %. High camber turns the flow on the upper side as compared to lower surface. For mitigation our focus is to obtain a low strength for the shock coming from the lower surface.

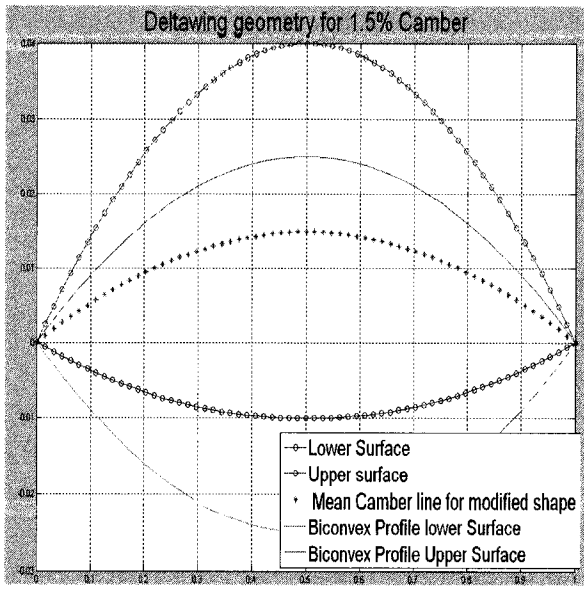

Fig 5.13 Wing profile with 1.5% of camber

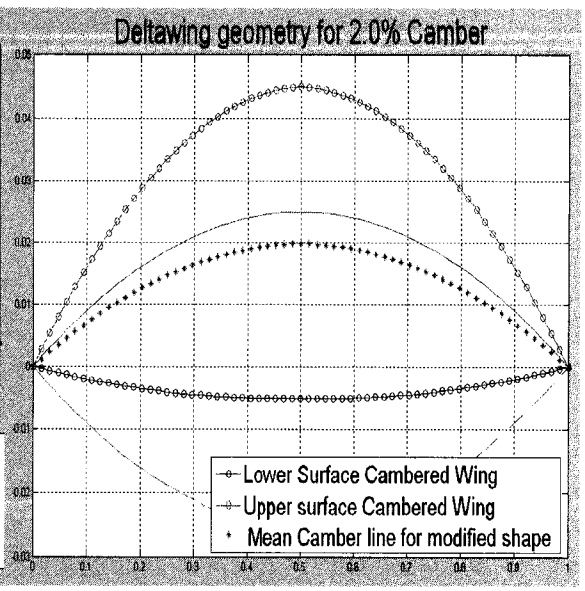

Fig 5.14 Wing profile with 2.0% of camber

a) Maximum camber at mid chord = 0.5 %

Figure 5.15 shows a comparison of the overpressure of the original case without the camber with 0.5% camber added at the mid chord of the biconvex delta wing. There is a decrease in the overpressure as compared to the original case without the camber. This signifies that introducing camber one can control the boom effect on the ground. The overpressure ratio is decreased from 0.065 to 0.06 in leading shock of the delta wing and negative overpressure with trailing shock is decreased to -0.092 from -0.08.

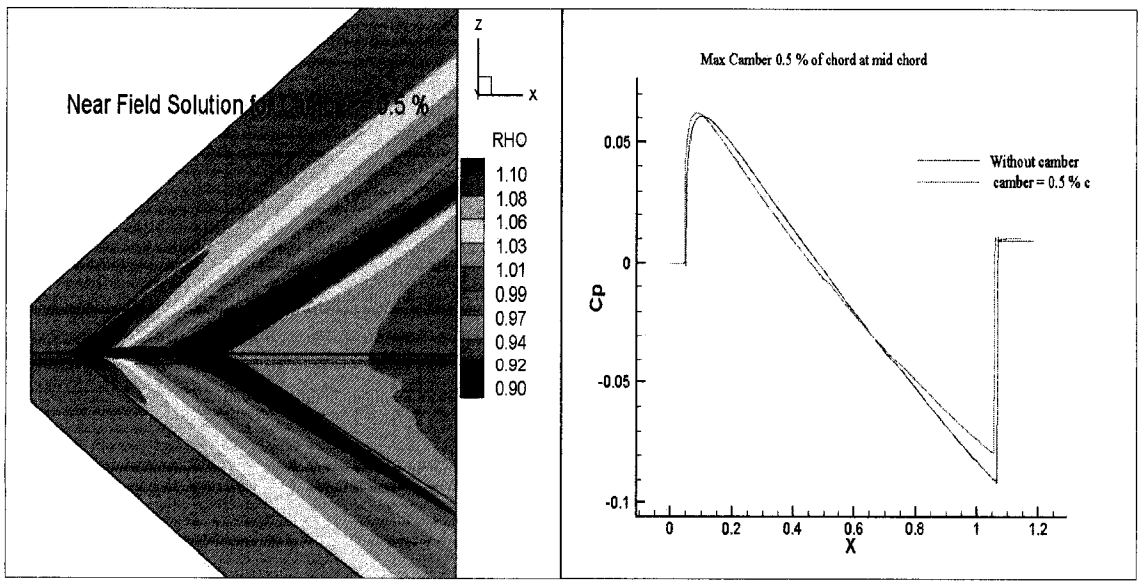

Fig 5.15 Overpressure ratio of 0.5% camber

b) Maximum camber at mid chord = 1.0 %

Figure 5.16 shows a comparison of the overpressure of the base case without the camber and with 1.0% of camber at the mid chord of the biconvex delta wing. There is a decrease in the overpressure as compared to the original case without the camber [76].

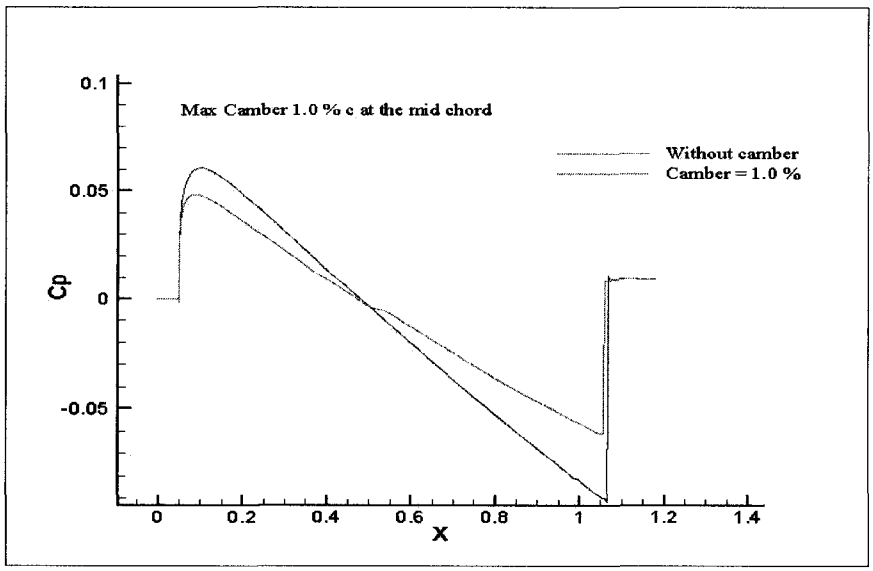

Fig 5.16 Overpressure ratio of 1% camber

This signifies that introducing camber one can control the boom effect on the ground. The overpressure ratio is decreased from 0.062 to 0.048 in leading shock of the delta wing and negative overpressure with trailing shock is decreased to -0.092 from -0.061.

c) Maximum camber at mid chord = 1.5 %

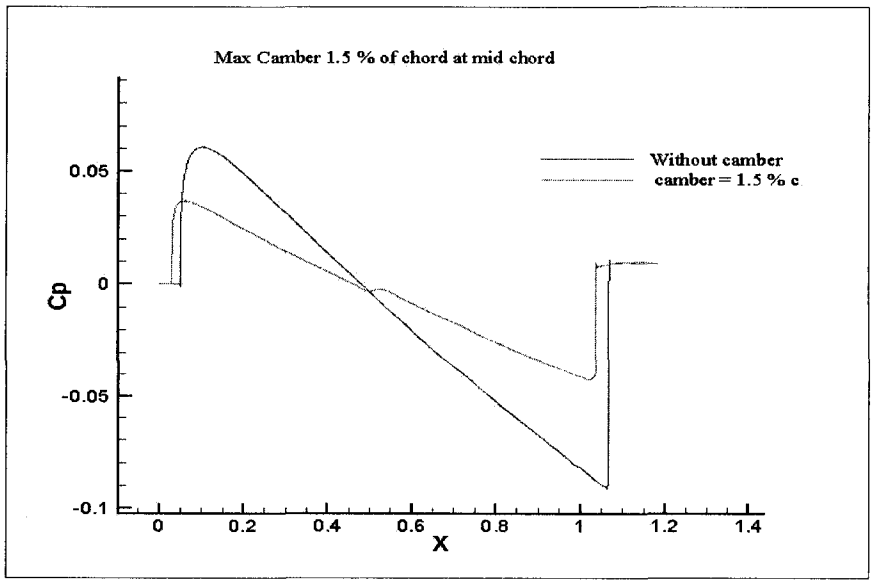

Fig 5.17 Overpressure ratio of 1.5% cambers

Figure 5.17 shows a comparison of the overpressure of the original case without the camber with 1.5% camber added at the mid chord of the biconvex delta wing. There is a decrease in the overpressure as compared to the original case of without the camber. This signifies that introducing camber one can control the boom effect on the ground. The overpressure ratio is decreased from 0.062 to 0.038 in leading shock of the delta wing and negative overpressure with trailing shock is decreased to -0.092 from -0.042.

d) Maximum camber at mid chord = 2.0 %

Figure 5.18 shows the density contours in the plane of symmetry for the maximum camber ratio of 2%. It is observed from the density contours that the lower shocks are weaker than the upper shocks with camber effect. It obvious that as the maximum camber ratio increases, the overpressure of the upper shock increases and the overpressure of the lower shocks decreases.

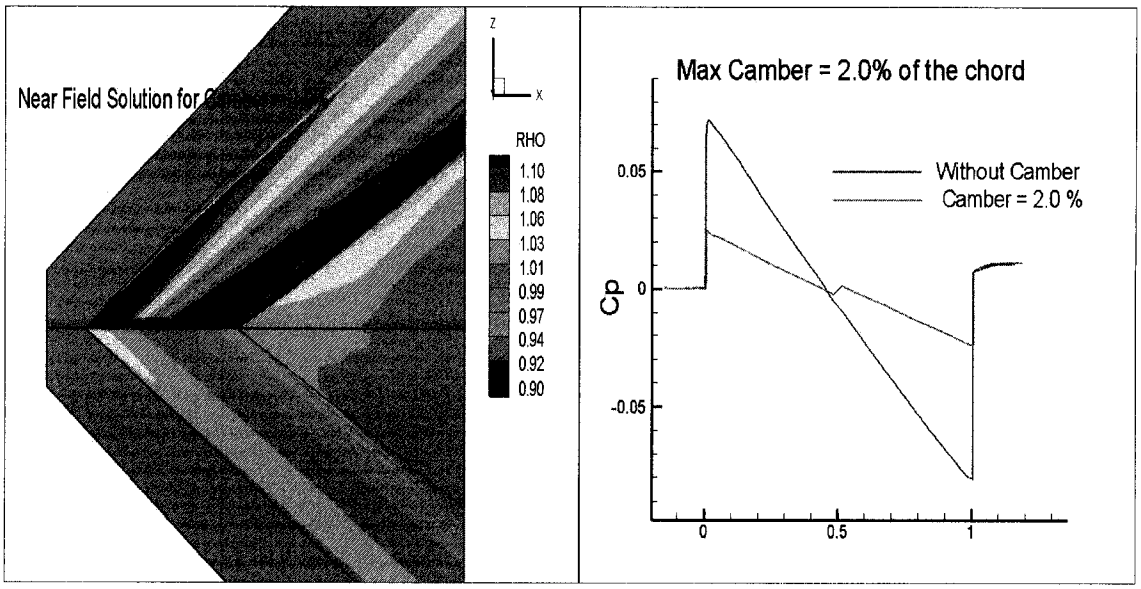

Fig 5.18 Density contours and overpressure ratio for 2.0% camber delta wing

As observed in Fig 5.18 the camber decreases the shock angle at the wing nose for the lower shock and increases the shock angle of the upper shock. Hence, the lower shock which propagates to the ground is weaker than the upper shock. Density contour shows that the shocks coming out from lower surface are much weaker than the shocks coming out from the upper surface of cambered delta wing.

The right part of Fig 5.18 shows a comparison of the overpressure of the base case without the camber and with 2.0% camber added at the mid chord of the biconvex delta wing. There is a decrease in the overpressure as compared to the original case without the camber. This signifies that introducing camber one can control the boom effect on the ground as observed with 0.5 and 1.0 % camber case. The overpressure ratio is decreased from 0.062 to 0.03 in leading shock of the delta wing and negative overpressure with trailing shock is decreased from -0.092 to -0.022 with 2.0 % of the max camber.

e. Summary of maximum camber study **CFL3D**

Maximum camber ratio is investigation shows favorable effects on mitigating the sonic boom ground signature. The original wing section is symmetric with zero camber ratio. In this investigation, a maximum camber ratio at the mid-chord location has been added to the biconvex section with a 5.0 % maximum thickness ratio. The maximum camber ratio has been assigned the values of 0.5 %, 1%, 1.5 % and 2 %, respectively.

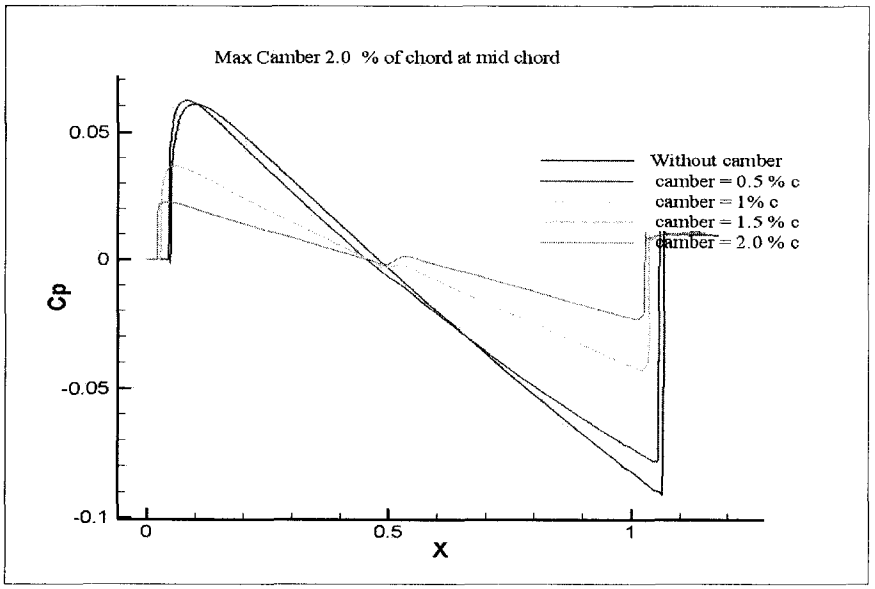

Fig 5.19 Comparison of overpressure ratio for camber CFL3D

Camber turns the flow on the upper surface with much greater angle than the lower surface and thus lower shocks which propagate to the ground are weaker than the upper shock and contribute in mitigating the sonic boom ground signature. Fig 5.19 compares the reduction in near field overpressure as compared to the wing without the camber. This signifies that introducing camber one can control the sonic boom ground effect.

5.3.2 Maximum Camber Effect on Aerodynamic Performance **CFL3D**

Figure 5.20 shows the effect of maximum camber ratio on the lift and drag coefficients. The lift and drag coefficients increase as the camber ratio increases. Increasing maximum camber ratio might help in reducing boom level on ground but it also degrade the aerodynamic performance. Increase in drag coefficient is not desired and one needs to come up with optimized camber value which is the best match for lowering the sonic boom with least gain in drag coefficient.

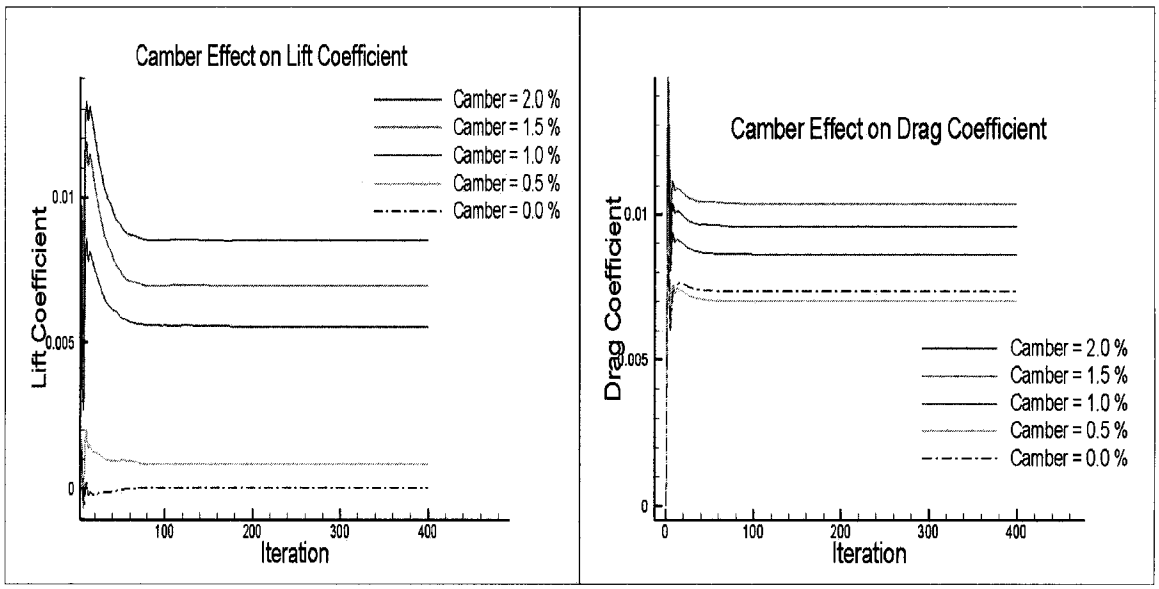

Fig 5.20 Camber effect on aerodynamic performance

5.4 Lower Surface Nose Angle Effects **CFL3D**

Next, the effect of the nose angle of the lower wing portion is investigated. Here, the wing upper portion is kept at one half of the original biconvex wing with a maximum thickness ratio of 5%. The lower wing portion has one half the maximum thickness ratio except the nose angle of this portion is modified to 2 deg., 3 deg., 4 deg. and 5 deg., respectively, all measured counter-clockwise from the x axis.

The nose surface of the lower portion of the wing is taken as a small flat surface which is connected smoothly to the rest of the wing section profile. The purpose behind the nose angle variation is to decrease the shock angle of the lower portion of the wing, since it is this shock which propagates to the ground.

5.4.1 Lower Surface Nose Angle Effect on Near Field Overpressure CFL3D

In the following section the effect of maximum nose angle of the front lower portion of the delta wing on near field density and overpressure ratio is presented. Thickness and camber has not been changed for this study, only front lower portion of the wing is change with new nose angle. The effect of nose angle on near field overpressure ratio is investigated and discussed how that can help in reducing the sonic boom on the ground. Lower nose angle already indicated a lowering the sonic boom with previous studies of Northrop Grumman [16] and some results published by Khasdeo et al. on delta wing [86]

a) Front lower surface nose angle of 2 deg

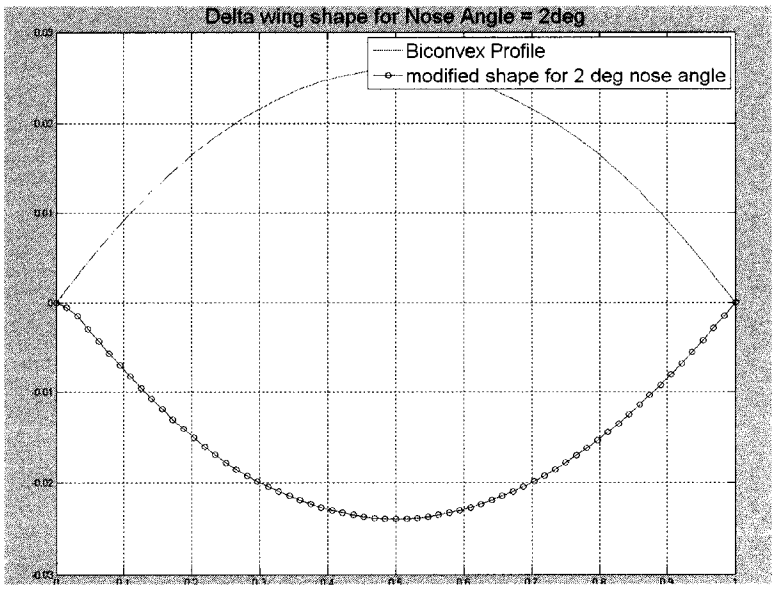

Fig 5.21 Delta wing profile with 2.0 deg of nose angle

Figure 5.21 shows a cross section for a delta wing with modified lower surface profile for nose angle of 2.0 degrees. Figure 5.22 shows the comparison of the overpressure ratio of the biconvex delta wing with 2.0 degree nose angle of the front lower portion of the delta wing. There is a sharp decrease in the strength of leading shock as compare to the original biconvex delta wing. This is clearly evident in the density contour of Fig 5.22. This leads to a conclusion that keeping low values of nose angle contributes in controlling the boom effect on the ground. The overpressure ratio is decreased from 0.07 to 0.06 in leading shock and the leading shock shift backward close to mid chord of the wing. There is a little increase in trailing shock strength with 2 deg of nose angle.

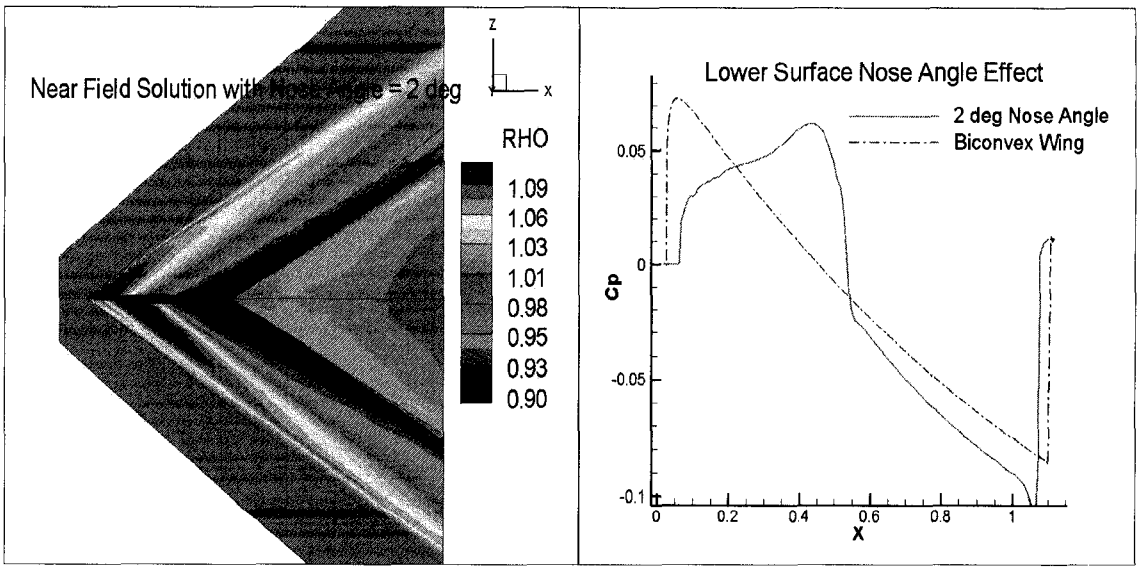

Fig 5.22 Density Contour and Overpressure ratio for 2.0 deg of nose angle

b) Front lower surface nose angle of 3 deg

Figure 5.23 shows a comparison of the overpressure ratio of the biconvex delta wing with 3.0 degree nose angle of the front lower portion of the delta wing. Thickness and camber has not been changed for this study, only the front lower portion of the wing is changed to provide the nose angle of 3.0 degree. There is a sharp decrease in the strength of leading shock and the pressure profiles become flat until the mid chord location of the wing. This also indicates that a lower nose angle can reduce the shock strength and hence the boom on the ground.

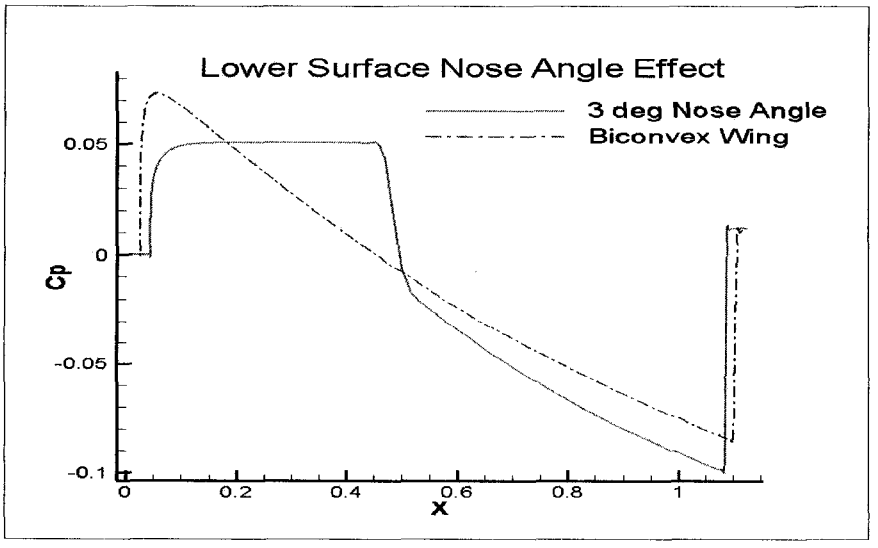

Fig 5.23 Overpressure ratio for 3.0 deg of nose angle

The overpressure ratio is decreased from 0.07 to 0.05 in leading shock of the delta wing whereas there is a little increase in the strength of the trailing shock.

c) Front lower surface nose angle of 4 deg

Figure 5.24 shows a comparison of the overpressure ratio of the biconvex delta wing with 4.0 degree nose angle of the front lower portion of the delta wing. As before only the front lower portion of the wing is kept at 4.0 degree of nose angle without any change in thickness and camber. There is a decrease in the strength of leading shock and the pressure profiles flatten up a bit. This also signifies the fact that having a low value of nose angle reduces the leading shock strength. The overpressure ratio is decreased from 0.07 to 0.055 in leading shock of the delta wing whereas there is a little increased in the strength of the trialing shock. However the decrease in shock strength is much lower than 2 and 3.0 degree of nose angle.

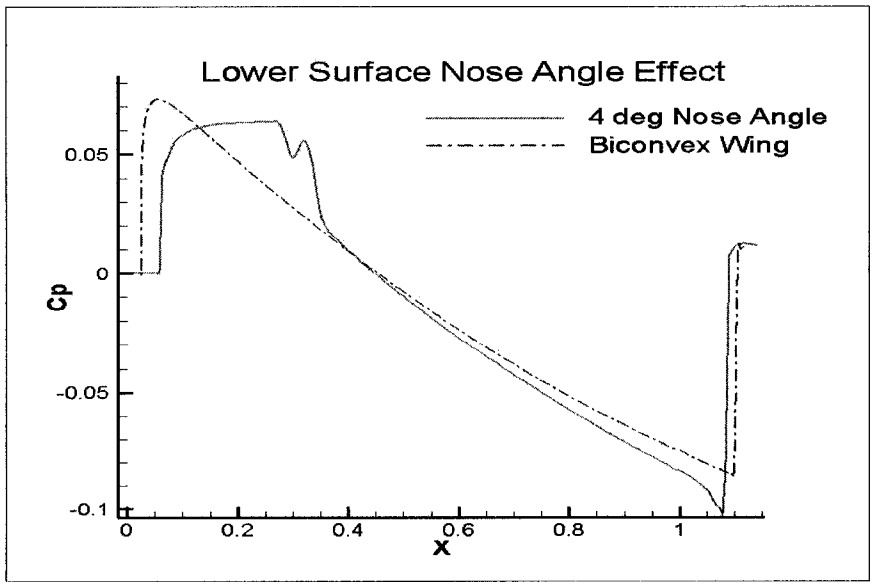

Fig 5.24 Overpressure ratio for 4.0 deg of nose angle

d) Front lower surface nose angle of 5 deg

Figure 5.25 shows a comparison of the overpressure ratio of the biconvex delta wing with 5.0 degree nose angle of the front lower portion of the delta wing. As before only front lower portion of the wing is changed to 4.0 degree of nose angle without any change in thickness and camber. There is an increase in the strength of leading shock as compared

to the base case. This indicated that at this stage we have reached the threshold values of nose angle and further increase in nose angle could seriously increase the boom impact on the ground. The overpressure ratio is increased from 0.007 to 0.078 in leading shock and there is an increase in the strength of the trailing shock as well.

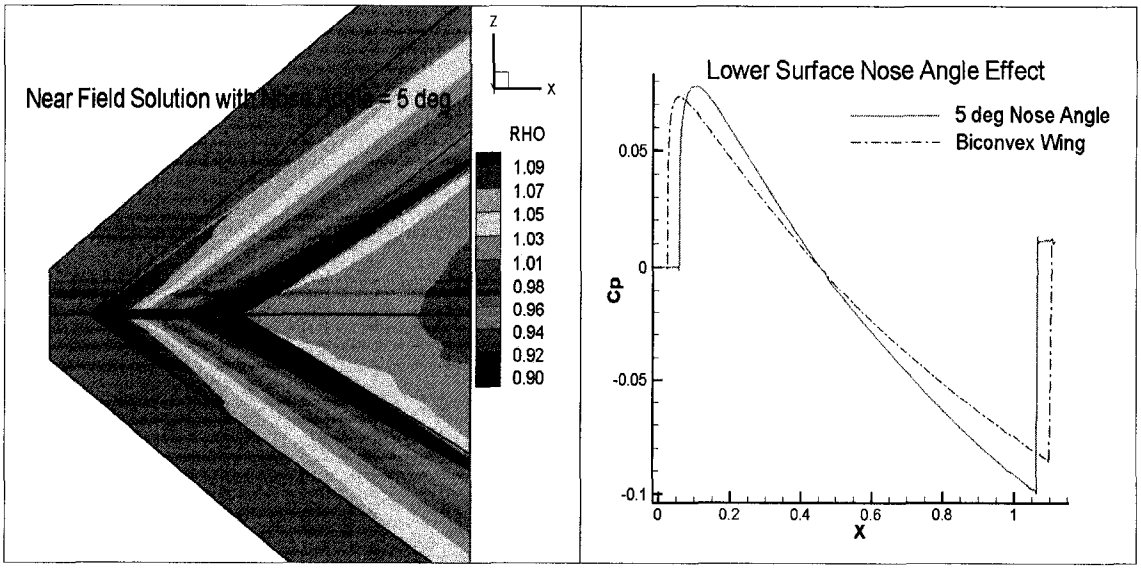

Fig 5.25 Overpressure ratio for 5.0 deg of nose angle

e) Summary of Nose Angle Study **CFL3D**

The nose surface of the lower portion of the wing is taken as a small flat surface which is connected smoothly to the rest of the wing section profile.

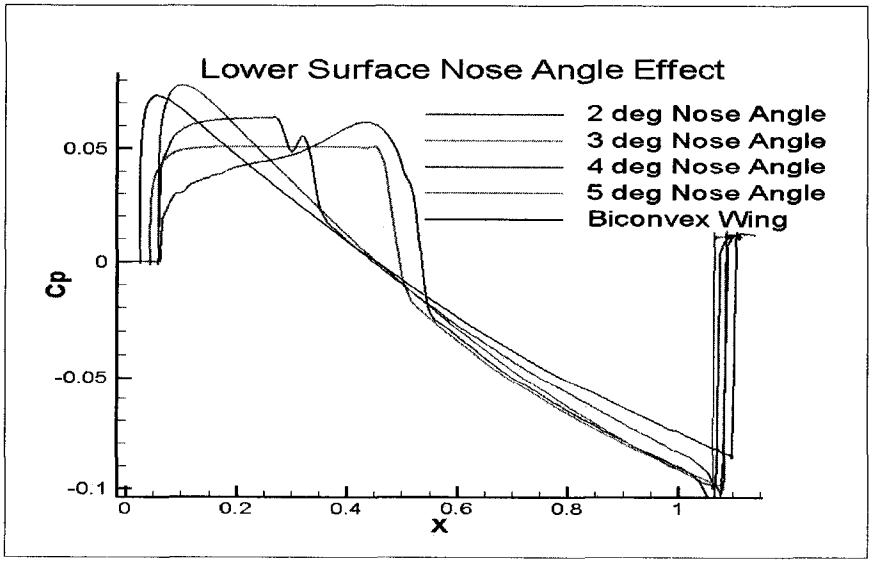

Fig 5.26 Overpressure ratio comparison for nose angle study

Figure 5.26 shows a comparison for the nose angle study for 2, 3, 4 and 5.0 degree of nose angle with biconvex delta wing. The purpose behind the nose angle variation is to decrease the shock angle of the lower portion of the wing, since it is this shock which propagates to the ground the 2 deg nose angle. For the 3 deg. nose angle, the nose shock produces a flat-top overpressure which is 30% lower than the original sharp rise over pressure. When the nose angle is further increased to 5 degrees, the flat top overpressure range is decreased and becomes sharp again with a higher value than that of the base biconvex wing shape. Overpressure observed with 5 degrees is shows in Fig 5.25

Hence, there is an optimum value of the nose angle that produces low flat-top overpressure. It is noted that the trailing edge overpressure is a little bit higher than that of the original wing shape in all the nose angle cases as compare to biconvex shape delta wing geometry.

5.4.2 Lower Surface Nose Angle Effects on Aerodynamic Performance

Figure 5.27 shows the effect of the nose angle value of the lower portion of the wing on the lift and drag coefficients. As the nose angle is decreased, the lift coefficient is increased and the drag coefficient is decreased. However reduction in nose angle has a beneficial effect on aerodynamic performance; it also needs to be looked at that change in lift and drag with change in nose angle is not significant.

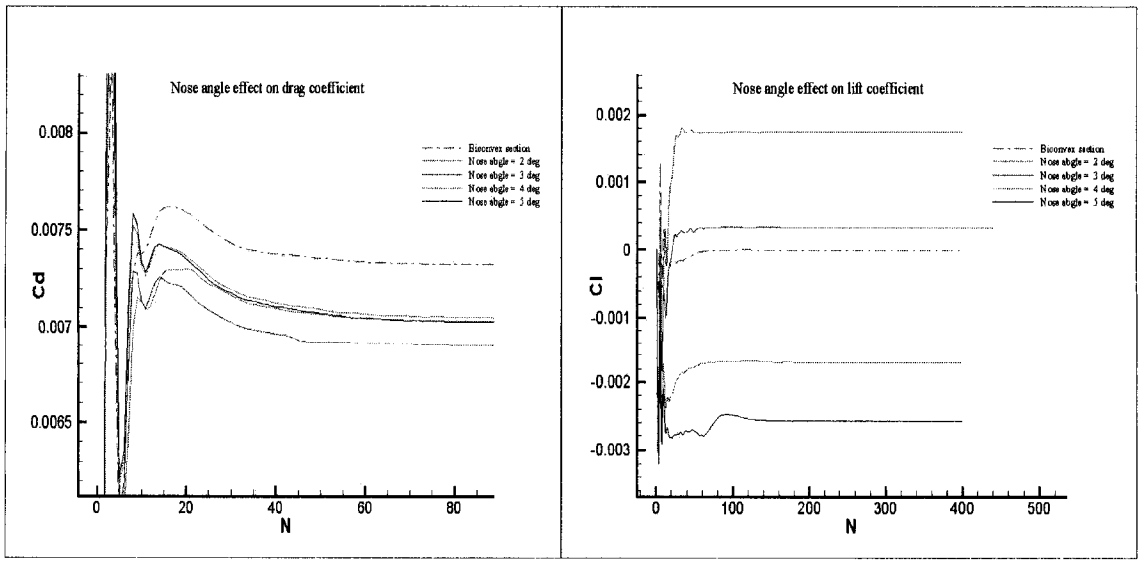

Fig 5.27 Nose angle effect on aerodynamic performance

Hence aerodynamic performance seems to be unaffected by change in nose angle of lower front portion of the delta wing geometry.

5.5 Dihedral Angle Effects CFL3D

The purpose behind the dihedral angle variation is to decrease the shock angle of the lower portion of the wing, since it is this shock which propagates to the ground. To investigate the dihedral angle effect a number of CFD runs are obtained with varying dihedral angle from 0, 5, 10, 15 and 20 degree. The structured grid size for these solutions is 137X113X155. It's observed that the overpressure ratio reduces with increases in dihedral angle [86]. The lower portion overpressure is plotted for the comparison.

5.5.1 Dihedral Angle Effect on Near Field Overpressure CFL3D

In the following section the effect of dihedral angle of the delta wing on near field density and overpressure ratio is presented. Figure 5.28 shows the delta wing orientation with different dihedral angles of 15 and 20 deg with respect to wing without dihedral. The shape of the wing is kept unchanged i.e. thickness, camber and nose angle changes are not considered for the study. The biconvex wing with 5.0 % maximum thickness is studied for varying dihedral angle.

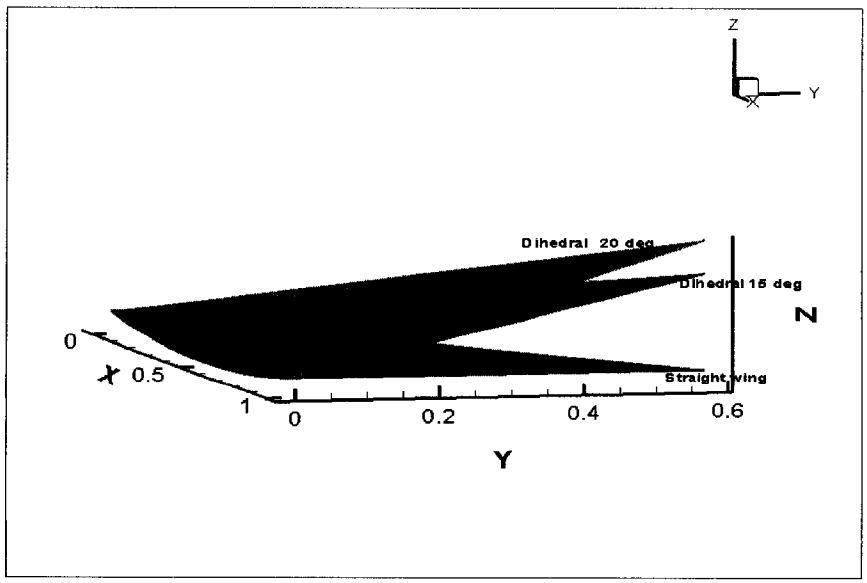

Fig 5.28 Orientation of wing for Dihedral angle

a) Dihedral angle of 5.0 deg

Figure 5.29 shows the density contour for a biconvex delta wing with a 5 degree dihedral angle. As shown in Fig 5.29 the lower surface shock is weaker than the upper surface shock. Figure 5.30 makes a comparison of the overpressure ratio of the biconvex delta wing without dihedral and a 5.0 degree dihedral angle.

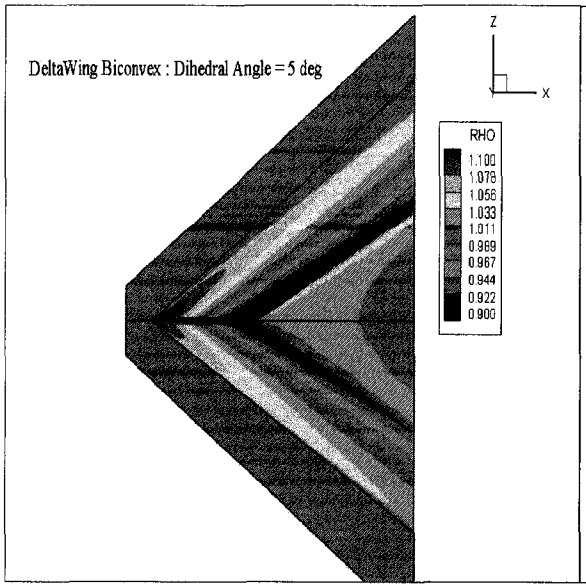

Fig 5.29 Density contour with 5 deg dihedral

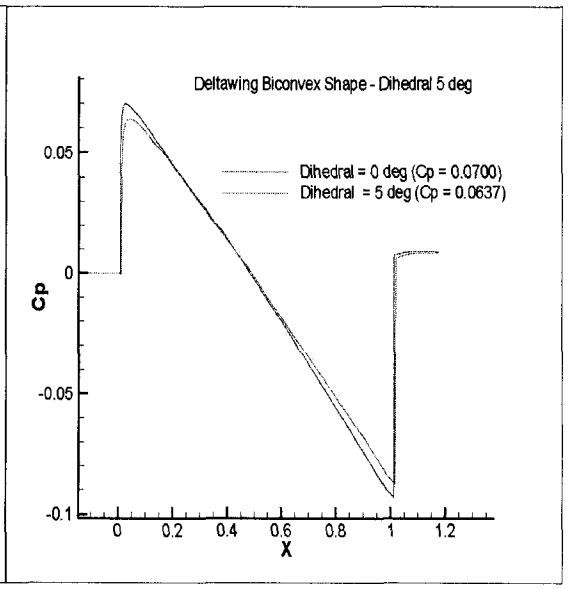

Fig 5.30 Overpressure ratio with 5deg dihedral

This study indicates that having a dihedral wing can reduce the sonic boom effect. The trailing shock also has low amplitude as compared with the base case. The overpressure ratio is decreased from 0.07 to 0.0637 in leading shock of the delta wing whereas the trialing shock strength is decreased from -092 to -0.088. The overpressure ratio is reduced by 5.27 % as compare to base case without dihedral.

b) Dihedral angle of 10.0 deg

Fig 5.31 shows the comparison of the overpressure ratio of the biconvex delta wing without dihedral and with 10.0 degree of dihedral angle. The overpressure ratio is decreased from 0.07 to 0.0614 in leading shock of the delta wing whereas the trialing shock strength is decreased from -092 to -0.08. The overpressure ratio has reduced by 7.27 % as compared to the case without dihedral with 10 deg of dihedral. Decrease in shock strength is increased by about 2.0 % as compared to 5.0 degree of dihedral angle.

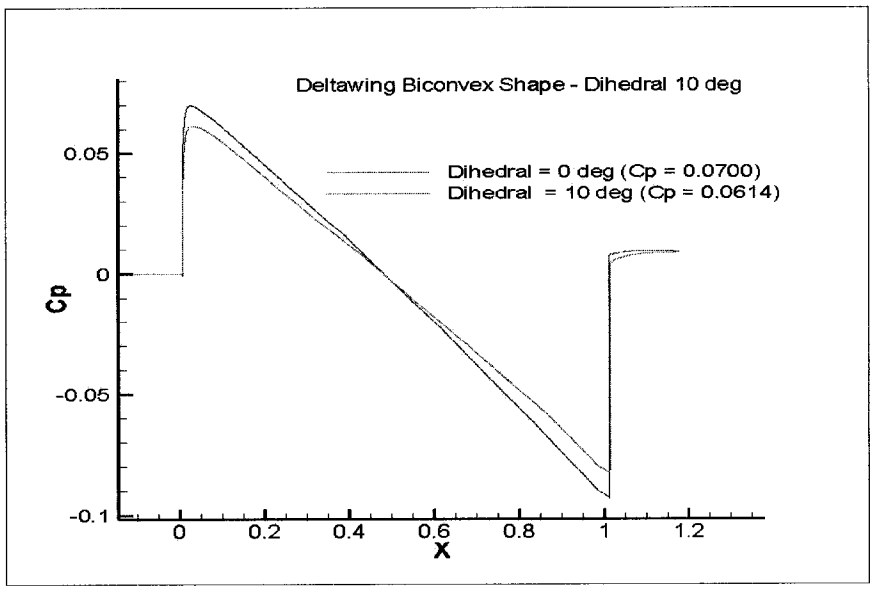

Fig 5.31 Overpressure Comparison – 10 deg

c) Dihedral angle of 15.0 deg

Fig 5.32 shows the comparison of the overpressure ratio of the biconvex delta wing without dihedral and with a 15.0 degree dihedral angle. The overpressure ratio is decreased from 0.07 to 0.061 in leading shock of the delta wing whereas the trailing shock strength is decreased from -092 to -0.08. The overpressure ratio reduction is found to be increasing with increase in dihedral angle.

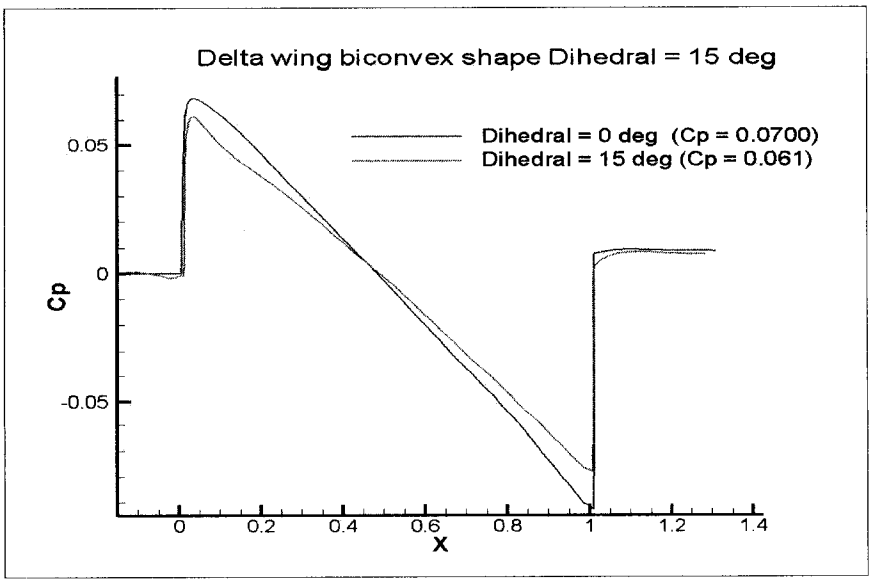

Fig 5.32 Overpressure Comparison – 15 deg

d) Dihedral angle of 20.0 deg

Fig 5.33 shows the comparison of the overpressure ratio of the biconvex delta wing without dihedral and a 15.0 degree dihedral angle. The overpressure ratio is decreased from 0.07 to 0.0567 in leading shock of the delta wing whereas the trailing shock strength is decreased from -092 to -0.078. Dihedral angle 20.0 degrees shows the maximum reduction in overpressure ratio and hence the sonic boom level.

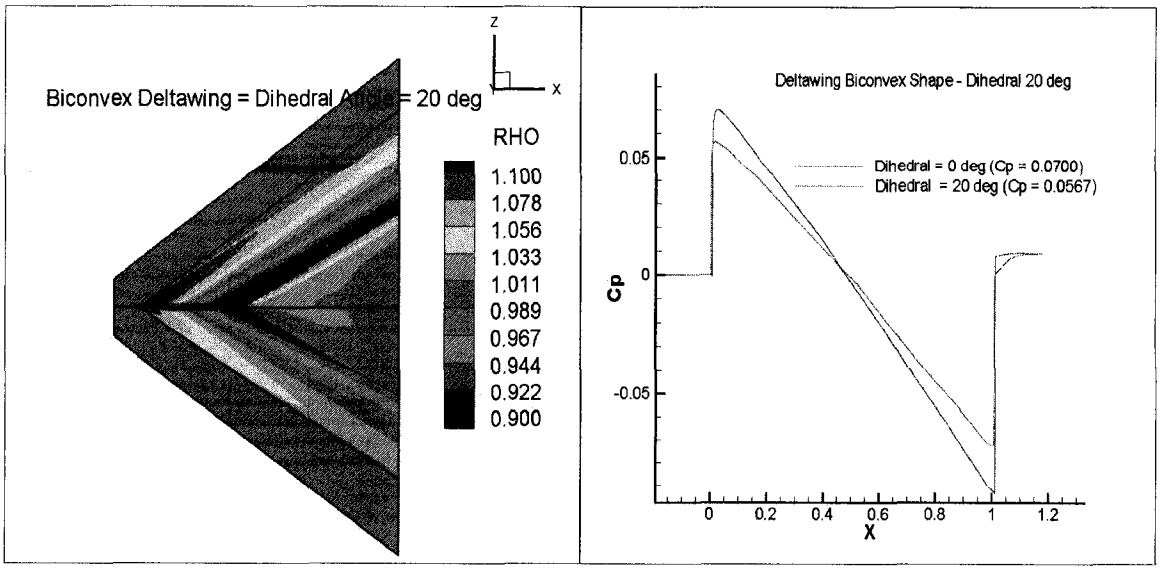

Fig 5.33 Overpressure Comparison – 20 deg

e) Summary of Dihedral angle Study **CFL3D**

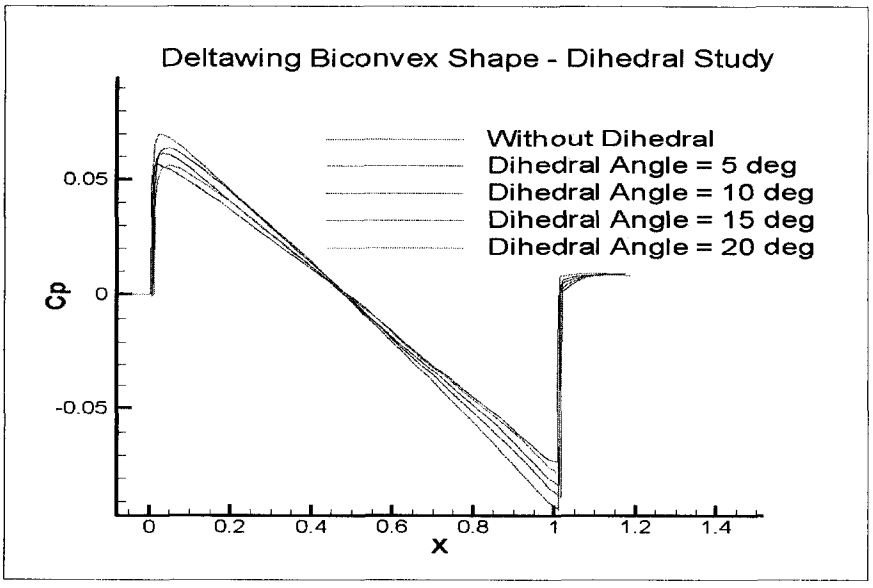

Fig 5.34 Overpressure Comparison – Dihedral study

Figure 5.34 summarizes the dihedral angle study for sonic boom mitigation. The lower portion overpressure is plotted for comparison in Fig 5.34. In the near field the biconvex delta wing had overpressure ratio of 0.070, while the 10°, 15° and 20° dihedral wings had overpressure ratio of 0.0614, 0.061 and 0.0567, respectively. Increase in dihedral up to 20 deg shows considerable decrease in overpressure ratio. The decrease in overpressure and hence sonic boom is about 19 % with dihedral angle of 20 deg.

5.5.2 Dihedral Angle Effects on Aerodynamic Performance **CFL3D**

Life coefficient is found to be decreasing with increase in dihedral angle [86]. Drag coefficient is found not to change with increasing dihedral for 0 degree AOA. The unfavorable change in lift and drag can be compromised with the sonic boom level reduction. Lift coefficient has decreased from 0.00644 to 0.00540, 0.00401, 0.00227 and 0.00147 with 5°, 10°, 15° and 20° deg of dihedral angle respectively. The drag coefficient is not changing with increasing dihedral for the study.

5.5.3 Dihedral angle Effects on Optimized Wing Shape **CFL3D**

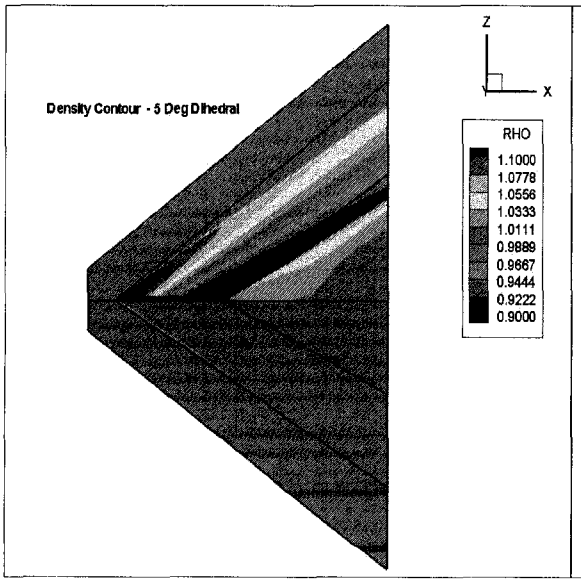

Fig 5.35 Density contour 20deg dihedral

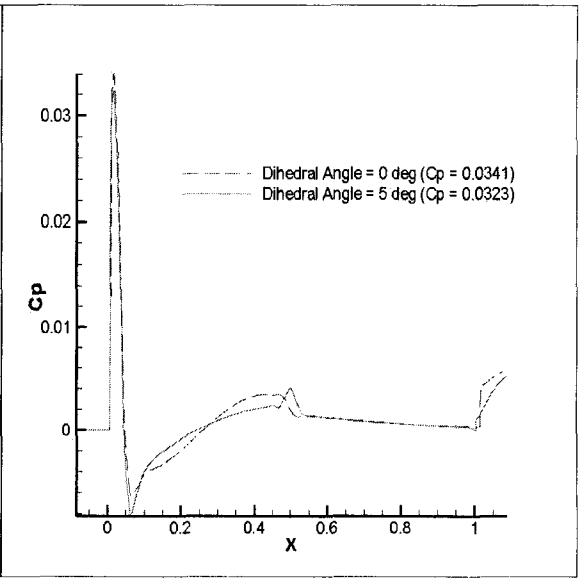

Fig 5.36 Overpressure Comparison – 15 deg

The biconvex delta wing is optimized for 3 design variable maximum thickness, camber and nose angle at this stage. Once the optimized design parameters are obtained the optimized shape further investigated for the effect of the dihedral angle on boom levels.

Fig 5.35 shows the density contour of near field computation with dihedral angle of 5 deg. Fig 5.36 shows the overpressure reduction from 0.0341 to 0.0323 with dihedral angle of 5 deg. The lower portion overpressure is plotted for comparison.

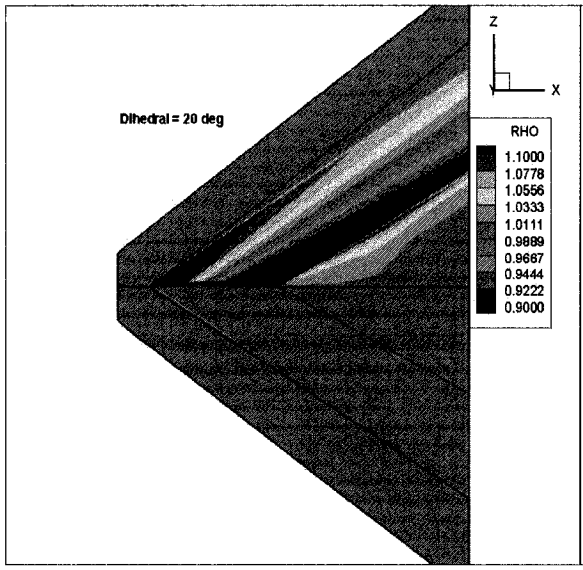

Fig 5.37 Density contour 20deg dihedral

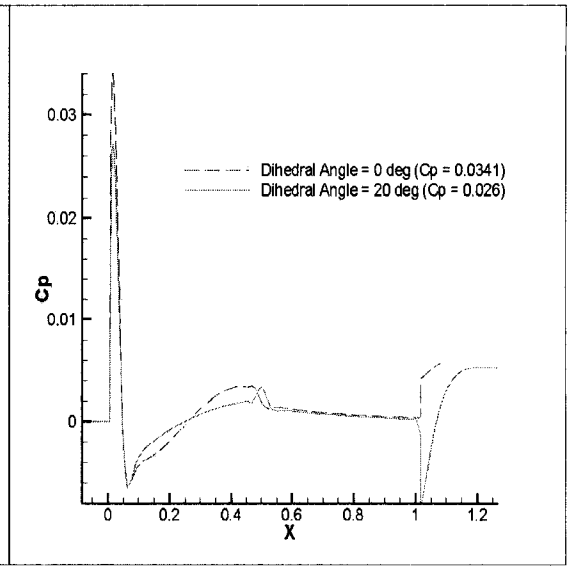

Fig 5.38 Overpressure Comparison – 20 deg

Fig 5.37 shows the density contour of near field computation with a dihedral angle of 20 deg. Fig 5.38 shows the overpressure reduction from 0.0341 to 0.026 with dihedral angle of 20 degrees. The lower portion overpressure is plotted for the comparison.

Figure 5.39 and Fig 5.40 shows the overpressure comparison without the dihedral and with dihedral angle of 10 and 15 deg. respectively. The decrease in overpressure is plotted for the comparison. At the near field the overpressure ratio has decreased from 0.0341 to 0.0298 and 0.0262 for 10° and 15° dihedral angle respectively. The reduction in overpressure is 23.16 % with a 15 degree dihedral angle.

Figure 5.41 shows the variations in lift and drag coefficient with the dihedral angle for optimized wing for 3 parameters (i.e. max. thickness, camber and nose angle). Aerodynamic performances i.e. lift and drag are found to be degrading with increasing dihedral angle. Life coefficient is found to be decreasing with increase in dihedral angle. Lift coefficient has decreased from 0.00644 to 0.00540, 0.00401, 0.00227 and 0.00147 with 5°, 10°, 15° and 20° deg of dihedral angle respectively.

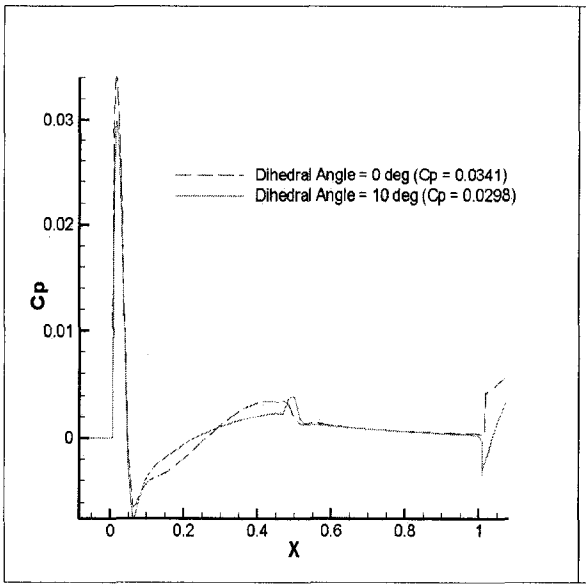

Fig 5.39 Overpressure Comparison – 10 deg

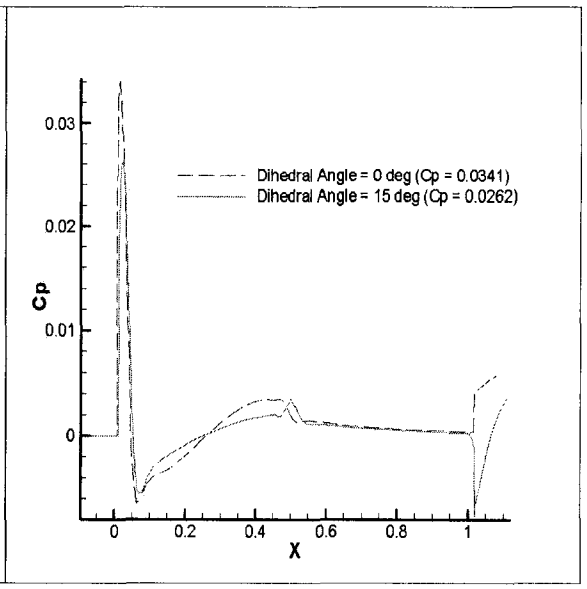

Fig 5.40 Overpressure Comparison – 15 deg

There is a little increase in drag with increasing dihedral. Drag coefficient has increased from 0.00464 to 0.00474, 0.00484, 0.00494 and 0.005 with 5°, 10°, 15° and 20° deg of dihedral angle respectively. The unfavorable change in lift and drag can be compromised with the sonic boom level reduction. The percentage gain is very high up to 15 deg of dihedral angle and there is a little gain after 15 deg to 20 deg. The dihedral angle does not increase any drag for biconvex shape with zero degree AOA. One can have better estimates for change in lift and drag coefficient at finite AOA study.

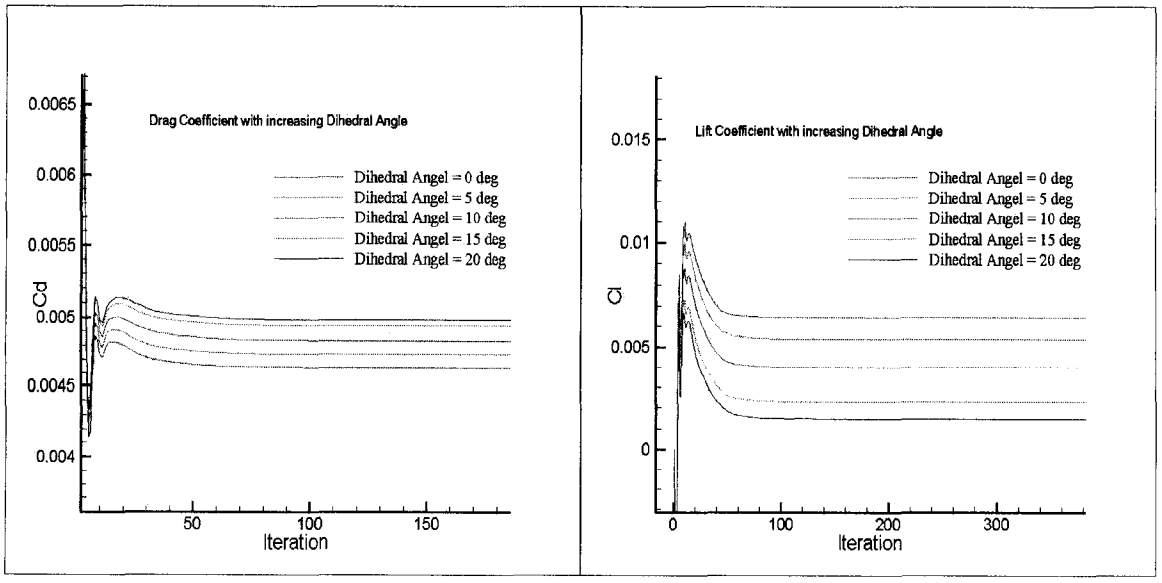

Fig 5.41 Dihedral angle effect on aerodynamic performance

5.6 Combined Effects of Design Parameters CFL3D

While carrying out the individual investigation of the considered factor it was discovered that simply increasing / decreasing these parameters leads to decrease in lift and increase in drag. A reduction in maximum thickness drastically reduces the near field overpressure ratio and hence the boom on the ground. With the camber its other way around increasing camber found to be favorable towards minimizing boom level. A viable design is concerned about least degradation of aerodynamic performance at the same time mitigating the boom. At this point it is decided to investigate the combined effect of all the design parameter and carry out the optimization study for minimizing the boom and maximizing aerodynamic performance i.e. maximizing L/D ratio.

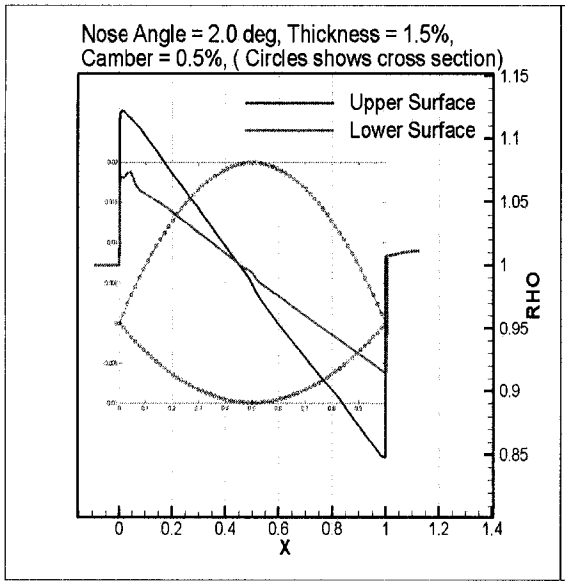

Fig 5.42 Combined effects case 1

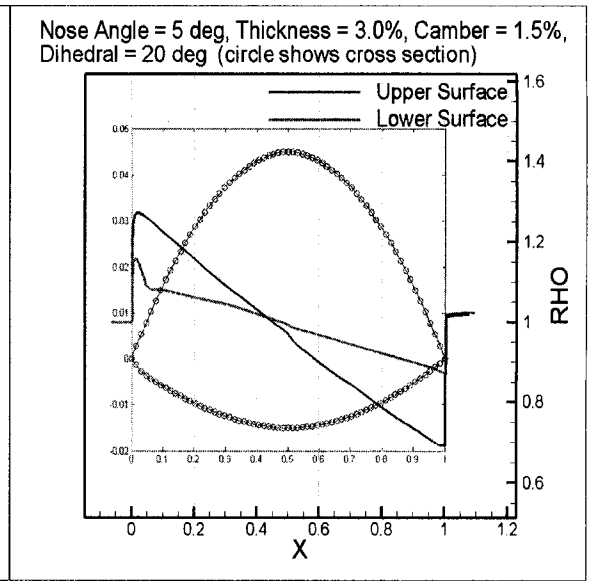

Fig 5.43 Combined effects case 2

Figures 5.42 and 5.43 shows the combined effect of varying all the design parameters simultaneously. The combined effects of the design variables have been investigated and they all showed up increasing camber and dihedral and decreasing thickness and nose angle are favorable towards minimizing boom on the ground. Figure 5.44 also suggest that having low values of thickness ratio and nose angle to 1.5% and 2.01 degree respectively result in low boom profile shape. Also observed in Fig 5.44 is a very high value of dihedral angle and camber ratio. On the other hand in Fig 5.45 high values of thickness ratio of 3.0 % result in high boom profile shape. The next thing was to go for

optimization analysis to come up with the final figure of dihedral, camber, thickness and nose angle. It is also observed with high boom profile shape that it has a low value of camber ratio as well. As observed with these four case low values of thickness and nose angle leads to lower shock strength whereas higher values of camber and dihedral gives the lower leading and trailing shock.

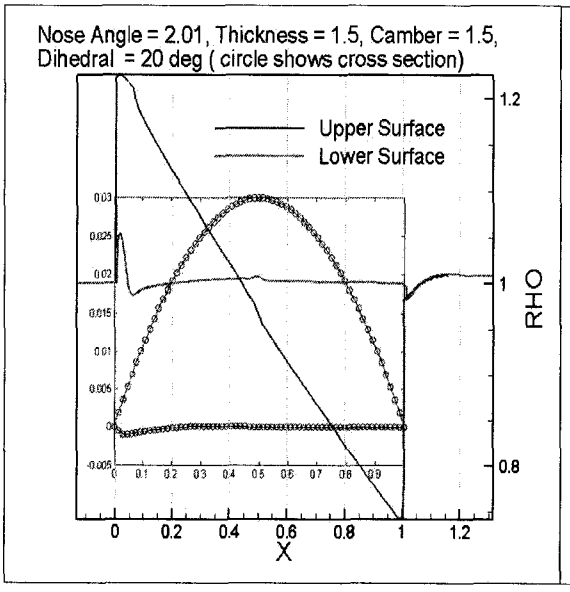

Fig 5.44 Combined Effects case 3

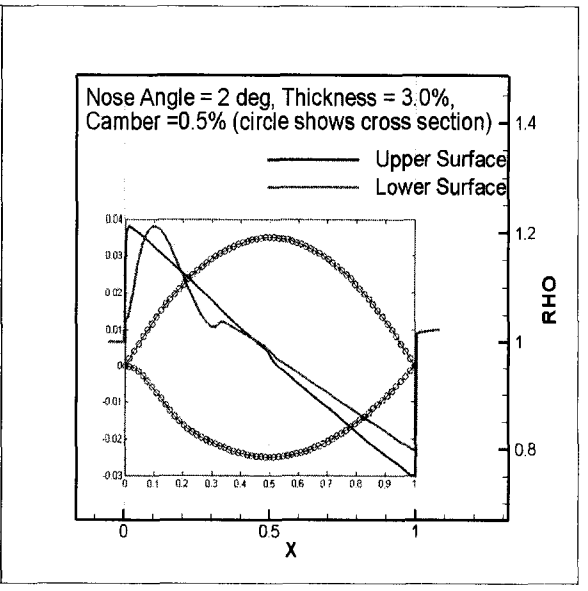

Fig 5.45 Combined Effects case 4

5.7 Delta Wing Optimization for AOA = 0 deg

The optimization module in Design-Expert [34] searches for a combination of factor levels that simultaneously satisfy the requirements placed on each of the responses and factors. To use optimization, one must first analyze each response to establish the appropriate model. Optimization of one response or the simultaneous optimization of multiple responses can be performed graphically or numerically.

Also, one can simultaneously evaluate all the response models for any value of the independent variables using the point prediction node. Two level factorial design permit estimation of all main effects and all interaction effects. For multi level factorial design goal for each of the factor must be specified. Possible options include maximize, minimize, move towards a target value. One can also set a factor to be "exactly equal to" a specific value.

By default, the factors are set "within range" for the goal, with the low and high limits to be equal to the low and high factor settings. One may choose to either modify the goal, or expand or restrict the factor range settings. One can decide on the importance of each of the design objective as show in Fig 5.46. This is the specified importance value for this factor in relation to the other factors and responses. The default is +++ (three pluses).

If it is more important to achieve one factor or response than another, give the more important factor or response a higher weight. This is the desirability value for this solution. Although this value can range from zero to one, it should only be evaluated relative to the upper and lower limits that were chosen for the responses and factors. In the current study both of the objective low boom level and high lift to drag ratio is given an equal importance.

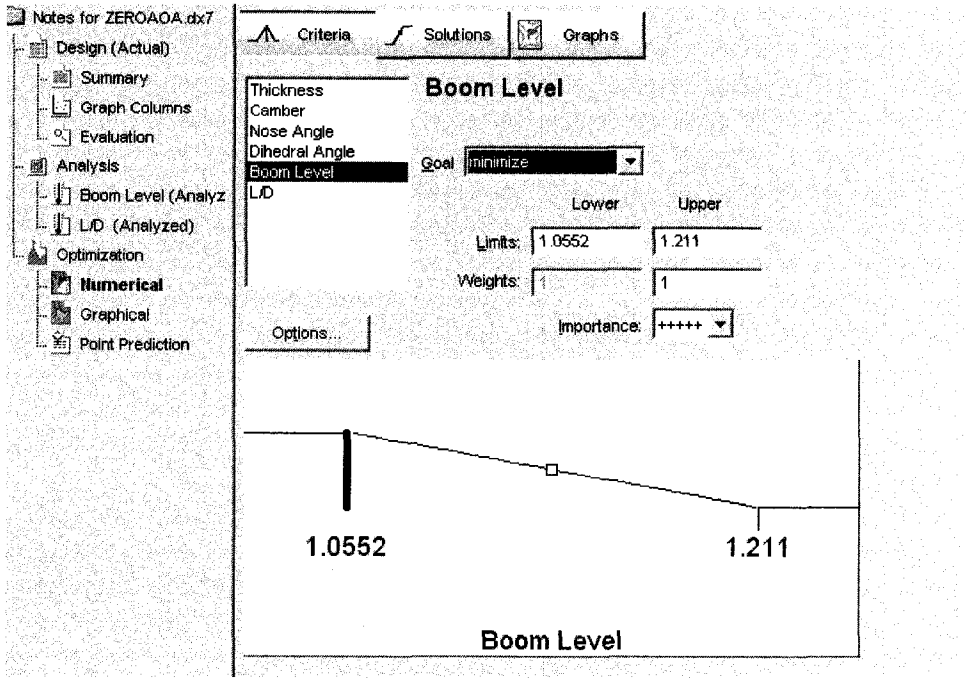

Fig 5.46 Importance of Objective functions

5.7.1 Response Surface Cases CFL3D

The number of CFD runs necessary to get significant results depends on how many factors are considered for the study and accuracy desired. Higher number of design factor or the variables requires higher number of runs. That's leads to running more number of CFD in this study. After clarifying the objectives, the next step is to figure out which

responses (quality characteristics) to measure and how to measure them. Identifying quantifiable responses is one of the most important steps of a successful optimization process. Response surface for the study measured the density jump across the leading shock as a measure to boom level and the ratio of lift and drag coefficients as the measure of aerodynamics performance.

The upper and lower bound for design variable are as follows:

Maximum Thickness Ratio = 1.0 % and 3.0 %

Maximum Camber Ratio = 0.5 % and 2.0 %

Lower surface nose angle = 2.0 deg and 5.0 deg

Dihedral Angle = 0.0 deg and 20.0 deg

Response Surface is created using a 16 CFD simulation result for 4 factor optimization study. Accuracy of the response surface is based on the number of CFD runs fed in DES. Results are obtained for multiple response surface (Max L/D and Min RHO) with equal weighted CFD input data for the response surface input is following

1. Nose Angle = 2 deg, max thickness = 1.5 %, max camber = 1.5 %, dihedral = 0 deg
2. Nose Angle = 5 deg, max thickness = 1.5 %, max camber = 1.5 %, dihedral = 0 deg
3. Nose Angle = 2 deg, max thickness = 1.5 %, max camber = 0.5 %, dihedral = 0 deg
4. Nose Angle = 5 deg, max thickness = 3.0 %, max camber = 1.5 %, dihedral = 0 deg
5. Nose Angle = 5 deg, max thickness = 1.5 %, max camber = 0.5 %, dihedral = 0 deg
6. Nose Angle = 2 deg, max thickness = 3.0 %, max camber = 0.5 %, dihedral = 0 deg
7. Nose Angle = 2 deg, max thickness = 3.0 %, max camber = 1.5 %, dihedral = 0 deg
8. Nose Angle = 5 deg, max thickness = 3.0 %, max camber = 0.5 %, dihedral = 0 deg
9. Nose Angle = 2 deg, max thickness = 1.5 %, max camber = 1.5 %, dihedral = 20 deg
10. Nose Angle = 5 deg, max thickness = 1.5 %, max camber = 1.5 %, dihedral = 20 deg
11. Nose Angle = 2 deg, max thickness = 1.5 %, max camber = 0.5 %, dihedral = 20 deg
12. Nose Angle = 5 deg, max thickness = 3.0 %, max camber = 1.5 %, dihedral = 20 deg
13. Nose Angle = 5 deg, max thickness = 1.5 %, max camber = 0.5 %, dihedral = 20 deg
14. Nose Angle = 2 deg, max thickness = 3.0 %, max camber = 0.5 %, dihedral =20 deg
15. Nose Angle = 2 deg, max thickness = 3.0 %, max camber = 1.5 %, dihedral = 20 deg
16. Nose Angle = 5 deg, max thickness = 3.0 %, max camber = 0.5 %, dihedral = 20 deg

Response surface cases and their CFD solutions are described in the following section. hey overall represent that having a low value of maximum thickness ratio and nose angle and having a higher value for camber and dihedral angle gives low boom profile for delta wing geometry.

CASE 1: (Nose Angle = 2 deg, Thickness = 1.5 %, Camber = 1.5 %, Dihedral = 0)

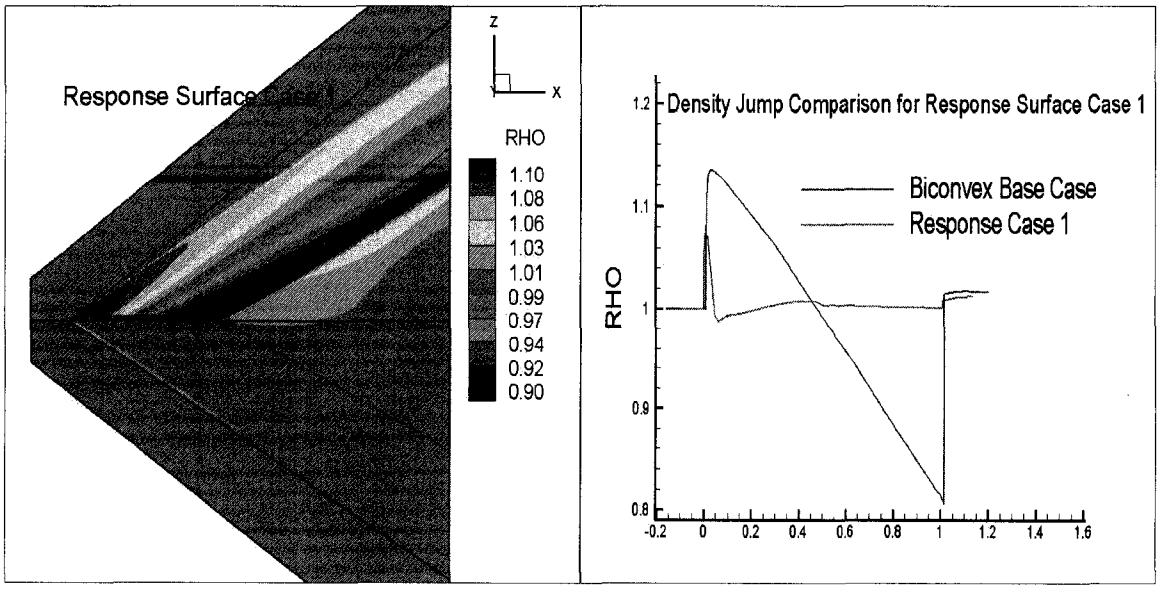

Fig 5.47 Response surface case 1 CFL3D

Figure 5.47 shows the response surface cases 1. Leading and trailing shock are of low strength as compared to the base case of biconvex profile wing. A density jump across the leading and trailing shock is also plotted in Fig 5.47 and compared to the biconvex surface shock strength. The shocks coming out from the lower surface are responsible for boom on the ground, so one need only be concerned about the lower shock strength.

CASE 2: (Nose Angle = 5 deg, Thickness = 1.5 %, Camber = 1.5 %, Dihedral = 0)

Figure 5.48 shows the response surface cases 2. Leading shock is of high strength as compared to trailing shock due to the high nose angle value of 5 deg. A density jump across the leading and trailing shock is also plotted in Fig 5.48 and compared to the biconvex shape delta wing surface shock strength.

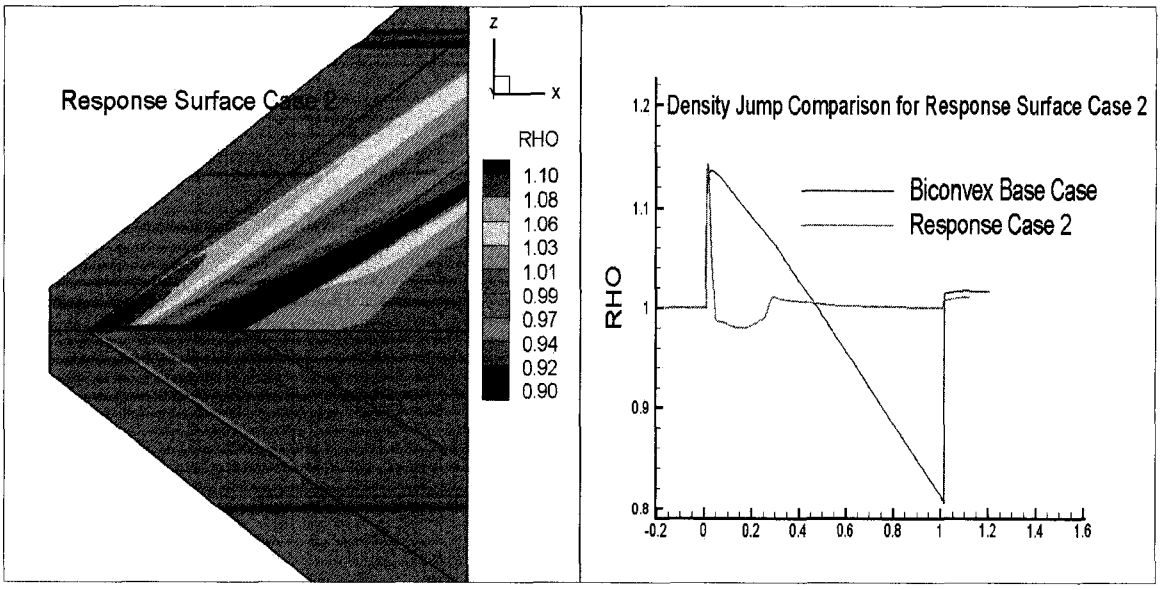

Fig 5.48 Response surface case 2 CFL3D

CASE 3: (Nose Angle = 2 deg, Thickness = 1.5 %, Camber = 0.5 %, Dihedral = 0)

Figure 5.49 the response surface case 3. Leading and trailing shock are of low strength as compared to the base case of biconvex profile wing.

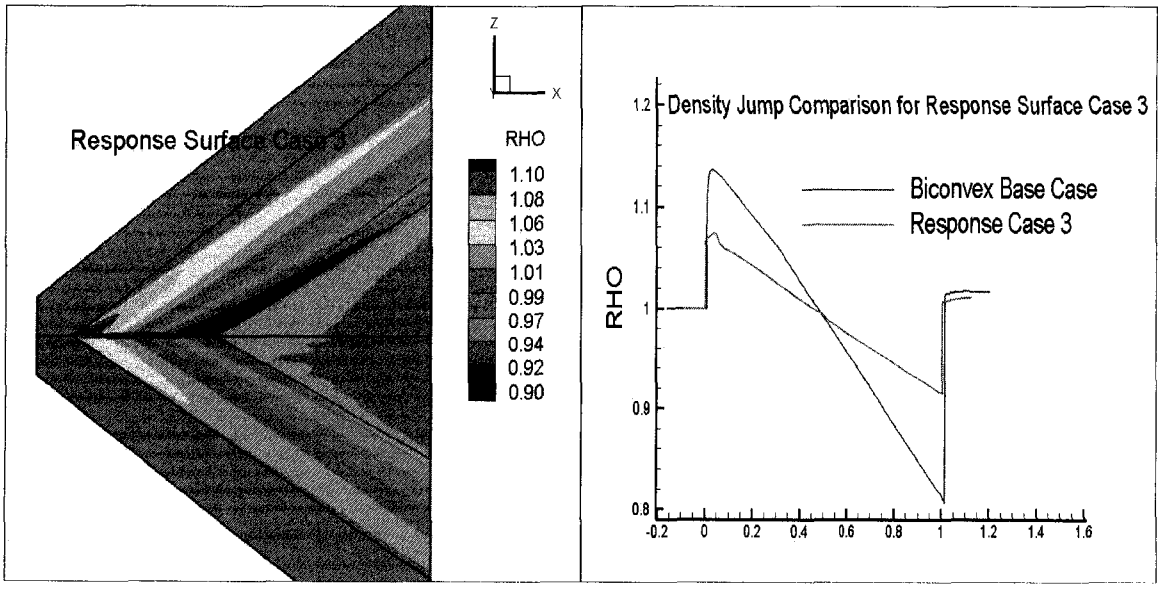

Fig 5.49 Response surface case 3 CFL3D

A density jump across the leading and trailing shock is also plotted in Fig 5.49 and compared to the biconvex surface shock strength.

CASE 4: (Nose Angle = 5 deg, Thickness = 3.0 %, Camber = 1.5 %, Dihedral = 0)

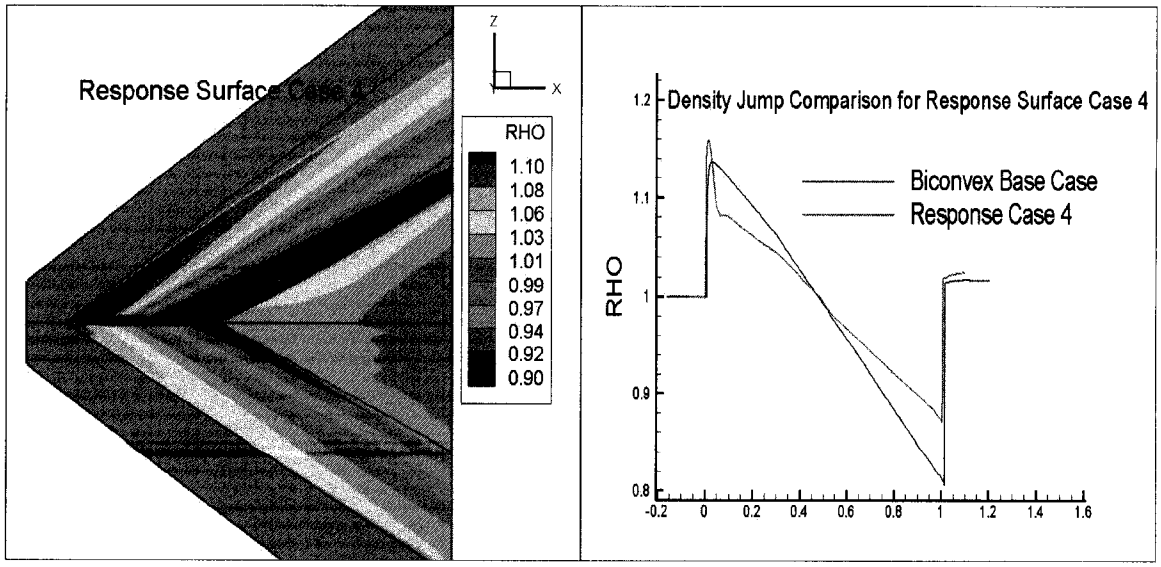

Fig 5.50 Response surface case 4 CFL3D

Figure 5.50 the response surface case 4. Leading shock is of high strength as compared to trailing shock due to the high nose angle value of 5 deg. A density jump across the leading and trailing shock is also plotted in Fig 5.50 shows higher strengths of shock as compared to previous cases. Higher thickness leads to high shock strength but in this case the high value of camber helps in reducing the density jump across the shock.

CASE 5: (Nose Angle = 5 deg, Thickness = 1.5 %, Camber = 0.5 %, Dihedral = 0)

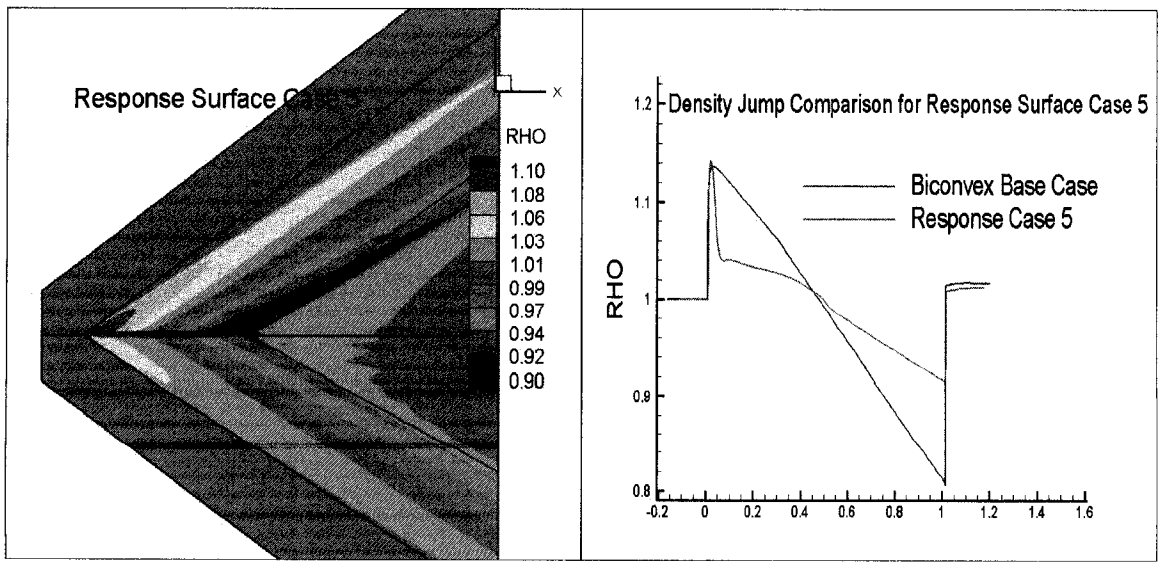

Fig 5.51 Response surface case 5 CFL3D

Figure 5.51 shows the response surface cases 5. Leading shock is of high strength as compared to trailing shock due to the high nose angle value of 5 deg. A density jump

across the leading and trailing shock is also plotted in right side of Fig 5.51 and compared to the biconvex surface shock strength.

CASE 6: (Nose Angle = 2 deg, Thickness = 3.0 %, Camber = 0.5 %, Dihedral = 0)

Figure 5.52 shows response surface case 6. Leading and trailing shock are of high strength due to high value of thickness ratio and low value of camber ratio. A density jump across the leading and trailing shock is also plotted in right side of Fig 5.52 and compared to the biconvex surface shock strength.

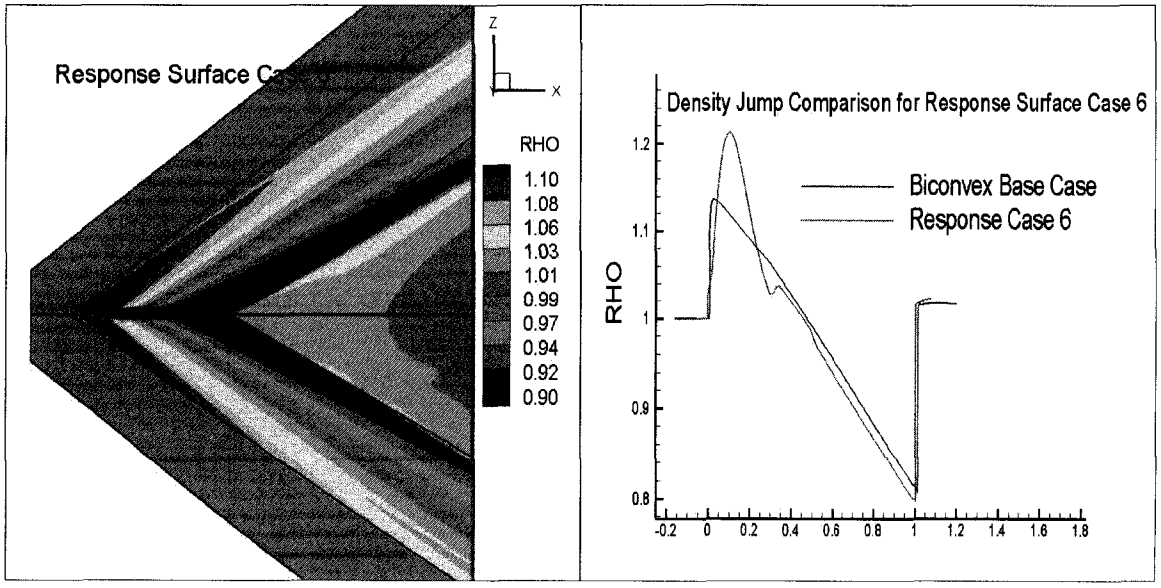

Fig 5.52 Response surface case 6 CFL3D

Lower shock location has shifted behind as compared to upper shock due to very small nose angle of lower front portion of the wing. With optimized value of nose angle one can obtained a flat top profile of the shock system.

CASE 7: Nose Angle = 2 deg, Thickness = 3.0 %, Camber = 1.5 %, Dihedral = 0

Figure 5.53 shows response surface case 1. Leading and trailing shock are of high strength as compared to the base case of biconvex profile wing. A density jump across the leading and trailing shock is also plotted in right side of Fig 5.53 and compared to the biconvex surface shock strength. This case is similar to case 6 with increase in camber to 1.5 % from 0.5 %. Due to the increased camber the leading shock density jump has reduced from 1.2 in case 6 to 1.1. This is a significant reduction just by increasing camber of the delta wing.

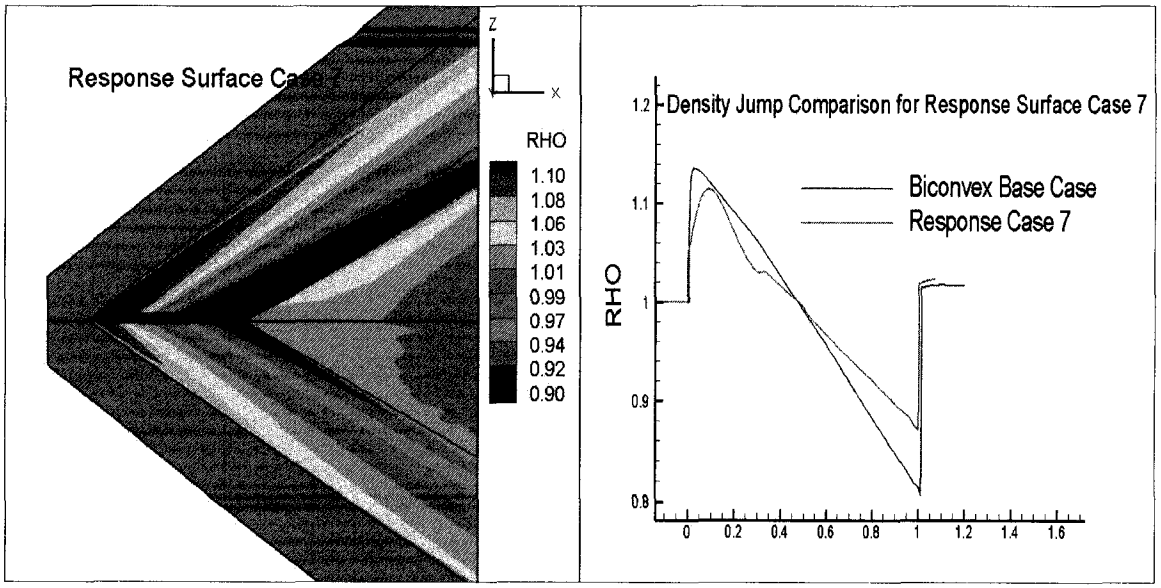

Fig 5.53 Response surface case 7 CFL3D

CASE 8: Nose Angle = 5 deg, Thickness = 3.0 %, Camber = 0.5 %, Dihedral =0

Figure 5.54 shows response surface case 8. Leading and trailing shock are of high strength due to high value of thickness ratio and low value of camber ratio. A density jump across the leading and trailing shock is also plotted in right side of Fig 5.54 and compared to the biconvex surface shock strength. This case clearly indicates that high thickness and nose angle can shoot up the leading shock heavily.

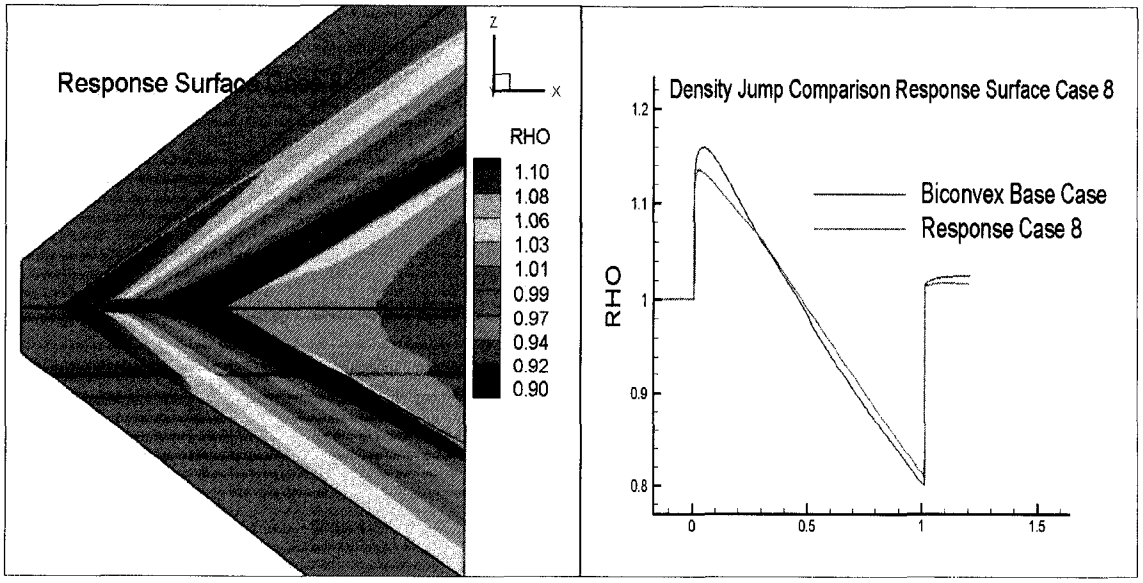

Fig 5.54 Response surface case 8 CFL3D

CASE 9: Nose Angle = 2 deg, Thickness = 1.5 %, Camber = 1.5 %, Dihedral = 20

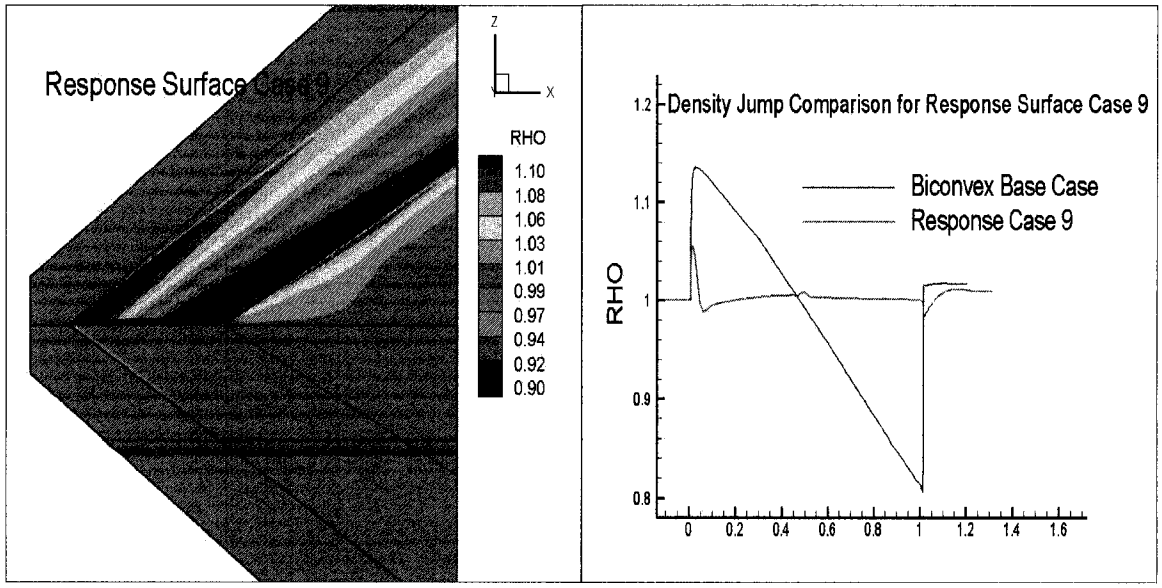

Fig 5.55 Response surface case 9 CFL3D

Figure 5.55 shows response surface case 9. Leading and trailing shock are of low strength as compared to the base case of biconvex profile wing. Higher vales of camber and the low value of thickness with low nose angle make this case favorable for low boom. Leading shock strength has a drastic jump to a much lower value as compare to upper surface and trailing shock has almost disappear due to very high value of dihedral angle. A density jump across the leading and trailing shock is also plotted in right side of Fig 5.55 and compared to the biconvex surface shock strength.

CASE 10: Nose Angle = 5 deg, Thickness = 1.5 %, Camber = 1.5 %, Dihedral = 20

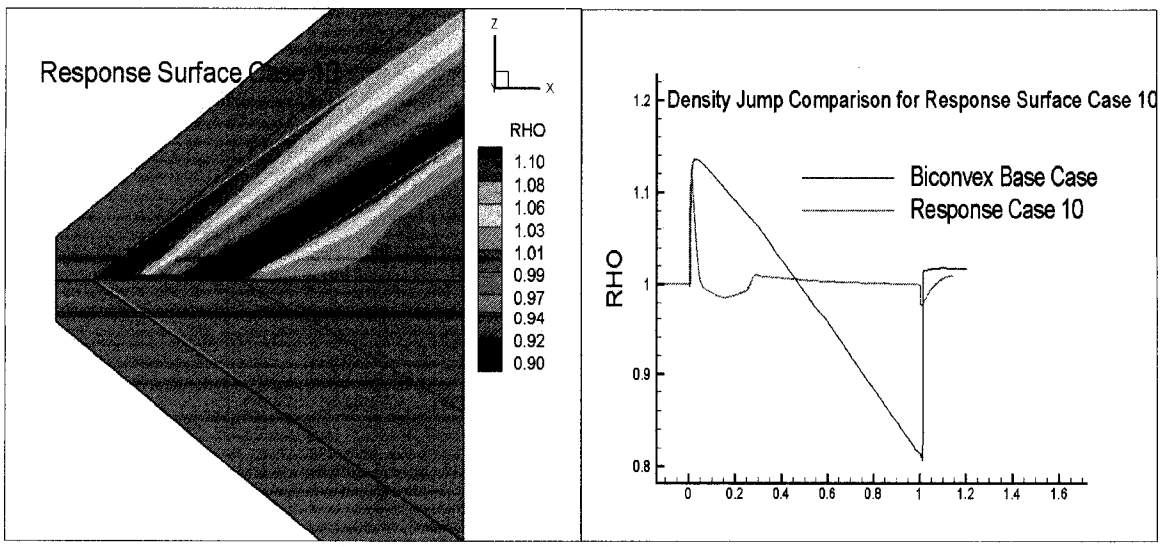

Fig 5.56 Response surface case 10 CFL3D

Figure 5.56 shows response surface case 10. Leading and trailing shock are of low strength as compared to the base case of biconvex profile wing. A density jump across the leading and trailing shock is also plotted in right side of Fig 5.56 and compared to the biconvex surface shock strength shows much lower shock strength due to the additional effect of high dihedral angle.

CASE 11: Nose Angle = 2 deg, Thickness = 1.5 %, Camber = 0.5 %, Dihedral = 20

Figure 5.57 shows response surface case 11. Leading and trailing shock are of low strength as compared to the base case of biconvex profile wing. A density jump across the leading and trailing shock is also plotted in the right side of Fig 5.57 compared to the upper surface shock strength.

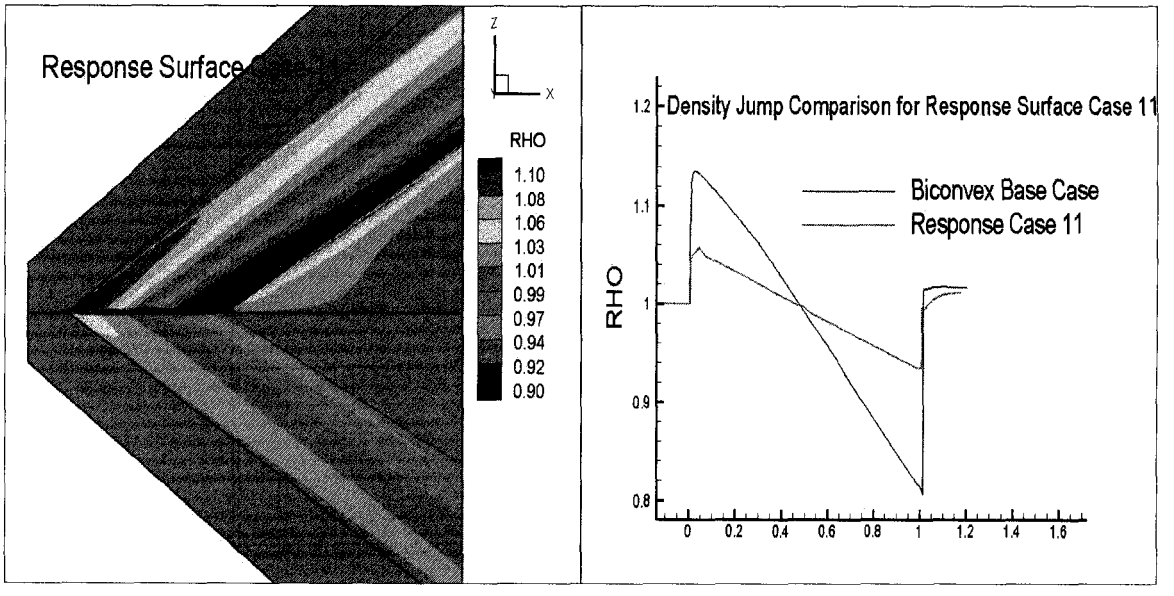

Fig 5.57 Response surface case 11 CFL3D

CASE 12: Nose Angle = 5 deg, Thickness = 3.0 %, Camber = 1.5 %, Dihedral = 20

Figure 5.58 shows response surface case 12. Leading and trailing shock are of high strength due to high value of thickness ratio and nose angle. There is an additional jump in leading shock as compared to trailing shock due to a 5.0 degrees nose angle at front lower portion of the delta wing. A density jump across the leading and trailing shock is also plotted in right side of Fig 5.58 and compared to the biconvex surface shock strength. Density contour shows very strong shocks on the upper surface due to the high

value of the camber ratio. Camber turns the flow with high angle on the upper surface and thus leads for stronger shock on the upper surface.

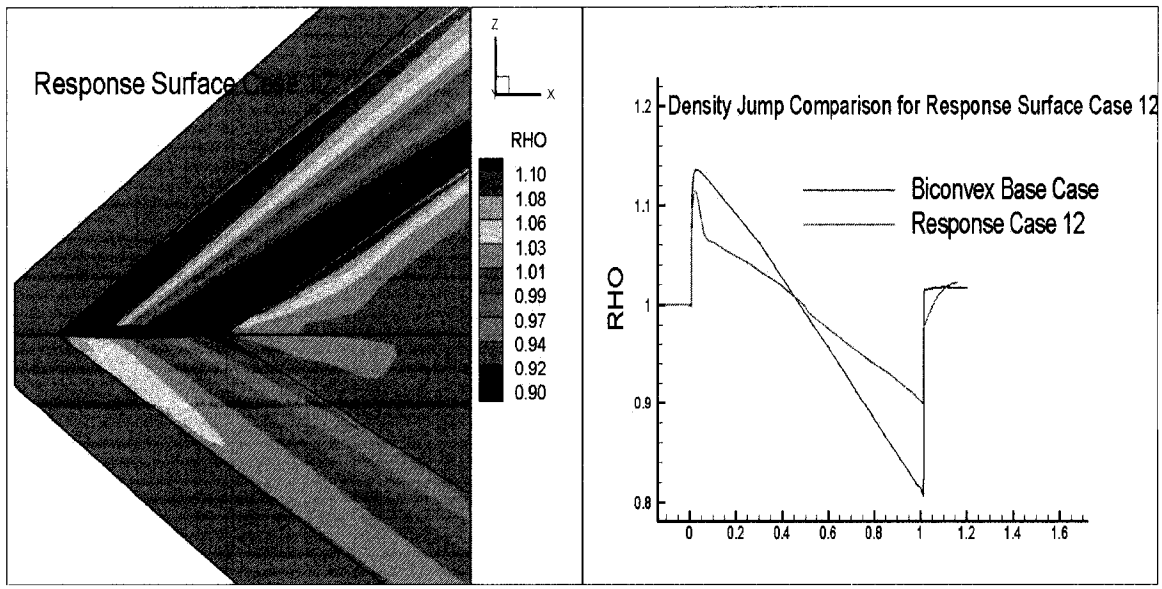

Fig 5.58 Response surface case 12 CFL3D

CASE 13: Nose Angle = 5 deg, Thickness = 1.5 %, Camber = 0.5 %, Dihedral = 20

Figure 5.59 shows response surface case 13. Leading shock is of high strength as compared to trailing shock due to the high nose angle value of 5 degrees. A density jump across the leading and trailing shock is also plotted in Fig 5.59 and compared to the biconvex surface shock strength.

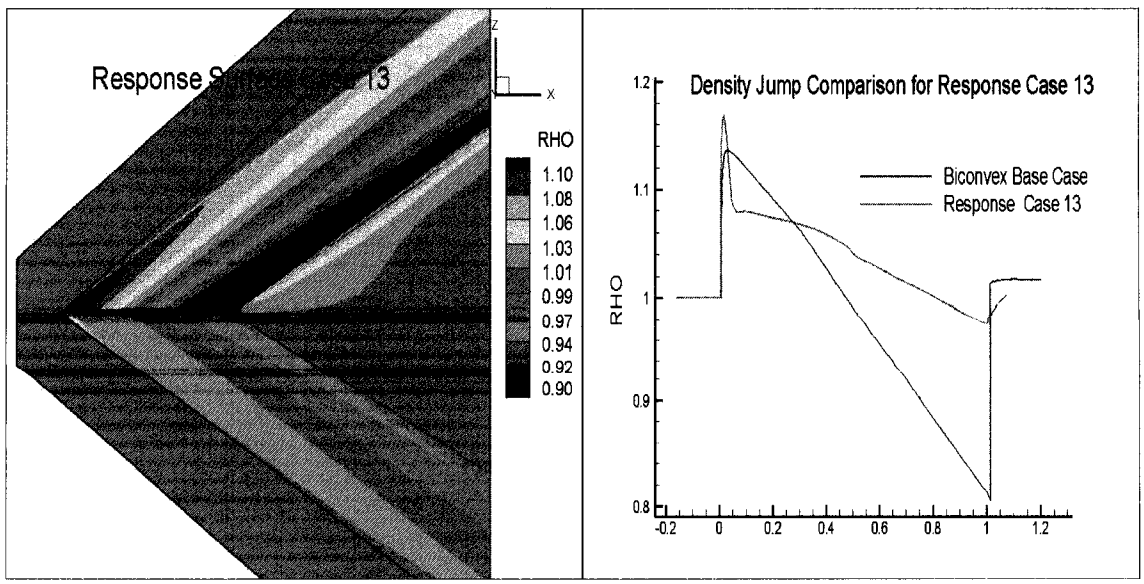

Fig 5.59 Response surface case 13 CFL3D

CASE 14: Nose Angle = 2 deg, Thickness = 3.0 %, Camber = 0.5 %, Dihedral = 20

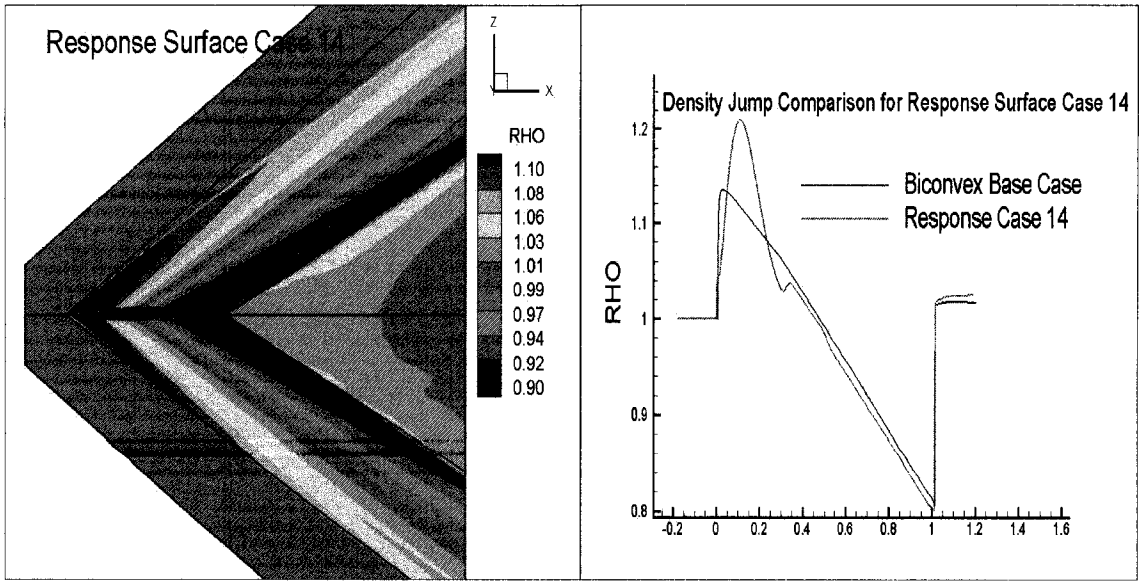

Fig 5.60 Response surface case 14 CFL3D

Figure 5.60 shows response surface case 14. Leading and trailing shocks are of high strength due to high value of thickness ratio and low value of camber ratio. A density jump across the leading and trailing shock is also plotted in the right side of Fig 5.60 and compared to the biconvex surface shock strength. This case is found to be the worst case for boom effect. The leading shock strength on the upper and lower surface is very high. The leading shock density jump in this case is 1.30544.

CASE 15: Nose Angle = 2 deg, Thickness = 3.0 %, Camber = 1.5 %, Dihedral = 20

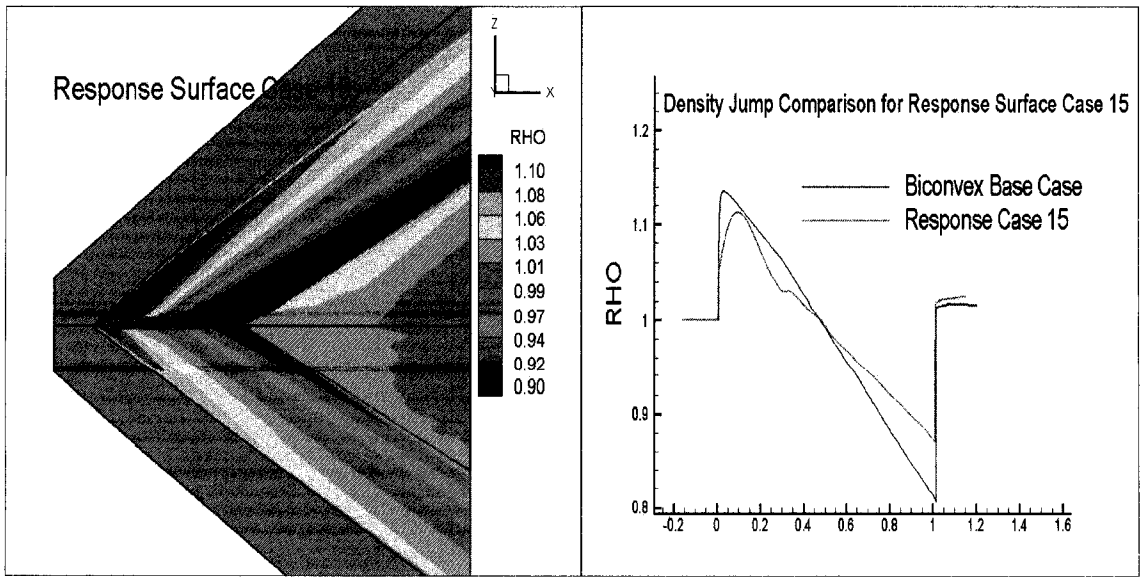

Fig 5.61 Response surface case 15 CFL3D

Figure 5.61 shows response surface case 15. Leading and trailing shock are of high strength due to high value of thickness ratio and low value of camber ratio. A density jump across the leading and trailing shock is also plotted in right side of Fig 5.61 and compared to the biconvex surface shock strength.

CASE 16: Nose Angle = 5 deg, Thickness = 3.0 %, Camber = 0.5 %, Dihedral = 20

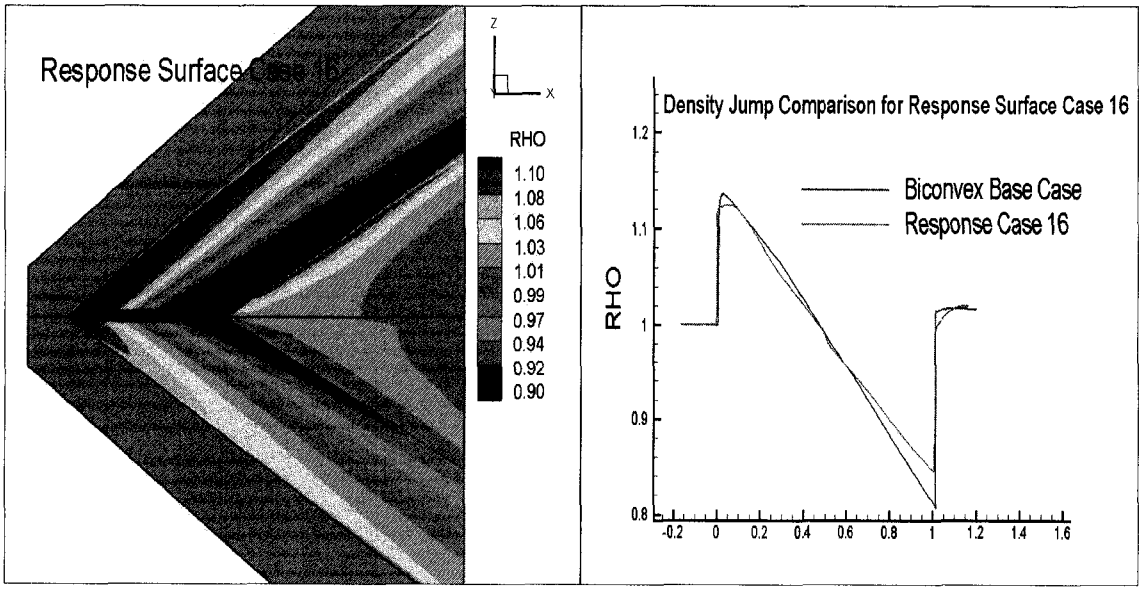

Fig 5.62 Response surface case 16 CFL3D

Figure 5.62 shows response surface case 16. It is discovered that dihedral has less influence on peak shock amplitude as compared to thickness and camber and thus having a very high value of dihedral angle also doesn't help much in reducing the peaks of the shocks. A density jump across the leading and trailing shock is also plotted in the right side of Fig 5.62 and compared to the base case of biconvex shape delta wing.

5.7.2 Optimization Result for AOA = 0 deg CFL3D

Once the design point response surface data is obtained Design Expert software is used to carry out the optimization study. CFD input data for the response surface input is listed in Table 5.1. The response surface for two objectives is obtained for sonic boom and aerodynamics performance. As observed with these16 response surface cases, low values of maximum thickness ratio and nose angle lead to lower shock strength whereas higher

values of maximum camber ratio and dihedral angles produce lower strength leading and trailing shock.

Case No.	Nose Angle	% Thickness	%Camber	Dihedral Angle	RHO	Cl/Cd
1.	2.0	1.5	1.5	0.0	1.07264	1.3872
2.	5.0	1.5	1.5	0.0	1.14800	0.0104
3.	2.0	1.5	0.5	0.0	1.07340	-0.8335
4.	5.0	3.0	1.5	0.0	1.15800	-0.26183
5.	5.0	1.5	0.5	0.0	1.15300	-0.91505
6.	2.0	3.0	0.5	0.0	1.21100	-0.20041
7.	2.0	3.0	1.5	0.0	1.11400	0.27411
8.	5.0	3.0	0.5	0.0	1.15900	-0.67159
9.	2.0	1.5	1.5	20.0	1.05520	1.33773
10.	5.0	1.5	1.5	20.0	1.14000	0.68051
11.	2.0	1.5	0.5	20.0	1.05700	0.61657
12.	5.0	3.0	1.5	20.0	1.11380	0.56501
13.	5.0	1.5	0.5	20.0	1.11500	0.08438
14.	2.0	3.0	0.5	20.0	1.21000	0.64897
15.	2.0	3.0	1.5	20.0	1.11300	0.05226
16.	5.0	3.0	0.5	20.0	1.12400	0.29597

Table 5.1 Response surface cases for zero degree AOA

Constraints

Name	Goal	Lower Limit	Upper Limit	Lower Weight	Upper Weight	Importance
Thickness	is in range	1.5	3	1	1	3
Camber	is in range	0.5	1.5	1	1	3
Nose Angle	is in range	2	5	1	1	3
Dihedral Angle	is in range	0	20	1	1	3
Boom Level	minimize	1.0552	1.211	1	1	5
L/D	maximize	-0.91505	1.3872	1	1	5

Solutions

Number	Thickness	Camber	Nose Angle	Dihedral Angle	Boom Level	L/D	Desirability	
1	1.50	1.50	2.00	19.80	1.05538	1.33822	0.989	Selected
2	1.50	1.50	2.00	19.05	1.05603	1.33965	0.987	
3	1.50	1.50	2.00	19.46	1.05584	1.33522	0.987	
4	1.50	1.50	2.00	18.65	1.05638	1.34107	0.986	
5	1.50	1.48	2.00	19.97	1.05526	1.32315	0.986	
6	1.50	1.50	2.02	19.57	1.05622	1.33351	0.985	
7	1.50	1.50	2.00	17.08	1.05775	1.34486	0.983	
8	1.50	1.45	2.00	20.00	1.0553	1.29947	0.980	
9	1.50	1.50	2.05	19.14	1.05747	1.32744	0.980	
10	1.51	1.50	2.00	16.30	1.05867	1.34126	0.979	

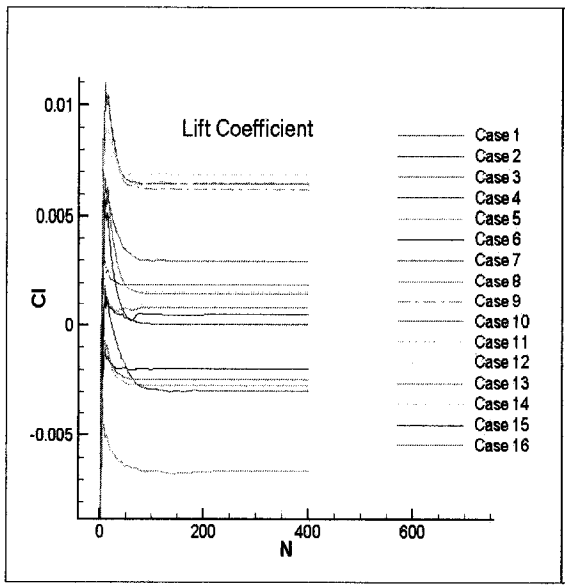

Fig 5.63 Response Surface Lift Coefficient

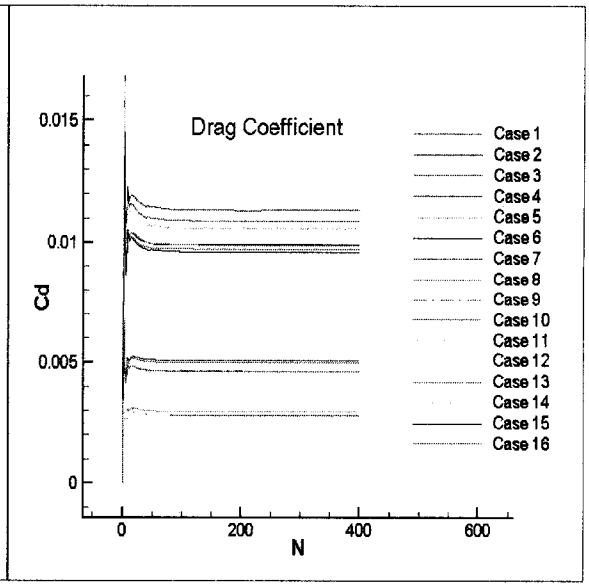

Fig 5.64 Response Surface Drag Coefficient

Optimization results are obtained considering two objectives of minimization of sonic boom ground signature and maximizing the L/D ratio. Both the objectives are given an equal importance. The response surface for low boom is created based on the shock strength (density amplitude) in near field. The second response surface for maximizing the aerodynamics performance is created by the ratio of lift to drag coefficient. Variation

in life coefficient along the response surface is shown in Fig 5.63. Variation in drag coefficient along the response surface is shown in Fig 5.64.

Response surface data points are taken from CFD runs. While carrying out optimization we have the freedom to choose the dependency of various design variable independent and coupled effects. It also indicates the positive and negative effect of these design variables on the objectives. Results from optimization recommend using the lowest nose angle and thickness ratio and a high value for camber ratio for keeping the lift to drag ratio high and overpressure low. The best optimum case is found not to be the case of maximum lift of minimum drag. For this case the optimization has further shown that the case with maximum thickness ratio = 1.5 %, maximum camber ratio = 1.5 %, nose angle = 2.0 deg. and dihedral angle = 19.80 deg is the best choice for high L/D and low overpressure.

Figure 5.65 shows the comparison of density contour for biconvex and optimized delta wing. In comparison with the overpressure of the original biconvex delta $C_p = 0.07$ wing the overpressure of the optimized delta wing is decreased to $C_p = 0.0269$. This represents a 61.57 % decrease in the sonic boom level. Fig 5.66 and Fig 5.67 shows the comparison of the overpressure with the optimized delta wing and original biconvex delta wing.

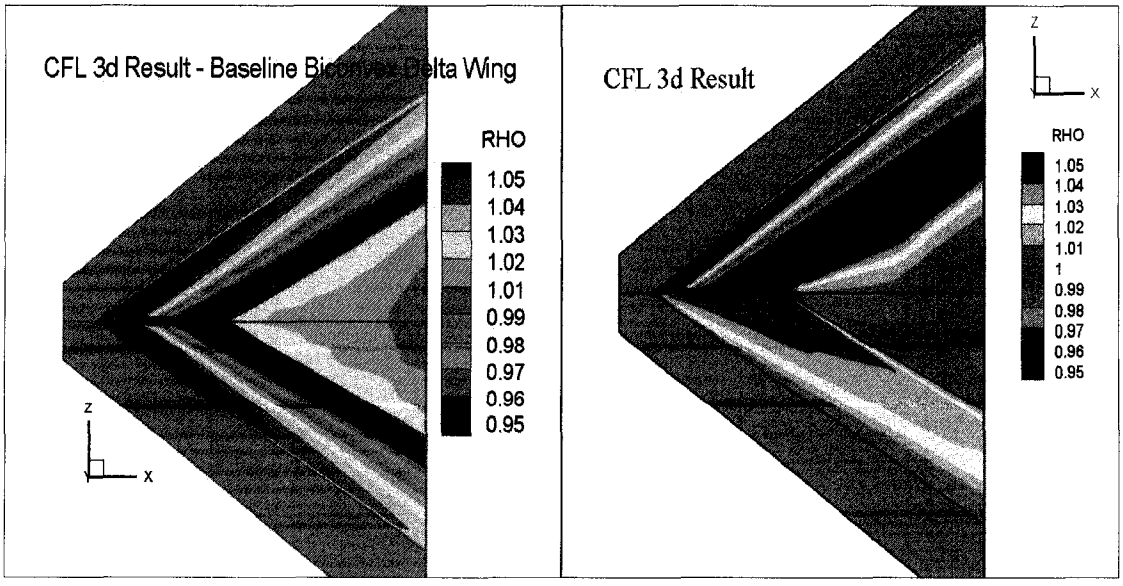

Fig 5.65 Density Contour Biconvex Vs Optimized Delta Wing at AOA = 0 deg

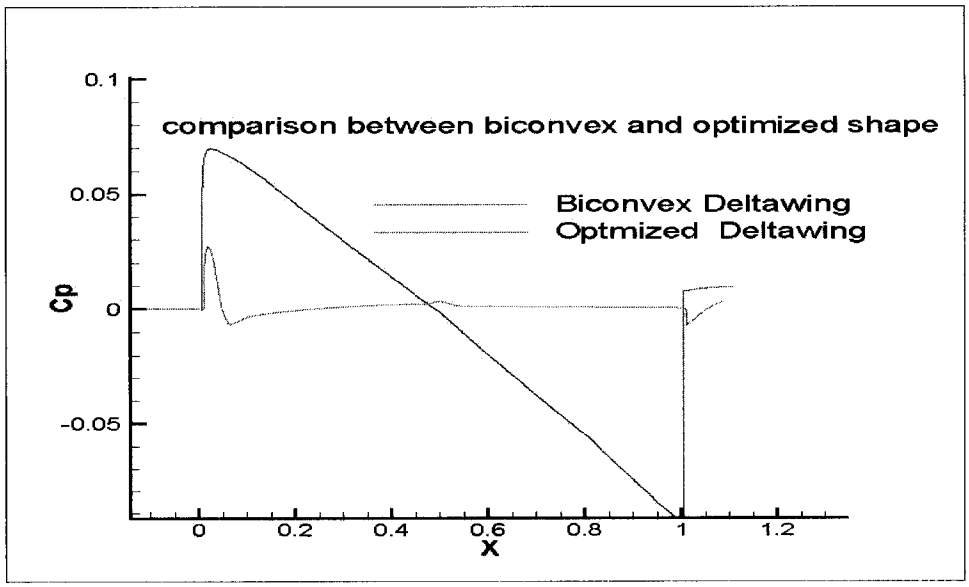

Fig 5.66 Optimized Delta Wing Vs Biconvex Wing for AOA = 0 deg.

Fig 5.67 shows the optimized case for minimum sonic boom (Nose Angle=2 deg, Thickness=1.5 %, Camber =1.5 %, Dihedral =19.80 deg). As shown in the figure only considering three design parameter excluding the dihedral can result in a lower decrease in sonic boom level. Including dihedral the overpressure and hence boom reduction is increased by 11.57%. The study conducted at zero angle of attack does not produce any lift for biconvex wing however within the design domain the loss in aerodynamic performance measured in term of C_l/C_d lift to drag ratio is found to be about 3.566 % with the best Cl/C_d.

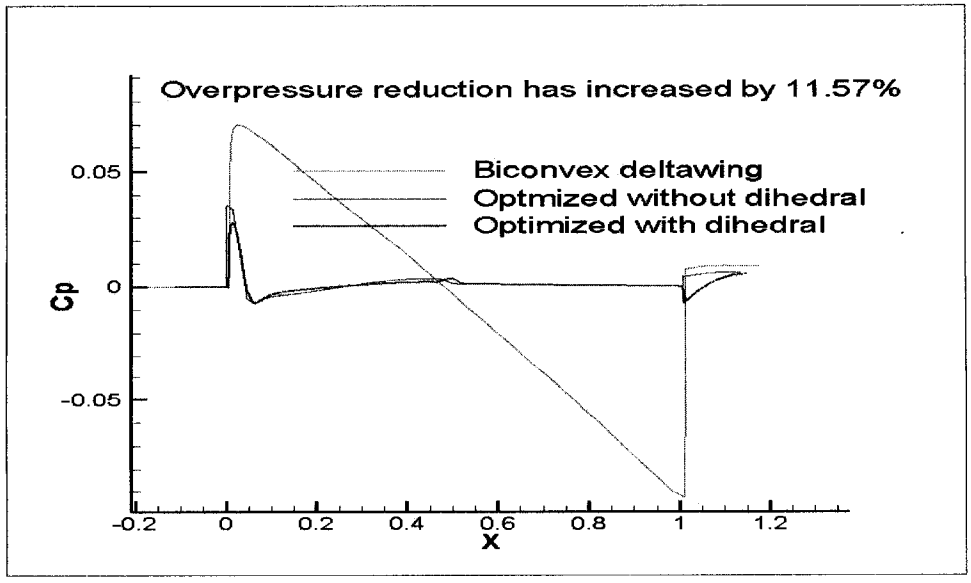

Fig 5.67 Optimized shape vs. Biconvex Shape CFL3D

5.7.3 Desirability Study for AOA = 0 deg

A desirability study has also been conducted keeping in mind the objectives and research goal. In Fig 5.68, desirability contour for camber and thickness shows that the region on the top left is most desired for the current goal. This in term suggest having a higher values of camber toward 1.5% and lower values of thickness lesser than of equal to 1.5%.

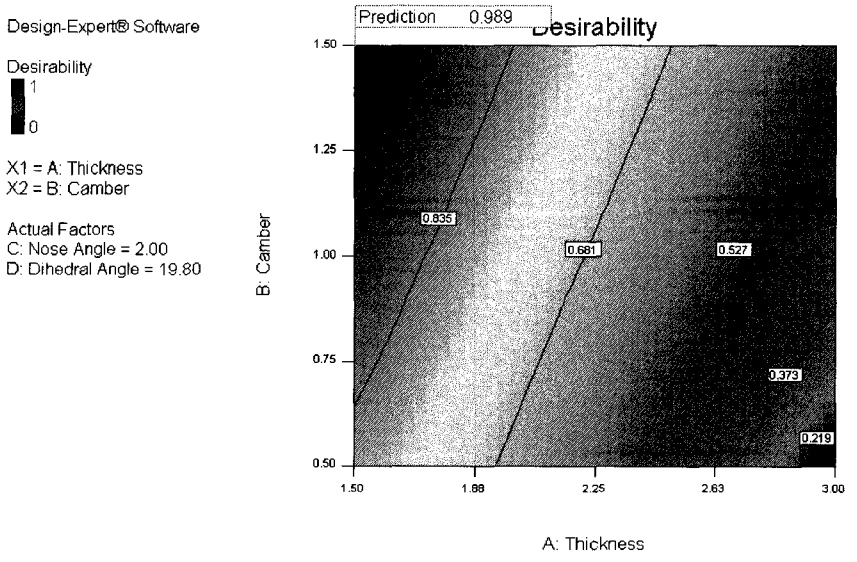

Fig 5.68 Desirability Study for Zero deg AOA

A desirability study for the boom level also suggests having a higher values of camber and lower values of thickness. As show in Fig 5.69 the minimum boom value lies in the region top left.

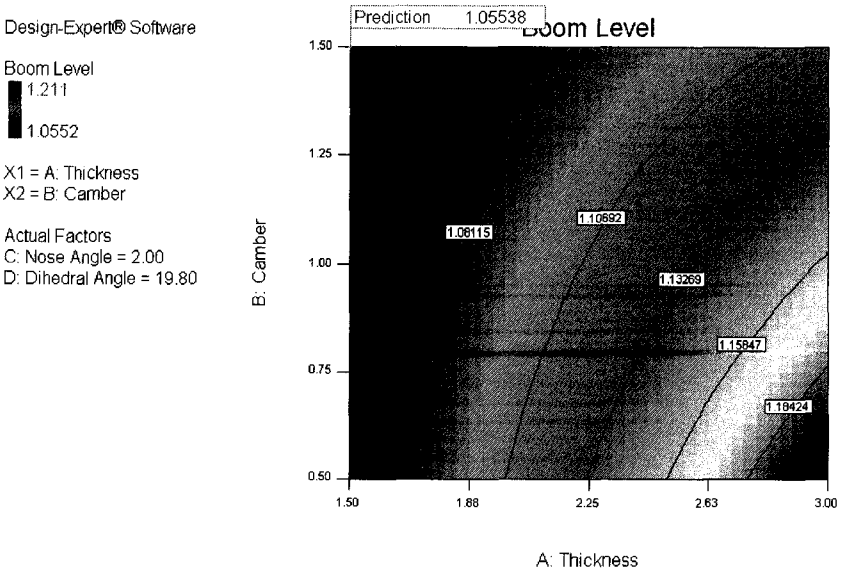

Fig 5.69 Desirability Study for Zero deg AOA

A desirability study for the lift to drag ratio also suggests having a higher values of camber and lower values of thickness. As shows in Fig 5.70 the max L/D value lies in the top left region. A desirability study for the lift to drag ratio for dihedral and nose angle suggests having a higher values of dihedral and lower values of nose angle. As shows in Fig 5.71 the max L/D value lies in the top left region.

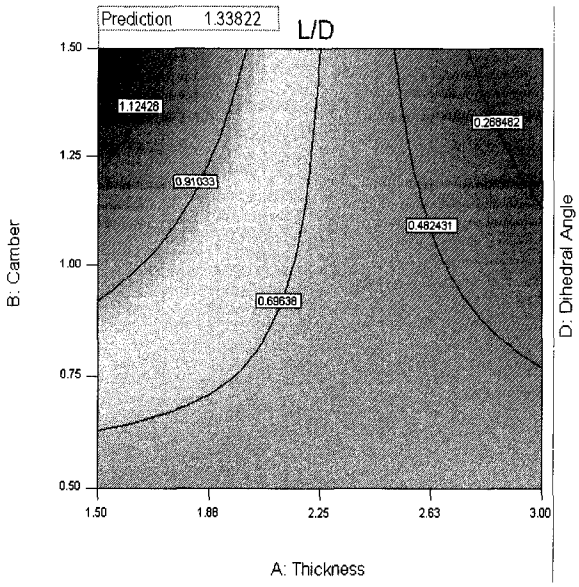

Fig 5.70 Desirability Study for L/D

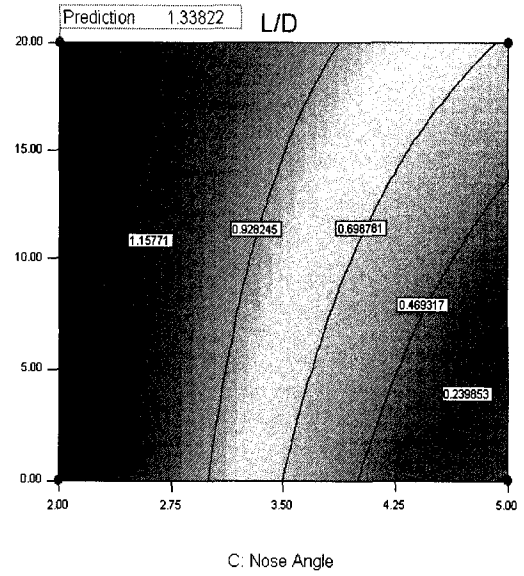

Fig 5.71 Desirability Study for L/D

Overall desirability also shows that having higher values of dihedral and lower values of nose angle. As shown in Fig 5.72 the desirability for the study lies in the top left region.

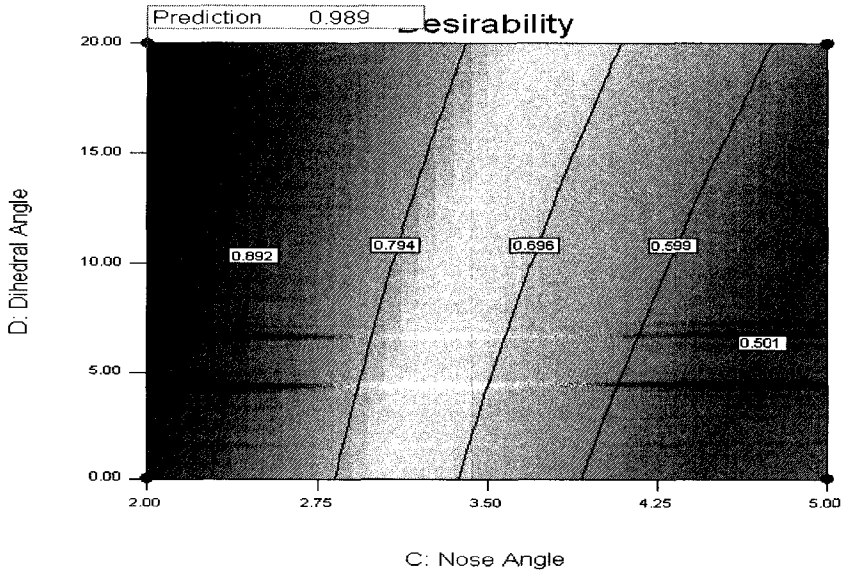

Fig 5.72 Desirability Study for Zero deg AOA

5.8 Boom Mitigation with FUN3D

Flow over the base line geometry of biconvex delta wing geometry is also solved on an unstructured grid using FUN3D [32] software. Gridgen software [33] is used to generate the unstructured mesh, in some cases ICEM CFD [84] and CFX mesh [84] is also used to generate the unstructured mesh. Grid adaptation to fit the leading shock and trailing shock is done using Optigrid software from Newmerical incorporation [78]. For all unstructured mesh at least grid size of 1.2 million is used for CFD computation.

5.8.1 Grid Adaptation for Unstructured Grid System

FUN3D support the gradient based adaptation strategies. In addition to inherent adaptation capability of FUN3D, external software can also be used in conjunction with FUN3D for grid adaptation purposes. Figure 5.73 shows the unstructured mesh without adaptation. Most of the unstructured meshes are generated using Gridgen software.

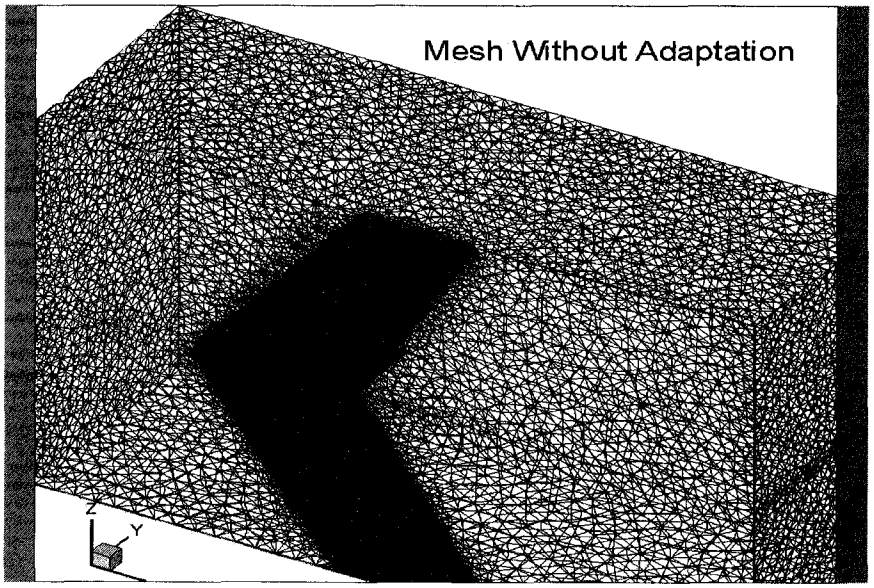

Fig 5.73 Unstructured mesh without adaptation

FUN3D provides multiple adaptation strategies to suit the user an automated ability to improve a computational mesh for a particular application. Some of the adaptation methods implemented in FUN3D solvers are

1. Mesh Movement Gradient-Based Adaptation
2. Full Gradient-Based Adaptation

3. Mesh Movement via Spring Analogy,
4. Mesh Movement via Frequency Analogy

The spring adaptation capability, integrated into the FUN3D solver, is a simple tool that can provide clustering of points to a shock for a relatively well designed initial mesh. A gradient-based adaptation capability that allows for node insertion and deletion, node movement, and edge swapping has been developed for FUN3D. Gradient-based adaptation method has some convenient parameters which user can choose to adapt the solution in the unstructured mesh.

Figure 5.74 shows the improvement in adapted mesh with increasing number of iteration of Optigrid [78] with FUN3D. Optigrid can be made to run number of times with FUN3D until the desired accuracy in adapting the solution on the mesh is achieved. It is observed in most of the cases four main iteration of Optigrid [78] is sufficient to adapt and fit the shock with unstructured mesh.

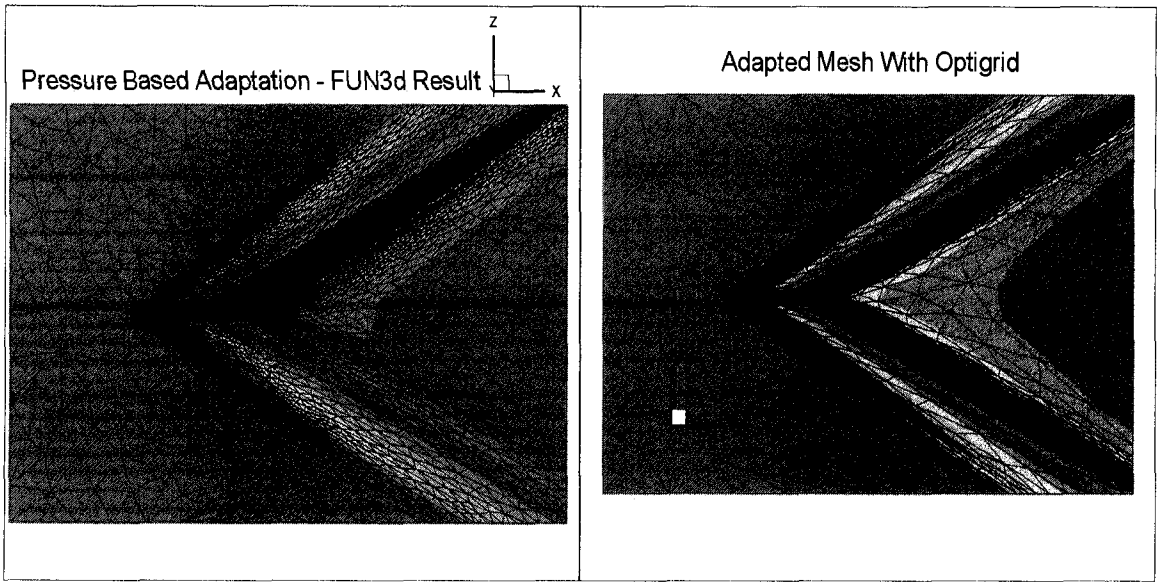

Fig 5.74 Density Contour with higher adaptation iteration

Figure 5.75 shows the 3D adapted meshes on biconvex delta wing. The grid clustering is very high on shock locations as clearly seen from Fig 5.75. With adapted mesh result are improved significantly with lesser number of grid points. Optigrid has option for adapting the mesh with node movement only, node movement, refinement and coarsening and full mesh optimization with swapping.

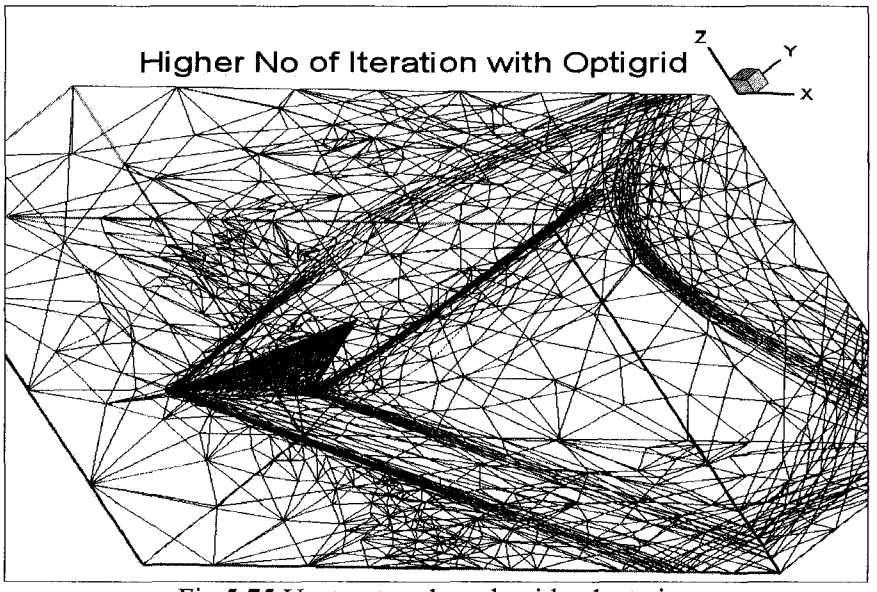

Fig 5.75 Unstructured mesh with adaptation

The number of main pre iteration runs for most of the cases is 5 to 8 and post iteration is 2. Maximum edge swapping iterations are limited to 3. Node movement convergence criterion is kept to 0.001. The tetra growth rate is kept to 1.2. It's possible in Optigrid to freeze the boundary surface for adaptation i.e. not to adapt the solution.

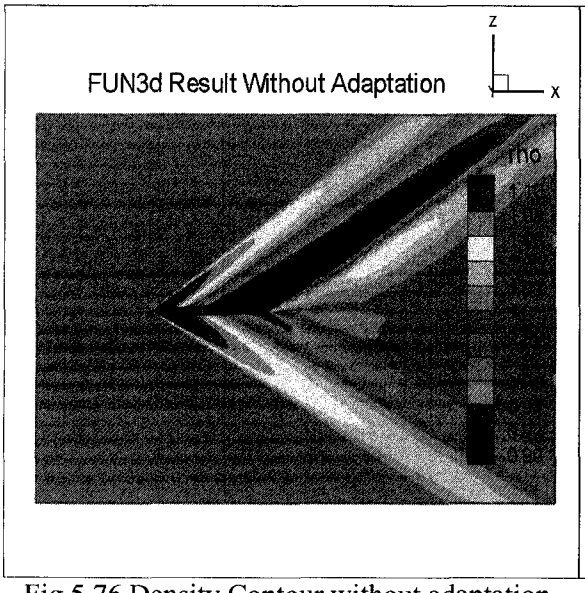

Fig 5.76 Density Contour without adaptation

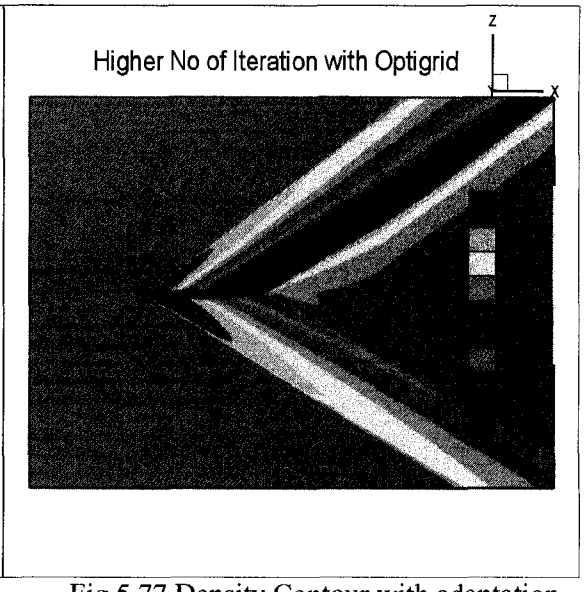

Fig 5.77 Density Contour with adaptation

Figure 5.76 shows the density contour without the grid adaptation and Fig 5.77 shows the density contour with adapted mesh. Shocks are clearly visible strong far from the delta wing in the case of adapted grid computation.

5.8.2 FUN3D and CFL3D Results Comparison

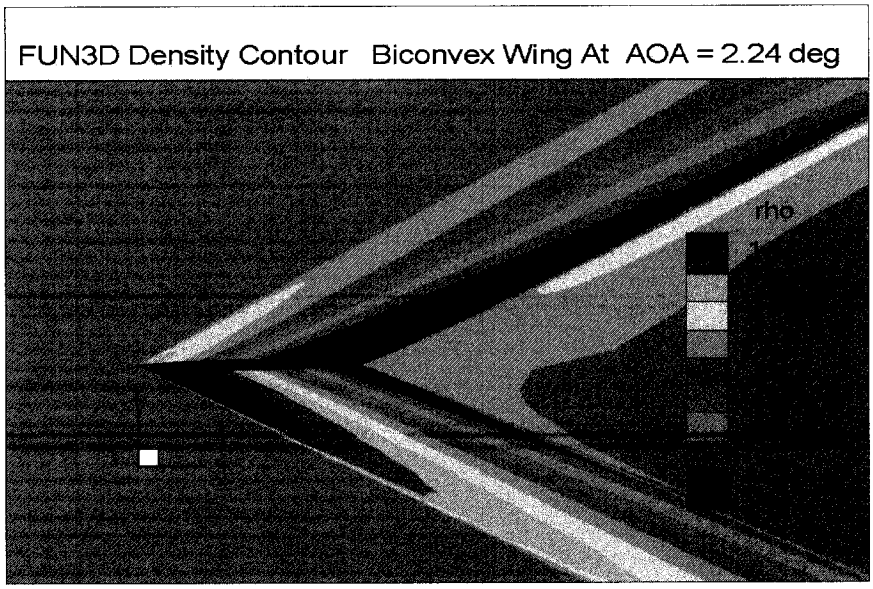

Fig 5.78 FUN3D near Field Density Contour

Figure 5.78 shows the density contour of the baseline biconvex delta wing geometry. Near field solution shows good match with the result obtained with CFL3D [30].

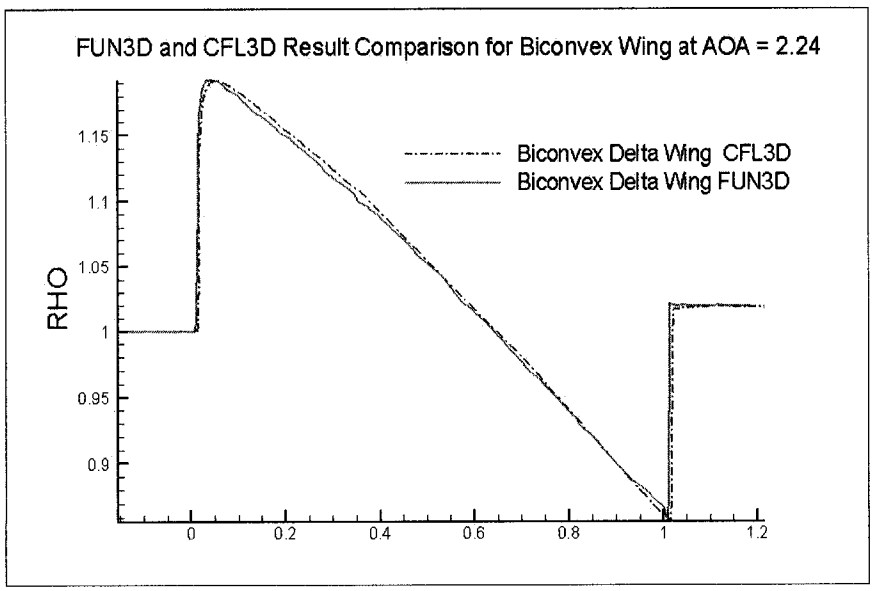

Fig 5.79 FUN3D comparison with CFL3D for biconvex wing at AOA = 2.24 degree

As observed earlier from CFL3D [30] near field solution a strong leading and trailing shocks. The wing is flying at Mach number 2.0 and biconvex delta wing profile is considered to carrying out the simulation. Figure 5.79 shows the density jump comparison of FUN3D with CFL3D for base case of biconvex delta wing. The density

jump shows good match of the results obtained by CFL3D and FUN3D solver for the biconvex delta wing at a 2.24 degrees of angle of attack.

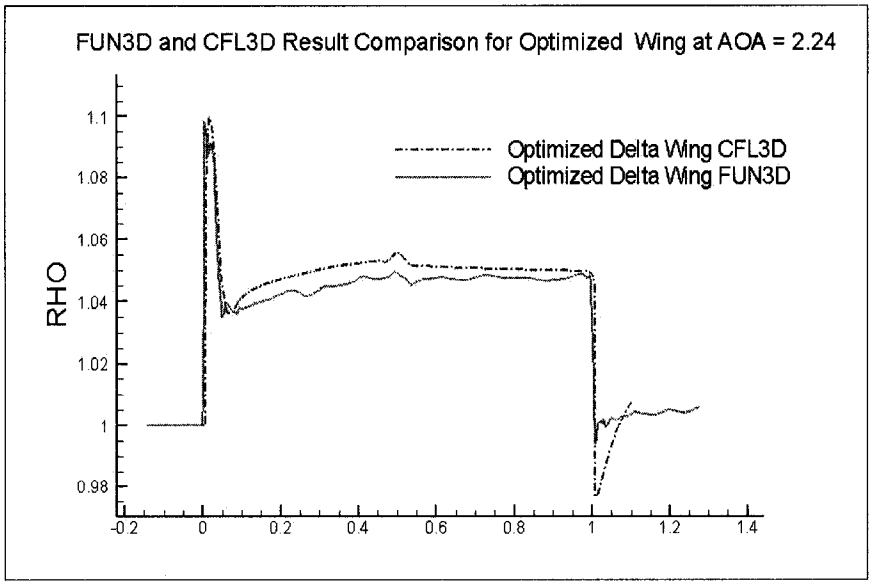

Fig 5.80 FUN3D Comparison with CFL3D for optimized wing at AOA = 2.24 degree

A similar comparison is also made for the optimized wing case in order to validate the results with each other i.e. with FUN3D and CFL3D solver. Figure 5.80 shows the density jump for optimized wing geometry for AOA = 2.24 degree case.

Leading shock peak has an excellent match with the CFL3D result but overall density signature is little lower as compared to CFL3D because of limitation of high density mesh at lower surface of optimized wing. During grid adaptation Optigrid [78] looks for high gradient of flow variables and adapt the flow with higher number of cells and at lower surface the flow parameters are almost constant and hence result in poor grid density at lower surface of the optimized wing.

5.8.3 Optimization Result for AOA = 2.24 deg

CFD input data for the response surface for angle of attack = 2.24 deg is listed in Table 5.2. A similar observation has been made as in case of zero degree angle of attack study that low values of maximum thickness ratio and nose angle lead to lower shock strength whereas higher values of maximum camber ratio and dihedral angles produce the lowest leading and trailing shock.

Case No.	Nose Angle	% Thickness	%Camber	Dihedral Angle	RHO	Cl/Cd
1.	2.0	1.5	1.5	0.0	1.11856	11.6106
2.	5.0	1.5	1.5	0.0	1.19432	10.5510
3.	2.0	1.5	0.5	0.0	1.13363	10.9144
4.	5.0	3.0	1.5	0.0	1.22320	5.35031
5.	5.0	1.5	0.5	0.0	1.20611	13.4887
6.	2.0	3.0	0.5	0.0	1.27576	5.77991
7.	2.0	3.0	1.5	0.0	1.17764	5.57550
8.	5.0	3.0	0.5	0.0	1.22376	11.5853
9.	2.0	1.5	1.5	20.0	1.09967	14.3035
10.	5.0	1.5	1.5	20.0	1.14854	6.12744
11.	2.0	1.5	0.5	20.0	1.10537	14.3406
12.	5.0	3.0	1.5	20.0	1.17276	6.13030
13.	5.0	1.5	0.5	20.0	1.16800	6.11323
14.	2.0	3.0	0.5	20.0	1.30544	5.86276
15.	2.0	3.0	1.5	20.0	1.15080	6.18772
16.	5.0	3.0	0.5	20.0	1.17635	10.7865

Table 5.2 Response surface cases for 2.24 degree AOA

Once the response surface is created after feeding the number of CFD run, one can conduct the optimization study. Result obtained from optimization study shows that having a thickness ratio = 1.5%, camber =1.5, nose angle = 2deg and dihedral angle =19.88 degree gives the best design for the objective set for the study. Shock strength measured in term of density jump and the aerodynamic performance is measured in terms of the ratio of lift to drag coefficient.

Constraints		Lower	Upper	Lower	Upper	
Name	Goal	Limit	Limit	Weight	Weight	Importance
Thickness	is in range	1.5	3	1	1	3
Camber	is in range	0.5	1.5	1	1	3
Nose Angle	is in range	2	5	1	1	3
Dihedral Angle	is in range	0	20	1	1	3

Boom Level	minimize	1.0996	1.30544	1	1	3
L/D	maximize	5.35031	14.3406	1	1	3

No.	Thickness	Camber	Nose Angle	Dihedral Angle	Boom Level	L/D	Desirability
1	1.50	1.50	2.00	19.88	1.09973	14.2855	0.997 Selected
2	1.50	1.35	2.00	20.00	1.10046	14.3088	0.996
3	1.50	1.31	2.00	20.00	1.10071	14.3106	0.996
4	1.50	1.12	2.00	20.00	1.10182	14.3177	0.993
5	1.50	1.10	2.00	20.00	1.10188	14.3181	0.993

Case number 1 is selected among the other solutions as it meets the desirability criteria with 99.7%. The leading shock density for optimization solution is 1.09973 with the ratio of lift to drag coefficient of 14.2855. There are of course other solutions with higher values of aerodynamics performance but they would increase the sonic boom level to undesired higher values as in the case of solution number 5.

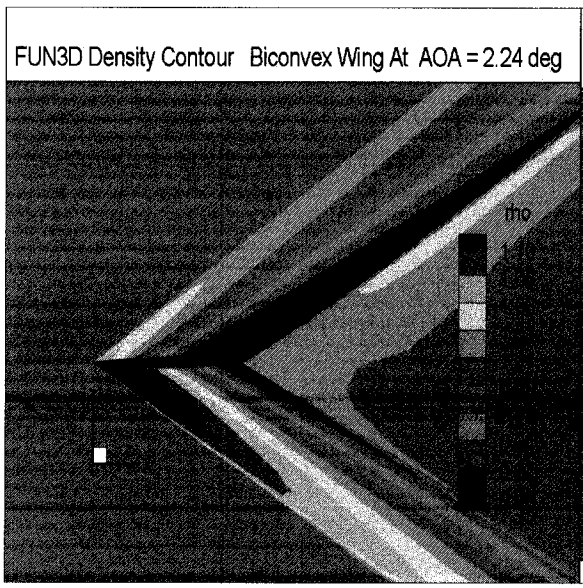

Fig 5.81 Density Contour Biconvex Wing

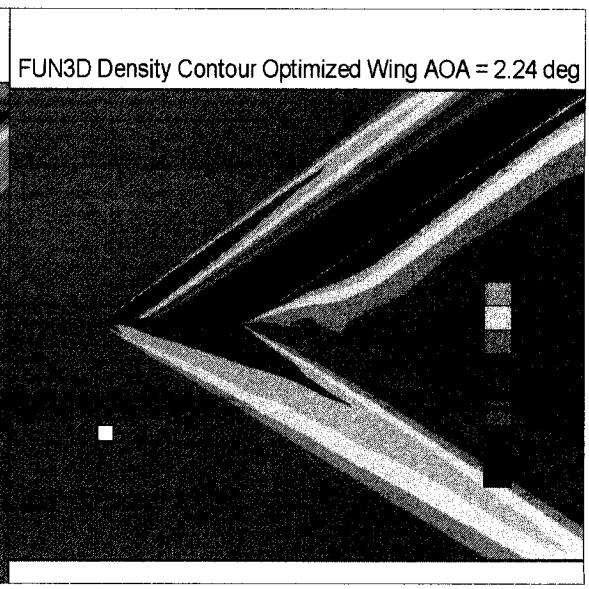

Fig 5.82 Density Contour Optimized Wing

Figure 5.81 shows the density contour for the base case biconvex delta wing for AOA = 2.24 deg. As seen from the contour there are much strong leading and trailing shocks are coming out from the lower surface of the wing as compare to the case of AOA= 0 deg. Figure 5.82 shows the density contour for the optimized delta wing shape at AOA=2.24.

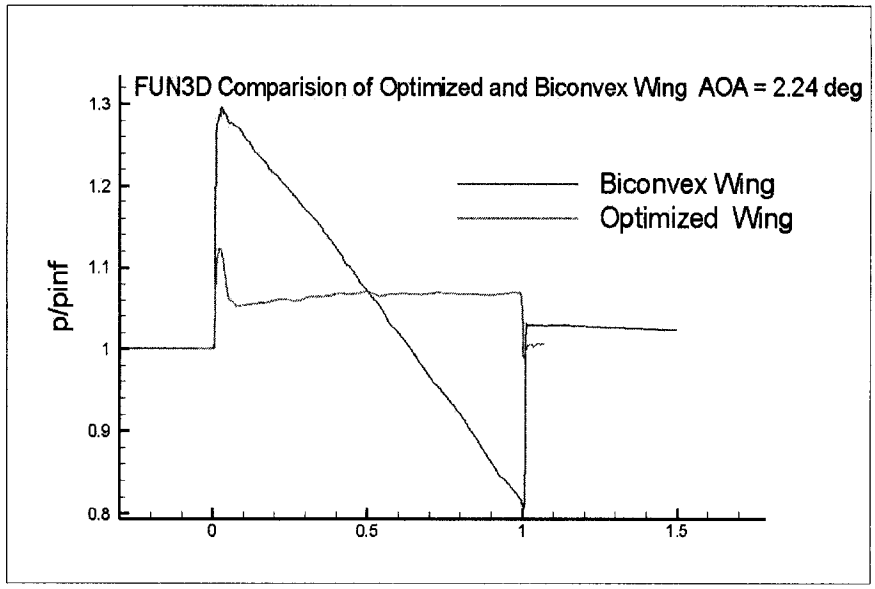

Fig 5.83 Pressure Jump - Optimized shape vs. Biconvex Shape

Figure 5.83 shows the comparison for change in pressure for biconvex delta wing and optimized delta wing. Figure 5.84 shows the near field density comparison. The Optimized geometry has a fat top density signature after the leading shock of the wing.

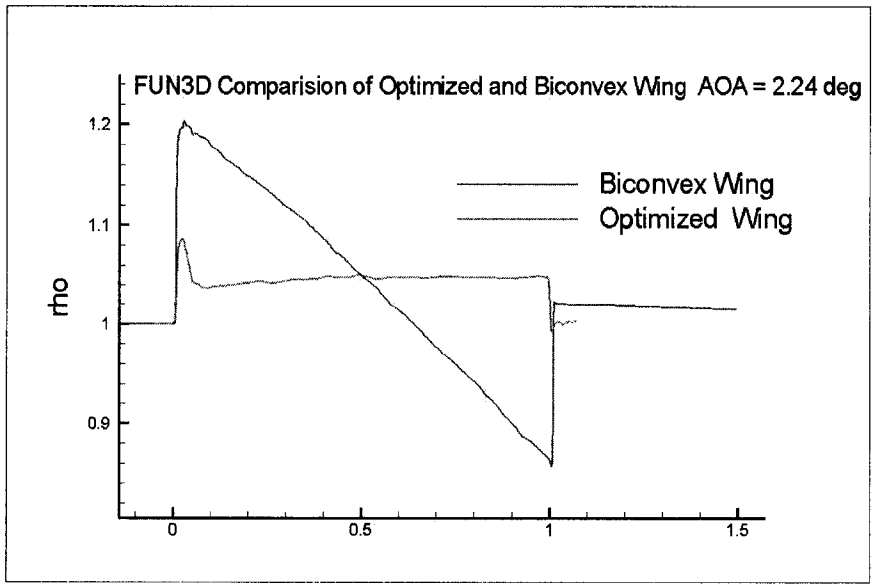

Fig 5.84 Density Jump - Optimized shape vs. Biconvex Shape

In comparison to the original biconvex delta wing the leading shock strength of the optimized wing has reduced by 64%.The trailing shock for optimized wing has almost disappeared Aerodynamic performance has not degraded as compared to the biconvex wing case with AOA = 2.24 degree. However within the design domain compared with the delta wing shape for the highest Cl/Cd, one looses about 1% of Cl/Cd.

5.8.4 Desirability Study for AOA = 2.24 deg

A study conducted for AOA =2.24 also shows that having a higher values of camber toward 1.5% and lower values of thickness lesser than of equal to 1.5% is most desired, keeping in mind the objectives and research goal. As shown in Fig 5.85, desirability contour for camber and thickness shows that top left region is most desired.

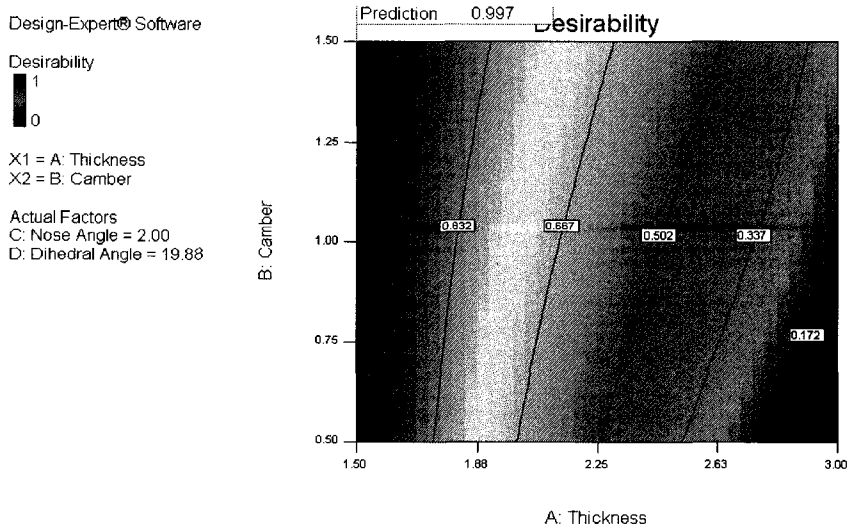

Fig 5.85 Desirability Study for 2.24 deg AOA

A desirability study for the boom level also suggests having a higher values of camber and lower values of thickness. As show in Fig 5.86 the minimum boom value lies in the region top left.

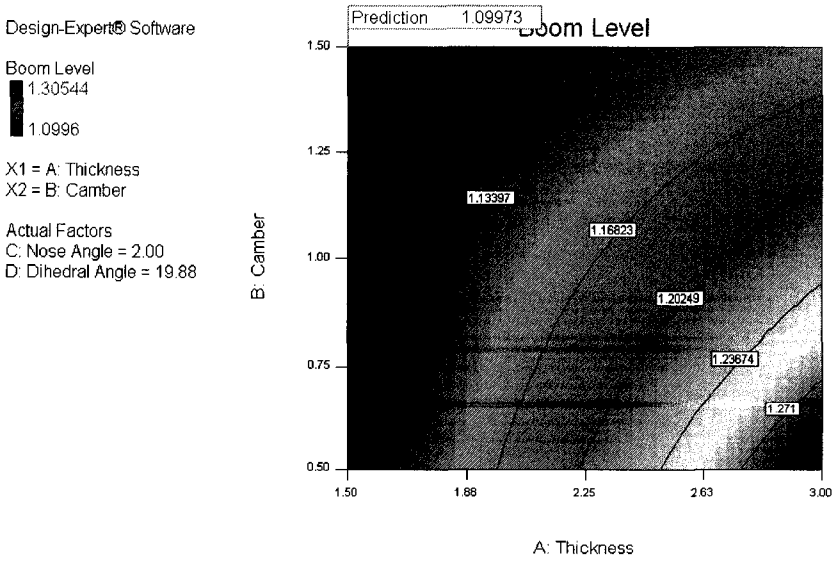

Fig 5.86 Desirability Study for 2.24 deg AOA

As shown in Fig 5.87 the max L/D value lies in the top left region. A desirability study for the lift to drag ratio for dihedral and nose angle suggests having a higher values of dihedral and lower values of nose angle. As shown in Fig 5.88 the min boom level lies in the top left region.

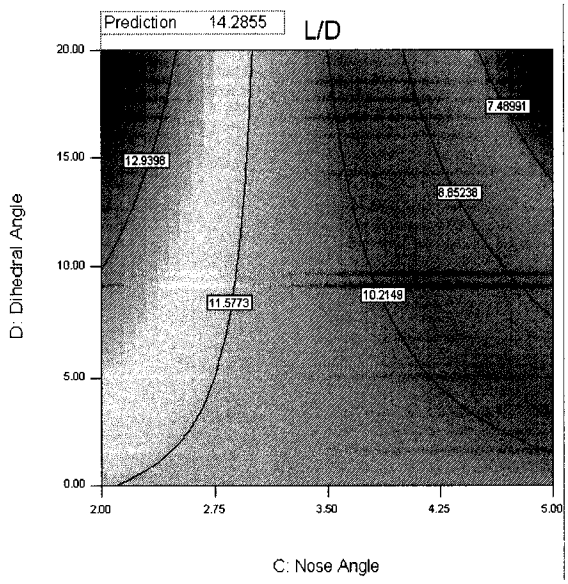

Fig 5.87 Desirability Study for L/D

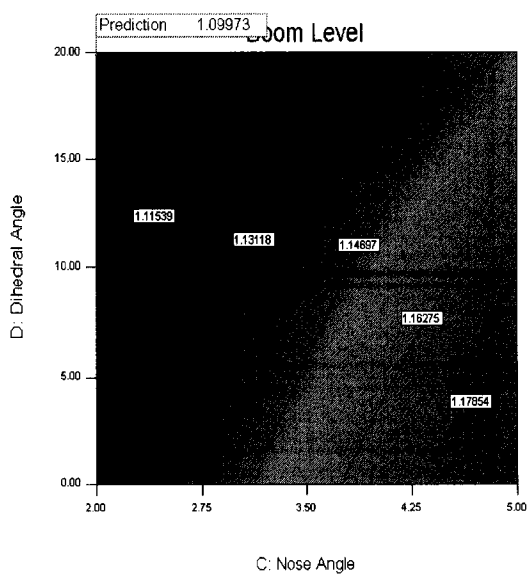

Fig 5.88 Desirability Study for Boom

As shown in Fig 5.89the max L/D value lies in the bottom left region. A desirability study for the lift to drag ratio for thickness and nose angle suggests having a lower values of thickness and lower values of nose angle. As shown in Fig 5.90 the min boom level lies in the bottom left region.

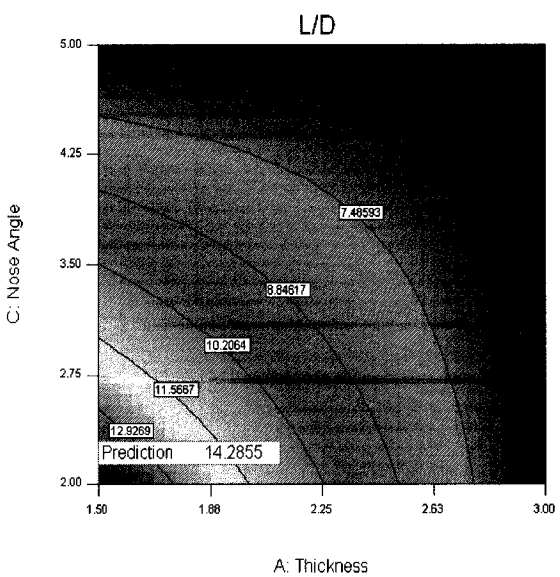

Fig 5.89 Desirability Study for L/D

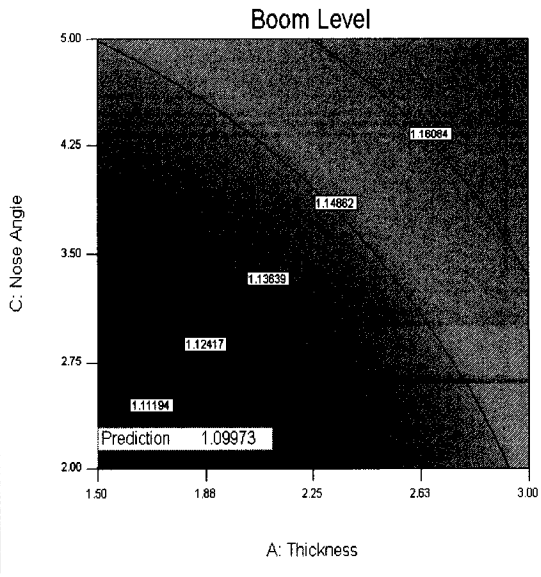

Fig 5.90 Desirability Study for Boom

As shown in Fig 5.91 the desired solution lies in the top left region for dihedral and nose angle study. A desirability study for the nose angle and thickness shows that having low values of both the parameter is desired for current research goal as seen in Fig 5.92. The desired region lies in bottom left of the Fig 5.92.

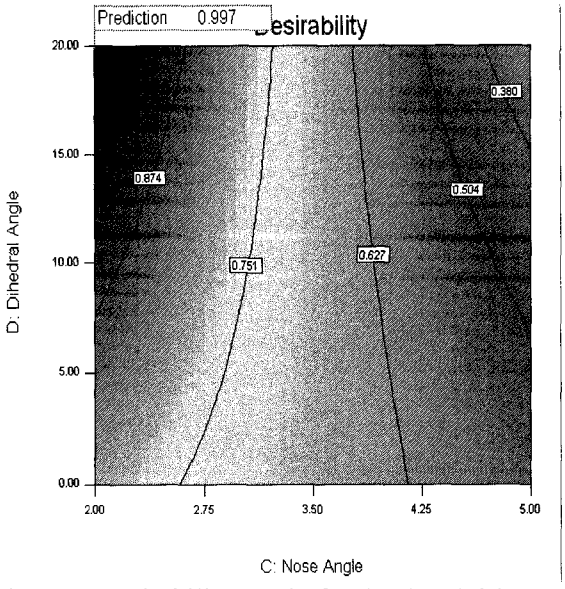

Fig 5.91 Desirability Study for AOA = 2.24

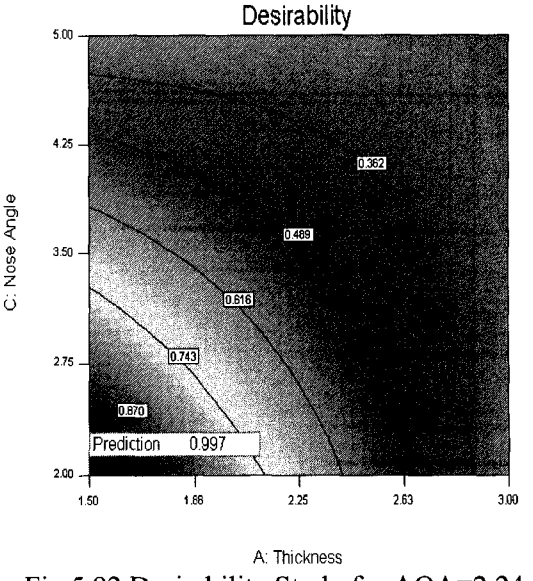

Fig 5.92 Desirability Study for AOA=2.24

5.9 Far Field Propagation

Far field computations are carried out to find out the impact of sonic boom on the ground. Non linear compressible full potential code [31] is used for computing the sonic boom ground signature. Full potential code includes the atmospheric non linearity effects and predicts the ground sonic boom signature with higher accuracy over the linear propagation methods [36].

Although due to the computational time and resource limitation Thomas code [36] is used for carrying out the sonic boom propagation for the optimized wing. Linear ray-tracing propagation codes represent state-of-the-art technology, and also shown excellent comparison with the full-potential propagation code. Figure 5.93 shows the overpressure at 40,000 ft and the ground overpressure with solid red line. Figure 5.93 also shows the overpressure ratio at 500 ft which is considered as ground level for the current research purposes.

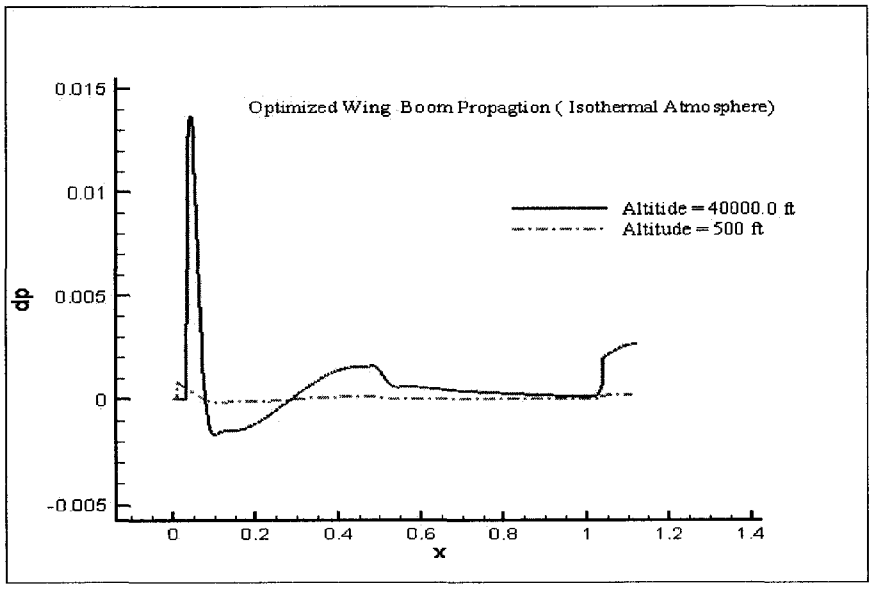

Fig 5.93 Overpressure Comparison with Ground

Figure 5.94 shows the variation of leading shock strength with altitude. As seen from Fig 5.94 most of the shock dissipates to lower strength values in the upper atmosphere at an altitude of 40,000 ft and 30,000 ft. and after a certain altitude the strength of the shock changes at a very slow rate. The far-field solution was obtained using the Thomas ray code for quick estimate of the ground overpressure. Ground pressure signatures calculated by the ray-tracing code are sensitive to starting locations

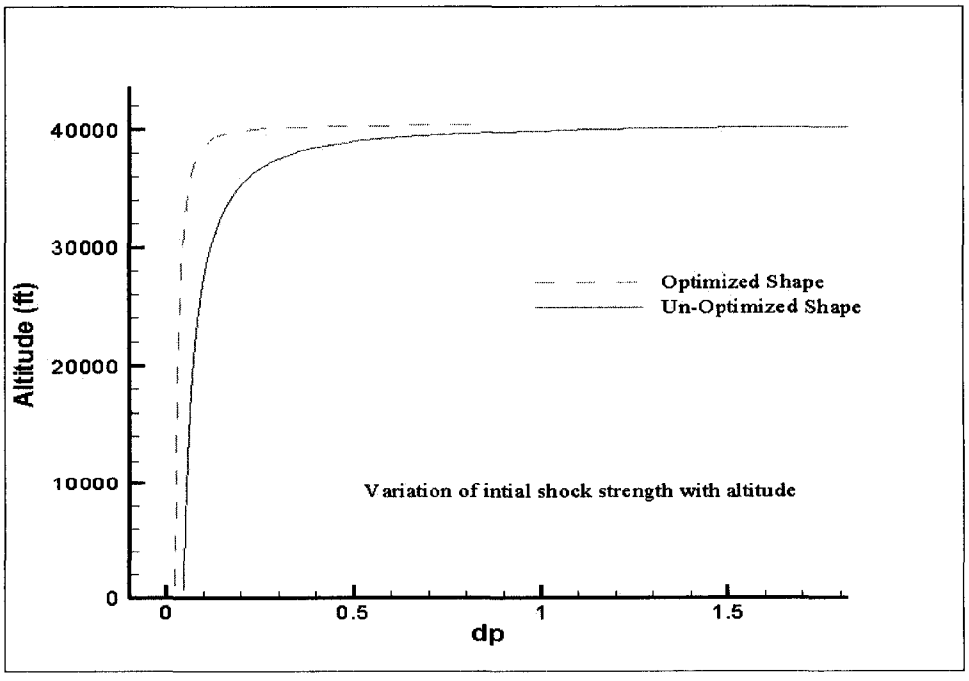

Fig 5.94 Sonic boom propagation through atmosphere

Detailed three-dimensional flow-field features in near field cannot, in general, be replicated by linear ray-tracing codes, so accuracy of propagated signatures will suffer. In some cases finding a starting location where the ground signature is less sensitive to changes and then switching to the ray-tracing codes may significantly save computational time with enhanced accuracy in predicting the boom ground impact. In Fig 5.94 the shock strength variation is also compared with the optimized shape and base line profile of biconvex delta wing shape.

5.10 Summary Mitigation and Optimization Study

Base line geometry of biconvex delta wing is considered for shape optimization to be able to mitigate sonic boom ground signature. The design parameters considered for shape optimization are wing thickness ratio, wing camber ratio, front lower surface wing nose angle and dihedral angle. Optimal shape design for low sonic-boom ground signature and the least degradation effect on the aircraft aerodynamic performance are the main goals of the present work. A multi objective optimization study carried out with AOA= 0 deg and AOA = 2.24 deg.

The individual effect of all the design parameters are show that having a lower bound value for maximum thickness ratio and nose angle is favorable for low boom design. For maximum camber ratio and dihedral its other way around and having higher values lead in favor of mitigating the boom impact in the ground. Least boom effect measured with 2 deg of nose angle, 1% of maximum thickness ratio for lower surface, maximum camber ratio of 2.0 % of the chord at the mid chord and 19.80 degree of dihedral angle for zero degree angle of attack case. The reduction leading shock strength is found to be about 61.57 % with about 3.566% loss in lift compared to best lift case.

For angle of attack study at AOA = 2.24 degree, the optimized parameters are 2.0 deg of nose angle, 1% of maximum thickness ratio for lower surface, maximum camber ratio of 2.0 % of the chord at the mid chord and 19.88 degree dihedral angle. The reduction leading shock strength is found to be about 64 % with about 1.0% loss in lift compared to best lift case within the design domain.

CHAPTER 6
CONCLUSIONS AND RECOMMENDATIONS FOR FUTURE WORK

In this chapter conclusions are drawn from the results obtained for sonic boom focusing prediction and sonic boom mitigation studies for delta wing geometry. Prediction results for wave focusing problem have improved with a conservative approach. Results obtained for mitigating the ground boom overpressure show promising design changes that can address the requirements of the FAA [11] for supersonic business jet development. In the end of the chapter 6 recommendations are made for sonic boom focusing and shape optimization research. Delta wing geometry parameters maximum thickness, maximum camber, lower surface nose angle and dihedral angle are considered as the dominant factors for the shape optimization study.

6.1 Summary - Sonic boom focusing

The nonlinear Tricomi equation has been solved for the sonic boom focusing prediction using a conservative type differencing scheme. Numerous types of incoming waves were simulated including an N-wave, a Concorde aircraft wave, asymmetric and symmetric incoming wave. Super boom of all these incoming signals at caustic surfaces have been predicted successfully. Boom prediction results obtained from conservative approach also validated against available solutions for linear and non linear cases [39, 50-52]. Linear case and non linear case of shock wave focusing validation show an excellent match with the magnitude of the wave amplification and location of caustics surface.

Parametric study has been carried out to investigate the effects of several parameters on the sonic-boom focusing. A numerous factors which can affect the focusing are considered among which location of boundary, footprint width and shock strength, type of input signal and effect of number of grid point are given importance. The first parameter is the effects of the longitudinal boundary size of the computational domain along with the locations of the boundaries. The results show that this parameter has

negligible effect on the sonic-boom focusing. The second investigated parameter is the effects of the lateral size of the computational domain along with the locations of the boundaries. The results show that this parameter has some effects on the sonic-Boom focusing within the investigated range of Z values.

The nonlinear parameter atmospheric viscosity μ is assumed to be constant and taken as 0.08. The criterion of convergence is kept to check on the residual or total error of the previous iteration and the current iteration. The simulation is run for 20000 time steps on a structured grid of 1000x8192 in z and τ direction respectively. The residual errors are minimized to the level of $10E^{-12.}$. The number if grid points in τ direction should not be less than 8192 in order to capture the focusing phenomenon accurately.

6.2 Conclusions – Sonic Boom Focusing and Parametric Study

Amplification of wave and the location of the caustic surface where amplification occurs is found to be very sensitive to shock strength and shape of incoming wave. Strength of the input shock wave is the dominant factor of the amplitude of focusing at caustic surface. Higher shock strength result in much amplified focused boom. It's also observed that the amplification is lesser in the case of ramp input wave as compare to straight N wave case. The N wave peak pressure is 2.896 and the caustic location at 0.137 and the ramp type case has the peak pressure of 1.172 and the caustic location at 0.205.

A similar observation has been made for the different type of asymmetric and symmetric type wave input. As observed in the super boom solution shock waves are bounced back in the illumination zone and die out in shadow zone after the z location -1.5 in all type of input waves. It has also been validated that merging happens just above the ground at caustic line. Numerical results obtained by conservative approach also satisfy the Guirad's scaling law [12]. Atmospheric turbulence effects have not been taken care and are expected to further decay the shock amplification due to the atmospheric turbulence. Grid independence is achieved in all computed case with convergence. Convergence and the grid independent test are also considered as a part of validation study.

Further in order to identify the parameter which can significantly affect the magnitude of amplification and location of caustic surface, a parametric study [76] is carried out. For the validation of computational domain the effect of top and bottom boundary and left and right boundary is investigated. The computational result for left and right boundary location does not show any appreciable change for magnitude of amplification and location for surface of amplification. For top and bottom boundary, changes with lower boundary are almost negligible but enlargement of upper boundary shows increase in focused boom with little shift in caustic surface to upper atmosphere in the illumination zone. For top and bottom boundaries set at Z [2.5, -3.0], the p_{max} increases by 3.01% and the second pressure peak increases by 2.7%. It's concluded that effect of the location of boundary is not very sensible for sonic boom focusing, except the change in top boundary which is the source location for incoming wave.

The third parameter for investigation is the effect of the incoming shock foot-print width and its initial shock strength. The results show that increasing shock strength along with footprint width significantly increases the peak overpressure at caustics. The reference case has dimensionless width and strength of 1.0 and 1.0 for the incoming N wave. If the footprint is increased to 1.5 without changing the initial shock strength shows increase in focused boom. It is observed that the footprint width (FPW) wave of 1.5 provides a longer time for interaction between the incoming wave and outgoing wave, producing higher super boom of 3.2. It is higher by 10.47% in comparison with the reference case.

However, when the FPW is increased to 2.0 keeping the strength as 1.0, then the super boom drops down to 2.3575, which is a decrease of 18.67% in comparison with the reference case. On the other hand, if the FPW is kept at 1.5 and the strength of the incoming shock increased to 1.5, then super boom increases to 5.47, which is about 88.73% increase in peak pressure level. Further increasing foot print width to 2.0 and initial shock strength to 2.0 shows about 98.30% increase with p_{max} = 5.7482in peak pressure at the caustic surface. The location of caustics surface found to be shifting upward with increase in footprint width and shock strength. The doubling the parameters give about 140 % shifts in caustics surface toward the upper atmosphere from the base

case. It is observed that the footprint width wave with 1.5 provides longer time for interaction between the incoming wave and outgoing wave, producing higher super boom.

Non linear atmosphere is may affect the sonic boom focusing phenomenon. Increasing viscosity of the atmosphere μ has direct effect on reduction in peak pressure at caustic surface. Grid must be fine enough to be able to predict the focusing phenomenon. The grid was refined in the τ direction keeping the grid fixed in the Z direction. The grid independence study result shows asymptotic convergence with a p_{max} increase of 5.49% and with the above comments the sonic boom focusing parametric study is concluded.

6.3 Summary - Boom Mitigation for Delta Wing Geometry

Biconvex delta wing is considered as base line geometry for mitigating the sonic boom ground signature. Base line aerodynamic component, biconvex delta wing has a maximum thickness ratio of 5.0% of the chord and considered flying at 40,000 ft altitude with Mach number of 2.0. Maximum thickness ratio, maximum camber ratio, dihedral angle and nose angle of the front lower portion of the wing are considered the important design parameters to be studies. Individual effects of the design variables on the near-field overpressure and the aerodynamic performance are presented and discussed [82, 83]. This is followed by combined effects and optimization of the wing parameters for low boom ground signature with least loss in lift to drag ratio.

CFL3D [30] Euler solver is used for the computational results produced for individual studies of thickness, camber, nose angle and dihedral angle. Later CFL3D [30] also used for combined studies and optimization work of delta wing design parameters at zero degree angle of attack study. Structured grid adaptation is done using grid adaptation and shock fitting algorithm GASF [35]. Shape optimization study for AOA = 2.24 degree is carried out using FUN3D [32] software on unstructured mesh. Unstructured meshes are produced using Gridgen software [33] and ICEM CFD meshing [84] software. Optigrid software [78] is used for improved mesh adaptation. Grid adaptation technique significantly improves the near field solution and thus vital for design and optimization of

the sonic boom problem where discontinuities in the CFD solution are important and need to be properly captured.

In the end optimization and desirability studies is carried out for low boom configuration. Optimal shape design for low sonic-boom ground signature and the least degradation effect on the aircraft aerodynamic performance are the main goals in the present work. Multi objective optimization is employed to obtain the optimized design variables. For the study both the objectives are given equal importance. A multi objective optimization study carried out with AOA= 0 deg and AOA = 2.24 deg.

6.4 Conclusion - Boom Mitigation for Delta Wing Geometry

According to individual effect study lower bound value for maximum thickness ratio and nose angle is favorable for low boom design. For maximum camber ratio and dihedral its other way around and having higher values lead in favor of mitigating the boom impact in the ground. However it is also discovered in individual investigating of design parameters that increasing camber also increases the drag coefficient and increasing dihedral result in loosing the lift. Nose angle is found not to be very sensitive to aerodynamic performance; however reduction in lower surface nose angle has a beneficial effect on aerodynamic performance. Increase in dihedral angle reduced the boom impact but found to be decreasing life coefficient.

Under the individual effects studies least boom effect measured with 2.0 deg of lower surface nose angle, 1.0 % of maximum thickness ratio for lower surface, maximum camber ratio of 2.0 % of the chord at the mid chord location and 20.0 degree of dihedral angle. The maximum reduction is boom level is noticed with thickness and camber of the delta wing. As compare to 2.5 % of lower surface thickness of base wing, 1.0 % lower surface thickness reduced the boom level from 0.07 to 0.03; about 150% reduction in thickness gives about 133 % reduction in leading shock overpressure for leading shock. A similar reduction is observed with trailing shock as well. Lower surface maximum thickness ratio has decreased the boom level as well found be favorable for both lift and

drag coefficient. For the thickness study only lower surface thickness is changed and upper surface thickness is kept unchanged to 2.5 % of the chord.

In maximum camber effect investigation the near field overpressure ratio is decreased from 0.062 to 0.03 in leading shock and trailing shock is decreased from -0.092 to -0.022 with 2.0 % of the max camber. This represents 51.61% decrease in leading shock strength. The lift coefficient is found to be increasing with camber but the drag coefficient has also shown significant increase. Camber and thickness plays major role in controlling the shock strength and thus the sonic boom ground signature.

Dihedral study show significant decrease in overpressure and hence sonic boom up to 20 deg. The maximum reduction in near field overpressure is achieved is about 19% with 20 degree of dihedral angle. Lift coefficient has decreased from 0.00644 to 0.000147 and drag coefficient has increased from 0.00464 to 0.005 with 20.0 deg. Nose angle does not change the shock at the rare portion of the wing but the leading shock is reduced by about 15 % with 2 deg of lower surface nose angle.

The Design-Expert [34] software is used for optimization of the combined parameters. The results of optimization show that a combination of values of the thickness ratio, camber ratio, nose angle and dihedral angle produces a substantial decrease in the sonic-boom ground signature up to 61.57% for AOA = 0 deg and 64% for AOA = 2.24 deg case. Decrease in lift coefficient and a small increase in the drag coefficient is discovered with huge reduction in sonic boom level. The design change shows an excellent potential of these parameters to substantially reduce the boom ground signature and meet the acceptable criteria by FAA [11].

The optimized case for minimum sonic boom is having a nose Angle=2.0 deg, thickness=1.5 %, camber =1.5 %, dihedral =19.80 deg for AOA = 0.0 deg. It was also discovered that only considering three design parameters excluding the dihedral can result in lower decrease in sonic boom level. Including dihedral the overpressure and hence boom reduction is increased by 11.57% for AOA = 0 deg case. The study

conducted at zero angle of attack does not produce any lift for biconvex wing however within the design domain the loss in aerodynamic performance measured in term of C_l/C_d lift to drag ratio is found to be about 3.566 % with the best C_l/C_d.

The individual study conducted for AOA =2.24 deg also shows that having a higher values of camber toward 1.5% and lower values of thickness lesser or equal to 1.5% is most desired, keeping in mind the objectives and research goal. Similar observation have been made to have a lower values for nose angle and higher values of dihedral angle as in the case of AOA= 0.0 deg.

Optimization result obtained for AOA = 2.24 [86] shows that having a maximum thickness ratio = 1.5%, maximum camber ratio =1.5, lower surface nose angle = 2.0 deg and dihedral angle =19.88 degree gives the best design for the objective set for the study. Shock strength measured in term of density jump and the aerodynamics performance is measured in term of the ratio of lift to drag coefficient.

The Optimized geometry has a flat top density signature after the leading shock of the wing. In comparison of the original biconvex delta wing the leading shock strength of the optimized wing has reduced by 64 %.The trailing shock for optimized wing has almost disappeared. Aerodynamic performance has not degraded as compared to biconvex wing, however within the design domain comparing with the other possible shape for the highest C_l/C_d, one looses about 1% of C_l/C_d for AOA = 2.24 degree case.

Multi factor interaction and desirability studies were conducted for design variables to see their effect in 2, 3 and 4 design parameters interactions. A desirability study for the lift to drag ratio also suggests having a higher values of camber and lower values of thickness. A desirability study for the lift to drag ratio for dihedral and nose angle suggests having a higher values of dihedral and lower values of nose angle. A desirability studies for aerodynamics performance also confirm the individual investigation of the design parameters.

6.5 Recommendation for Future Work

Future recommendations are made for sonic boom focusing and shape optimization for sonic boom mitigation research.

6.5.1 Recommendation for Sonic Boom Focusing Research

1. All the studies are conducted for constant non linear viscosity values of $\mu = 0.08$. Non linear atmospheric effects are ignored and recommended for future work.
2. Atmospheric turbulence effects are also ignored for sonic boom focusing problem and may be included in future work.
3. Secondary boom effects [26] are not included in the current work considering it's only involved with the interaction of very weak shock waves and may be included in further studies.
4. All the computational results obtained for two dimensional flow situations and a complete three dimensional solution might improve the predictability of super boom effect and is recommended for future work.
5. Computational methods based on characteristic grid system would drastically reduce the computational time and is recommended for future work.

6.5.2 Recommendations for Mitigation and Optimization Research

1. The current work is limited to investigation and optimization of the delta wing geometry for sonic boom studies. One probably needs to consider the wing body configuration to better understand sonic boom problem of supersonic transport aircraft design.
2. Distribution of thickness and camber can be used instead of maximum thickness and maximum camber ratio as a criterion for optimization.
3. Dihedral angle effects are considered for the study. Anhedral wing effect can also be considered as a parameter for mitigation study.
4. Active boom controlling strategies to address the mitigation problem can also be employed nose piece addition, suction and blowing, spray of plasma flow and variable nose geometry are just a few.

5. Gradient based optimization or genetic algorithm can be used for the optimization process with enhanced accuracy in optimizing the design variables. Inverse design optimization can also be used as a choice for the optimization problem.
6. In this study as in many other design studies, only the outdoor effect on humans has been considered as the minimizing criterion. However, due to the high energy content of the sonic boom ground signature at low frequencies that excite structural vibrations, indoor noise and building response could be critical. Future design studies should involve a frequency analysis of the pressure signature. The important parameters in this respect would be the rise time and the duration of the pressure signature.

REFERENCES:

1. Whitham, G. B., "The flow pattern of a supersonic projectile," Communications on pure and applied mathematics, vol. V, PP 301–347, 1952.
2. Whitham G.B., "On the propagation of weak shocks." J. Fluid Mech., PP 290–318, 1956.
3. Busemann, A., "The relation between minimizing drag and noise at supersonic speeds," Proceedings of the conference on high-speed aeronautics, PP 133–144, Jan. 1955.
4. Walkden, F., "The Shock Pattern of a Wing-Body Combination Far From the Flight Path." Aeronautical Quarterly, Vol. 9, PP 164-194, May 1958
5. Jones, L. B., "Lower Bounds for Sonic Bangs." J. Royal Aeronautical Soc. 65, 1-4 (1961)
6. McLean F. E., "Some Non-asymptotic Effects on the Sonic Boom of Large Airplanes" NASA TN D-2877, 1965
7. Carlson H. W., "Influence of Airplane Configuration on Sonic Boom Characteristics" , J. Aircraft 1, No. 2, 82-86, 1964
8. Hunton, Lynn W., "Current Research in Sonic Boom." NASA SP-180, PP 57-66, May 1968.
9. George, A. R, "Reduction of Sonic Boom by Azimuthal Redistribution of Overpressure," AIAA Paper No. 68-159, 1968.
10. Seebass, R., "Sonic boom theory," Journal of Aircraft, vol. 6, PP 177–184, May 1969.
11. Federal Aviation Authority, Federal Register / Vol. 68, No. 100 / Friday, May 23, 2003 / Proposed Rules 14 CFR Part 91
12. Guiraud J. P., "Geometrical Acoustics, Ballistic Noise of Supersonic Aircraft and Focusing", J. Mech. 4, 1965, PP 215-267 (in French)
13. Pawlowski, J. W., "DARPA QSP Supersonic Shaped Boom Flight Experiment (Invited)," AIAA paper 2003-3577
14. Henne, P. A., "A Gulf stream perspective on the DARPA QSP program and future supersonic initiatives." http://www.aee.faa.gov/noise/aee100files/SonicWkshp/3-Panel1-HenneGulfstream.pdf, 2003

15. Aerion Business Jet Program, http://www.aerioncorp.com/tech_sonic-boom-compliance.html
16. Coen Peter, "Shaped sonic boom demonstration." , http://www.aee.faa.gov noise/aee100_files/SonicWkshp/2-Panel1-Graham-Northrop.pdf, 2003
17. Pederson, "Sonic boom technologies and challenges." http://www.aee.faa.gov noise/aee100_files/SonicWkshp/3-Panel2-Pederson-Lockheed.pdf, 2003
18. George, A. R., "Lower bounds for sonic booms in the midfield," AIAA Journal, vol. 7, no. 8, PP 1542–1545, 1969
19. Seebass, R., "Minimum Sonic Boom Shock Strengths and Overpressures." Nature 221, PP 651-653, 1969
20. Darden C, M., "Minimization of Sonic-Boom Parameters in Real and Isothermal Atmospheres". NASA TN D-7842, 1975.
21. Seebass, R., and George, A. R.,"Sonic-Boom Minimization." J. Acoustic. Soc. America, Vol. 51, No. 2 (pt. 3), PP. 686-694, Feb. 1972
22. Hunton, Lynn W. "Current research in sonic boom". NASA SP-180, PP 57-66, May 1968.
23. Carlson, Harry W., Barger, Raymond L.; and Mack, Robert J. "Application of Sonic-Boom Minimization Concepts in Supersonic Transport Design." NASA TN-D-7218, 1973.
24. Bobbitt, P., Kandil, O. A. and Yang, Z., "The Beneficial Effects of Wing Dihedral on Sonic Boom," AIAA 2003-3273-CP, Aero acoustics Conf., Hilton Head, SC.
25. Chan K M, "Supersonic aircraft optimization for minimizing drag and sonic boom", PhD Dissertation Stanford University Aug 2003
26. Kaouri K., " Secondary Sonic Boom", PhD Dissertation Somerville College Oxford University 2004
27. Leatherwood Jack D., Brenda M. Sullivan, Kevin P. Shepherd, David A. McCurdy, and Sherilyn A. Brown, " Summary of recent NASA studies of human response to sonic booms" Jan 2002 J. Acoustical Society of America. PP 586-598
28. Change H.K., Lee C.J. and Edwards J.R. "Sonic-boom generated sound field under a wavy air–water interface: Analyses for incident N waves", J. Acoust. Soc. Am. 118 (4) PP 2201-2209, October 2005

29. Plotkin, K. J., "Sonic Boom: Origins, Modeling and Effects", Wyle laboratories June 2004
30. CFL3d Version 6.0, web site http://cfl3d.larc.nasa.gov/Cfl3dv6/cfl3dv6.html
31. Kandil, O. A.; Yang, Z.; Bobbitt, P. J.: Prediction of Sonic Boom Signature Using Euler-Full Potential CFD with Grid Adaptation and Shock Fitting. AIAA CP 2002-2543, June 2002.
32. FUN3D CFD Software http://fun3d.larc.nasa.gov
33. Gridgen software from Pointwise Inc www.pointwise.com
34. Design-Expert and Design-Ease software from Stat-Ease www.statease.com
35. Kandil O.A. and Yang Z. "Codes and applications for the full potential equation methodology of three dimensional sonic boom propagation", Report Submitted to Eagle Aeronautics and NASA LaRC, Aug 2004.
36. Thomas C.L. "Extrapolation of sonic boom pressure signatures by the waveform parameter method" NASA TN, D-6832, 1972
37. Thom R., "Structural Stability and Morphogenesis", Benjamin Reading 1972, PP 72-107
38. Berry, M. V. ''Waves and Thom's theorem,'' Adv. Phys. 25, 1–26, 1976
39. Airy G.B., "On the intensity of light in the neighborhood of a caustic" Trans. Camb Phil. Soc., PP 379–401, 1838
40. Sturtevant B. and Kulkarny V.A., "The focusing of weak shock waves". J. Fluid Mech., PP 651–671, 1976
41. Keller J.B., "A geometrical theory of diffraction", In Proc. Symposia Applied Math., PP 27–32 McGraw-Hill, 1958
42. Buchal, R. N., and Keller, J. B. ''Boundary layer problems in diffraction theory,'' Comm. Pure Applied Math 13, PP 85–114. 1960
43. Seebass A. R., "Nonlinear acoustic behavior at a caustic". (Proceedings of the third conference on sonic boom research.). NASA SP, 255:87–120, 1971.
44. Gill, P. M. and Seebass, A. R., "Nonlinear Acoustic Behavior at a Caustic: An Approximate Analytical Solution," AIAA Paper 73-1037, 1973
45. Plotkin, K, J.; and Cantril, J. M., "Prediction of Sonic Boom at a Focus," Wyle Laboratories Res. Staff Report. WR 75-7, Oct. 1975

46. Downing, M., Zamot, N., Moss, C., Morin, D., Wolski, E., Chung, S., Plotkin, K., and Maglieri, D., "Controlled focused sonic booms from maneuvering aircraft", J. Acoust. Soc. America., 104, PP 112–121, 1998

47. Cramer M.S., and Seebass A. R., Focusing of a Weak Shock Wave at an arête, J. Fluid. Mech., 88, PP 209-222, 1978

48. Zabolotkkaya, E. A. and Khokhlov, R. V., "Quasi-plane waves in the non-linear caustics of confined beams," Sov. Phys. Acoust. 15, PP 35-40, 1969

49. Rosales R.R. and Tabak E.G., "Caustics of weak shock waves". Phys. Fluids, 10(1), PP 206–222, 1998

50. Auger, T. and Coulouvrat F., "Numerical Simulation of Sonic Boom Focusing," AIAA J., Vol. 40, No. 9, PP 1726- 1734, September 2002

51. Coulouvrat, F., "Focusing of Weak Acoustic Shock Waves at a Caustic Cusp", Wave Motion, 32, PP 233-245, 2000

52. Hays, W.D., Haefeli, R. C.; and Kulsrud, H. E., "Sonic Boom Propagation in a stratified Atmosphere, With Computer Program," NASA CR 1299, Aero. Res. Associates of Princeton, Inc., April 1969

53. Hayes, W. D., "Similarity rules for Nonlinear Acoustic Propagation through a Caustic," Proceedings of the Sound Conference on Sonic Boom Research, NASA SP-180, PP 165-171, 1968

54. Coulouvrat, F., "Sonic Boom in the Shadow Zone: a Geometrical Theory of Diffraction", J. Acoustic. Soc. Am. 111, PP 499-508, 2002

55. Coulouvrat, F. and Marchiano, R. ," Nonlinear Fresnel diffraction of weak shock waves", J. Acoust. Soc. Am., 114, PP 1749-1757, 2003

56. Marchiano, R. and Coulouvrat, F., "Numerical Simulation of Shock Wave Focusing at Fold Caustics with Application to Sonic Boom," J. Acoustic. Soc. Am. 114, No 4, PP 1758-1771, October 2003

57. Coulouvrat F., "Equations of weakly nonlinear acoustics in a strongly heterogeneous , high speed moving fluid – Paraxial approximation in generalized ray coordinates" Paris, February 2005

58. Kandil, O. A. and Zheng, X., "Prediction of Super boom using Computational solution of Nonlinear Tricomi Equation," AIAA Paper 2005-6335, AIAA Atmospheric Flight Mechanics Conference, San Francisco, CA, August 2005.
59. Plotkin, K. J. ''State of the art of sonic boom modeling,'' J. Acoust. Soc. Am. 104, 1998
60. Page J. A. and Plotkin K. J., ''An Efficient Method for Incorporating Computational Fluid Dynamics into Sonic Boom Prediction,'' AIAA-91-3275 September 1991
61. SOBER Sonic Boom European Research program: Numerical and laboratory-scale experimental simulation http://www.pa.op.dlr.de/acoustics/sober.html
62. Siclari, M. J.; and Fouladi, Karoran, "A CFD Study of Component Configuration Effects on the Sonic Boom of Several High-Speed Civil Transport Concepts," NASA Conf. Pub. 10133, Ames Research Center, May 12-14, 1993.
63. George, A. R. and Seebass, R. "Sonic Boom Minimization Including Both Front and Real Shocks." AIAA J. 9, 2091-2093 (1971)
64. Seebass, R. and George, A., "Design and operation of aircraft to minimize their sonic boom," Journal of aircraft, vol. 11, no. 9, PP 509–517, 1974
65. Darden C M., "Sonic Boom Minimization with Nose-Bluntness Relaxation." NASA TP 1348, Jan. 1979
66. Darden, C. M., "The importance of sonic boom research in the development of future high speed aircraft" Journal of the NTA, PP 54–62, 1992.
67. Darden C M., Hayes Wallace D., George A. R., Pierce A. D., "Status of Sonic Boom Methodology and Understanding" NASA TP 3027, Jan. 1988
68. Darden, C. M., "Study of the limitations of linear theory methods as applied to sonic boom calculations," in Proceedings of the 28th Aerospace Sciences Meeting, American Institute for Aeronautics and Astronautics, Jan. 1990
69. Darden, C. M., "The importance of sonic boom research in the development of future high speed aircraft," Journal of the NTA, PP 54–62, 1992.

70. Alonso J., Jameson A. and Kroo I., "Advanced algorithms for design and optimization of quite supersonic platforms" AIAA 2002-0144, 40th Aerospace Science Meetings and Exhibits, Reno NV Jan 2002
71. Hyoung-Seog, Chung and Alonso J., "Supersonic business jet design using knowledge-based genetic algorithm with adaptive, unstructured grid methodology," 21st AIAA Applied Aerodynamics Conference, AIAA, June 2003.
72. Nadarajah S., Jameson A. and Alonso J., "Adjoint based sonic boom reduction for wing body configuration in supersonic flow", AIAA 2002-5547 Symposium on multidisciplinary analysis and optimization conference Atlanta GA Sept 2002
73. Myers R. and Montgomery D. C., "Response Surface Methodology: Process and Product Optimization Using Designed Experiments, 2nd Edition", Wiley Publication, Feb 2002
74. Kandil O.A., Ozcer I. A. , Zheng X. and Bobbitt P.J., "Comparison of full potential propagation code computations with the F-5E shaped sonic boom experiment program", AIAA 2005-0013, Reno NV, Jan 2005
75. Murman E. M. AND Cole J. D., "Calculations of plane steady transonic flows", AIAA J., PP 114-121, 1971
76. Kandil O. A. and Khasdeo Nitin, "Parametric Investigation of Sonic Boom Focusing Using Solution of Nonlinear Tricomi Equation" , AIAA 2006-0415, 44th AIAA Aerospace Sciences Meeting and Exhibit, Reno, Nevada, January 2006
77. Kandil O.A, Ozcer I. A. and Khasdeo Nitin, Sonic Boom Prediction, Mitigation and Focusing, 25th International Congress on Aeronautical Sciences , ICAS Hamburg Germany 2006.
78. Optigrid software from Numerical methods, http://www.newmerical.com/
79. Van Leer B., "Flux-Vector Splitting for the Euler Equations" 8th International Conference on Numerical Methods in Fluid Dynamics, Springer Lecture Notes in Physics no. 170, ed. E. Krause 1983
80. Roe, P. L., "The Use of the Riemann Problem in Finite Difference Schemes", Presented at the 7th International Conference on Numerical Methods in Fluid Dynamics, Stanford, CA 1980
81. USM3D CFD Software http://tetruss.larc.nasa.gov/usm3d/intro.html

82. Kandil O.A., Khasdeo Nitin and Isik Ozcer, "Sonic Boom Mitigation through Thickness, Camber and Nose Angle Optimizations for a Delta Wing," AIAA 2006-6636, keystone, CO, Aug. 2006

83. Khasdeo Nitin, Kandil Osama and Isik Ozcer, "Optimal Design Parameters for Sonic Boom Ground Mitigation", AIAA 2007-4109, 25th AIAA Applied Aerodynamics Conference, Miami Florida, June 2007

84. ICEM-CFD Mesh Generation Software, www.ansys.com/products/icemcfd.asp

85. Dervieux A., Courty, F., Vazquez, M. and Koobus, B., "Additive Multilevel Optimization and its Application to Sonic Boom Reduction," Numerical Methods for Scientific Computing – JP60 Meeting, Finland. June, 2002.

86. Khasdeo N. and Kandil O.A., "Sonic Boom Mitigation and Optimization for a Delta Wing Using Grid Adaptation Feature", AIAA YPSE, Johns Hopkins APL, Laurel MD, Nov 2007

VITA

I grew up in the central part of India; my native place is Betul Madhya Pradesh. I completed high school at Pandhurna and Betul. 2000, I completed my Bachelor's degree in Aerospace Engineering at the Aeronautical Society of India. In 2002I completed my Master degree in Aerospace Engineering at Indian Institute of Technology, Kharagpur India. I came to the United States for my PhD in Aerospace Engineering in January of 2005.

I like watching movies a lot; rather, I used to like it. Recently I just don't get enough time to watch movies. I'm found of visiting places and I travel, to every single opportunity I get to see new places. There are a few things I didn't get a chance to explore in the past; I am going to spent time on those. They include fishing, learning music (especially the drums) and participating in rural development projects.

This Dissertation was edited by Cathleen Rhodes.